UNIVERSITY OF SOUTHAMPTON

Direct UV-written Bragg gratings for waveguide characterisation and advanced applications

by

Helen L. Rogers

Thesis for the
degree of Doctor of Philosophy

in the
Faculty of Physical and Applied Sciences
Optoelectronics Research Centre

April 2013

UNIVERSITY OF SOUTHAMPTON

ABSTRACT

FACULTY OF PHYSICAL AND APPLIED SCIENCES
OPTOELECTRONICS RESEARCH CENTRE

Doctor of Philosophy

by Helen L. Rogers

Direct UV writing is an established fabrication technique allowing channel waveguides and photonic circuits to be defined in a photosensitive glass via an inscription method. A related technique, direct grating writing, enables Bragg grating structures to be defined in an interferometric dual beam set up, with definition of Bragg grating planes achieved via the periodic modulation of the interference pattern between the beams. A decade of prior work investigating the technique has led to devices for use in sensing, telecommunications, lasing and amplification applications. A requirement for greater understanding of the propagation characteristics of the waveguides has been identified, in order to maximise the efficiency and effectiveness of these devices.

In this thesis, a propagation loss measurement technique and a wavelength-dependent dispersion measurement technique are presented. Both depend on the presence of integrated Bragg grating structures which enable the propagation characteristics of the waveguides to be investigated. The loss measurement technique involves measurement of the Bragg grating strength, whilst the dispersion measurement technique enables the effective refractive index of the waveguide to be inferred from a measurement of reflected central grating wavelength. Applications of both techniques in a variety of situations have been investigated, with devices fabricated for use in quantum technologies and cold matter experiments amongst those produced.

Contents

List of Figures

List of Tables

DECLARATION OF AUTHORSHIP

I, Helen Louise Rogers, declare that the thesis entitled "Direct UV-written Bragg gratings for waveguide characterisation and advanced applications" and the work presented in it are my own. I confirm that:

- this work was done wholly or mainly while in candidature for a research degree at this University;
- where any part of this thesis has previously been submitted for a degree or any other qualification at this University or any other institution, this has been clearly stated;
- where I have consulted the published work of others, this is always clearly attributed;
- where I have quoted from the work of others, the source is always given. With the exception of such quotations, this thesis is entirely my own work;
- I have acknowledged all main sources of help;
- where the thesis is based on work done by myself jointly with others, I have made clear exactly what was done by others and what I have contributed myself;

Signed: _____

Date: _____

Acknowledgements

Suffice to say, this thesis would not have come about without the support of a great number of people, to whom I am truly grateful.

Prof. Peter Smith and Dr. James Gates, my supervisors, for providing a unique blend of ideas and an approachable source of information. Thank you for taking me on, and for enabling me to reach this point. And to Dr. Corin Gawith, for being there at the end, and volunteering to read my thesis, without you I would not be in a position to write this today.

Those who came before, Huw Major, Chris Holmes, Ben Snow and Richard Parker, for answering my questions without too many lies, and for making the lab an entertaining place to be. And to my fellow fourth years, Lewis Carpenter, Sumiaty Ambran, Chaotan Sima and Dominic Wales, thank you for your support and guidance, and for making me question everything I say.

Those who follow, Peter Cooper, Paolo Mennea and Stephen Lynch, and the others I have worked with, Sam Crabb and Matthew Posner. Thanks for all the questions, and I wish you all the best.

Those who I not only work with, but am happy to call my friends (you know who you are!), thank you for all the tea, cake and good times. To my OSA committee, for making my life easier than it could have been. And to Francesca Mountfort, Kate Sloyan, Kat Morgan, Jess Butcher and Siobhan Smith, thank you for all the cake and support, from near and afar.

To Jotham, my housemate, thank you for enabling baking.

To my family, to Mum, Jen and Clare especially, for putting up with Dad and I nattering about work. Thank you for everything.

And finally, to Tom, my better half, for putting up with the tears, tantrums and insane amounts of pudding. Thank you for always being there.

"What our ancestors would really be thinking, if they were alive today, is: "Why is it so dark in here?"

Terry Pratchett

Chapter 1

Introduction

In the consumer-driven telecommunications market of the 21st century, with technology such as on-demand high speed domestic internet access common place, it is easy to forget the significance of the advances in technology achieved to enable such wide-spread use. Only fifty-two years ago, the invention of the laser [1], a coherent source of radiation, enabled the later suggestion that photonic systems could be used to process and transport information with higher capacity than their electronic equivalents. In the intervening period, the use of photonic telecommunications systems has become prevalent, to such an extent that optical fibre is now cheap enough to be used to replace copper transmission wires from the local exchanges to the home, enabling improved data transmission speeds on the local scale.

For the long distance transport of information, photonic technologies have been widely used for decades, with the invention of optical systems such as the erbium doped fibre amplifier (EDFA) [2] allowing the replacement of electronic amplification systems by more efficient photonic equivalents. On a smaller scale, following Miller's vision of 'laser beam circuitry' in 1969 [3], on-chip optical equivalents of small electronic circuits have been proposed and demonstrated in the growing field known as 'Integrated Optics'. In order to compete with their electronic equivalents, integrated optical circuits are required to be cheap and efficient, and the fabrication technology suitable for mass production. The devices are also required to interface effectively with current silica fibre optical transmission systems, to avoid the costly replacement of the existing technology.

The investigation into integrated optics based on a planar silica platform is thus a logical step in the development of future telecommunications technology. The optical connection between an input silica telecommunications fibre and the silica on-chip circuitry is simpler in comparison to other materials, as low losses can be achieved at the fibre-planar boundary between similar materials. Indeed, devices such as the arrayed waveguide grating, for wavelength division multiplexing, have been produced in silica-on-silicon for a

number of years. It is investigation into the characteristics of silica-on-silicon waveguides that forms the majority of the work described in this thesis.

Investigation into integrated optical devices can be split into a number of broad research areas. One involves the emulation of equivalent electronic functionality, such as an all-optical switching device, which aims to improve the speed of data transmission and interpretation whilst maintaining a cheap, compact and readily manufacturable device. In addition, the development of equivalent optical systems to those achievable in bulk and fibre optics, including the EDFA, would result in cheaper, smaller devices with similar or increased efficiency, with the capability of mass production. This allows the implementation of integrated optical circuitry in a number of applications, including traditional telecommunications devices, but also in environmental sensing, biophotonics and quantum optics fields. In order for the technology to be deemed useful in these areas, various optical functions must be achieved on a single chip.

Many optical functions can be achieved in silica-on-silicon by varying the properties of the host planar layer. The simplest function is the guidance of radiation, via a channel of increased refractive index compared to the surrounding material, known as a waveguide, which has similar function to the core of an optical fibre. By bringing waveguides within close proximity of one another, coupling of radiation between the guides can be achieved. Interaction of the guided radiation with the external environment can be achieved by fabricating a waveguide close to the edge of a chip or machined channel, or exposing the waveguide to external influences by removing the cladding layer. These functions are similar to those observed in optical fibre systems, with the advantage of ease of interaction and the robust nature of the integrated on-chip components. Another function which can be introduced is the planar Bragg grating, a planarised version of the fibre Bragg grating, an element which has been subject to decades of investigation and application.

A Bragg grating is a series of weak reflectors within a bulk material or optical waveguide, achieved by varying the local refractive index of the glass on the wavelength scale. Each reflector is positioned a specific distance away from the next, known as the Bragg period, such that the radiation is reflected at the equivalent wavelength in the material, adding constructively in phase. Thus, the grating is a distributed reflector of a specific wavelength of radiation. The Bragg grating is a useful device in many of the above mentioned fields. For example, in telecommunications, the grating can be used to filter a specific wavelength within a channel, and in sensing, the change in the reflected spectrum of a grating can be shown to correspond to a specific change in environmental conditions, such as temperature, strain, or the presence of a specific chemical given pre-sensitisation of the device.

A decade of prior research by previous members of the author's group has led to a reliable method of fabricating Bragg gratings in silica-on-silicon waveguides. Direct

grating writing was first demonstrated by the group at the Optoelectronics Research Centre [4], and involves focussing two interfering UV beams into the photosensitive core layer of, typically, a doped silica-on-silicon chip. The interference pattern at the focus of the intersecting beams is inscribed into the core layer, creating the periodic index modulation required to form a Bragg grating structure. The waveguide sections between Bragg gratings can be inscribed within the same fabrication step, by translating the sample at speed so as to blur the interference fringes. The suitability of the method for inexpensive mass production of waveguide devices has been proved by the successful implementation of a similar system at spin-out company Stratophase.

In order for an integrated optical device to operate efficiently, however, measures must be taken to improve performance-inhibiting characteristics of the optical components. Propagation loss of an optical waveguide is important to consider, as in many fields, particularly telecommunications, loss inhibits the efficient transfer of data, or the extent to which a signal can be amplified in a device. In addition, dispersion of an optical signal as it propagates along an optical waveguide can lead to unwanted broadening of the optical signal in time, decreasing the efficiency of waveguides for signal processing applications. In order to minimise these effects, and thus improve device performance, a measurement must first be made of the characteristics of specific devices.

Given the nature of integrated optics and the aim to emulate and miniaturise bulk and fibre-based optical systems, it seems appropriate that the vast majority of techniques used to measure the loss and dispersion characteristics of planar waveguides are based on bulk and fibre based predecessors. However, as the waveguides under test are typically short and exhibit low loss and little dispersion over their length, these techniques typically exhibit large measurement errors as a result of the non-optimised techniques. New techniques must be sought to enable accurate and precise measurement of these application-defining waveguide characteristics.

The integration of Bragg gratings into planar waveguides provides a means of interrogating these waveguide characteristics. Via observation of grating parameters such as central wavelength and peak reflectivity, information about the dispersion and propagation losses of the waveguide can be gleaned. This thesis presents a propagation loss measurement technique and a total chromatic dispersion measurement technique, both based on integrated Bragg grating structures. These techniques are suitable for the accurate and precise measurement of these parameters in short waveguides.

1.1 Context

All research detailed within this thesis was carried out at the Optoelectronics Research Centre, where a decade of prior work into the materials and fabrication processes of UV-written waveguides has enabled a firm footing for the work described here. In this

section, the work described in this thesis is given context within the wider research of the group as a whole, enabling an understanding of the starting point and subsequent impact of the work undertaken.

Prior to 2005, research into fabrication of doped silica-on-silicon layers was undertaken, with the aim of producing samples suitable for both traditional etched channel waveguide fabrication, and also in the development of laser written waveguides based on the work by Svalgaard [5]. Research into fabrication of flame hydrolysis deposition (FHD) layers [6] and plasma enhanced chemical vapour deposition (PECVD) layers [7] was undertaken, via design and implementation of soot deposition systems and furnaces. Running concurrently with these projects, research into the fabrication of channel waveguides and Bragg gratings using a laser definition method was undertaken, with the resulting demonstration of the first single-step waveguide and Bragg grating laser definition process, direct grating writing (DGW) [8]. This enabled the design and implementation of waveguides in rare-earth doped materials fit for use as waveguide amplification and lasing devices [9], as well as telecommunications and sensing devices in more traditional silica fibre-like materials.

In October 2005, a fire in the Mountbatten clean room complex at the Optoelectronics Research Centre destroyed the material fabrication systems. A subsequent shift in research efforts was made away from material research, toward the design and implementation of waveguide and grating-based devices using the laser lab based DGW system. Photosensitive FHD wafers were bought in, enabling research in this broad area to continue until the FHD system at the University of Southampton came back online in autumn 2011. Devices for environmental sensing, including temperature, strain and chemical interactions were investigated [10,11], and developments were made in telecommunications devices with on-chip adaptive functionality [12]. In addition, research into waveguides at short wavelengths, suitable for quantum technologies, was undertaken [13].

Given that this thesis is based on work starting in autumn 2009, the majority of research described was undertaken using the DGW system and commercially purchased FHD wafers. The prior use of the waveguide and grating devices fabricated in this way was application based, with a wide variety of uses in multiple fields. Little research had been undertaken into the propagation characteristics of the fabricated waveguide channels, and the opportunity to interrogate waveguides using the integrated Bragg grating structures was identified. This led to research into the two major components to this thesis, the implementation of a propagation loss and a dispersion measurement technique based on integrated Bragg grating structures.

In addition, during the course of this project, a number of further related projects were undertaken. Collaboration with other research institutions, including the University of Oxford, Imperial College London and the University of Malaya, applied these measurement techniques to a variety of applications, for use in quantum information

technology, cold matter research and rare-earth doped waveguides respectively. Additional collaboration within the author's research group led to the use of the measurement techniques in other materials, including flat fibre, and the use of fabricated waveguides and Bragg gratings in conjunction with micromachined elements for environmental and chemical sensing applications. The implementation of improvements to the DGW system, primarily the inclusion of a phase control interferometer modulation system, was also undertaken in collaboration with other group members. Thus the use of DGW as an integrated optical fabrication and analysis tool has been investigated, with potential implementation in a vast range of applications.

1.2 Alternative planar waveguide and Bragg grating realisation

As one can imagine, the breadth of methods suitable for fabrication of structures used in integrated optics is wide and varied. For the means of justifying the choice of FHD and DGW as the primary fabrication methods considered in this thesis, a brief review of similar techniques is provided. In the case of waveguide fabrication, only buried channel waveguide manufacturing methods are considered, as these form the majority of waveguides fabricated throughout the course of this project. In the case of Bragg gratings, a review of other methods which take advantage of the photosensitivity mechanisms of materials are discussed.

The most common method of defining buried channel waveguides is by etching a rib waveguide structure in a planar substrate, then subsequently depositing a cladding layer to bury the guide. The planar substrate in this case could be fabricated by one of a vast number of techniques, including soot deposition techniques [14], laser deposition techniques [15] or spin-coating of solutions onto substrates [16]. The etching step is achieved by first spinning a photoresist on top of the core layer, and then using a contact mask during the resist developing stage to form the desired waveguide pattern on the sample surface [17]. The unwanted area can then be etched away via a wet chemical etch or an ion-beam-sputter etch. A suitable cladding layer can be deposited to enclose the waveguide, forming the buried channel structure desired.

The photolithographic process of creating a pattern on a sample surface can also be used in strip-loading, where a dielectric or metal strip is defined on top of the core guiding layer [16]. The effect of the strip on the propagating electric field is to cause radiation to be confined in the lateral direction, and the technique can be used on the surface of a slab waveguide to create a buried channel waveguide. Figure 1.1 shows waveguides obtained via the photolithographic rib and strip-loading methods, and the UV writing technique used to fabricated buried channel waveguides.

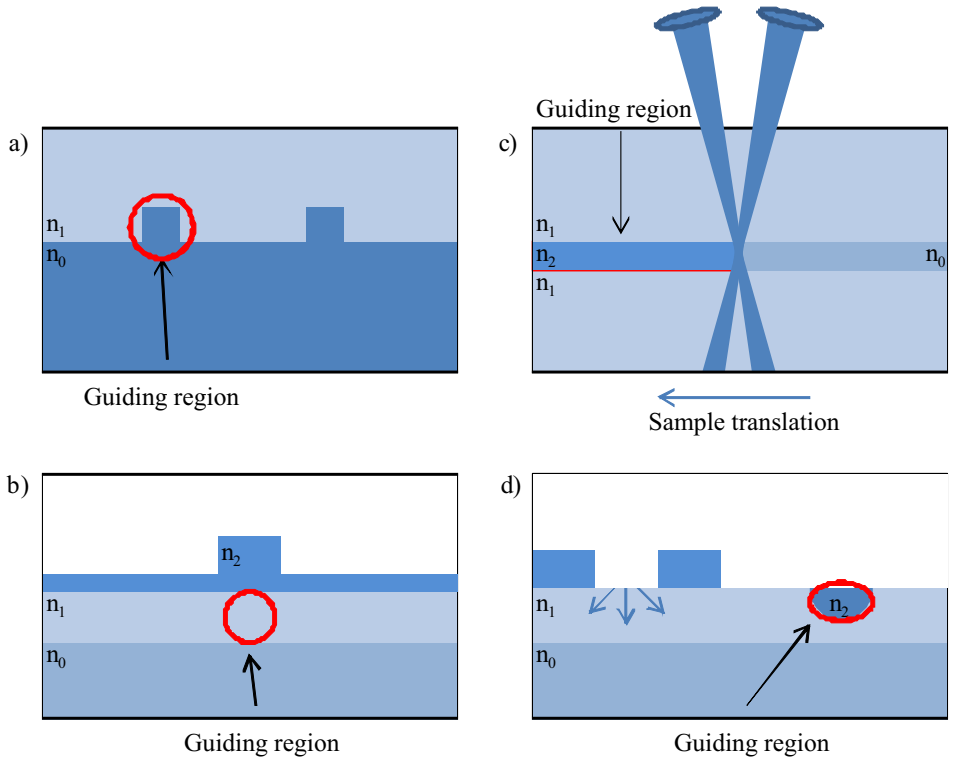

Figure 1.1: Fabrication techniques typically used to obtain buried channel waveguides. Photolithography is used to obtain the etched rib waveguide, a), the strip-loaded waveguide, b), and the ion implanted waveguide, d). Direct UV writing, c), can also be used to fabricate buried channel waveguides within a photosensitive core layer.

These methods all start with a planar slab waveguide, post-processed to allow confinement in the lateral direction. In contrast, ion implantation [18] or ion exchange [19] can be used to dope a prospective core region with atoms to create a guiding channel. A mask is used to define the dimensions of the channel waveguide and thus a buried waveguide can be achieved. Focussed beam writing, such as electron beam writing [20], has been demonstrated to create three-dimensional buried guiding structures in mainly silicon-based materials, by modification of material buried within an initial block. Femtosecond laser writing techniques [21] also produce a buried core waveguide, defined by the tight focus of the beam. These techniques have the advantage that they can be performed outside of the clean room environment, as the buried core avoids the surface contamination issues common in photolithographic techniques.

Bragg grating fabrication in these buried waveguides is achieveable, but limitations defined by the fabrication methods can restrict the quality of produced structures. In any method using a photolithographic mask to define the structure, the mask quality and resist exposure define the smallest magnitude of structure that can be fabricated. Structures hundred of nanometres wide, on a similar scale to the Bragg period required for a 1550 nm grating in silica, can be achieved, but the repeatability of spacing required for a Bragg grating structure could be hard to obtain, given the difficulty of creating perfectly vertical structures using the mask techniques. The beam writing techniques

could provide a better alternative, but the point-by-point definition of grating planes in the single focussed beam set up, via translation of the sample over one grating period between exposures, compounds errors in sample position over the millimetre scale of the completed grating. In the case of long period gratings, however, the point-by-point technique is an effective fabrication method, due to the larger grating planes involved [22].

Other techniques of fabricating Bragg grating structures involve using photosensitive silica-based glasses along with a UV irradiation system to create the refractive index modulation in the core necessary for Bragg grating operation. As well as the point-by-point method [23], phase masks or an interferometric set up could be implemented. In the case of phase masks, a relief silica mask is designed so that the first diffracted orders from the mask interfere with one another, creating a beam modulation, and thus refractive index modulation, in the photosensitive core layer. The spatial coherence of the input beam is critical to ensure the modulation is uniform throughout. To fabricate Bragg gratings with different central wavelengths [24], both the incident beam and the fibre or phase mask must be moved to create different inscribed periods, a process which is not trivial. An alternative method of creating an interference pattern is by use of an interferometer, focussing and overlapping the two arms to create a modulation in the focussed spot, within the photosensitive core, of the period of the Bragg grating desired [4]. This, once again, creates the refractive index modulation necessary to create a Bragg grating. The interferometric method does not involve expensive phase masks or the small spatial errors associated with phase masks and point-by-point techniques respectively. Any spatial errors can be averaged over a number of exposures, causing fewer errors in the spectral response of the grating.

Having chosen the interferometric Bragg grating definition technique for its flexibility and low cost in comparison to other methods, an appropriate photosensitive silica slab waveguide is required to enable grating production in an integration-suited platform. Two common methods for producing these structures are by FHD and PECVD, techniques suitable for effective fabrication of doped silica layers for enhanced photosensitivity. PECVD involves pumping gas phase chemical precursors into a deposition chamber where an applied radio frequency electric field causes free electrons to be accelerated and collide with precursor molecules [25]. This results in the production of free radicals, which can then be adsorbed onto the wafer surface, creating a uniform stable glass film on the substrate. A consolidation phase is required to obtain suitably low losses for optical applications. In comparison, the gaseous precursors in an FHD chamber are burned in a hydrogen-oxygen flame, causing hydrolysis and oxidation, to deposit doped silica soot on the substrate surface [26]. A consolidation phase is then required to create a dense glass layer suitable for DGW.

Either PECVD or FHD could be used for the fabrication of the devices described in this thesis. Both have advantages for use in different circumstances. PECVD is an industrial

standard and has the advantage for mass production of uniform wafers, but cannot produce the material thickness required to provide the cladding layers for many integrated optics applications [27]. For research purposes, FHD allows small scale multiple wafer production over a period of around one day, including consolidation, enabling wafer prototyping to be readily achieved. In addition, during the period when in-house wafer fabrication facilities were unavailable, FHD wafers manufactured to our specification could be obtained from industry.

1.3 Presentation structure

The work undertaken during the course of this project builds upon previous research, and thus some cross-over in the content of chapters between prior art and new research is to be expected. In addition to the experimental work described in the two chapters on measurement technique development (Chapters 5 and 6), additional experimental developments were made toward improved fabrication of UV written Bragg gratings (Chapter 4). Background theory relating to the work described in each chapter is included in that specific chapter rather than in a theory or prior art section, as a means of emphasising the relevant information when appropriate. As such, the initial theoretical consideration of the propagation of radiation in waveguides and Bragg grating structures (Chapter 2) does not include information about propagation loss and dispersion characteristics, which are included in the relevant experimental chapters. However, these initial theoretical considerations enable an understanding of the interaction of radiation with all fabricated structures discussed, providing a basic foundation to enable the characteristics of measured devices to be correctly interpreted.

Chapter 3 introduces the fabrication and characterisation procedures necessary for the devices described in this thesis. Drawing comparison to the theoretical considerations, the preparation of the photosensitive slab waveguide is introduced by description of the FHD process. A section discussing photosensitivity and the proposed mechanisms for the fabricated FHD substrates follows, leading into a description of the DGW system most commonly used in this project, with the modulation provided by an acousto-optic component. Chapter 3 also decribes the basic fabrication steps necessary to produce simple Bragg grating structures and channel waveguides. Following this, a description of the methods used to characterise the grating structures is provided, for use as a reference in later chapters. This chapter provides the basic information necessary to understand the methods of fabrication and data collection for the devices described later in this thesis.

Having dealt with the fabrication techniques required to physically realise the simple grating structures, Chapter 4 describes the parameters by which more complex structures can be formed. The scope of the system to produce structures with different

central wavelength, strength and bandwidth is discussed, with reference to uniform grating structures. In addition, more complex structures involving apodisation, phase shifts and spectral chirp have been fabricated and the means of manufacture will be described. To conclude, physical modifications to the system introduced during the course of the project will be described. The phase control system for improved refractive index contrast, and the extension of the achievable central wavelength band to shorter and longer periods have been implemented and will be discussed.

Given the previous discussion of fabrication and characterisation methods, the later chapters describe the development of the grating-based loss and dispersion measurement techniques, and the effective application of these methods in various scenarios. Chapter 5 describes the propagation loss measurement technique development phase, first outlining the sources of loss within a waveguide and what is required of an effective measurement technique. A review of other techniques is given for comparison and to promote the need for a robust measurement method suitable for short, low-loss planar waveguides. The theoretical basis for the technique is then described, outlining the considerations necessary throughout the fabrication and data analysis stages when applying the technique, before the specific waveguide used for method verification is introduced. To conclude, various applications of the loss technique carried out in collaboration with other researchers are presented, highlighting the versatility and potential scope of the method in the broader field of integrated optics. Use of the technique in different materials and to interrogate physically micromachined components is described.

Chapter 6, describing the development of a dispersion measurement technique using planar Bragg gratings, follows a similar structure. The introduction and description of dispersion nomenclature is provided, alongside theoretical determination of the material and waveguide dispersion components which contribute to the overall measured total dispersion. A description of the device fabrication and characterisation follows, with calculation of the waveguide and material dispersion components of this guide. Once again, applications of the technique are presented, with scope to use the technique in the measurement of the dispersion of higher order modes of the waveguide. To conclude, a collaborative venture with the Oxford Quantum Technologies Laboratory is described, as use of the dispersion measurement technique to aid in predicting the spectral position of four wave mixing components has led to an effort to investigate the use of direct UV written silica-on-silicon waveguides as on-chip single photon sources.

Given the investigation into these techniques, and the ongoing improvements to the DGW system, as well as recent access to FHD fabrication facilities once again, the scope to use the techniques described here to produce devices for a wide range of applications grows considerably. To conclude this thesis, the final chapter summarises the advances made and potential applications of the combination of FHD and DGW considering these characterisation methods.

Chapter 2

Waveguide and Bragg grating theory

The experimental work presented in this thesis is fundamentally linked to the theoretical considerations of the behaviour of waveguides and Bragg grating structures. In order to understand the guidance characteristics of a waveguide, or the reflective properties of a specific Bragg grating filter, an appreciation of waveguide and Bragg grating theory is required. The analysis of such structures forms the basis of the experimental work described in this thesis.

The UV written waveguides and Bragg gratings presented in this thesis are complex structures, with graded index behaviour dependent on the UV writing conditions and photosensitivity of the specific sample on the day of fabrication. To consider each of these factors in a rigorous manner is superfluous to the understanding required to carry out the fabrication and analysis described in this work. This chapter presents a simplified version of the system, the step index waveguide, starting from the principles of light interaction at a plane interface. The modelling techniques applied using mode solving software will also be presented. Following the consideration of waveguide theory, coupled mode theory will be applied to enable understanding of the Bragg grating devices. A description of the various types and applications of Bragg gratings will precede presentation of the results of application of coupled mode theory in order to obtain grating parameters such as wavelength detuning, maximum grating reflection strength and bandwidth of the gratings. Knowledge of the theoretical basis of these parameters enables advanced grating characterisation as described later in this thesis.

2.1 Waveguide theory

A waveguide is a structure that confines and directs the propagation of radiation. The propagation depends not only on the optical properties of the materials used to fabricate the guide, but also the geometry of the materials and how the incident radiation interacts with the structure. When considering a simplified step-index case, there are distinct refractive index boundaries which contribute to both the propagation losses and dispersion of the waveguide, as discussed in the experimental sections of this thesis.

This section describes the waveguide theory required to understand propagation of radiation in a step index waveguide. In the case of weakly guiding waveguides, the approximation of our graded index UV-written structure to a step index guide can be made [28]. From the principle behaviour of radiation at a plane interface, the step index guide in one dimension is formulated given appropriate boundary conditions. This analytical basis is considered in the description of a number of numerical methods used to solve for modes within waveguiding structures, such as the effective index method, the finite element method, the finite difference method and the beam propagation method.

2.1.1 Plane interfaces

A plane interface is a boundary between two materials with different refractive indices. The reflection and refraction of radiation at a plane interface forms the basis for waveguiding within an optical material. The angles of reflection and refraction are dependent on the angle of incidence and the refractive indices of the materials forming the plane interface, a relationship known as Snell's law.

$$n_1 \sin\theta_1 = n_2 \sin\theta_2 \tag{2.1}$$

n_1 and n_2 are the refractive indices of the materials forming the interface, and θ_1 and θ_2 are the angles of incidence and refraction respectively. Figure 2.1 shows the angles of incidence, reflection and refraction for a boundary with $n_1 > n_2$.

In the case of an optical waveguide, with $n_1 > n_2$, there exists an incident angle θ_c, the critical angle, above which there is no refracted component of the incident radiation. In this case, where $\theta_1 = \theta_c = \sin^{-1}\left(\frac{n_2}{n_1}\right)$, the refracted wave travels along the interface between the two materials at an angle $\theta_2 = \frac{\pi}{2}$. For angles $\theta_1 > \theta_c$, there is no refracted component, and radiation propagates within the higher refractive index region by total internal reflection. In the case where $n_1 < n_2$, total internal reflection is not possible, as the angle $\theta_2 = \frac{\pi}{2}$ can never be achieved. Total internal reflection is the mechanism by which radiation is guided within a waveguiding structure, such as the slab waveguide outlined in the following section.

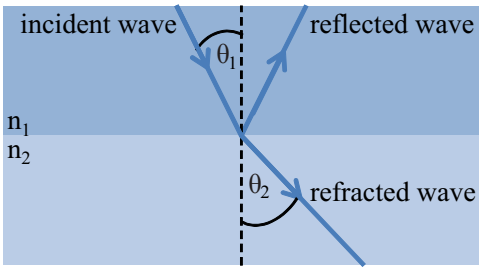

Figure 2.1: Reflection and refraction at a plane interface. The incoming wave at angle θ_1 in material with refractive index n_1 is refracted at angle θ_2 in material with refractive index n_2. The angle of reflection is equal to the angle of incidence.

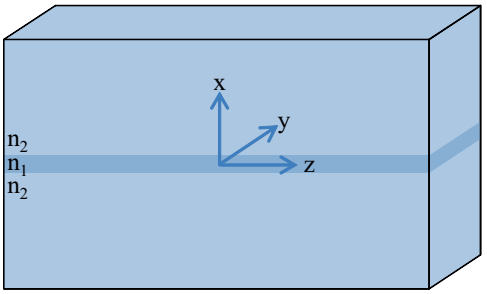

Figure 2.2: Schematic of the slab waveguide, with coordinate system origin at the centre of the core layer.

2.1.2 The symmetric slab waveguide

The symmetric slab waveguide is a relatively simple structure exhibiting the fundamental propagation characteristics of optical waveguides. Whilst not physically representative of the waveguides produced during the course of this work, investigation into the guidance characteristics of the symmetric slab waveguide can be undertaken analytically, providing useful insight into waveguide propagation characteristics in general, without the need for computationally intensive numerical modelling methods. Useful insight into the behaviour of the channel waveguides produced during the course of this work can thus be achieved. The analysis of the symmetric slab waveguide described below is well documented in the literature [29, 30].

The symmetric slab waveguide analysed in this section is depicted in Figure 2.2. It consists of a planar core layer with refractive index n_1 and thickness d, encased between two cladding layers with refractive index n_2. As stated in the previous section, n_1 is greater than n_2 to allow total internal reflection and thus waveguiding to occur. The figure depicts the notation of the coordinate system, with the origin at the physical centre of the core layer. The modes calculated propagate in the $+z$-direction, with confinement by the cladding layers at $|x| = \frac{d}{2}$.

Analysis of this system starts from Maxwell's equations. The general form of Maxwell's equations in matter is given in Equation 2.2 [31].

$$\nabla \cdot \boldsymbol{\mathcal{D}} = \rho_f \tag{2.2a}$$

$$\nabla \cdot \boldsymbol{\mathcal{B}} = 0 \tag{2.2b}$$

$$\nabla \times \boldsymbol{\mathcal{E}} = -\frac{\partial \boldsymbol{\mathcal{B}}}{\partial t} \tag{2.2c}$$

$$\nabla \times \boldsymbol{\mathcal{H}} = \boldsymbol{\mathcal{J}}_f + \frac{\partial \boldsymbol{\mathcal{D}}}{\partial t} \tag{2.2d}$$

$\boldsymbol{\mathcal{E}}$ is the electric field, $\boldsymbol{\mathcal{B}}$ is the magnetic field, $\boldsymbol{\mathcal{H}}$ is the magnetising field and $\boldsymbol{\mathcal{D}}$ is the electric displacement field. $\boldsymbol{\mathcal{J}}_f$ is the total current density and ρ_f is the total charge density. For the case of the symmetric slab waveguide depicted previously, Maxwell's equations for an isotropic, linear, non-conducting and non-magnetising field are required. These are achieved by modification of the equations above considering these restrictions, allowing ρ_f and $\boldsymbol{\mathcal{J}}_f$ to go to zero for the non-conducting case, and expressing $\boldsymbol{\mathcal{B}}$ in terms of the magnetizing field $\boldsymbol{\mathcal{H}}$, defined by

$$\boldsymbol{\mathcal{B}} = \mu \boldsymbol{\mathcal{H}} = \mu_0 \mu_r \boldsymbol{\mathcal{H}} = \mu_0 \boldsymbol{\mathcal{H}}, \tag{2.3}$$

$$\boldsymbol{\mathcal{D}} = \epsilon \boldsymbol{\mathcal{E}} = \epsilon_0 n^2 \boldsymbol{\mathcal{E}}. \tag{2.4}$$

n is the refractive index. ϵ and μ are the permittivity and permeability of the material in which radiation propagates, respectively. μ_0 and ϵ_0 are the permeability and permittivity of free space, respectively. μ_r is the relative permeability of the medium, which is equal to 1 for all non-magnetic materials, as required here.

Applying these conditions yields the adapted Maxwell's equations.

$$\epsilon_0 \nabla \cdot \left(n^2 \boldsymbol{\mathcal{E}}\right) = 0 \tag{2.5a}$$

$$\nabla \cdot \boldsymbol{\mathcal{H}} = 0 \tag{2.5b}$$

$$\nabla \times \boldsymbol{\mathcal{E}} = -\mu_0 \frac{\partial \boldsymbol{\mathcal{H}}}{\partial t} \tag{2.5c}$$

$$\nabla \times \boldsymbol{\mathcal{H}} = \epsilon_0 n^2 \frac{\partial \boldsymbol{\mathcal{E}}}{\partial t} \tag{2.5d}$$

Analysis of the electric and magnetic fields via Maxwell's equations yields vectorial wave equations for the propagation of radiation in an optical medium. Considering the electric field, taking the curl of Equation 2.5c yields

$$\nabla \times (\nabla \times \boldsymbol{\mathcal{E}}) = -\mu_0 \frac{\partial}{\partial t} (\nabla \times \boldsymbol{\mathcal{H}}) . \tag{2.6}$$

Rearranging, and substituting Equation 2.5d gives

$$\nabla\left(\nabla\cdot\boldsymbol{\mathcal{E}}\right)-\nabla^2\boldsymbol{\mathcal{E}}=-\mu_0\epsilon_0 n^2\frac{\partial^2\boldsymbol{\mathcal{E}}}{\partial t^2}. \tag{2.7}$$

Equation 2.5a can be written as

$$0=\epsilon_0\nabla\cdot\left(n^2\boldsymbol{\mathcal{E}}\right)=\epsilon_0\left[n^2\nabla\cdot\boldsymbol{\mathcal{E}}+\boldsymbol{\mathcal{E}}\cdot\nabla n^2\right] \tag{2.8}$$

thus

$$\nabla\cdot\boldsymbol{\mathcal{E}}=\frac{-1}{n^2}\nabla n^2\cdot\boldsymbol{\mathcal{E}} \tag{2.9}$$

Substituting this into Equation 2.7, the wave equation for the propagation of the electric field through a material with refractive index n can be obtained.

$$\nabla^2\boldsymbol{\mathcal{E}}+\nabla\left(\frac{1}{n^2}\nabla n^2\cdot\boldsymbol{\mathcal{E}}\right)-\mu_0\epsilon_0 n^2\frac{\partial^2\boldsymbol{\mathcal{E}}}{\partial t^2}=0 \tag{2.10}$$

The second term in this equation concerns the inhomogeneity of the optical medium. In this case, as uniform materials are considered, this term can be neglected, leaving

$$\nabla^2\boldsymbol{\mathcal{E}}-\mu_0\epsilon_0 n^2\frac{\partial^2\boldsymbol{\mathcal{E}}}{\partial t^2}=0. \tag{2.11}$$

A similar procedure can be applied in the case of the magnetic field, yielding the following wave equation.

$$\nabla^2\boldsymbol{\mathcal{H}}-\mu_0\epsilon_0 n^2\frac{\partial^2\boldsymbol{\mathcal{H}}}{\partial t^2}=0 \tag{2.12}$$

Once again referring to the schematic of the symmetric slab waveguide, conditions are now set in order to obtain solutions of this wave equation. The assumption is made that the refractive index changes only in the x direction. In addition, the propagation direction is defined as parallel to the z-direction of the coordinate system. These assumptions allow the following solutions to the wave equation, where $j=x,y,z$.

$$\mathcal{E}_j=E_j\left(x\right)e^{i(\omega t-\beta z)} \tag{2.13}$$

$$\mathcal{H}_j=H_j\left(x\right)e^{i(\omega t-\beta z)} \tag{2.14}$$

β is the propagation constant, ω is the angular frequency of oscillation and t allows the propagation to be expressed in terms of time as well as space. These solutions to the wave equation describe propagation of electric and magnetic fields within the structure defined previously (Figure 2.2), and are defined as the modes of the waveguide. Modes are field distributions that can propagate so that the transverse field distributions in x and y are constant as the field propagates through the waveguide in the z-direction.

In order to determine the physical representation of these solutions, they are inserted back into the initial Maxwell's equations (Equations 2.5a-2.5d). This action reveals that the solutions can be interpreted as two modes, one with its electric field oscillating in the y-plane, and one with its magnetic field oscillating in the y-plane. These modes are commonly referred to as the transverse electric (TE) and transverse magnetic (TM) modes respectively, and can each be described by a second order differential equation obtained from the solution to the wave equation. A rigorous description of how to obtain these equations is given in Appendix B.

Taking the case of the TE modes, the electric field is described by

$$\frac{d^2E_y}{dx^2} + \left[k_0^2n^2 - \beta^2\right]E_y = 0 \tag{2.15}$$

n now describes the refractive index structure varying in the x-direction only. k_0, the free space wavenumber, is given by $\omega\left(\epsilon_0\mu_0\right)^{\frac{1}{2}}$. Now, boundary conditions can be applied considering the specific parameters of the symmetric slab waveguide described above. With a core layer of refractive index n_1, centred around x=0 and with thickness d, and cladding layer with refractive index n_2, the electric field within the core and cladding layers can be described as follows.

$$\frac{d^2E_y}{dx^2} + \left[k_0^2n_1^2 - \beta^2\right]E_y = 0, \qquad |x| < \frac{d}{2} \tag{2.16}$$

$$\frac{d^2E_y}{dx^2} + \left[k_0^2n_2^2 - \beta^2\right]E_y = 0, \qquad |x| > \frac{d}{2} \tag{2.17}$$

At this point, substitution of $\kappa^2 = k_0^2n_1^2 - \beta^2$ and $\gamma^2 = \beta^2 - k_0^2n_2^2$ are made, to form the following simplified relations.

$$\frac{d^2E_y}{dx^2} + \kappa^2E_y = 0, \qquad |x| < \frac{d}{2} \tag{2.18}$$

$$\frac{d^2E_y}{dx^2} - \gamma^2E_y = 0, \qquad |x| > \frac{d}{2} \tag{2.19}$$

The solutions of these equations can be written as follows. Equation 2.18, representing the electric field within the core, has solution of the form:

$$E_y(x) = A\cos(\kappa x) + B\sin(\kappa x), \qquad |x| < \frac{d}{2} \tag{2.20}$$

where A and B are constants.

Equation 2.19, representing the exponential decay of the electric field within the cladding, has solutions of the form:

$$E_y(x) = \begin{cases} Ce^{\gamma x}, & x < \frac{-d}{2} \\ De^{-\gamma x}, & x > \frac{d}{2}. \end{cases} \tag{2.21}$$

At this point, further boundary conditions are applied to obtain solutions to these equations. The solution must be continuous at the core/cladding interface, ie. E_y and $\frac{dE_y}{dx}$ are continuous. The solution must also be symmetric or antisymmetric around $x = 0$ as the refractive index distribution is symmetric about this point. This leads to the solutions

$$E_y(x) = \begin{cases} A\cos(\kappa x), & |x| < \frac{d}{2} \\ Ce^{-\gamma x}, & |x| > \frac{d}{2}, \end{cases} \tag{2.22}$$

in the symmetric case, and in the antisymmetric case

$$E_y(x) = \begin{cases} B\sin(\kappa x), & |x| < \frac{d}{2} \\ \frac{x}{|x|}De^{-\gamma x}, & |x| > \frac{d}{2}. \end{cases} \tag{2.23}$$

Application of the boundary conditions in the symmetric case leads to continuities at the boundary of E_y and $\frac{dE_y}{dx}$ respectively.

$$A\cos\left(\frac{\kappa d}{2}\right) = Ce^{-\frac{\gamma d}{2}} \tag{2.24}$$

$$-\kappa A\sin\left(\frac{\kappa d}{2}\right) = -\gamma Ce^{-\frac{\gamma d}{2}} \tag{2.25}$$

Dividing Equation 2.25 by Equation 2.24, and multiplying each side by $\frac{d}{2}$, you obtain

$$\frac{\kappa d}{2}\tan\left(\frac{\kappa d}{2}\right) = \frac{\gamma d}{2}. \tag{2.26}$$

Applying the same boundary conditions to the antisymmetric case leads to

$$-\frac{\kappa d}{2}\cot\left(\frac{\kappa d}{2}\right)=\frac{\gamma d}{2}. \tag{2.27}$$

These relations for the symmetric and antisymmetric modes of the guide describe the supported modes of the structure.

It can be more convenient, in certain situations, to display the equations describing the waveguide modes in terms of dimensionless parameters. Thus, at this point, the dimensionless waveguide parameter, or V number is introduced. The V number is dependent on the core dimension d and refractive indices of the waveguide at wavelength λ, and can be determined via the following relation.

$$V=k_0 d\left(n_1^2-n_2^2\right)^{\frac{1}{2}} \tag{2.28}$$

In addition, V can be related to κ and γ by the following relation.

$$\frac{\gamma d}{2}=\left(\frac{V^2}{4}-\frac{\kappa^2 d^2}{4}\right)^{\frac{1}{2}}. \tag{2.29}$$

By rewriting Equations 2.26 and 2.27 in terms of V, it can be shown that

$$\frac{\kappa d}{2}\tan\left(\frac{\kappa d}{2}\right)=\left(\frac{V^2}{4}-\frac{\kappa^2 d^2}{4}\right)^{\frac{1}{2}} \tag{2.30}$$

and

$$-\frac{\kappa d}{2}\cot\left(\frac{\kappa d}{2}\right)=\left(\frac{V^2}{4}-\frac{\kappa^2 d^2}{4}\right)^{\frac{1}{2}} \tag{2.31}$$

for symmetric and antisymmetric modes respectively.

The right hand side of these equations represent circles of radius $\frac{V}{2}$, which can be seen in Figure 2.3, plotted alongside the symmetric and antisymmetric modes obtained from the left hand side of each equation. The circles of radius $\frac{V}{2}$ intersect the allowed modes of the guide defined by the V number. In the plot shown, the refractive indices and core dimensions are chosen such that a single mode (inner red circle) and multimode (outer red circle) V number curve can be displayed. The single mode circle (inner) intersects one symmetric mode (blue lines), whilst the multimode circle intersects one symmetric and one antisymmetric mode (black). This plot was used to determine the expected number of modes of the multimode guide used in the dispersion measurement

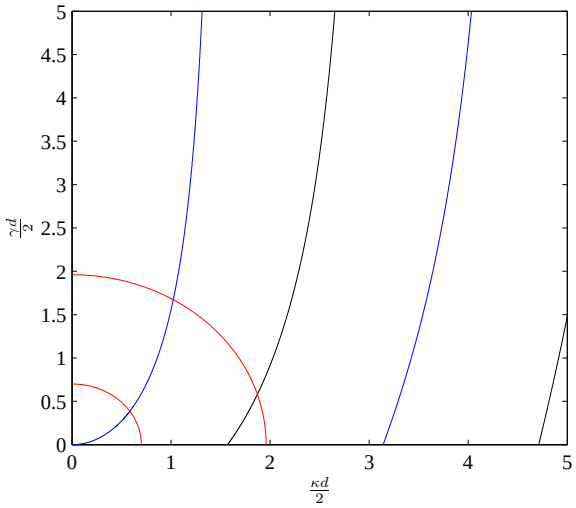

Figure 2.3: Graphical solution for the guided modes of a slab waveguide. The V number radii are calculated from the experimental determination of V number given effective refractive index and thickness data of the fabricated FHD slab. The inner red circle represents a single mode waveguide ($V = 1.40$), the outer a multimode guide ($V = 3.92$). The symmetric and asymmetric modes supported (blue and black respectively) intersect the circle representing the multimode guide.

work (Chapter 6). For a larger V number, with larger core dimension and/or refractive index difference $n_1 - n_2$, it can be seen from the plot and Equation 2.28 that more modes will be supported by the waveguide.

This analytical process shows the steps required to determine the TE guided modes of the slab waveguide. The TM modes can be obtained following a similar process, given in Appendix B. The process is well documented in literature [30, 32]. This analytical description of the mode propagation in the simplest waveguide case enables the understanding of the concepts behind the numerical modelling techniques applied in order to effectively predict the behaviour of supported modes within complex waveguide structures. A description of some of these techniques is provided in the following section.

2.1.3 The effective index method and numerical mode solving

There are a number of commercially available software systems designed to enable the computation of mode propagation in waveguide structures. These systems employ numerical modelling techniques in order to analyse the characteristics of the guide. A typical method involves dividing the waveguide into a number of individually solvable sections, before providing an overall solution to the wave equation of the guide based on consideration of the individual contributions to the behaviour of the entire system.

This section is included in order to introduce the numerical systems typically available and used to model the waveguides described in this thesis. An analytical approach to mode solving, the effective index method, is introduced to describe the implications of

using a basic segmented modelling system to analyse waveguides. Following this description, discussion of a number of numerical solving techniques, including appropriate application of the methods to specific problems, will be presented. The techniques described include the finite difference method, the finite element method and the beam propagation method of mode solving.

2.1.4 The effective index method

The effective index method is an analytical technique commonly used to obtain solutions of the wave equation. The technique is widely applied in mode solving software as it is a fast and reliable method to obtain approximate solutions to the wave equation. Based on the analytical approach to solve the modes of the symmetric slab waveguide, the effective index method enables the modelling of waveguide structures which confine radiation in multiple dimensions. In this section, the application of the technique to a two dimensional waveguide structure will be described. Once again, the procedure is widely described in the literature [33, 34].

In the case of the 2D waveguide, the assumption is made that, by separation of variables, the electromagnetic field propagating within the guide can be expressed in the following form.

$$H_y(x,y) = X(x)\,Y(y) \tag{2.32}$$

Therefore, via steps similar to those presented previously (Section 2.1.2), the following relation can be obtained from Maxwell's equations.

$$\frac{\partial^2 H_y}{\partial x^2} + \frac{\partial^2 H_y}{\partial y^2} + \left[k_0^2 n^2(x,y) - \beta^2\right] = 0 \tag{2.33}$$

At this point, a waveguide structure suitable for demonstration of this technique is introduced. Figure 2.4 shows a schematic (right) of the chosen rib waveguide, alongside the refractive index profile in the y-direction. Note the y-independence of the effective index in the x-direction.

Given that the field can be expressed in the form given above (Equation 2.32), the wave equation can then be expressed via two independent contributions.

$$\frac{1}{Y}\frac{\partial^2 Y}{\partial y^2} + \left[k_0^2 n^2(x,y) - k_0^2 n_{eff}^2(x)\right] = 0 \tag{2.34a}$$

$$\frac{1}{X}\frac{\partial^2 X}{\partial x^2} + \left[k_0^2 n_{eff}^2(x) - \beta^2\right] = 0 \tag{2.34b}$$

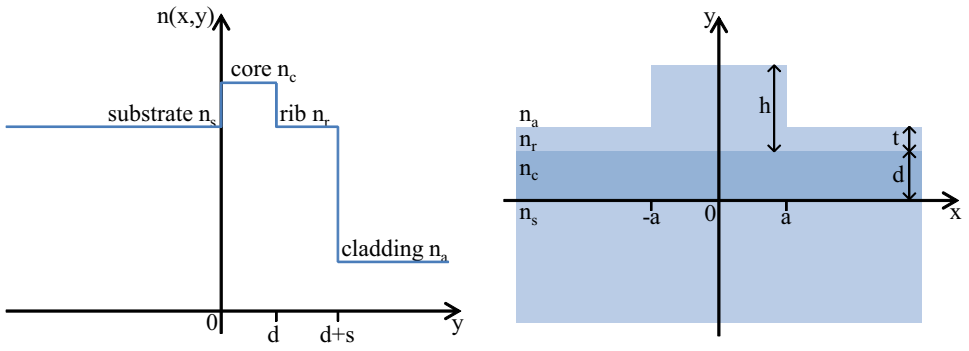

Figure 2.4: Schematic of the rib waveguide (right), alongside the refractive index profile of the guide in y (left).

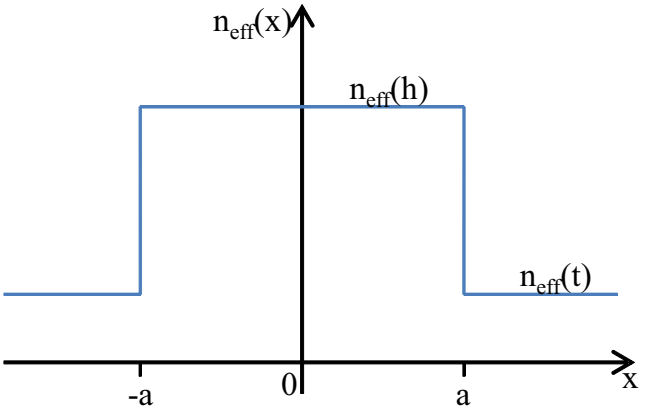

Figure 2.5: Effective refractive index profile of the rib structure in x, calculated via the effective index method.

The parameter n_{eff} introduced here is the effective index distribution. Given the y-independence of $n_{eff}(x)$, Equation 2.34a can now be solved to obtain the effective index distribution in terms of x. The equation is solved at the boundaries $y = 0$, $y = d$ and $y = d + s$, where $s = h$ for $0 < |x| < a$ and $s = t$ for $|x| > a$, to achieve the effective refractive index profile in these regions. A plot of the effective refractive index in x is shown in Figure 2.5.

Once this solution to the wave equation is obtained, the second wave equation (Equation 2.34b) can be solved for this three layer slab guide. Solving this wave equation yields an approximate analytical solution for the mode propagation within the guide, by separating the wave equation over each dimension. This analytical approach can therefore be used to solve, via approximations, the wave equation for complex waveguiding structures. The following section describes numerical techniques based on the same principles, involving the division of the waveguide into several distinct problems.

2.1.5 Numerical mode solving

In order to determine non-approximate solutions to the wave equations, the move away from analytic to numerical solving methods must be implemented. Numerical solutions can be obtained via a number of computational programs designed for the purpose. During the course of this thesis, the 'FIMMWAVE' mode solver program was used to determine the propagation characteristics of modes within the guides. FIMMWAVE, a Photon Design product, utilises one of a number of available numerical approaches to solve modal distribution of the waveguide, depending on the geometry and characteristics of the guide itself. In this section, some of these approaches, the finite difference method, the finite element method, and the beam propagation method will be briefly introduced, with the aim of describing the implementation of the models.

The finite difference method [35] of solving numerical differential equations is particularly suited to the partial differential form of the wave equations detailed above. The method involves replacing the partial derivatives by 'finite differences' that approximate them. The relevant finite differences are formulated by dividing the effective index cross-section of the waveguide into a rectangular grid structure, and solving for the effective refractive index of each grid section. The solutions of each grid area are then reconstructed considering the grid boundaries to give solutions of the wave equation. The finite difference method is particularly suited to finding the solutions of rectangular waveguide structures, with and without graded refractive index profiles.

Formulated in a similar physical manner, the finite element method [35], with a typically triangular mesh of varying element dimensions, enables the numerical analysis of waveguides with complex geometry. These include circular, elliptical and polygonal geometries, with and without graded refractive index profiles. The mesh size is chosen to fit the areas of interest of the specific waveguide, thus effectively enhancing the resolution of the technique at regions of interest. The partial differential equation governing the wave equation of each grid space is then approximated to an ordinary differential equation, and the effective index and solutions to the wave equation then reconstructed. The method is of particular use when modelling photonic crystal structures and holey fibres, where the circular geometry in specific regions requires careful consideration.

Whilst enabling the calculation of the solutions of the wave equation in order to calculate the modes present at a single point in the waveguide, the finite difference and element methods do not produce accurate numerical solutions for the case where radiation propagates along the guide. These are difficult to achieve once propagation length has exceeded the wavelength of radiation within the guide. An alternative approximation technique, the beam propagation method, can be employed in this case to solve the wave equations for slowly-varying optical waveguides, allowing calculation of the modal behaviour of the guide along its length.

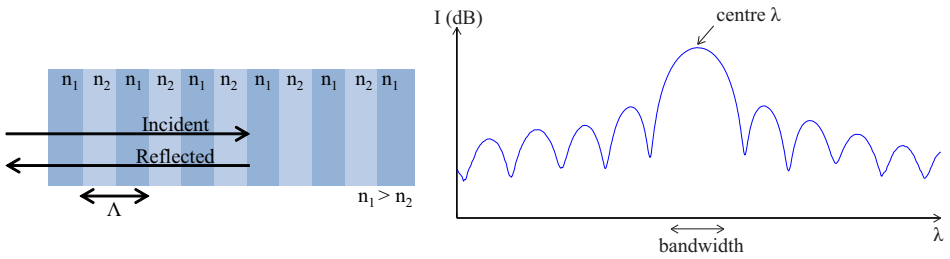

Figure 2.6: Schematic of the periodic structure of a typical uniform Bragg grating (left), alongside an experimentally obtained spectrum from such a device (right). Note the centre wavelength and bandwidth of the reflector defined on the plot.

The beam propagation model [36] works under the slowly varying envelope approximation to solve the 'one-way' models, approximate differential equations with only the spatial variable z. Solving these equations leads to the solutions of the wave equation at all points along the waveguide. The fields can then be visualised along the propagation direction, or at discrete points in the form of a waveguide cross section. This allows complex structures such as multimode interference devices to be modelled quickly and relatively accurately, given the initial approximations.

The modelling techniques described here are just a few of the vast tool kit available to model the modes present in waveguiding structures. This brief overview enables the work presented here, particularly the multimode structures in Chapter 6, to be analysed and understood. An understanding of waveguide theory in general is required in order to understand the guidance characteristics required to support components such as Bragg grating structures. The next section will introduce the theory required to enable understanding of the behaviour of typical Bragg grating devices.

2.2 Bragg grating theory

A Bragg grating can be thought of, in its simplest form, as a distributed optical wavelength filter. Incoming radiation is reflected from each element of an array of periodically placed effective refractive index boundaries, created by varying the local refractive index of the waveguide, or by varying the dimensions of the waveguide channel. The periodicity of the placement of the boundaries causes radiation at a specific wavelength, the Bragg wavelength, to be reflected, as the individually reflected components interfere constructively with one another. All other wavelengths are transmitted through the filter, experiencing destructive interference of reflected components. The result is a narrow band reflection filter centred around the Bragg wavelength (Figure 2.6).

In order to carry out the experimental work undertaken during the course of this project, an understanding is required not only of the waveguide characteristics and mode propagation described in the previous section, but of the behaviour of the fabricated Bragg

gratings under differing experimental conditions. In this section, an overview of Bragg grating theory will be presented, referring to the literature concerning fibre Bragg gratings. The planar Bragg gratings fabricated via direct UV writing can be analysed and described via fibre Bragg grating considerations due to similarities of the photosensitivity mechanisms and effective refractive index profile involved. A description of the different types of Bragg grating, and differences between their fabrication and spectral characteristics will be discussed. Following this, a section on the theoretical considerations necessary when fabricating and interrogating Bragg grating structures, including k-vector arguments and coupled mode theory, will be presented.

2.2.1 Classification of Bragg gratings

Bragg gratings are classified by the type of photosensitivity mechanism exploited during the fabrication process to produce the periodic fringes. The photosensitivity mechanism used determines how the Bragg grating responds under different environmental conditions, especially at high temperatures, and thus limits the applications of the grating to different thermal regimes. In addition, the strength of a Bragg grating can determine the spectral behaviour. This section describes the differences between the types of Bragg grating which can be experimentally realised.

Bragg gratings are formed when a photosensitive material is irradiated at a wavelength necessary to cause a photosensitive reaction (Section 3.2). The radiation can be used to create a periodic modulation of the refractive index of the material, created by either point-by-point inscription [37] or the inscription of a modulation pattern, which is created by an interferometer [38] or phase mask set up [39]. The type of Bragg grating formed is determined by the photosensitivity mechanism exploited [40], which is related to the intensity of radiation and the pre-sensitisation of the fibre.

Type I Bragg gratings are fabricated in all types of fibres under all hydrogenation conditions. Hydrogenation, or hydrogen loading, is the pre-sensitisation of fibres by the addition of hydrogen to the glass matrix, and is described further in Section 3.2.2. Type I gratings are produced in glasses by causing chemical changes to the glass matrix via the photosensitivity mechanisms described in the following chapter (Section 3.2). Chemical bonds are broken and formed when irradiated, creating defects and thus changing the local refractive index of the glass in the region exposed to radiation. Hydrogen loading increases the photosensitivity of the glass and thus the prevalence of the effect. The refractive index contrast typically achieved is around 1×10^{-4}. Type I Bragg gratings are generally formed at low intensities, below the damage threshold of the glass, and cannot stand environmental temperatures of above around 400 °C before erasing of the grating planes is observed. The spectral characteristics of a Type I Bragg grating are complementary in reflection and transmission, i.e. $R = 1 - T$. This implies the Bragg

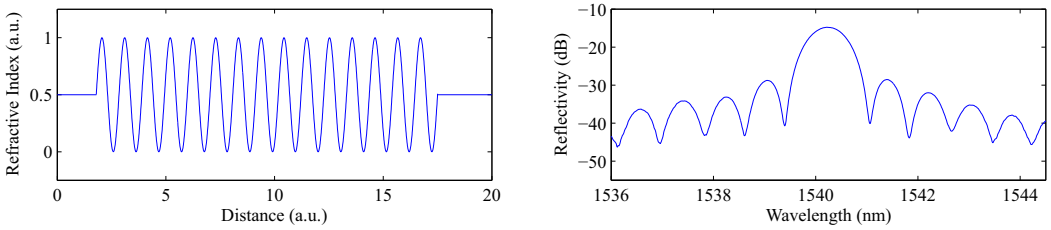

Figure 2.7: A uniform-apodised Bragg grating refractive index modulation, and an experimentally obtained reflected spectrum. The 'top-hat' modulation produces a sinc-squared apodised Bragg grating spectrum in reflection.

grating has negligible absorption losses at all wavelengths, and reflection loss to the cladding is minimal.

Type II Bragg gratings are formed in non-hydrogenated fibres at high intensities, above the damage threshold of the glass. Also called 'damage gratings', Type II structures rely not only on the chemical photosensitivity of the glass, but on structural damage to the glass which creates a large refractive index modulation, around an order of magnitude greater than for Type I structures. The damage manifests itself as either ionisation and glass melting, or as voids caused by microexplosions, which create more dense, higher refractive index regions of glass. The large index modulation causes a proportion of the reflected radiation to be coupled into the cladding, reducing the efficiency of the device, and creating irregular spectral features in the short wavelength region. However, the Type II devices can withstand temperatures up to around 700 °C, increasing the scope for the use of Bragg gratings as environmental sensors. Research into these structures is mainly undertaken using femtosecond laser systems [21] to achieve large enough energies to exceed the damage threshold of the glass.

As well as dependence on the photosensitivity mechanism, classification of Bragg gratings can also be made considering the Bragg grating strength. A weak Bragg grating is defined as a grating with less than 20 % reflectivity [41]. In this case, the reflected spectral shape of the grating can be calculated via the Fourier transform of the refractive index modulation [42]. So a periodic modulation of the same magnitude along the grating length, a uniform grating, with a 'top-hat' refractive index modulation, will produce a sinc^2-apodised grating spectrum (as in Figure 2.7), whilst a Gaussian enveloped refractive index modulation will produce a Gaussian-apodised Bragg grating. Apodisation is covered in more detail in Chapter 4. Weak Type I Bragg gratings are critical to the work conducted over the course of this project, as they can be effectively apodised and are uni-directional. Characterisation of these devices allows simple grating analysis and data fitting, yielding low-error Gaussian fitted parameters for the analysis techniques described in the loss and dispersion measurement chapters.

As gratings become stronger, via additional grating planes or increased refractive index contrast, the spectral response changes. No longer related to the Fourier transform,

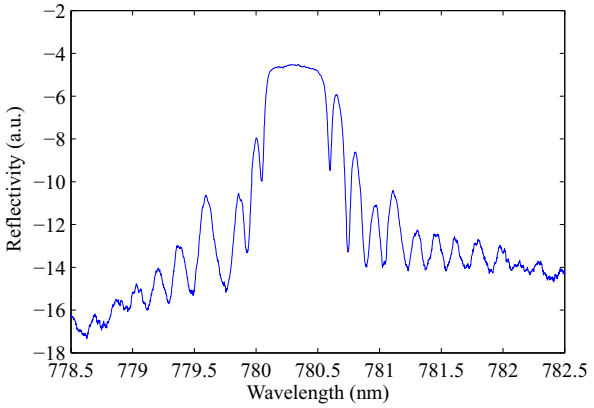

Figure 2.8: An example of the reflected spectral profile of a saturated Bragg grating. Note the flat-topped form of the spectrum, and the lack of sideband suppression in comparison to the weak uniform grating shown in Figure 2.7.

the spectral response becomes flat-topped, with increased bandwidth and greater error encountered when determining the central wavelength. The cause is that 100 % of the incident radiation at the central wavelength is reflected before the physical end of the Bragg grating structure, causing any apodisation function to be cut short. This causes a mis-shaped spectral profile to be obtained, an example of which is shown in Figure 2.8. Careful control of the fabrication parameters can be implemented to ensure the grating has a desired reflectivity profile whilst retaining the desired spectrum.

This discussion of the types of Bragg grating which can be produced enables the design of a desired grating structure fit for purpose. Weak Type I Bragg gratings are implemented in the work described later in this thesis, for ease of analysis and use in specific waveguide characterisation situations as they are unidirectional and can be apodised obeying the Fourier transform weak grating limit. The analysis of the structures is dependent on knowledge of the behaviour of the Bragg gratings and theoretical considerations governing the grating characteristics. The following section will introduce the Bragg grating theory required to undertake the research described.

2.2.2 Bragg grating behaviour

This section will introduce the key concepts necessary to understand the fundamental behaviour of Bragg grating elements within an optical waveguide. In this case, once again, the analogy is made to fibre Bragg grating theory, given the similar refractive index profile and weakly guiding approximation suitable for description of the direct UV written waveguides. In addition, the theoretical considerations presented here are accurate only for weak Type I Bragg grating structures, with periodic effective refractive index modulation planes perpendicular to the direction of propagation of the incoming radiation. The considerations do, however, enable a fundamental understanding of the

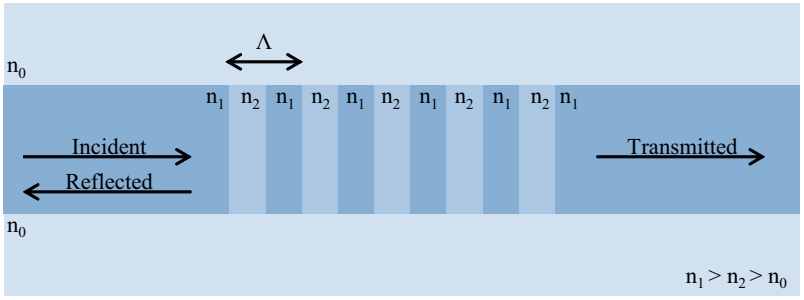

Figure 2.9: Refractive index profile of Bragg grating structure, with incident, reflected and transmitted radiation directions noted.

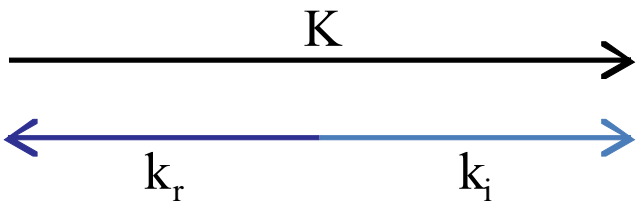

Figure 2.10: Illustration of the k-vector argument for the Bragg condition, $|k_i| = |k_r|$.

interaction of incoming radiation with a Bragg grating structure, key to aiding interpretation of the spectra obtained during the course of this project.

As previously defined (Equation 2.1), radiation incident at a plane interface obeys Snell's law. Each refractive index modulation within the Bragg grating structure, shown in Figure 2.9, causes radiation to be reflected into the counter-propagating mode of the waveguide. This reflection occurs at all wavelengths, however, due to the periodicity of the structure, only reflections with wavelength corresponding to the period of the grating planes interfere constructively in the counter-propagating direction. Thus, only radiation with wavelength equal to the central wavelength of the Bragg grating (or frequency doubled etc.) can be reflected from the structure. All other wavelengths will interfere destructively in the counter-propagating direction, and, thus, are effectively transmitted through the structure. As mentioned previously, for weak Type I Bragg gratings, the absorption losses and stray reflections into the cladding are negligible, ensuring that transmitted power is not lost outside the bandwidth of the grating structure.

In order to better understand the coupling to the counter-propagating mode, a k-vector argument is proposed.

Energy must be conserved as a result of interaction with the Bragg grating, so the frequency of radiation does not change as a result of the reflection. This requires that the reflected wave vector $\boldsymbol{k}_r$ must equal the sum of the incident wave vector $\boldsymbol{k}_i$ and the wave vector of the Bragg grating, $\boldsymbol{K}$.

$$\boldsymbol{k}_i + \boldsymbol{K} = \boldsymbol{k}_r \tag{2.35}$$

If the Bragg condition is satisfied, and the reflected components from each plane $\boldsymbol{k}_r$ are to constructively interfere, the magnitude of the incident wave vector must equal that of the reflected wave vector, $|k_i| = |k_r|$, shown in Figure 2.10. Considering this, and substituting $k = \frac{2\pi}{\lambda}$, we obtain the Bragg equation, for a material with n_{eff} at λ_B.

$$\lambda_B = 2n_{eff}\Lambda \tag{2.36}$$

λ_B is the Bragg wavelength, the central reflected wavelength of the Bragg grating, and Λ is the period of the effective refractive index modulation. An additional factor, m, can be included on the left hand side of Equation 2.36 to indicate the order of the reflected mode from the Bragg grating. For simplicity's sake, from here on in, we observe the first order reflection, ie. $m = 1$.

The Bragg equation allows the central wavelength of the grating to be obtained, given the known period of the grating structure. However, it does not give any information about the other spectral characteristics of the grating, the bandwidth or the reflection strength. In order to investigate these components, coupled mode theory is introduced. This enables modelling of not only uniform Bragg gratings, but also the apodised and structured grating profiles described in Chapter 4. In this section, the relevant results of coupled mode theory, including detuning, maximum reflectivity and bandwidth, are presented, given the detailed reports of the application of coupled mode theory elsewhere in the literature [41, 43].

The refractive index profile along the Bragg grating, $n(z)$, in the direction of forward propagation z, is given by

$$\delta n_{eff}(z) = \overline{\delta n_{eff}(z)}\left\{1 + \nu\cos\left[\frac{2\pi}{\Lambda}z + \phi(z)\right]\right\} \tag{2.37}$$

$\overline{\delta n_{eff}(z)}$ is the refractive index perturbation averaged over one grating period, and K is the grating k-vector, as before. ν is the fringe visibility of the index change, and $\phi(z)$ decribes the grating chirp. In the case of the uniform grating, assuming $\nu = 1$, the relation can be rewritten as

$$\delta n_{eff}(z) = \overline{\delta n_{eff}(z)}\left[1 + \cos(Kz)\right]. \tag{2.38}$$

The reflection coefficient of the Bragg grating is then given by [43],

$$r = \frac{\sinh^2\left(L\sqrt{\kappa^2 - \acute{\sigma}^2}\right)}{\cosh^2\left(L\sqrt{\kappa^2 - \acute{\sigma}^2}\right) - \frac{\acute{\sigma}^2}{\kappa^2}}. \tag{2.39}$$

L is the length of the grating, and κ and $\acute{\sigma}$ are coupling coefficients. Inspection of these coupling coefficients allows investigation of the detuning δ.

$$\kappa = \frac{\pi\overline{\delta n_{eff}(z)}}{\lambda} \tag{2.40}$$

$$\acute{\sigma} = \delta + \sigma \tag{2.41}$$

$$\sigma = \frac{2\pi\overline{\delta n_{eff}(z)}}{\lambda} \tag{2.42}$$

$$\delta = 2\pi n_{eff}\left(\frac{1}{\lambda} - \frac{1}{\lambda_B}\right) \tag{2.43}$$

The detuning, δ, is obtained from the difference between the propagating wavelengths, λ, and the design wavelength of the Bragg grating, λ_B, from Equation 2.36. This is valid for an infinitesimally weak grating, with $\overline{\delta n_{eff}(z)} \to 0$. Note that for $\delta = 0$, the Bragg condition (Equation 2.36) can be obtained.

Taking Equation 2.39, the maximum reflectivity r_{max} can be obtained.

$$r_{max} = \tanh^2(\kappa L) \tag{2.44}$$

The maximum reflectivity occurs when $\acute{\sigma} = 0$, or at the wavelength

$$\lambda_{max} = \left(1 + \frac{\overline{\delta n_{eff}(z)}}{n_{eff}}\right)\lambda_B. \tag{2.45}$$

In the case of a uniform Bragg grating structure, the sinc-squared spectral profile obtained depends on the grating parameters used. For constant grating length L, increasing the coupling coefficient κ by increasing the magnitude of the refractive index modulation increases the strength of the grating. The sinc-squared profile becomes flat-topped as the index modulation increases the Bragg grating strength into the strong regime, where $\overline{\delta n_{eff}(z)} \gg \frac{\lambda_B}{L}$. This also increases the spectral bandwidth of the grating response. A comparison of the spectral response of a weak and a strong Bragg grating is shown in Figure 2.11.

In order to define the spectral bandwidth of the grating response, the minima of the sinc-squared spectral profile are considered. The two zeros immediately adjacent to the maximum reflectivity of the grating are taken, and the bandwidth determined as the measurement between the two. The bandwidth can then be expressed as

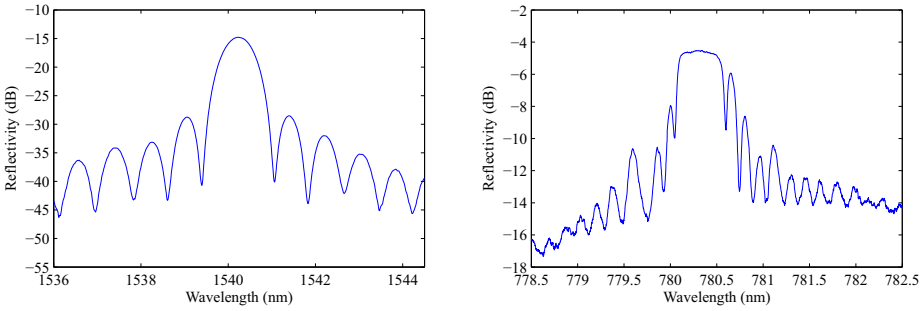

Figure 2.11: Comparison of the reflected spectrum of a Bragg grating in the weak regime (left) and the strong regime (right). The weak Bragg grating response shows a sinc-squared spectral profile; in the case of the strong Bragg grating, the flat-topped profile can be observed. A corresponding increase in the 3 dB bandwidth can be inferred (although a direct comparison cannot be made between the bandwidths of the gratings at 1540 nm and 780 nm as shown here).

$$\frac{\Delta\lambda_0}{\lambda} = \frac{\overline{\delta n_{eff}(z)}}{n_{eff}} \sqrt{1 + \left(\frac{\lambda_B}{\overline{\delta n_{eff}(z)} L} \right)^2} \tag{2.46}$$

Thus, the dependence of the bandwidth on the grating length L and refractive index modulation $\overline{\delta n_{eff}(z)}$ can be observed.

The bandwidth of the grating is dependent on whether the refractive index modulation or the grating length is the dominant term in this equation. In the case of weak modulation, $\overline{\delta n_{eff}(z)} \ll \frac{\lambda_B}{L}$, the right hand side of the equation reduces to $\frac{\lambda_B}{n_{eff} L}$, indicating that the bandwidth depends on the grating length. In the case of strong modulation, $\overline{\delta n_{eff}(z)} \gg \frac{\lambda_B}{L}$, the right hand side reduces to $\frac{\overline{\delta n_{eff}(z)}}{n_{eff}}$, indicating that the bandwidth has a greater dependence on the refractive index modulation. By this definition we can distinguish between the weak and strong gratings mentioned previously. Note that in the case of the strong grating, dependent on the strong refractive index modulation, radiation spectrally close to the Bragg wavelength will not penetrate the full length of the grating structure, and the grating will have reflectivity close to 100 %.

Figure 2.12 shows a pictorial representation of the components of refractive index in a Bragg grating, with the definition of the terms used in the theory above. In this case, a Gaussian apodisation profile is chosen. The labelling to the left of the comma relates to the fibre Bragg grating theory presented here. The labelling to the right shows the interchangeable naming procedure for the planar Bragg grating case.

This section has described the fundamental theory behind the operation of the Bragg grating filter. Through consideration of the various forms of Bragg grating, from weak to strong, and through different photosensitivity mechanisms, the form and behaviour of the weak Type I Bragg grating has been described. Analysis of both the k-vector arguments and coupled mode theory have led to a description of the Bragg grating

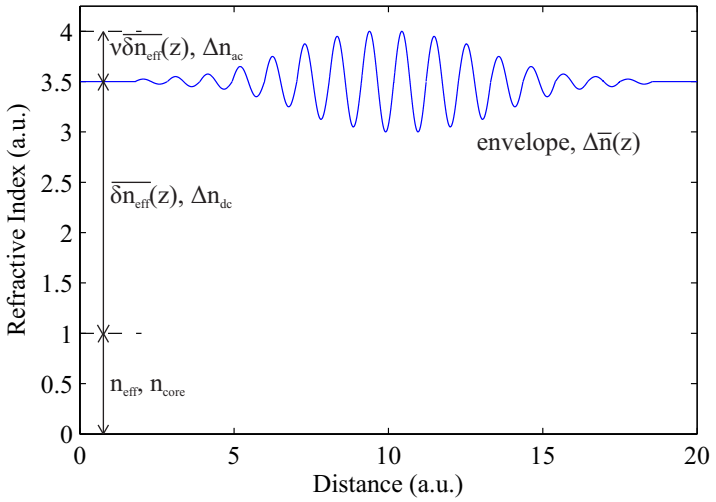

Figure 2.12: Theoretical refractive index profile of a Bragg grating structure, showing the underlying refractive index of the fibre/waveguide, and the refractive index modulation of the Bragg grating. The grating shown has a Gaussian apodisation envelope.

spectral characteristics, including central wavelength, reflectivity and bandwidth. An interpretation of these concepts is required to carry out the analysis of data collected for subsequent chapters, in particular where the spectral characteristics of the grating are used in dispersion and loss measurement techniques.

2.3 Conclusions

The aim of this chapter was to provide a theoretical basis for the operation of the waveguides and Bragg gratings fabricated for use in the experimental work described in this thesis. Through analysis of fibre Bragg grating considerations, an understanding of the expected behaviour of the gratings and supporting waveguides has been achieved, given the weakly guiding, step index approximations applied.

Through presentation of analytical models, the behaviour of guided modes within the waveguide structure has been considered. Analytical approaches to solving for modes in a symmetric slab waveguide and a rib waveguide have been presented. A description of numerical modelling methods has been provided to enable an understanding of the rigorous mathematical approaches available to solve for modes in commercial software systems. These approaches enable modelling of the guidance characteristics of the waveguides, enabling judgement on whether the waveguides are suitable for support of Bragg grating structures amongst other integrated optical components.

The theoretical basis for the operation of Bragg grating filters has been described, first considering the specification of the grating defined by its fabrication processes. The application of coupled mode theory has been described to enable the physical meaning

of grating parameters to be understood. The central wavelength, bandwidth and reflectivity of the Bragg grating has been defined, and the relation to the grating strength explained.

Mode solving software has been used in this project to model the behaviour of multimode waveguides. Grating parameters, particularly the central wavelength and the peak reflectivity, have been obtained via data analysis, and manipulation of these parameters led to the development of dispersion measurement technique (Chapter 6) and the loss measurement technique (Chapter 5) respectively. An appreciation of the theory described in this chapter is critical when forming an understanding of the behaviour of the optical components fabricated.

Chapter 3

Basic fabrication and characterisation of waveguides and Bragg gratings

The optical properties of glass waveguides are fundamentally dependent on the techniques used to fabricate them. Investigation into fabrication techniques allows the exploration of different waveguide geometries, materials and waveguiding properties. The formation of Bragg grating structures within optical waveguides is even more critically dependent on the fabrication techniques employed, as small variations in the composition of the glass can lead to large changes in the spectral and temporal grating characteristics. These spectral and temporal properties also provide a precise route to interrogate the composition of the glass.

All waveguides and Bragg gratings discussed in this thesis were fabricated using the same fundamental techniques, based on a decade of prior work within the Optoelectronics Research Centre. The research started with development of slab wafers suitable for ultraviolet (UV) inscription, consisting of refractive index-controlled photosensitive core and cladding layers on a silicon wafer base, fabricated via the flame hydrolysis deposition (FHD) technique [6]. These FHD wafers were then processed via a UV inscription technique, taking advantage of the photosensitive nature of the core layer to create channel waveguides. In a further advancement reported by Emmerson [8], an interference pattern created at the combined focus of two beams provided the periodic modulation necessary to inscribe Bragg grating regions within the channel waveguide. These fundamental steps allow the creation of the complex waveguides and Bragg grating structures described in this thesis.

This chapter will introduce the fabrication techniques in more detail, outlining the methods involved in both initial slab waveguide production, channel waveguide, and Bragg

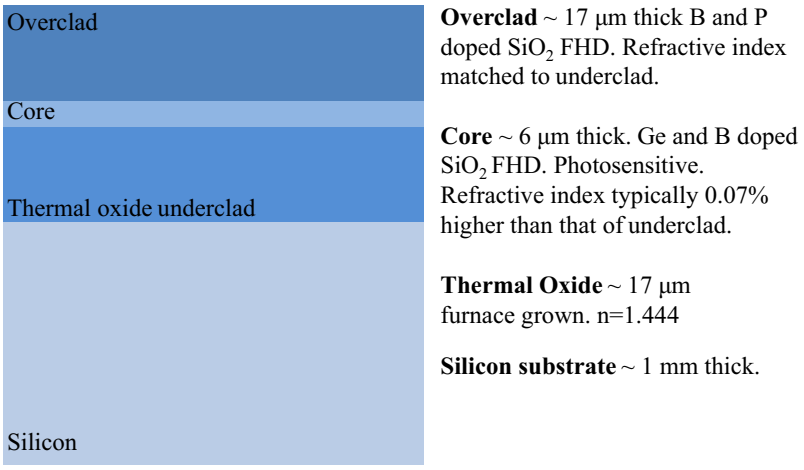

Figure 3.1: Schematic of the desired glass layers on the silicon substrate. The thermal oxide layer is furnace grown, followed by deposition of core and cladding layers by FHD.

grating fabrication. Characterisation techniques will be introduced to illustrate the information that is readily obtainable from the waveguides and Bragg gratings fabricated. Intricacies of the composition and characterised parameters of individual devices produced for experiments will be discussed in detail in the relevant chapters of this thesis.

3.1 Preparation of the slab waveguide

The slab waveguides fabricated to produce devices described in this thesis were prepared employing similar physical processes to those used to fabricate silica fibre preforms. This section describes the fabrication process in detail, from silicon wafer to slab waveguide, to provide an understanding of the nature of the devices in the plane of the wafer.

3.1.1 The base wafer

The base substrates used in the fabrication of all devices used in this thesis are 6-inch silicon wafers. The photosensitive core and cladding layers were deposited on the wafer, in order to achieve the silica-on-silicon structure desired, depicted in Figure 3.1.

An important point to note at this stage is the difference in thermal expansion coefficient between the deposited silica waveguiding layer and the base silicon wafer. The large thermal expansion coefficient of silicon ($\approx 2.5\times10^{-6}/^{\circ}\mathrm{C}$) in comparison to silica ($\approx 0.4\times10^{-6}/^{\circ}\mathrm{C}$), [44], causes the silica layers to be under compression as they cool during the consolidation process. This compressive stress leads to birefringence and bowing in the fabricated glass layer, and can be manipulated by control of the consolidation process (Section 3.1.2.3).

In order to alleviate this stress, a 'buffer' layer of thermal oxide can be grown on the base silicon wafer prior to silica deposition. In the samples described in this thesis, this thermal oxide layer also forms the optical underclad silica layer of the device, and is typically 15-17 μm thick. The thermal oxide layer is fabricated by placing the silicon wafers in a high temperature, wet environment for a number of days or weeks. The silicon surface oxidises to form silica when in contact with the oxygen rich atmosphere, with the silica/silicon boundary moving increasingly towards the centre of the silicon wafer the longer the reaction progresses. It takes around 20 days to grow a layer suitable for use as an underclad as described above. Due to the extreme time scales of this process, wafers with the desired thickness thermal oxide were purchased from a commercial source.

The addition of the thermal oxide layer alleviates some of the effects of the thermal expansion coefficient mismatch, due to the absence of the large step difference between the silica and silicon coefficients. This leads to glass layers with more uniform stresses across the entire 6-inch wafer. This thermal oxide clad wafer is suitable for flame hydrolysis deposition (FHD), allowing direct deposition of photosensitive core and overcladding layers on the surface.

3.1.2 Core and cladding layer deposition

The photosensitive core and index-matched overclad layers were deposited using the FHD technique. The layers used to complete this work were designed at the Optoelectronics Research Centre (ORC), and fabricated on FHD systems designed by the Centre for Integrated Photonics (CIP). Early fabrication work was carried out on a system at CIP, whilst installation of an equivalent system was undertaken at the ORC to replace a system designed within the group [6], but destroyed by fire in 2005. The silica-on-silicon wafers used to create the devices and techniques described in this thesis were designed and fabricated by the author at the ORC. The specifics of layers used for individual devices are detailed in the appropriate chapters and referenced appendices.

Flame hydrolysis deposition is very similar to the chemical vapour deposition (CVD) processes used in the fabrication of silica fibre preforms. The chemical processes undertaken are well documented in the fibre case, ensuring a broad knowledge of the chemical capabilities of the system used to design layer compositions. This section will describe and discuss the FHD technique itself and the resulting layer compositions achieved. More substantial reviews can be found elsewhere [6, 7].

3.1.2.1 Flame hydrolysis deposition: layer composition and refractive index control

The FHD technique draws many comparisons with the CVD processes used in fibre preform fabrication. The closest comparisons are vapour-phase axial deposition (VAD)

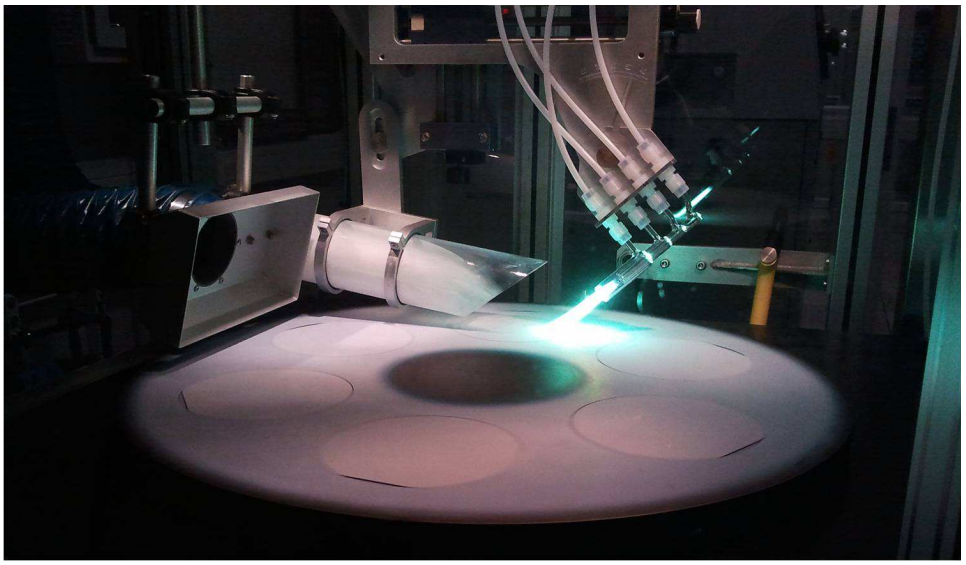

Figure 3.2: Photograph of the working FHD system. The doped hydrogen oxygen flame passes over the wafers depositing a soot layer. Boron vapour causes the green flame colour.

[45] and outside vapour deposition (OVD) [46], where a silica soot is first deposited on the base preform, followed by a high temperature consolidation step during which the low density soot is converted into a dense glass at high temperature. FHD is a planarised version of these techniques, using the existing chemical reactions to produce a planar glass layer on a base wafer.

$$SiCl_4 + O_2 \longrightarrow SiO_2 + 2Cl_2 \tag{3.1}$$

$$SiCl_4 + 2H_2O \longrightarrow SiO_2 + 4HCl \tag{3.2}$$

The silica soot is produced by burning a silicon tetrachloride vapour in an oxygen-hydrogen flame. The main chemical processes occuring are oxidation (Equation 3.1) and hydrolysis (Equation 3.2) of the vapour. The vapour is produced by bubbling a carrier gas, in this case nitrogen, through the liquid chloride precursor. Direct oxidation occurs in flames above 1200°C, and hydrolysis at temperatures below [14]. Dopants are added to the flame via a similar chemical vapour production process. Germanium tetrachloride ($GeCl_4$) and phosphorus trichloride (PCl_3) are subject to nitrogen bubbling, producing the vapour required to add dopants to the glass layer. Boron trichloride (BCl_3) is a gas at room temperature, and thus is used in the gaseous state.

A photograph of the FHD system, with soot production in progress can be seen in Figure 3.2. The vapours travel to the torch via trace heated pipework, ensuring they reach the torch in the vapour phase. The torch ensures the dopants are injected into the centre of the flame. Surrounding the dopants, oxygen and hydrogen in the gaseous

phase provide the oxygen-hydrogen flame required for hydrolysis. The outermost part of the gas stream is argon gas, to provide directionality to the flame. The green flame colour in the image is due to the presence of boron vapour within the flame.

The characteristics of each doped layer are defined by the amount of dopant within the flame. Germanium and boron are added to the core layer to enhance photosensitivity [47]. Photosensitivity is key to the direct UV writing process, and will be discussed in more detail in Section 3.2. The addition of germanium to the silicate matrix also causes an increase in refractive index of the consolidated glass. Conversely, the addition of boron causes a decrease in refractive index. Controlling the amounts of these dopants present in the flame leads to both an increase in the photosensitivity of the core layer, and control of the absolute refractive index of the consolidated glass.

Doping is also employed within the fabrication of the glass overclad to control the refractive index of the consolidated glass layer. This allows design of the modal confinement characteristics of the slab waveguide in the vertical direction. The refractive index of the layer is controlled in a similar manner to that of the core. Boron and phosphorus dopants are added to the flame to control the refractive index of the consolidated layer.

3.1.2.2 Control of layer thickness

The thickness of the consolidated glass layer is a critical design parameter, defining the single- or multi-mode guidance characteristics of the core layer at specific wavelengths. The thickness of the consolidated glass layer is controlled by the number of passes of the torch over the thermal oxide wafer, and the amount of precursor within the flame.

The doped silica soot produced by the hydrolysis reaction is deposited on the thermal oxide wafers described above (Section 3.1.1) within a controlled environment. The wafers sit on a turntable which is heated from beneath to 180°C to ensure evaporation of the HCl and excess water to the extract system. The turntable is rotated to ensure an even distribution of soot on the wafer. At the same time, the flame translates laterally, and the speed of rotation is adjusted to ensure an even distribution of soot across all points on the wafer.

Control of the precursor levels in the flame, rotation of the wafers and translation of the torch leads to a controllable deposited average soot composition and thickness per pass. The deposition rate must be calculated empirically from previous fabrication runs or test wafers.

3.1.2.3 Layer consolidation

Thermal consolidation, or sintering, of the deposited soot defines the final structure of the glass layer. During this phase, the specific thermal profile applied to the soot layer can

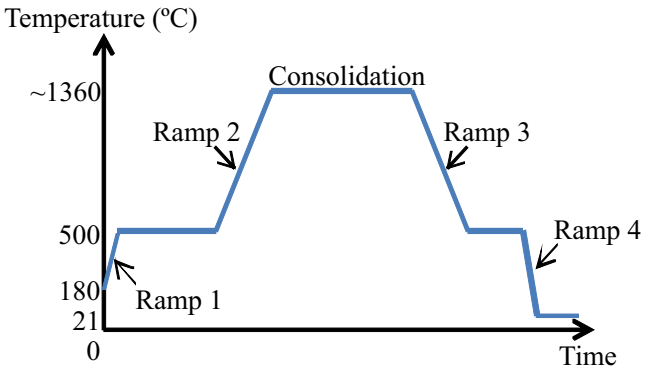

Figure 3.3: Typical thermal cycle for a core layer consolidation. The soot is deposited whilst the wafer is heated to 180°C, and the soot-covered wafer then moved to the furnace where a temperature of 500°C is maintained (Ramp 1). The temperature is ramped over several hours to around 1360°C (Ramp 2), and maintained to enable the core consolidation. A controlled ramp is used to reduce the furnace temperature to 500°C (Ramp 3), and the wafer removed from the furnace at this temperature and cooled to room temperature (Ramp 4).

lead to consolidated glasses with widely differing structure, and thus optical properties. Control of the thermal environment and gases present during the consolidation stage is critical in achieving the desired optical layer. The consolidation parameters were discussed in depth in development of the FHD process at Southampton [6]. This section will briefly describe the effect of a number of consolidation parameters on the FHD layers.

Once the required soot thickness has been deposited on the thermal oxide wafer, the consolidation phase takes place. The samples are moved to a furnace where they sit at 500°C in an oxygen and helium environment. The furnace temperature is then increased to a maximum consolidation temperature via a thermal ramp over several hours. This temperature is maintained for a consolidation period, and then ramped down, producing the dense glass layer required. Figure 3.3 shows a typical thermal cycle for core layer consolidation.

The temperatures required during each phase are defined by the dopant levels within the soot. Increasing the dopant content of the soot not only changes the photosensitivity and refractive index of the glass, it also lowers the consolidation temperature required to form the dense glass layer. Boron has the biggest effect, and control of the boron level in the soot is critical to lowering the consolidation temperature to that achievable with modern furnaces.

Consolidation of an FHD layer should be carried out at a temperature lower than that of the previously consolidated FHD layer, in order to prevent dopant mobility between the layers. A core consolidation typically takes place at around 1360°C, and a cladding deposition at around 1100°C.

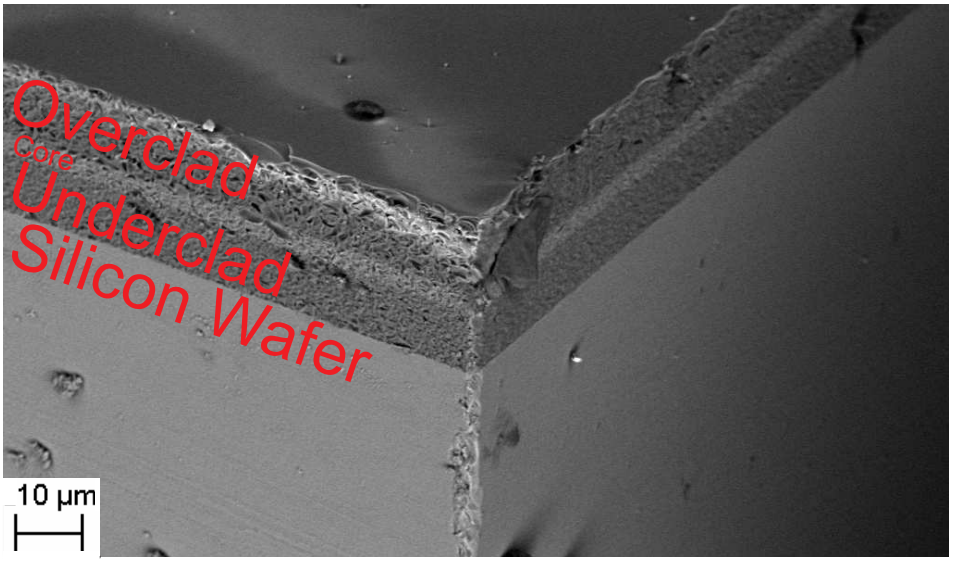

Figure 3.4: SEM image of completed silica-on-silicon wafer. The approx. 17 μm thick overclad and approx. 6 μm core layer are consolidated onto the approx. 17 μm thick thermal oxide layer, grown on the base silicon wafer. Sample image obtained by Dr. Christopher Holmes. Wafer dicing undertaken at CIP.

The consolidation temperature and the consolidation time are inextricably linked. A lower temperature requires a longer consolidation time, and vice versa. However, a longer consolidation time can lead to enhanced dopant volatility, an undesired effect which can lead to alterations in the dopant concentration within the soot and the final glass layer.

Control of the ramp rate desired to reach these consolidation temperatures also affects the optical properties of the final glass. If the ramp rate is too slow, the soot sits at a temperature close to that required to sinter the glass, for a long period of time. This can lead to increased dopant volatility, altering the final glass composition.

Control of the cooling rate is also important in order to achieve the desired amorphous glass structure. Obtaining a high quality glass layer is a compromise between cooling quickly enough to prevent crystallisation and cracks within the layer, and cooling slowly enough to prevent wafer warping [48]. There are two cooling ramp rates to consider. The first, between the consolidation temperature and 500°C, has the greater effect on glass composition and uniformity. The second, between 500°C and ambient room temperature, is less critical, as the viscosity of the layer below 500°C is such as to prevent significant crystallisation and cracking.

Once removed from the furnace and cooled, the wafers are ready for post-processing. A scanning electron microscope (SEM) image of a typical silica-on-silicon wafer can be seen in Figure 3.4. The figure shows the doped silica overclad and core layers on the thermal oxide underclad layer, all supported by the base silicon wafer. Such FHD wafers can be processed via chemical etching to produce physical and chemical sensors [49,50].

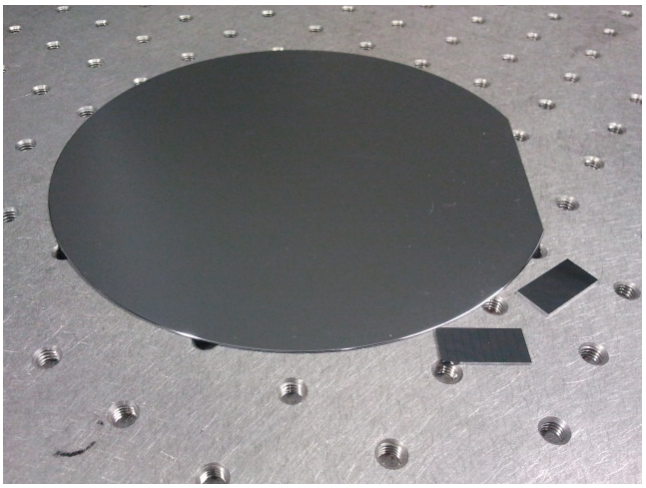

Figure 3.5: Image of an unpolished silicon wafer, and two diced 10 × 20 mm silica-on-silicon chips.

Prior to full consolidation, sintering and solution doping of the wafer can be used to produce rare-earth doped glass layers suitable for lasing and amplification applications [51]. For the work described here, optical machining and direct UV writing were employed to produce the waveguides and Bragg gratings required. Figure 3.5 shows a six-inch unpolished silicon wafer, and two diced 10 × 20 mm chips of the magnitude typically used to create the devices described in this thesis.

3.1.2.4 Preparation of sample facets

As with any optical waveguide, the desire to reduce Fresnel reflection losses at the input and output facets of waveguides is important when considering potential applications. Termination of waveguides is particularly important when considering Bragg gratings, as observing the reflected spectrum of the grating is often the most appropriate form of characterisation. In order to reduce the broadband Fresnel reflections and promote waveguide termination, one of a number of physical processes could be carried out. The most widely used method in this thesis was to write the UV written waveguides and Bragg gratings such that the waveguide was not perpendicular to the facet edge of the sample (Figure 3.6 (a)). An angle of 8° was chosen, as this is greater than the numerical aperture of the waveguide, and appropriate fibre pigtail connectors are commercially available to interrogate such devices. The resulting chip has an output facet at an angle greater than normal incidence, so any reflected power at the output facet is not coupled back into the waveguide. A similar effect is obtained when the silica-on-silicon sample is diced at an angle prior to, or after, UV writing (Figure 3.6 (b)).

In addition, the quality of the input and output facets must be considered in all applications. Traditionally, a polishing regime is undertaken on the silica-on-silicon chips, enabling material removal via lapping and a final polishing routine to obtain the required

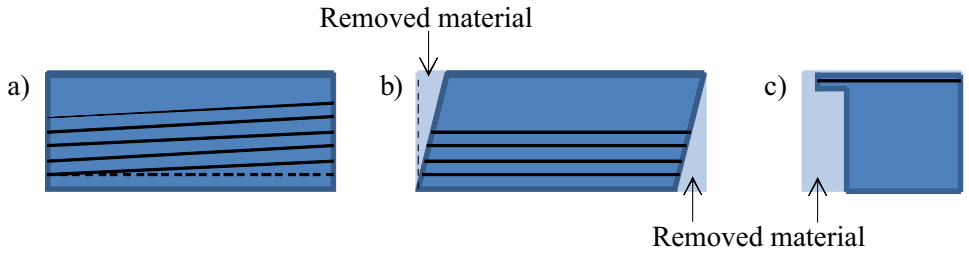

Figure 3.6: Facet preparation for silica-on-silicon devices. (a) Waveguides are written at an angle (typically 8° to the waveguide facet. (b) The sample is diced at an angle so waveguides have angled facets. (c) Dicing technique for optical finish output facets. Waveguides are marked in black.

surface roughness values for the specific application. The lapping and polishing steps are, however, time-consuming, and leave significant room for error in both technique and final surface quality. A technique for rapid realisation of the desired surface roughness for waveguiding applications in silica-on-silicon has been developed by Lewis Carpenter, and used on the parametric pair production waveguides described in Chapter 6. An initial dicing process on the silicon side of the silica-on-silicon chip removes around 900 μm of material rapidly with a coarse blade. A finer blade is then used on the silica side of the chip to remove the final 100 μm, with the waste material ejected beneath the sample rather than causing scratches to be formed on the optical surfaces. A diagrammatic representation of the resulting device after this process is shown in Figure 3.6 (c). A desired facet average surface roughness of as little as 4.9 nm can be achieved in this manner, comparable to that achieved by polishing facets, but achievable faster and with relative ease.

Prior to post-processing, the material thickness and refractive index must be obtained to ensure the correct processing procedures are undertaken.

3.1.2.5 Measurement of material properties

Knowledge of the thickness and refractive index of our fabricated glass layers is required prior to UV writing. This ensures that subsequent waveguides can be fabricated with the intended modal profile. The information allows detailed modelling of the fabricated waveguide to be undertaken, using the data for each individual layer.

The thickness and refractive index of our FHD-deposited layers are measured using a prism coupling device, the Metricon 2010 Prism Coupler. The measurement is carried out on a 'dummy wafer', typically a thin thermal oxide (approx. 1 μm thick) layer on a silicon wafer, or a plain silicon wafer, which is present on the deposition table at the same time as the soot layer is deposited. The deposited glass layer on the 'dummy wafer' has been shown to have identical material properties to that on the device wafer, through previous demonstration and discussion with CIP. The measurement method involves

coupling light into the wafer under test via a measurement prism, and observing the angular dependency of coupling to the waveguide.

The wafer and prism are put in contact via a pneumatic coupling device, which exerts pressure on a small region on the reverse of the wafer, causing a tight couple between the surfaces. Light at the wavelength of interest is then launched into the prism and coupled into the waveguiding slab layer, via the contact point. A photodetector close to the prism measures the intensity of light reflected from the glass interface. If light is coupled into the waveguide, a reduction in this reflected intensity is observed. Light is launched from a variety of angles, and the guided mode strength recorded at each incidence angle. Once the guided mode positions and strengths are known, the refractive index and thickness of the film can be calculated via the following relation (Equation 3.3) [52].

$$\frac{2\pi}{\lambda} n \cos\theta_2 T + \Psi_{10} + \Psi_{12} = m\pi \tag{3.3}$$

n and T are the refractive index and thickness of the layer respectively, with m the integer denoting the order of the mode. λ is the wavelength of incident light, and θ_2 the angle of incidence on the coupling spot. Ψ_{10} and Ψ_{12} are the Fresnel phase shifts at the film-air and film-substrate interfaces respectively, and are calculated given Fresnel reflection theory. Solving the equation for two modes, m, of the guide yields thickness and index values. The quoted accuracy values for the refractive index and thickness measurements are ± 0.0005 and ± 0.5 % respectively, enabling confidence in the obtained results for our silica-on-silicon layers. Knowledge of these parameters allow gratings at specific wavelengths to be fabricated, and the design of single and multi-mode devices to take place. This information proves invaluable when designing complex planar lightwave circuits.

3.1.3 Properties of specific devices

Individual control of the refractive index, photosensitivity and thickness as described above allows investigation into numerous devices which require different slab waveguide properties.

Experiments described in Chapters 5 and 6, investigating the loss and dispersion of UV written waveguides, were carried out in materials with 'index-matched' core and cladding layers; the relative and absolute proportions of dopants within the flame were controlled so the core layer and the cladding layer have similar refractive index. UV writing is then used to increase the refractive index only in the core region, allowing a symmetrical profile of a similar refractive index surrounding the higher index core region. The core thickness was designed so that only a single mode waveguide at 1550 nm was supported within the device.

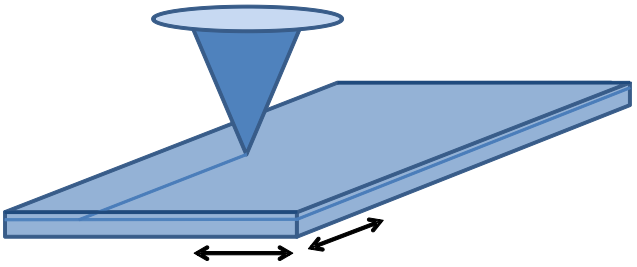

Figure 3.7: Basic UV writing schematic. A beam is focussed into the photosensitive core layer of a silica-on-silicon chip. A waveguide is created where the photosensitive core is exposed to UV radiation.

Devices required to support higher order mode propagation take advantage of a higher index core within the slab waveguide. The core layer was relatively heavily doped to increase the refractive index of the layer, while the over cladding layer was index matched to the thermal oxide to provide a core/cladding index contrast of 0.7 %. The increased refractive index of the core layer compared to the surrounding glass, coupled with a thicker core layer enable higher order modes to be supported.

Fabrication parameters for the specific core and cladding layers used in this thesis are presented in Appendix C.

3.2 Photosensitivity

Direct UV writing relies on photosensitive mechanisms to allow definition of waveguides and Bragg gratings within the doped silica-on-silicon platform. These mechanisms allow light-induced refractive index modifications in the glass layer. Waveguiding is promoted within the region of increased refractive index caused by exposure of the photosensitive glass to intense UV radiation, as shown in Figure 3.7.

There are two contributions to the overall photosensitivity of the sample prior to waveguide inscription. The first is the intrinsic photosensitivity of the core layer of the slab waveguide itself, made photosensitive by the addition of germanium and boron dopants, the production of which was described in the previous section (Section 3.1.2.1). The second is the effect of hydrogen loading the samples prior to UV-irradiation, which increases the photosensitivity of the sample. This section will address these two contributions in turn, providing discussion of the mechanisms behind the formation of waveguiding regions by direct UV writing.

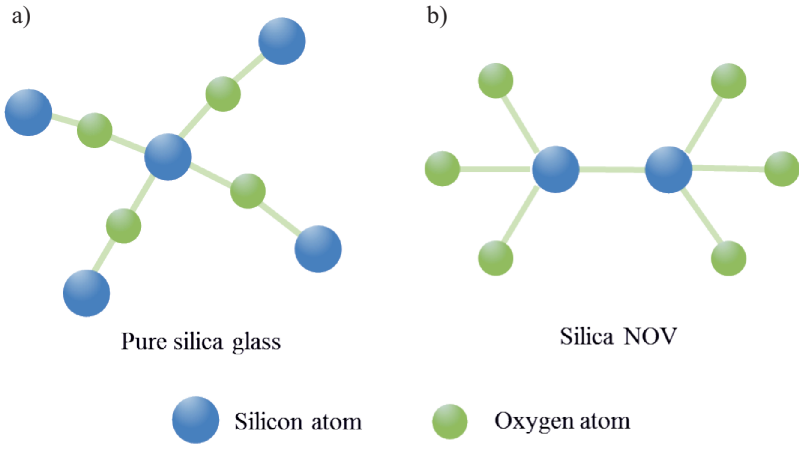

Figure 3.8: Figure shows chemical structure of a) pure amorphous silica matrix, and b) silica NOV.

3.2.1 Photosensitivity in the glass layer

The inherent photosensitivity of the fabricated core layer is the means by which waveguides and Bragg gratings are fabricated, when the core is exposed to focused UV radiation. The physical mechanisms behind the photosensitive reaction are complex, with various schemes described in the literature offering widely differing explanations of the processes involved [47, 53, 54]. The aim of this section is to introduce the physical processes thought to be occurring, whilst emphasising the alterations to the doping of the material which can increase photosensitivity, given experimental experience.

The photosensitive response of the glass discussed here is a Type *I* photosensitive reaction [55]; a monotonic increase of refractive index with time as the material is exposed to UV radiation. The photosensitivity of the glass is caused by the dopants incorporated in the glass structure itself. When dopants are added to the silica soot, point defects are formed within the post-consolidation glass matrix. These are known as 'colour centres'.

The pure amorphous silica matrix is shown in Figure 3.8a. The glass matrix has a tetrahedral structure, with four oxygen atoms bonded to each silicon atom within the matrix. In the situation where the glass layer forms in an oxygen deficient environment, silica neutral oxygen vacancies (NOVs) are formed as a direct bond between two silicon atoms (Figure 3.8b).

It is the colour centres that are formed within the germanium doped glass structure that have absorptions at the appropriate wavelengths to make the glass photosensitive in the UV. Colour centres typically have absorptions within the 240 nm to 250 nm wavelength band. It is for this reason that a photosensitive reaction occurs within the glass when it is irradiated at these wavelengths. The magnitude and resulting structure of the region where the reaction occurs is determined by the intensity of the UV radiation, and the nature of the colour centres present at the site. The germanosilicate NOV and

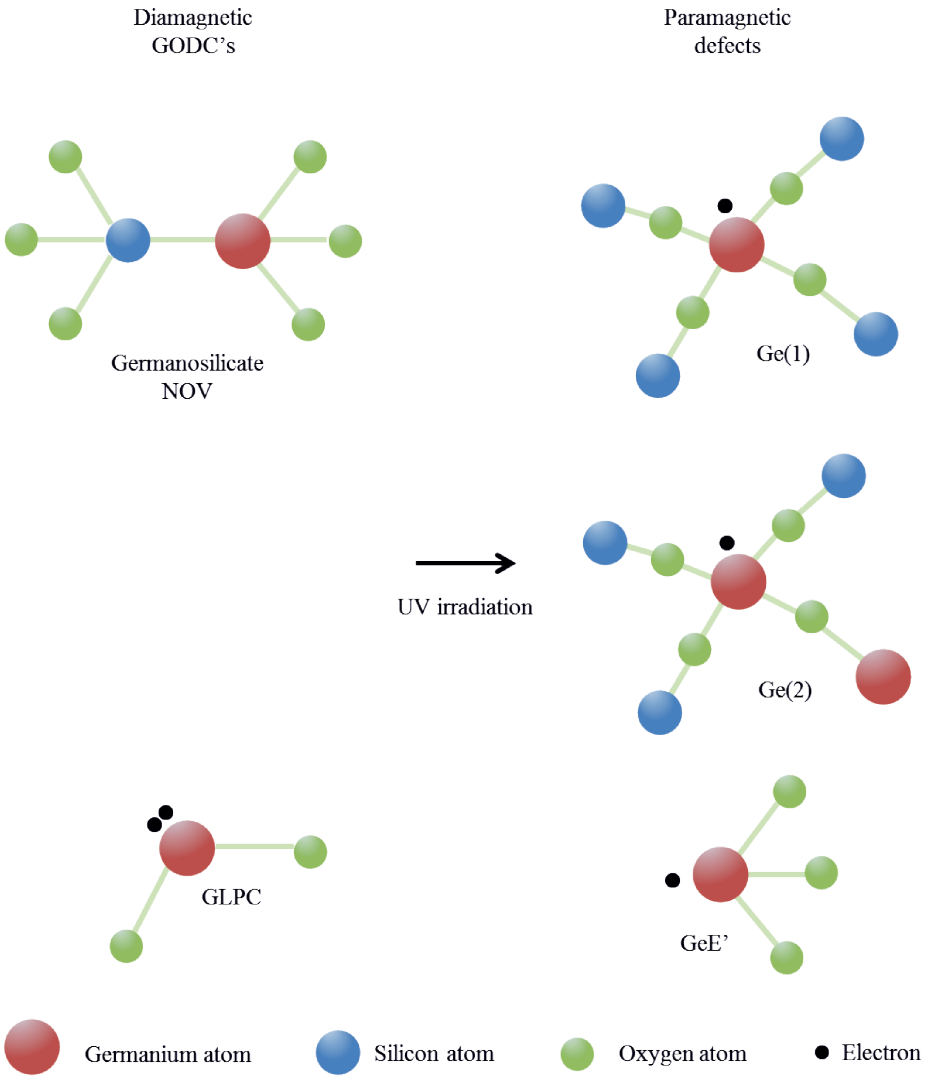

Figure 3.9: Figure shows structures produced during irradiation of germanium-doped silica. The GLPC and germanosilicate NOV colour centres on the left form the GeE', Ge(1) and Ge(2) defects on the right when irradiated. Note the diamagnetic and paramagnetic forms of the pre- and post-reaction structures respectively.

the germanium lone pair centre (GLPC) are absorbing within this region [56]. These germanium oxygen deficient centres (GODCs) are shown in the left portion of Figure 3.9. The right portion of the figure shows the structures thought to be present in the glass after UV irradiation. The GLPC forms the GeE' defect, and permits the free electron e^-. The subsequent electron is thought to move within the matrix and form another defect, such as the Ge(1) or Ge(2) pictured.

It is widely thought that the change between diamagnetic colour centres (where all electrons are paired) and paramagnetic defects (where electrons can be unpaired) causes the observed change in refractive index of the glass. A number of reports show investigation into this subject [57, 58], and all come to similar conclusions. The nature of the colour centres has an overall effect on the photosensitivity of the doped glass, but

Precursor	Nitrogen flow rate (l/min)	Pressure (kPa)	Temperature
$SiCl_4$	114 - 142	25.9 kPa	20°C
$GeCl_4$	43 - 51	10.1 kPa	20°C
PCl_3	31	13.33 kPa	21°C
BCl_4	26 - 61	-	-

Table 3.1: Range of values of nitrogen flow and precursor pressure used in bubbling of precursors for slab layer fabrication.

the extent to which the mechanisms cause the change in refractive index is unknown. It is thought that an additional refractive index change occurs due to thermal effects and stress changes within the glass whilst irradiation occurs. Douay et al. [55] report an additional refractive index modification due to densification of the glass layer during the irradiation.

The quantity of germanium dopant within the germanosilicate glass determines the level of photosensitivity the glass exhibits. As more germanium dopant is added to the glass, the number of colour centres present within the structure increases. Although from a photosensitivity point of view this is a positive effect, excessive levels of germanium dopant within the glass can adversely affect the mechanical strength of the glass itself. This can introduce additional losses to the waveguiding structure, and leads to a refractive index which is higher than desired.

To counter the undesired effects of this high doping level, other dopants can be used which enhance the photosensitivity of the glass, but counter the other effects. Boron co-doping is found to lower the refractive index of the glass, but also enhances the photosensitivity [47]. By co-doping in this way, and controlling the relative proportions and absolute quantities of germanium and boron dopants within the soot, a glass layer can be fabricated with a controllable refractive index and sufficient photosensitivity to allow direct UV writing of waveguides.

Table 3.1 gives typical ranges of nitrogen flows and precursor pressures measured during the bubbling technique used to transport precursor vapours. The larger flow and precursor pressure of the nitrogen used to transport the $SiCl_4$ vapour leads to more dopant being present in the flame. This leads to a larger relative proportion of silica soot deposited compared to the germanium and phosphorus dopants. This allows the relative proportion of germanium and boron in the glass to be controlled. Actual wafer compositions are shown in Appendix C.

3.2.2 Hydrogen loading

The addition of germanium and boron dopants to the amorphous silica matrix enhances the photosensitivity of the glass layer. However, the increase in absolute dopant levels leads to an increase in defects within the glass layer, which in turn introduces additional propagation losses within the waveguiding layer and leads to mechanical strains within the glass matrix. These undesired effects can be prevented if an alternative means of photosensitising the glass is found, which does not change the physical properties of the glass matrix but ensures the photosensitivity is great enough to allow the formation of inscribed waveguides.

Hydrogen loading is one method of increasing the photosensitivity whilst ensuring the physical properties of the glass matrix do not suffer. First implemented by Lemaire et al. [59], the glass substrates are kept in a high-pressure hydrogen environment for a number of days to allow the hydrogen to diffuse into the glass matrix. This enhances the photosensitive response of the glass within the UV writing region.

The chemical mechanisms involved in explaining the photosensitivity enhancement due to hydrogen loading are as complex as those involved in the case of the colour centres in glass. It is thought that the hydrogen creates Si-OH and Ge-OH bonds within the matrix post-irradiation, and also interacts with the GLPC and germanosilicate NOV to produce additional GODC colour centres. These colour centres absorb within the same 240 nm to 250 nm wavelength band, enhancing the photosensitivity of the glass structure.

Hydrogen loading allows the gas to diffuse into the glass matrix over a period of time prior to UV writing. This time period is dependent on the glass structure; the thicker the glass layer, the longer diffusion takes. For the samples described in this thesis, approximately 25 μm of doped silica (combined core and overclad layers) require approximately five days within the hydrogen rich environment to achieve 95 % of the equilibrium value defined by [60],

$$\tau_{0.95} = \frac{0.8d^2}{D}, \tag{3.4}$$

where D is the diffusivity of hydrogen in silica, and d is the thickness of the silica layers. D can be obtained from the literature [7], and has a value of 4.3 μm^2 per hour. The time to reach this 95 % does not depend on the pressure of the hydrogen environment; the pressure defines the concentration of the indiffused hydrogen. The equilibrium concentration is found to vary linearly with pressure, assuming no interactions occur between the hydrogen molecules [58]. The equipment available during this project allowed hydrogen loading to occur at a pressure of around 120 bar at room temperature, and for periods of greater than three days, to encourage diffusion towards equilibrium prior to

UV writing. This allows saturation of the samples, reducing the effect of this parameter in the UV writing process.

As hydrogen is able to diffuse into the silica matrix, similarly it is capable of diffusing out of the glass once removed from the hydrogen rich environment. For the samples with an overclad layer, this is found to occur over a number of hours, and, thus, for waveguides written over a period of a few minutes, little change in the index contrast is observed. For samples designed with no overclad, however, the rate of hydrogen out-diffusion can adversely affect the UV written grating responses over a period of a few minutes. As a preventative measure, samples removed from the hydrogen rich environment were stored in liquid nitrogen to inhibit rapid out-diffusion of hydrogen prior to UV writing. This out-diffusion can, however, be thought of as an advantage of the photosensitising process; post-irradiation, the remaining hydrogen within the glass matrix diffuses out of the sample, returning the surrounding glass structure to its original pre-loading state.

The above discussion has outlined the basic systems involved in producing a photosensitive glass capable of waveguide and Bragg grating inscription via UV irradiation. The conversion of NOVs to defects within the glass matrix, both in the presence of hydrogen and not, causes the change in refractive index observed when the glass is exposed to intense UV radiation. The direct grating writing process relies upon these reactions occuring in order for waveguide and Bragg grating formation to occur. The following section describes the direct grating writing process in detail, taking into consideration the photosensitive nature of the glasses described here.

3.3 Direct grating writing - waveguide and Bragg grating definition

The waveguides and Bragg gratings discussed in this thesis were fabricated using the direct grating writing (DGW) method. Developed within the Optoelectronics Research Centre [4], DGW allows single-step fabrication of waveguides and integrated Bragg gratings. DGW is a rapid prototyping technique, suitable for the design and implementation of complex planar lightwave components, such as x-couplers, y-splitters and tilted waveguide geometries.

A detailed desciption of the DGW technique is given in this section. A description of the history of DGW will be followed by a discussion of the optical set-up and control methods used to define grating planes within waveguides. Advances and modifications to the DGW system which influence the work carried out in this thesis, including the development of the phase control Bragg grating definition method, will be discussed.

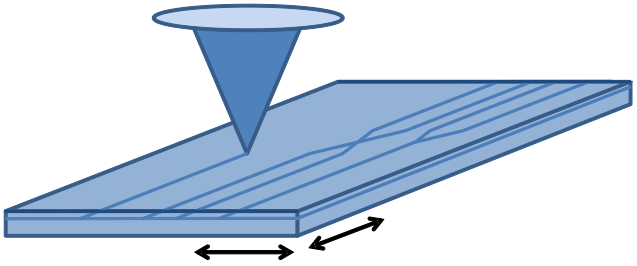

Figure 3.10: UV writing schematic. A beam is focussed into the photosensitive core layer of a silica-on-silicon chip. A waveguide is created where the photosensitive core is exposed to UV radiation. x-couplers and y-splitters can be achieved by translating the sample whilst maintaining the focus in the photosensitive core.

3.3.1 The development of direct grating writing

Direct grating writing takes the processes involved in two fabrication techniques and combines them to allow single-step production of waveguides and Bragg gratings in photosensitive glass structures. The direct UV writing waveguide inscription technique and the transverse holographic Bragg grating definition method are combined to allow UV inscription of waveguides and Bragg gratings simultaneously. This section provides an overview of these mechanisms in relation to the DGW technique.

Direct UV writing was developed by Svalgaard [5] as a means of creating waveguiding channels within glass structures. Traditionally, buried channel waveguides are fabricated in glass waveguides via numerous intensive clean room based steps. A rib waveguide is first fabricated by etching into a glass core layer, then a cladding layer is deposited to surround the core. The rib waveguides allow high index contrast if desired, and thus small bend radii, but the waveguide performance suffers if fabricated outside of the clean room environment, increasing the cost of fabrication for prototype devices.

The direct UV writing method takes advantage of a photosensitive core layer, typically within a three layer glass structure. A UV laser, with wavelength within the defect band of the photosensitive material, is focussed into the core layer of the sample, causing a change in refractive index of the core material within the high intensity focal point of the beam. The sample is translated within the focus of the beam to change the refractive index of the core within the exposed region. The waveguide is effectively 'drawn' within the core region using the focussed UV beam, as shown in Figure 3.10. The direct UV writing system allows buried waveguide fabrication outside the clean room, as waveguide fabrication takes place after the overclad is deposited thus protecting the core. The maximum achievable refractive index contrast is smaller than that of rib waveguides, as it is wholly defined by the contrast achieved by UV irradiation of the core. Due to the fire at the Optoelectronics Research Centre in October 2005, during which the clean room complex was destroyed, the ability to fabricate waveguides outside the clean room environment was exploited, and UV writing developed to allow rapid prototyping of small volumes of devices at low cost.

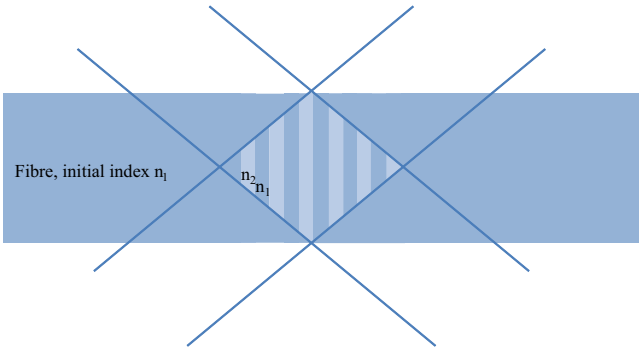

Figure 3.11: Schematic depicting the transverse holographic method of fibre Bragg grating formation. A periodic refractive index modulation is created by irradiating a fibre core with a crossed beam interference pattern.

The transverse holographic method of defining Bragg grating structures was developed in photosensitive fibre by Meltz et al. [38]. A coherent beam is split into two equal intensity components, which travel an equal length before recombination to create an interference pattern within the core region of the fibre, normal to the fibre axis. The refractive index change created by the UV irradiation is periodic due to the combination of the interference pattern present in the beam and the intensity modulation of the incident UV light, creating a number of grating planes within the fibre core as shown in Figure 3.11.

The goal of combining these two schemes to enable planar Bragg gratings in integrated photonic circuits led to the development of the DGW system. The novel optical set up allowed combination of two focussed UV beams in a 5 μm spot, enabling inscription of a Bragg grating within a simultaneously defined direct UV written waveguide. The DGW system has developed over the course of this project to include modifications improving both the efficiency and scope of the system.

3.3.2 The amplitude modulation system

The DGW system comprises a number of optical components necessary to manipulate light in such a way as to be able to fabricate both waveguides and grating planes. This design was first implemented by Emmerson et al. in 2002 [4], and the fundamental optical set-up remains the same. A schematic of the amplitude modulation system is given in Figure 3.12.

The 100 mW, 244 nm output of a frequency-doubled argon-ion laser (Lexel 95-SHG) passes through an acousto-optic modulator (AOM). The AOM allows control over the amplitude of the beam, creating the modulation necessary to fabricate Bragg grating periods. An acoustic wave is applied across the quartz optic, creating a refractive index modulation in the quartz which diffracts the beam as it passes through. The first order diffracted beam from the AOM is optimised for maximum intensity by aligning the path

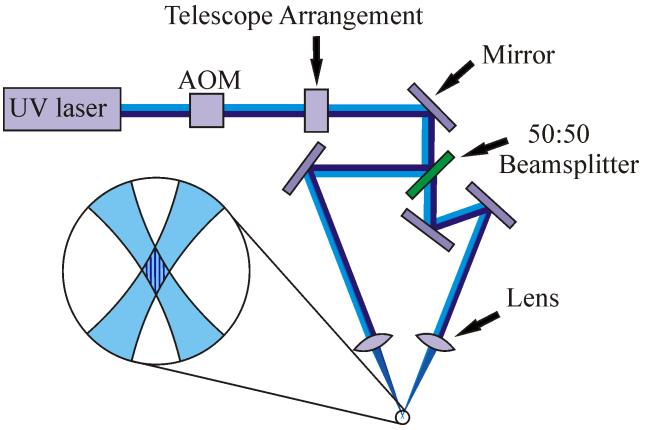

Figure 3.12: Schematic of amplitude modulation optical set-up of direct grating writing system.

of the beam through the AOM. The first order diffracted mode from the AOM is chosen as it provides the greatest range of laser intensity including the zero point when the amplitude of the acoustic wave within the AOM is modulated (0 % to 80 % of the incident light). A well-defined zero is required in order to achieve the best intensity contrast, and therefore refractive index contrast during grating formation. This leads to the strongest possible grating response.

Upon exiting the AOM, the beam passes through a series of irises, lenses and steering optics in order to clean, expand and direct the beam. The expanded beam is incident on an interferometric set-up to create the interference pattern necessary to form Bragg grating planes. The beam is split via a 50:50 beam splitter and travels a similar path length to the focussing lenses, with the difference in path length less than the coherence length of the laser. The additional mirror in one arm conserves spatial coherence at the focal point by equalising the number of reflections.

The photosensitive silica-on-silicon sample is held by vacuum on an air-bearing stage system (Aerotech ABL 9000), featuring four-axis control and feedback systems, capable of resolving the position of the stage system with precision of ≈1 nm. An image of the entire system, including optical set up and air-bearing stage system, is shown in Figure 3.13. Control over the translation of the sample, and control over the amplitude of the UV input beam, allows waveguides and Bragg gratings to be fabricated in photosensitive materials. The following sections will describe waveguide and Bragg grating definition in turn, followed by discussion of the system parameters which control the attributes of the fabricated devices.

3.3.2.1 Waveguide definition

Definition of waveguiding regions within the photosensitive core layer is performed in one simple step. By translating the sample so the photosensitive core layer is within the stationary crossed beams, an averaging of the interference pattern within the spot

Figure 3.13: The DGW system, showing air-bearing stage system and optical set up.

occurs, creating a uniform change in refractive index of the glass layer and defining a channel waveguide. This creates a channel in exactly the same way as in standard UV writing.

The size of the focal spot is critical in the fabrication of the channel waveguides. In order to achieve single mode confinement at various wavelengths, the spot size of the beam must be changed. A shorter wavelength requires a smaller core for single mode guiding, and, thus, a smaller focal spot during the definition process. The single mode nature of the waveguide is defined by the spot size in the horizontal plane, and by the physical thickness of the core layer in the vertical direction. The physical dimensions of the core are defined during the fabrication of the layer (Section 3.1.2.2). Care is taken to match the focal spot size to the core thickness when symmetrical waveguides are required. Control of the spot size and vertical dimensions of the waveguide allows both single- and multi-mode structures to be fabricated via direct control of the DGW system.

In order to support Bragg grating structures within a waveguide, the waveguide must guide light strongly enough to allow light to couple into the counter-propagating mode. The degree of confinement of the waveguide is controlled by varying the amount of energy per unit area present in the focal point of the crossed beams, or 'fluence'. Fluence is defined by the following relationship:

$$F = \frac{I_{UV} a}{\nu_{trans}} \tag{3.5}$$

where F is the fluence in kJcm^{-2}, a is the spot diameter in cm, I_{UV} is the average power density of the writing spot (kWcm^{-2}) and ν_{trans} is the speed of sample translation (cms^{-1}). A higher fluence induces a larger refractive index change, tending towards a saturation point due to the limited photosensitive response of the material (Section 3.2).

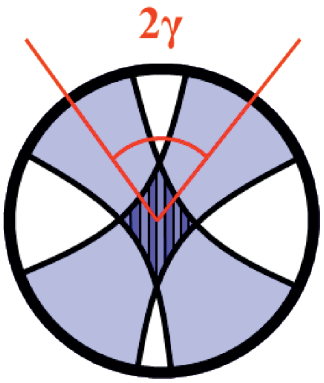

Figure 3.14: Detail of creation of interference pattern within the crossed beam focal point. γ defines the intersection angle of the beams. The interference fringes are created where the beams intersect.

3.3.2.2 Bragg grating definition

Definition of Bragg grating structures is achieved by exploiting the dual-beam system, using the inherent interference pattern between two focussed spots and modulation of the beam to create the index modulation within the glass layer.

The Bragg grating period is partially defined by the period of the interference pattern within the focal point (see interference pattern detail in Figure 3.12). The interference pattern is inherent to the crossed beam focal point, so long as the beams are precisely overlapped, and that the two arms of the interferometer are of equal path length to within an error defined by the coherence length of the incident beam. The period of the interference pattern is defined by the intersection angle at the focal point. Figure 3.14 shows the creation of the interference pattern between the crossed beams.

The period can be calculated from the intersection angle via:

$$\gamma = \sin^{-1}\left(\frac{\lambda_{UV}}{2\Lambda}\right) \tag{3.6}$$

where λ_{UV} is the wavelength of incident light (in our case 244 nm), and Λ is the grating period obtained from the Bragg equation (Equation 2.36).

The grating period obtained during the direct grating writing process is not wholly defined by the period of the interference fringes within the focal point of the beam. A Bragg grating is created by modulating the amplitude of the beam at a temporal period the same as that required for the sample to translate by an integer number of grating periods. The interference pattern is superimposed upon the previous section, and so on, creating the periodic refractive index contrast desired. This is described fully in Section 4.1.

A number of parameters can be altered in order to fabricate Bragg gratings with differing spectral responses. The central wavelength of the Bragg grating, the grating strength and the shape of the spectral response are controlled via a combination of the fluence, duty cycle and speed of translation of the sample within the UV focus. The typical operating range of these parameters is shown in Table 3.2. Chapter 4 describes the development of the Bragg grating spectral response in detail.

Parameter	Value at 780 nm	Value at 1550 nm
Spot size (for single mode guide)	≈ 5 μm	≈ 7 μm
Intersection angle (2γ)	≈ 54 °	≈ 26 °
Fluence	12 - 16 kJ/cm^2	12 - 16 kJ/cm^2
Speed	2.5 - 10 mm/min	2.5 - 10 mm/min
Duty Cycle	0.4 - 0.6	0.4 - 0.6

Table 3.2: Typical range of DGW parameters for 780 nm and 1550 nm single mode waveguides.

3.4 Bragg grating spectral characterisation

Characterisation of the Bragg gratings fabricated is necessary to obtain information about the spectral profile of the gratings. In particular, knowledge of the central wavelength and the peak height of the grating reflection are requirements for the dispersion measurement technique (Chapter 6) and the loss measurement technique (Chapter 5) respectively. This section provides a description of the characterisation set-up typically used to interrogate the fabricated gratings and waveguides. The standard 1550 nm set-up is described, alongside the Gaussian fitting algorithm used to obtain information about the grating profiles. The final section describes the alterations made to the set-up to make it suitable for grating characterisation in the 780 nm region.

3.4.1 The standard 1550 nm grating characterisation set-up

The characterisation set-up used for basic analysis of the grating spectra is based around fiberised telecommunications system components. A schematic of a simplified version of the system used to collect the reflected spectrum from a Bragg grating is shown in Figure 3.15.

Broadband light from a combined multi-SLED source (Amonics ASLD-CWDM-5-B-FA) passes through a polarisation controller and broadband fibre in-line polariser to ensure single polarisation across the broad spectrum (1250 to 1625 nm). This custom polariser consists of input and output collimators with a broadband plate polariser between. The power extinction ratio between the maximum and minimum output power is maintained

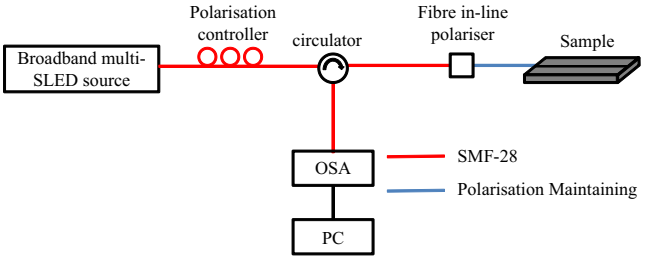

Figure 3.15: Characterisation set-up for gratings in the telecommunications band. Shows system components and denotes fibre type (single mode, polarisation maintaining).

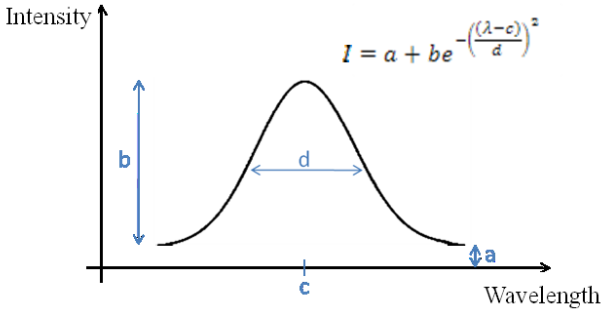

Figure 3.16: Parameters obtained using the Gaussian fitting program, with fitted function. The parameters measured are the offset of the peak from the zero intensity level (a), the height of the Gaussian peak (b), the central wavelength of the grating (c) and the 3 dB width of the Gaussian peak (d). Parameters can be used to reconstruct the grating profile.

over a broad band as the input polarisation state changes. The polarised light is carried to the sample via a polarisation maintaining fibre pigtail. The reflected light from the gratings within the waveguide is returned via the circulator to the optical spectrum analyser (OSA) (Ando AQ 6317B). All fibre is single mode telecommunications fibre at 1550 nm (SMF-28), with polarisation maintaining fibre used between circulator and sample to ensure single polarisation measurements.

The data from the OSA is collected using a LabView data acquisition program, in which the reflected spectrum is analysed and a Gaussian fitting algorithm applied to all Bragg reflections. The program returns fitting parameters for the measured peaks; the central wavelength of the grating (c), the 3 dB width of the Gaussian peak (d), the height of the Gaussian peak (b) and the offset of the peak from the zero intensity level (a). A schematic of the obtained parameters can be seen in Figure 3.16.

The Gaussian fitting algorithm can determine the central wavelength of the grating with an accuracy of 0.01 nm, and is dependent on the spectral shape of the grating. An example of a Gaussian fit to an experimental grating reflection spectrum is shown in Figure 3.17. The more Gaussian-like the grating profile, the better the fit, leading to requirements of between 5 % and 95 % reflectivity and the equivalent number of grating periods required to achieve this. The number of grating periods is defined by the length of the grating, and their strength controlled by the fluence and duty cycle

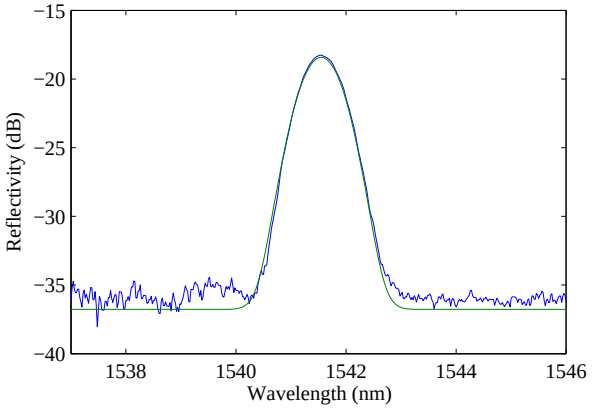

Figure 3.17: An example of a Gaussian fit (green) to experimental data (blue).

of DGW. In addition, appropriate background suppression during characterisation leads to an increase in the accuracy of the fit, and is achieved by ensuring the end facets do not cause additional broadband reflections. Dicing the output facet at an appropriate angle, typically 8°, to prevent back reflection into the waveguide is the most efficient way of achieving this. Consideration of these parameters ensures the accuracy detailed above is achieved.

In addition, the reflectivity of the Bragg gratings can be measured. The true reflectivity is typically measured by obtaining the transmission spectrum of the grating. This involves a similar characterisation set up to that presented here, only with an additional pigtail at the output of the waveguide, connected to an OSA. Thus, a dip in the transmitted power can be observed at the Bragg grating central wavelength, and the relation $R = 1 - T$ used to calculated the reflectivity.

For ease of measurement, in this case we measure just the reflected spectrum. Measuring in transmission can be time consuming and involves non-trivial alignment procedures, particularly in the cases where angled facets are used to reduce stray reflections coupling back into the channel. In this case, the reflectivity is estimated by also obtaining the background spectrum of the characterisation source. A spectrum is taken of the reflection from the output facet of the fibre connector adjacent to the channel waveguide. For the SMF-28 telecommunications fibre with a plane output coupler, this reflection should represent 3.35 % of the input power, and is the calculated Fresnel reflection. The reflected power from the grating is then compared to this value, and the 'reflectivity' obtained. This value does not take into account the coupling losses between the pigtail and waveguide, and assumes that the reflection from the fibre facet is perfect. This is the reflectivity value referred to throughout the rest of this thesis.

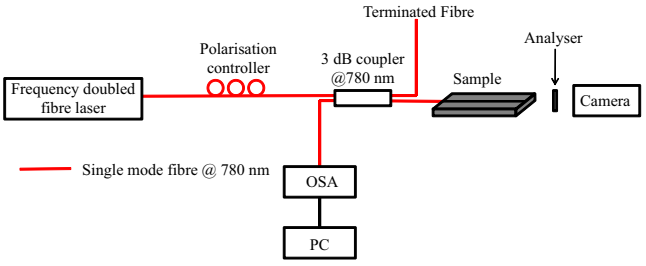

Figure 3.18: Characterisation set-up used to interrogate 780 nm gratings. Schematic shows system components, and denotes single mode 633 nm fibre.

3.4.2 The 780 nm characterisation set-up

The 780 nm characterisation set-up differs slightly from the 1550 nm set-up. The broadband source used at this wavelength is a periodically poled lithium niobate (PPLN) frequency doubled 1550 nm femtosecond fibre laser. The source has a bandwidth of 20 nm around 780 nm, and the central wavelength and spectrum of the source is tunable by control of the PPLN temperature. The fibre used is single mode at 780 nm, and although not polarisation maintaining, is immobilised to ensure a single polarisation measurement. The polarisation is controlled via the fibre polarisation controller and a free space analyser at the output of the waveguide, to choose TE or TM polarisation through the waveguide. A 3 dB coupler designed for use at 780 nm was used to measure the back reflected signal from the sample, as seen in Figure 3.18. The collected spectrum is analysed using the same Gaussian fitting algorithm as detailed above.

3.5 Conclusions

The fabrication techniques described in this chapter allow the production of repeatable, reliable optical waveguides, useful in a variety of planar lightwave circuit applications.

The FHD technique allows scope for different waveguide profiles to be investigated, with control over the thickness, refractive index and dopant levels within the glass. The glass layers produced by FHD can also be post-processed to allow additional dopants to be added in specific regions, or the glass or underlying silicon can be selectively machined and/or etched. These techniques promote the use of glass for lasing and amplification applications [51], and the use of devices as environmental sensors [49, 61].

The combination of the use of FHD layers and the direct grating writing technique allow a number of waveguide geometries to be investigated. As well as traditional straight waveguides, progress has been made in the investigation of cosine-bend waveguides, mainly in the cross-coupled geometry [13]. The inclusion of Bragg gratings within the waveguides has allowed insight into the optical properties of the waveguides themselves,

using the fluence-matching ability of the DGW system [62,63]. The interaction of waveguides with machined components has also been investigated [64, 65], using the Bragg gratings to monitor the waveguide behaviour, and will be presented in Chapter 5.

The use of Bragg gratings to interrogate waveguide behaviour requires knowledge of the Bragg grating characteristics. These are obtained via characterisation of the reflected spectrum from the Bragg gratings, implementing telecommunications components to obtain the fitted parameters of the grating spectra.

This overview of the general techniques used within the thesis provides the basic knowledge required to carry out fabrication and characterisation of waveguides and Bragg gratings. In the case of the individual devices described in the following chapters, more specific device-dependent techniques are implemented. These techniques and parameters will be described in detail in the relevant sections.

Chapter 4

Advanced fabrication and design of Bragg grating response

The spectral response of a Bragg grating can differ widely given the effect of dependent parameters contributing to the fabrication of the device. The peak reflectivity, bandwidth and central wavelength of the Bragg grating, as well as the specific shape of the spectral response, depend not only on the material and waveguide properties such as core thickness and refractive index, but on the fine control of the laser beam modulation and stage system movement employed during the DGW process.

The previous chapter describes the fabrication process required to manufacture waveguides and Bragg gratings in photosensitive silica-on-silicon. The specific parameters required to fabricate gratings were touched on in Section 3.3.2.2, with typical spot size and intersection angle given alongside Bragg grating definition parameters. This chapter will expand on the physical interpretation of these parameters, in order to develop an understanding of the controlled fabrication of Bragg gratings using the AOM system.

The chapter will deal with the following Bragg grating parameters. Control of the central wavelength is achieved via modulation of the interference pattern and stage system response. The strength of the Bragg grating planes is controlled by altering the fluence and duty cycle of writing, and will be discussed with reference to fluence matching, the technique used to ensure a constant average refractive index modification along the waveguide. Following this, the processes involved in the design of different spectral profiles will be presented, with demonstration of apodisation, phase shift and linear chirp. The introduction of the phase control grating writing system developed during this project will be described, highlighting improvements in the grating structures produced. The chapter will conclude with demonstration of short period Bragg gratings with central wavelength at 780 nm, and discussion of the issues encountered when fabricating gratings at this shorter wavelength.

4.1 Central wavelength design

The ability to arbitrarily choose the central wavelength of a Bragg grating response has uses in a number of typical applications. In sensing devices, the choice of Bragg grating central wavelength to coincide with the absorption peak of a substance leads to effective measurement capability and the detection of known substances in a mixture. In wavelength division multiplexing telecommunications devices, the key parameter is the precise spectral positioning at the Bragg grating response within the channel dealing with a specific signal frequency, allowing effective filtering of the chosen wavelength with high efficiency. As demonstrated by Carpenter et al. [66], the control of the central Bragg wavelength of a pair of gratings provides the ability to compensate for spectral shifts due to strain, thereby allowing the creation of a Fabry-Pérot cavity with deep fringes suitable for environmental sensing. These applications, amongst many others, require precise control of the central wavelength of the Bragg grating.

As described in Section 3.3.2.2, the central wavelength of a Bragg grating inscribed by DGW is partially defined by the period of the interference pattern. This is caused by the intersection of the two focussed arms of the interferometer at a specific angle 2γ, related to the wavelength of incident UV radiation, λ_{UV}, and the period of the Bragg grating desired, Λ, by the following relation (Equation 4.1).

$$\sin\gamma = \frac{\lambda_{UV}}{2\Lambda} \tag{4.1}$$

To create Bragg gratings with a central wavelength away from that defined by the period of the interference pattern, the wide detuning range of the direct grating writing system is considered. The small spot size (approx. 5 μm), in comparison to that of traditional phase mask based Bragg grating definition techniques ($\geq$ 100 μm), contains far fewer grating periods, around ten interference fringes in the 5 μm spot. When superimposing the interference pattern on the previously defined fringes, the exposure can be slightly offset from the previous exposure by a predetermined amount, creating effectively longer or shorter grating periods within the overlapped region [67]. A pictorial representation of the first few periods defined by modulation of the system is shown in Figure 4.1.

The blue curve shows the situation in which the translation of the stage system during laser modulation corresponds to the period Λ of the interference pattern created between the beams. The gradual build up to maximum refractive index modification occurs as the first few grating planes do not experience multiple exposures. The red curve represents the case where the stage translation is equivalent to $\Lambda + \delta$. The maximum refractive index modification in this case is slightly lower as the modulation does not allow the inscribed fringes from one exposure to entirely overlap with the fringes from the previous exposure.

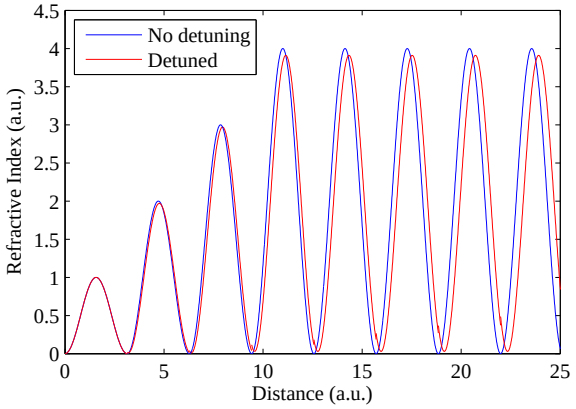

Figure 4.1: Simple simulation of the effect of detuning on the Bragg grating period. The writing spot in this case contains four periods of the interference pattern. The plot shows the difference in period achieved with a small change in modulation period. Also note the slightly lower peak refractive index for the detuned grating.

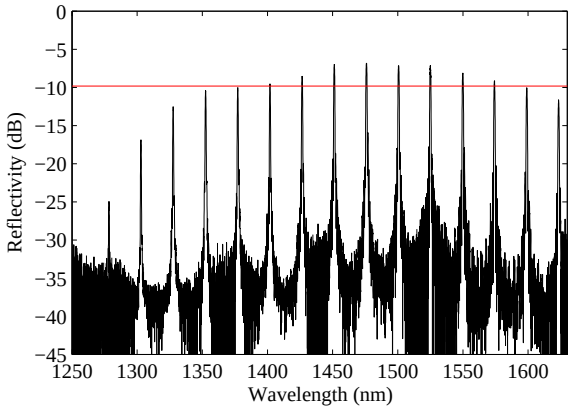

Figure 4.2: Experimental demonstration of the range of Bragg grating wavelengths available using the detuning process and the 1475 nm optimised DGW set up. The -3 dB range of available central wavelengths is approximately 220 nm.

In comparison to the phase mask technique, the small spot size and the number of periods defined during each exposure allows a greater detuning range from the original grating period. Figure 4.2 shows an experimental array of Bragg gratings fabricated over the range 1275 to 1625 nm using the AOM DGW set up. The grating contrast at the extreme of the detuning range suffers; however, approx. 110 nm detuning from the original grating central wavelength can be achieved whilst the grating reflectivity remains above 50 % of that of the original period grating.

The detuning technique allows Bragg gratings to be fabricated with central wavelengths approximately 200 nm away from that defined by the period of the interference pattern. In order to achieve the best grating response possible, or to fabricate Bragg gratings in a spectral range far from the 1475 nm optimised central wavelength, the intersection angle between the beams can be modified. During the course of the work described here, four separate optical arrangements were used, with interference pattern periods

Wavelength	Angle
780 nm	26.9 °
1060 nm	19.5 °
1550 nm	13.2 °
2000 nm	10.2 °

Table 4.1: Angles required to achieve central Bragg wavelengths in silica-on-silicon.

corresponding to Bragg gratings with reflectance wavelengths at 780 nm, 1060 nm, 1550 nm and 2000 nm in silica. The angles required to form the interference pattern in each case are shown in Table 4.1, from Equation 4.1.

Adjustment of the intersection angle between the beams, alongside the wavelength detuning scheme described above, allow Bragg gratings to be fabricated over a large range of central wavelengths, from around 650 nm to 2.2 μm using the four different interferometer arrangements described above. The strength of the gratings, whilst affected by the magnitude of detuning involved, can also be adjusted via additional control of the laser modulation and stage system movement during the DGW process. The concept of grating strength design is dealt with in the following section.

4.2 Control of Bragg grating strength and bandwidth

The 'Bragg grating strength' is defined in this case as the efficiency of the reflection filter operation, and can be observed in both the reflection and transmission spectra obtained from the grating. The strength of the individual grating planes is controlled by the fluence and the duty cycle of the amplitude modulation system, which directly controls the incident power on the photosensitive core layer and thus the extent of the photoinduced refractive index modification. The number of grating planes within the grating then controls the overall strength of the grating, as well as the spectral width of the filter.

As previously defined, fluence is the energy per unit area present in the focal point of the crossed beams. The fluence directly controls the strength of the waveguide and its guidance characteristics, as a larger fluence will increase the photoinduced modification magnitude and thus produce a larger refractive index modification, wider channel and a 'stronger' guide. The fluence can be altered by changing the power of the beam incident on the sample and/or the speed of translation of the sample. The desired average fluence of a waveguide can be chosen prior to writing, and this value is achieved during AOM grating writing, where the incident power is typically less than in the waveguide sections, via control of the speed of translation of the sample.

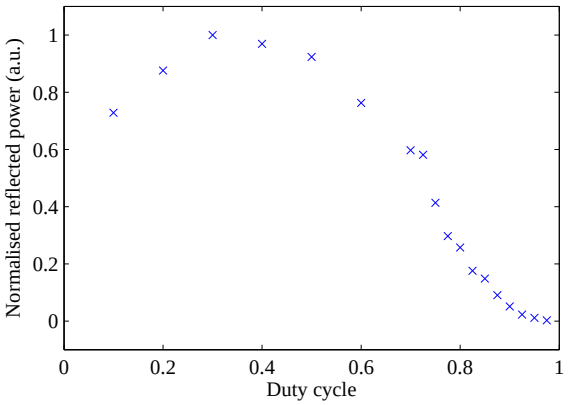

Figure 4.3: Experimental comparison of normalised reflected power for Bragg gratings fabricated with different duty cycles. An optimal value of approximately 0.35 was obtained.

Consider a Bragg grating to consist of a series of alternating high and low refractive index planes, as described previously (Section 2.2). Each period of the Bragg grating contains one high and one low index plane. The proportion of high index region to the entire period is known as the duty cycle, and control of this parameter leads to a change in the strength of the fabricated Bragg grating planes via the grating contrast achieved.

The duty cycle is defined as the proportion of the period where the control is 'high', corresponding to the laser being on. A duty cycle of '1' corresponds to the laser always being on, and a duty cycle of '0' occurs when the laser is always off. Any value of duty cycle between 1 and 0 will produce an amount of index modulation, and thus analogue control of the grating strength is achieved.

The optimal duty cycle required to achieve the largest grating contrast using the AOM system was empirically found to be 0.35. A number of Bragg gratings with different duty cycles were fabricated with the same central wavelength, and the reflected power data analysed to obtain a plot of the reflected power against the duty cycle. This is shown in Figure 4.3. Theoretically, the smaller the duty cycle, the greater the index contrast. However the slow sample translation required to fluence match the lower duty cycle gratings causes instability in the positional accuracy of the system, reducing the index contrast achievable. Experimentally it was found that a duty cycle of 0.35 provides the best grating modulation contrast, $\Delta n = 3 \times 10^{-4}$.

The choice of laser on/off duty cycle can be readily seen to have an effect on the overall fluence of the writing spot, given that the average fluence delivered over one period is defined by the proportion of the period over which the sample is illuminated. In order to compensate for this, the fluence matching technique is employed. The technique involves changing the speed of translation of the sample during grating and waveguide sections to ensure the average power incident on the sample is the same at all points. The intricacies and effects of fluence matching as a design tool will be discussed in the following section (Section 4.3).

The grating contrast achieved via fluence and duty cycle engineering contribute to the overall strength of the reflection at each grating plane, which, when concatenated, produce the Bragg gratings desired. The number of grating planes defines the overall strength of the gratings; stronger grating responses are achieved by increasing the number of grating planes within the device. For devices fabricated using the AOM grating writing system, a duty cycle 0.5, with appropriate fluence (dependent on the sample characteristics), and a grating length of approx. 3000 grating periods was sufficient to achieve a near 100 % reflector. These parameters are dependent on other UV writing conditions, such as hydrogen out-gassing and laser alignment.

Altering the number of grating planes in a device also changes the bandwidth of the fabricated grating. As the number of grating planes increases toward this near 100 % reflector, the bandwidth of the grating narrows to maintain the sinc-squared or Gaussian spectral profile. This enables filters of a specific reflectivity or bandwidth to be designed given prior characterisation of the photosensitive wafer to determine typical fabrication parameters.

If more grating planes are added to the device, the grating becomes 'saturated' and near 100 % reflecting. Although effectively a more efficient reflecting device, saturation changes the spectral response of the Bragg grating. Saturation occurs when 100 % of the input signal is reflected within a fraction of the grating length, changing the spectral profile. The grating becomes flat-topped, creating a wider flat central lobe in the sinc-squared or Gaussian grating profile (Section 4.4). Depending on the application, this could be a desired feature, but, in the cases described in this thesis, introduces increased grating fitting errors due to the definition of the Gaussian fitting algorithm (Section 3.4.1).

This section describes the design features available within the DGW system to control the spectral response of the fabricated Bragg gratings. The refractive index contrast of the grating planes, controlled by the fluence and duty cycle of the writing process, allows reflecting grating planes of different strength to be realised. Concatenation of a number of these planes leads to fabrication of Bragg gratings with the desired reflectivity or bandwidth. The following section describes the concept of fluence matching in more detail, and the advantages the technique has in terms of the physical gratings designed during this project.

4.3 Fluence matching

As mentioned previously, the concept of fluence matching can be employed to ensure the incident power present in the core layer of the sample is consistent throughout the waveguide and grating regions of the desired device. The technique ensures constant effective refractive index within the fabricated waveguide and grating device. The boundaries

between waveguide regions and Bragg gratings must be defined so as to prevent large refractive index changes at these localised points. These can cause large broadband reflections, and therefore introduce propagation loss within the waveguide. The concept of 'fluence matching' overcomes this issue by ensuring that the average fluence throughout the entire waveguide, including the Bragg grating regions, is the same.

Fluence matching using the AOM system is achieved by controlling the speed of sample translation during the writing process. Altering the speed at which the sample translates during the grating region by applying the duty cycle ratio to the original channel definition speed allows the same average intensity to be applied along the entire length of the waveguide, maintaining the average effective refractive index value.

Fluence matching allows some interesting features of the waveguide and grating systems to be explored. The fluence matched system allows the possibility of Bragg grating profiles where no change in the average effective index occurs over the entire waveguide and grating system. This is a feature unique to the DGW system, as any other grating definition technique requires the refractive index modulation of the grating to be superimposed onto the background refractive index of the pre-defined core [43]. An additional advantage of the fluence matched system is that the waveguide and gratings are fabricated under the same UV exposure conditions, and should therefore behave in the same fashion over time, thermal and environmental changes. The effective refractive index of the waveguide and grating should be the same, therefore the modal information of the waveguide can be inferred by monitoring the Bragg gratings. This point is key to the work carried out in this thesis, allowing loss and dispersion information to be obtained (Chapters 5 and 6 respectively).

4.4 Apodisation

An additional application of the duty cycle parameter is to alter the spectral profile of the grating. Literally meaning 'to remove the feet', apodisation of the grating structure can be performed to redistribute the reflected power within the grating region, altering the spectral profile of the fabricated device.

A uniform Bragg grating structure, with equal magnitude reflection from each grating plane (Chapter 2), has a sinc-squared spectral profile. Figure 4.4 shows the expected refractive index modulation and a measured spectral profile for a uniform Bragg grating. The refractive index modulation has constant peak value and equal duty cycle along the length (in the case depicted, the duty cycle is 0.5).

Apodisation involves controlling the amplitude of the reflection at each plane within the grating, creating a spectral dependence in the resulting grating profile. In this way, the

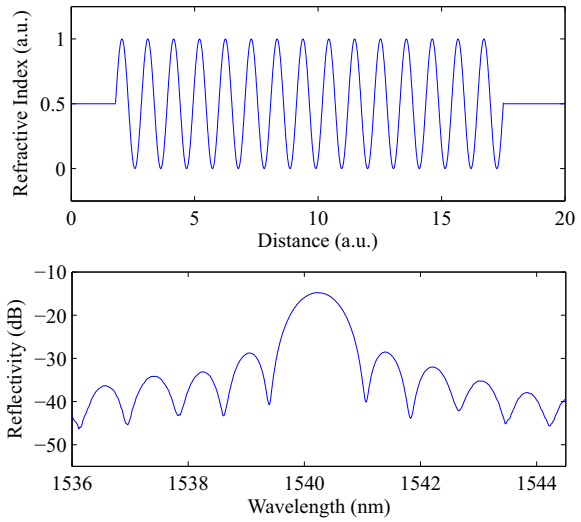

Figure 4.4: A schematic of the typical refractive index modulation present in a uniform Bragg grating structure (uppermost image), and the experimentally collected spectrum from a typical grating (lowermost image).

side-lobes of the sinc-squared function can be suppressed, and the spectral profile of the grating altered.

In order to achieve this change in magnitude of the reflection from each grating plane, the local grating modulation strength is altered. This is achieved via a combination of altering the speed of translation of the sample (and thus the fluence at each position within the grating), and the duty cycle (index modulation depth) as the grating is fabricated. In this manner, a fluence matched, apodised grating structure can be achieved.

The apodisation structure used in subsequent chapters is the Gaussian apodised grating profile, an example of which can be seen in Figure 4.5. Note the degree of side-lobe suppression in comparison to the uniform grating profile depicted previously (Figure 4.4). This structure was achieved by applying a Gaussian profile to the translation speed within the grating region, and to the duty cycle ratio, to achieve the changing reflectivity of grating planes whilst maintaining the fluence matched nature of the grating. The Gaussian apodisation profile provides advantages over the sinc-squared profile. Side-lobe suppression allows narrower bandwidth filters to be realised, and characterisation and fitting of a Gaussian profile is simpler than fitting to a sinc-squared function. For the grating spectra dependent characterisation techniques developed during the course of this project, a Gaussian apodised grating function allows improved data analysis techniques and less uncertainty in results, providing precise amplitude and centre wavelength data for waveguide characterisation.

The amplitude modulation DGW system has been used to fabricate various waveguides and Bragg gratings suitable for the study of characteristics of the waveguides themselves. Via control of the sample translation speed and duty cycle parameter, fluence matched

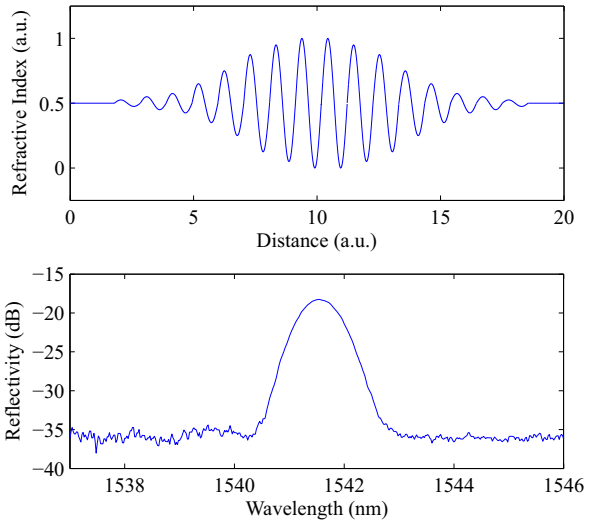

Figure 4.5: A schematic of the typical refractive index modulation present in a Gaussian apodised Bragg grating structure (uppermost image), and the collected spectrum from a typical planar Bragg grating (lowermost image).

waveguides and Bragg gratings have been fabricated, allowing consistent refractive index profiles along the length of the grating. This consistent profile allows the gratings to be used to characterise the losses (Chapter 5) and the dispersion (Chapter 6) of the waveguides, without adding any additional grating induced components.

4.5 Complex grating profiles

In addition to the apodisation of Bragg grating planes, additional spectral engineering can be implemented to create gratings with complex spectral profiles. During the course of this project, the author undertook fabrication of two such complex grating profiles, linearly chirped and phase shifted Bragg gratings. The fabrication parameters used to defined these gratings are discussed in this section.

4.5.1 Linearly chirped Bragg gratings

Chirped Bragg gratings are of interest in dispersion compensation schemes. Linearly chirped Bragg gratings have a linear group delay dependence on wavelength. These devices have been shown to compress broadened pulses in fibres [68]. Non-linearly chirped gratings can also be realised, and used to correct residual dispersion caused by improper dispersion slope matching in dispersion compensating fibre.

A linearly chirped Bragg grating structure is one in which the refractive index contrast remains constant whilst the period of the Bragg grating increases linearly along the

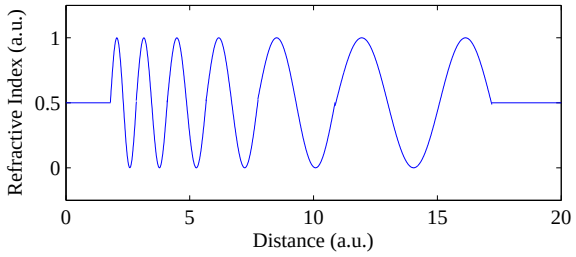

Figure 4.6: A schematic of the typical refractive index modulation present in a linearly chirped Bragg grating structure.

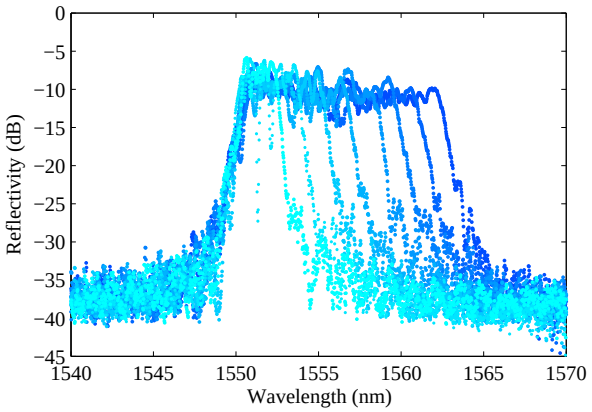

Figure 4.7: A plot of the reflectivity of several chirped Bragg gratings fabricated with increasing linear chirp between 2.8 and 14.4 nm.

grating length. A schematic of a refractive index modulation pattern created to achieve a linearly polarised chirped spectral response is shown in Figure 4.6.

In collaboration with Benjamin Snow and Christopher Holmes, linearly chirped Bragg gratings were fabricated early in the course of this project [69]. A plot of the reflected spectra from a number of linearly chirped Bragg gratings is shown (Figure 4.7). Gratings fabricated were 9 mm long, with varying chirp in period between 2.8 and 14.4 nm/cm. The image shows the increase in FWHM bandwidth achieved by increasing the chirp, and the related drop in peak reflectivity associated with the broader band reflection.

These chirped Bragg gratings show the capability of the DGW system to accurately produce such complicated structures. The ability to arbitrarily change the period of the refractive index modulation throughout the length of the grating is a parameter available only in DGW type fabrication systems. In traditional Bragg grating fabrication techniques such as phase mask methods, the chirp rate is predefined by the fixed mask parameters. In DGW, the central wavelength detuning described in Section 4.1 provides the means to modify the period of the inscribed grating fringes smoothly whilst grating fabrication is in progress. This allows the chirp rates observed here to be achieved with ease, and the capability to add more complex features such as phase shifts or apodisation within the chirped Bragg grating profile. More information about chirped

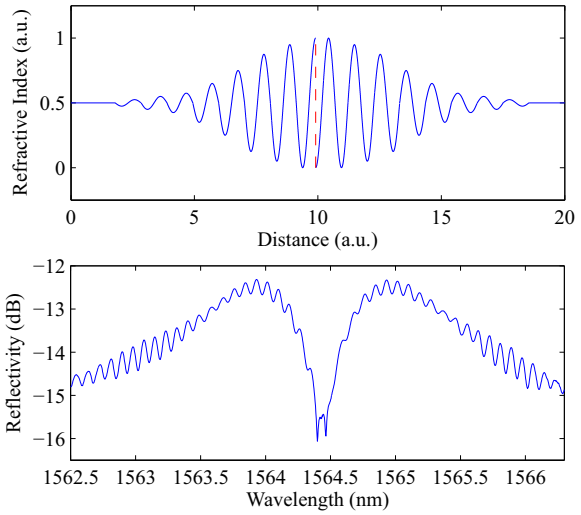

Figure 4.8: A schematic of the typical refractive index modulation present in a Bragg grating structure with π-phase shift at the physical centre of the grating (uppermost image), and the collected spectrum from a typical grating with a similar refractive index profile (lowermost image). The fabricated grating in this case is apodised, and spectral fringes are due to etalon fringes from the facets of the chip. Chip fabrication by the author, data collected by Chaotan Sima.

Bragg gratings, including use as a tunable dispersion compensation device, can be found in Benjamin Snow's thesis [12].

4.5.2 Phase shifted Bragg gratings

Bragg gratings including a phase shift element have been the subject of extensive research due to their unique spectral and temporal properties. Adding a phase shift to a Bragg grating introduces a temporal delay, and a single spectral dip which is controlled by the magnitude of the phase shift. Gratings of this type have previously been investigated for use as all-optical telecommunications filters, using the intrinsic speed of the optical filter to improve efficiency [70]. Work carried out in collaboration with Chaotan Sima, detailed in his thesis, involved fabrication of apodised planar Bragg gratings with phase shifts by DGW, for use as photonic Hilbert transformers.

The Bragg gratings were fabricated using the DGW method as detailed before, with the introduction of an arbitrary phase shift at the physical centre of the Bragg grating. In terms of refractive index, a typical phase-shifted refractive index modulation pattern can be observed in the upper section of Figure 4.8. A π-phase shift has been introduced at the centre of the grating. The spectral response of a typical grating with π-phase shift can be observed in the lower part of the figure.

The ability to arbitrarily choose the position and magnitude of the phase shift is a further advantage of the DGW system. The air-bearing stage system has the ability to resolve its relative position with a precision of just 1 nm, enabling position shifts of tens

or hundreds of nanometres to be achieved with small experimental uncertainty. This allows arbitrary phase shifts to be fabricated within waveguide systems with complex spectral and temporal profiles, allowing systems such as the integrated all-optical single side band modulation device demonstrated by Sima et al. [71] to be fabricated with ease.

4.6 The phase control system

Several important modifications have been made to the DGW system during the course of this project. One change in particular, the implementation of the phase control writing system, enables greater fabrication control and improved writing speed, enabling devices to be fabricated more readily and swiftly. In this section, the theory behind the phase control system and the changes necessary to the amplitude modulation set up will be presented. An example Bragg grating fabricated using a rudimentary set up will be presented, with discussion of the subsequent developments and improvements to the grating fabrication process afforded by these changes. The first steps in the development of this technique were implemented by the author to the point of obtaining Bragg grating spectra from a new system with an interferometer design containing a piezo mirror mount for phase control.

The 'phase control' of the system refers, in this case, to the control of the relative phase of the interference pattern. In the DGW system, the absolute phase relationship between the two arms of the interferometer is unknown, however, given knowledge of the wavelength of UV radiation, the relative phase between the two arms at the focal crossing position can be controlled to give a known position shift in the interference pattern. This can be realised by use of one of a number of components, which achieve the optical shift by changing the path difference between the arms of the interferometer.

The phase control set up then allows positional modulation of the interference fringe intensity within the spot. Grating planes of different strength can be achieved by control of this modulation, enabling the fabrication of complex grating profiles such as those described previously. The initial component used to achieve the phase shift was a modified mirror mount with a 1-inch diameter speaker piezo set behind one mirror in the DGW system. 'Mirror A' in Figure 4.9 was the modulated mirror in this case. Application of a voltage to the piezo-electric material caused the material to swell, causing the mirror to move by the amount required to achieve the desired phase shift in the interference pattern.

In addition to the inclusion of the piezo mirror mount, additional changes were required to the laser and stage programming code to achieve the required relationship between modulation of the beam and stage system movement required to inscribe Bragg grating planes. A stepped ramp saw-tooth wave voltage change was implemented in the programmed code, with the maximum voltage defined by the voltage applied to the piezo

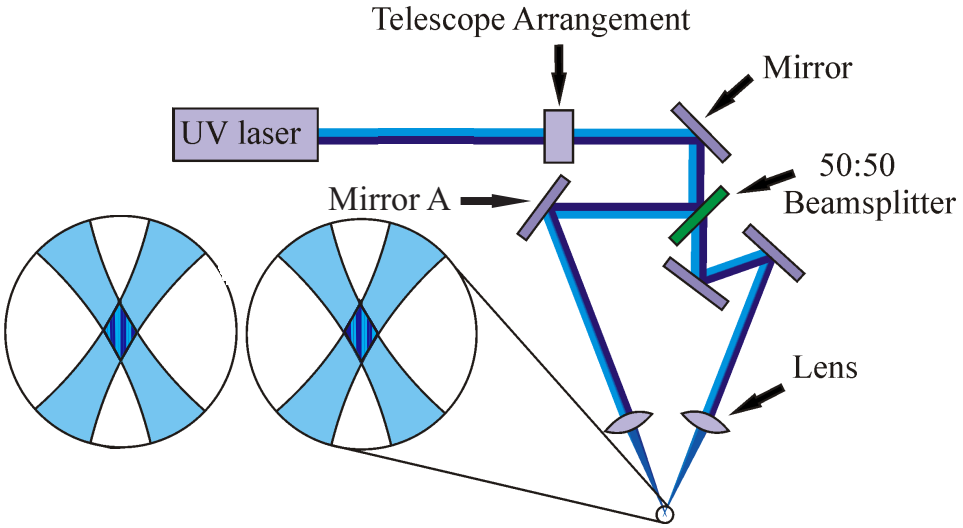

Figure 4.9: A schematic of the optical set up of the direct grating writing system. Note 'Mirror A', the modulated mirror in the phase control set up. Inset images show the interference pattern between the two beams, and the shift in fringes that occurs when Mirror A is modulated.

to obtain a 2π phase shift in the beam arm. The ramp period corresponded to the time taken for the stage to translate the sample by one grating period, thus creating the periodic fringes required to inscribe Bragg grating planes. In the phase control case, only the duty cycle of the modulation is changed during apodisation, as the grating periods are created solely by modulation of the phase of the interference pattern and thus the fluence is constant. This causes an increase in fabrication speed as a reduction in speed of the stage system is not required to achieve fluence matching in the grating region. In addition, removal of the redundant AOM increases the available writing power.

The spectrum from a grating inscribed using this rudimentary technique is shown in the left half of Figure 4.10. The uniform apodised grating shows the typical sinc-squared profile, but with noise present on all lobes. The suitability of the modified mirror mount was questioned, and replaced with a Thorlabs piezo mirror mount designed for similar purposes. Rather than using the programmed code to create the saw-tooth wave, an integrator circuit was fabricated to allow the correct voltage ramp for the phase shift to be applied via a simpler 'on-off' control by the computerised system. An example of a uniform apodised grating spectrum is shown in the right part of Figure 4.10, showing marked improvement in the spectral noise of the grating response.

When investigating the capabilities of the system when attempting to produce more complicated grating profiles such as Gaussian apodisation, problems were encountered relating to the actuation of the piezo mirror mount. The mount had piezo blocks on three corners, so small discrepancies in the swell of each corner caused large effects in the subsequent spectral profile of the grating. The decision to change the mirror mount for an electro-optic modulator (EOM) in the arm of the beam was made. A schematic of the adjusted interferometer is shown in Figure 4.11. In an EOM, the refractive index

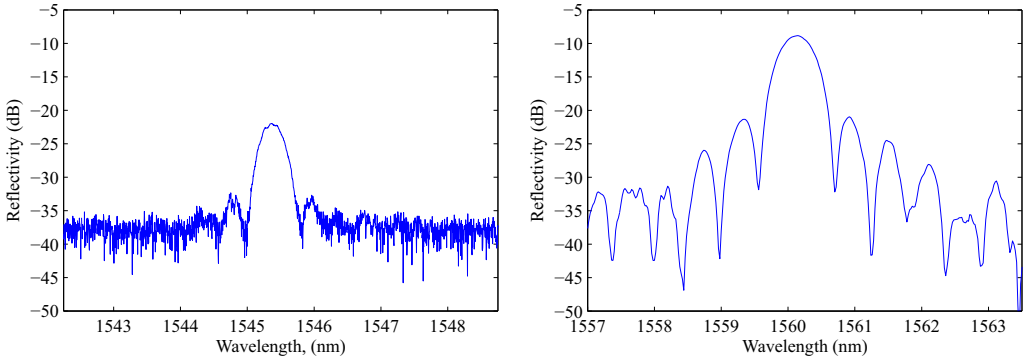

Figure 4.10: Collected spectra from uniform Bragg gratings fabricated using the phase control system. The grating with spectra shown on the left was fabricated using the modified speaker mirror mount, and the spectra on the right produced from a grating written with a Thorlabs piezo mirror mount.

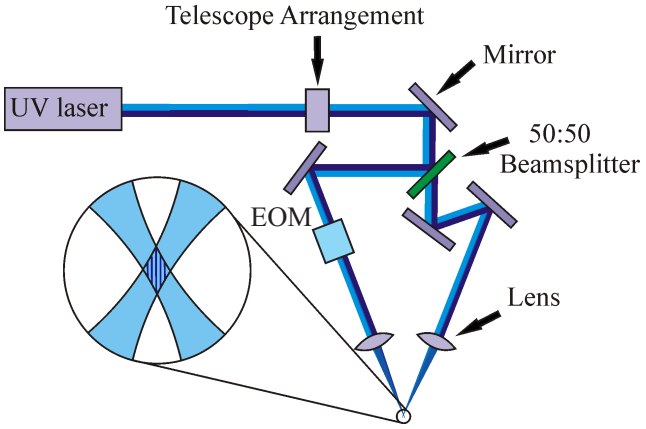

Figure 4.11: A schematic of the optical set up of the direct grating writing system with an EOM implemented. Note the removal of the AOM, and inclusion of the EOM in the beam path of one arm of the interferometer.

of the non-linear, non-centrosymmetric material changes when a DC voltage is applied, causing a delay in the beam and an associated phase shift in the interference pattern. The changes in the duty cycle and strength of the saw-tooth modulation enable Bragg grating periods to be formed without the need for control of the speed of the stage system. This more stable system enabled investigation into apodisation and a comparison of the gratings produced using the phase control system and the AOM method.

Figure 4.12 shows Gaussian apodised Bragg gratings fabricated using the amplitude modulation method (left) and the phase control method (right) respectively. The spectra show marginal improvement in the suppression of the side lobes in the phase control case, with the spectrum showing increased reflectivity and bandwidth. The phase control grating also shows a super-Gaussian spectral profile, caused by the stronger individual grating planes in these equivalent length gratings. The major improvements afforded by the system become apparent when considering grating strength. The grating modulation strength, Δn_{AC} is related to the bandwidth of the grating, as shown during the

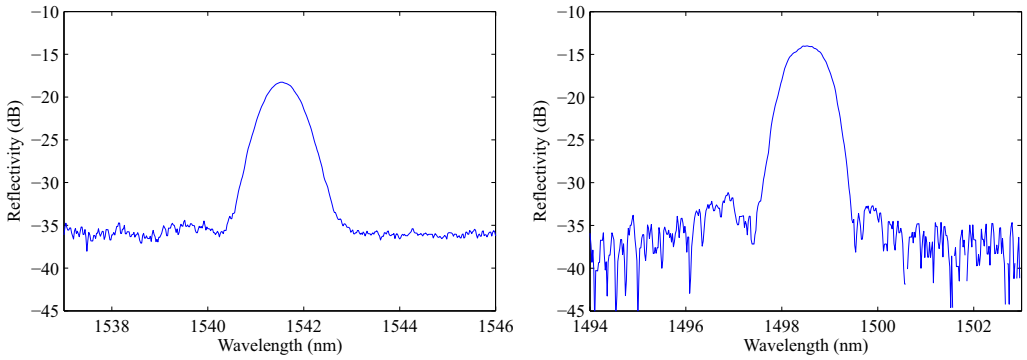

Figure 4.12: Collected spectra from Gaussian apodised Bragg gratings fabricated using the amplitude modulation method (left) and the phase control method (right). Phase control gratings fabricated and analysed by Chaotan Sima.

theoretical consideration of the Bragg grating, Equation 2.46. The 3 dB bandwidth of the grating produced using the AOM technique is 0.88 nm, whilst in the EOM case is 0.95 nm.

The effective refractive index contrast of the Bragg grating fabricated with the phase control method is almost twice that of the AOM technique, providing Δn in the region of 7×10^{-4}. This improvement allows shorter gratings with fewer grating planes to be fabricated with the same reflectivity characteristics, enabling integration of shorter optical components. A final practical improvement is the increase in speed of fabrication. Removing the AOM from the system has increased the laser power incident on the sample by around 30 %. This increase, in addition to the removal of the amplitude modulation technique of fluence matching has increased the speed of manufacture of devices, which is now wholly dependent on the maximum output power of the laser.

The new phase control system has improved the DGW grating fabrication process in a number of ways. Via implementation of a series of modulation components, the characteristics of the system were developed and understood, and the most appropriate element, the EOM, chosen. Gratings have been fabricated with improved grating contrast, leading to stronger Bragg grating planes and shorter fabricated components. The fabrication time of simple devices has been reduced to a few seconds, given the removal of the amplitude modulation system and the associated intensity drop of the laser. This, in addition, counters the hydrogen outgassing occurring over the UV writing period, creating waveguides with more consistent refractive index contrast over an entire chip. Initially implemented on the 1550 nm central wavelength fabrication set up, the EOM is potentially interchangeable between the different set ups. This allows the system to be implemented at 780 nm, improving the plane strength and grating contrast in the shorter wavelength regime. The following section describes the AOM technique of fabricating short wavelength gratings.

4.7 Short wavelength gratings

The use of planarised Bragg gratings in biochemistry or quantum optics requires optimisation of waveguides and Bragg gratings at shorter wavelengths. For sensing of water-based analytes, work between 1400 nm and 1600 nm is compromised by the strong absorption of O-H bonds in this band, reducing the sensitivity of devices. In quantum optics, the interaction between light and matter is of interest in a wide range of fields, particularly in cavity quantum electrodynamics (QED), which is a constituent factor in the development of quantum information processing systems. The 'matter' concerned is typically atoms of rubidium which have an atomic transition at 780 nm. Investigation of single mode waveguides and Bragg gratings at this wavelength provides scope for future applications of UV written devices in these influential fields.

The move to fabrication of shorter wavelength single-mode devices in silica is not trivial, with consideration of a number of fabrication factors required to optimise the devices. These include the adjustments required to fabricate single mode waveguides at 780 nm, as well as consideration of the shorter period required for Bragg grating fabrication. This section will provide discussion of these factors, alongside demonstration of Bragg grating spectra fabricated at 780 nm. Further analysis of the developments in collaboration with the Centre for Cold Matter at Imperial College, London, towards the fabrication of devices suitable for coupled cavity QED, will be presented.

In order to fabricate single mode waveguides at 780 nm, the core diameter of the waveguide must be small enough so that higher order modes cannot be guided. In UV writing, this is achieved in two steps. First, the FHD wafer must be fabricated to have the desired core thickness. For 780 nm, and with the refractive index contrast afforded by the AOM writing system, a core layer thickness of 5.6 μm provides a single mode core in the vertical plane once the waveguide is UV written. Then, in the UV writing phase, the lateral core dimension is controlled by the spot size of the focussed beams. In the case of the 780 nm system, a spot diameter of around 5 μm FWHM is chosen to create the desired single mode guide. This is achieved by changing the focussing lenses of the UV writing system.

Additional changes to the UV writing set up are made to create the shorter period grating planes required for 780 nm reflection. The plane period required is 268 nm and is achieved by altering the intersection angle between the two focussed beams. As explained previously (Section 4.1), the intersection angle defines the central period of the detuning range of the UV writing set up. To create 780 nm Bragg gratings, a beam propagation angle of 26.9 ° from vertical is required. This is achieved by changing the optical set up to incorporate the extended angle, whilst maintaining the path length difference between the arms to within the coherence length of the UV laser. For practicality, we have interchangeable breadboards supporting the 1550 nm and the 780 nm optical set ups, which are depicted in Figure 4.13.

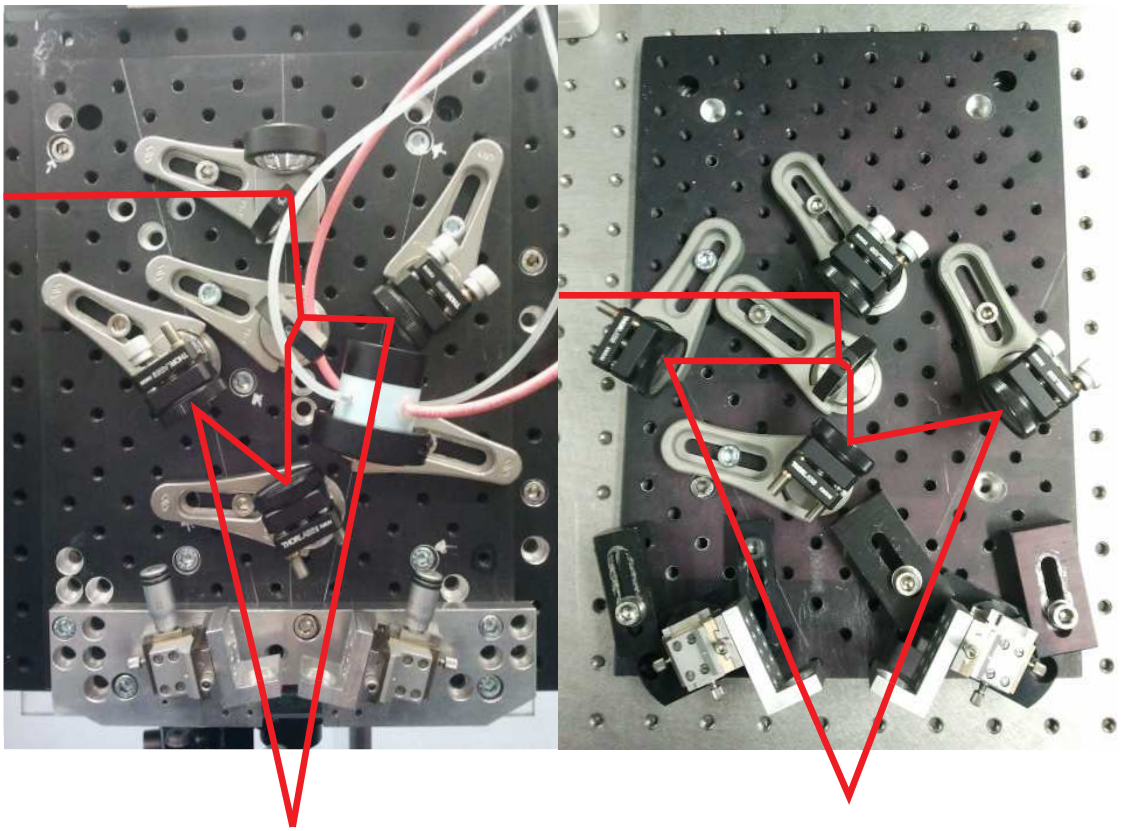

Figure 4.13: Images of the 1550 nm (left) and 780 nm (right) interferometer set ups. Note the larger angle of intersection between the two beams in the 780 nm case. The 1550 nm set up shows the EOM version of the board, for the phase control DGW technique.

The smaller core size and the larger angle between the beams causes a significant reduction in the tolerance of the grating writing process to alignment errors. Focussing into a smaller core layer requires finer control of vertical alignment within the focus of the beams, which can be achieved accurately using the air bearing stage system. The wider angle also increases the alignment error in crossing the beams to achieve the interference pattern. Adequate control of these alignment issues enables gratings to be fabricated with similar efficiency and repeatability to those at 1550 nm.

Figure 4.14 shows a sample grating spectrum fabricated using the new 780 nm DGW set up. The figure shows a uniform Bragg grating spectrum. The grating was 1.5 mm long and thus has twice as many grating planes as the 1.5 mm long 1560 nm gratings. This is observed in the flat-top reflected spectrum with equivalent duty cycle. The grating fabricated has lower central lobe reflectivity than those fabricated with 1550 nm central wavelength, and shows little side-band suppression due to the increased grating strength. Gaussian apodised Bragg gratings can also be achieved in this wavelength range. Techniques for waveguide characterisation, such as the measurement of loss, dispersion and birefringence described later in this thesis, can be carried out on Bragg gratings with central wavelengths in the 780 nm region, given that the Bragg gratings have sufficient reflectivity to provide little uncertainty in the Gaussian fit parameters.

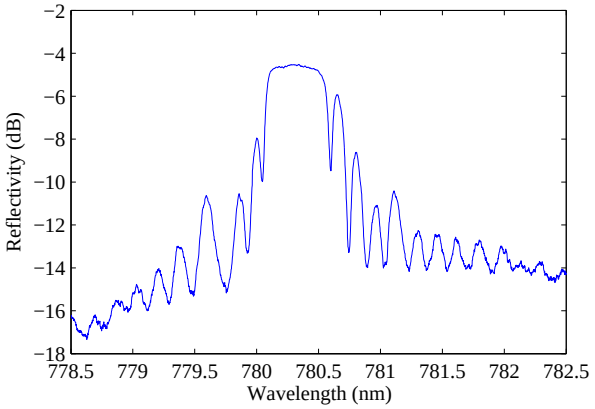

Figure 4.14: Collected spectrum from a Bragg grating written with central wavelength at 780 nm. The uniform grating shows flat-top saturation of the expected sinc-squared uniform profile, due to the large number of grating planes present in the device.

This investigation into fabrication of Bragg gratings at 780 nm was presented in Optics Express in 2011 by our collaborators at Imperial College London, Guillaume Lepert and Ed Hinds [72]. The paper describes the problems associated with fabrication of single mode waveguides and gratings at 780 nm, alongside a novel group delay measurement of the gratings relying on cavities formed of identical pairs of gratings. The work done in this project enabled this result for the first time.

Samples were supplied from this project to Imperial College London for use in cavity QED experiments. Coupling multiple cavities together in an integrated platform will provide a stable system with the ability to individually thermally tune the gratings to achieve optimum coupling between the cavities. Potentially, rubidium atoms with atomic transitions at the same wavelength can also be coupled to the cavities, allowing systems suitable for quantum information transmission to be fabricated in an integrated platform.

4.8 Conclusions and future work

The content described in this chapter was included in this thesis as a means of understanding the considerations undertaken when fabricating Bragg gratings and UV written waveguides for specific purposes. The parameters which are controlled during the fabrication process, such as central wavelength, duty cycle and fluence matching, and their relationship with each other and the obtained spectral profile of the grating, were described. The ability of the standard AOM writing system to fabricate Bragg gratings with apodised and complex grating structures was explained, alongside practical demonstration of such devices.

In addition, new modifications to the DGW system have enabled production of Bragg gratings in different experimental regimes. The 780 nm DGW set up allows fabrication of

single mode waveguides for improved biological sensing and quantum applications. The introduction of the phase control system enables faster fabrication speeds, along with improved grating contrast for shorter devices, and equivalent spectral profiles. These changes enable a wider variety of devices to be fabricated than was previously possible.

Future work in the grating fabrication area would further investigate the ability to fabricate more complex grating profiles. Tilted Bragg gratings and long period gratings have been achieved given further modifications to the system. These could be used in surface plasmon coupling experiments [73] and also as side tap gratings for improved sensing performance. Additional optical set ups have been built to extend the ability to produce Bragg gratings at additional central wavelengths for application-specific devices. Further investigation into chirped Bragg gratings and phase shift devices would enable optimisation of devices suitable for integration in telecommunications systems. Additional spectral engineering and apodisation functionality will enable the fabrication of Bragg gratings with desirable spectral features at specific wavelengths.

Chapter 5

Grating-based loss measurement technique

Loss is a fundamental limitation for optical waveguides, and techniques for its effective measurement have long been desired. The low total losses of optical waveguides, coupled with the short length scales of typical devices, require techniques which can provide low-error measurement of small propagation losses. Current techniques enable the propagation losses of waveguides to be measured, however distinction can rarely be made between propagation loss and other loss sources, such as coupling losses and Fresnel reflection losses.

The most rudimentary loss measurement technique is the cut back method, in which the propagation loss of a length of fibre is measured for various lengths of the same sample by literally cutting back the fibre length. An analogous method can be used in the case of low loss planar waveguides, but the ability to ensure a consistent end facet is trickier given the polishing techniques necessary to create low loss end facets in the planar case. An effective propagation loss measurement technique must have the capability to distinguish the small propagation losses of the waveguide from other sources of loss, such as these facet losses. Modal mismatch and Fresnel reflections can account for a large component of the total loss of a short length of waveguide. A loss measurement technique suitable for the interrogation of short waveguides, typically millimetres long, must be able to effectively distinguish the relatively small propagation loss of the waveguide from other loss contributions, over the short length of waveguide available to test.

This chapter focusses on the development of a new propagation loss measurement technique. The technique relies on the measurement of a number of integrated Bragg grating structures within the waveguide under test. A brief description of the sources of loss within planar waveguides will precede a review of relevant waveguide loss measurement techniques, highlighting the development of these techniques from roots in fibre characterisation. The development of the loss measurement technique is presented in both

theoretical and experimental form. The losses measured in samples developed via the methods described in Chapters 3 and 4 are presented alongside error analysis in order to show the significance of the technique within the field of planar waveguide characterisation.

5.1 Sources of propagation loss

The propagation loss, or attenuation, of light travelling through an optical medium can be broadly described as the reduction of intensity as light propagates through the material. Contributions to the total propagation loss come from the absorption characteristics of the material itself, and scattering phenomena occurring within the medium.

The absorption of a material is the degree to which the medium reduces the intensity of light propagation due to the composition of the material itself. The intensity of radiation at a specific wavelength is reduced by a repeatable amount over a known distance travelled in the material. This absorption is due to the structure of the material on the atomic and molecular level, as energy levels within the chemical structure cause absorption of radiation at specific wavelengths [74]. By selective doping, optical fibres and waveguides are designed to have low absorption at the wavelength of operation, thus reducing the need for expensive amplifying devices within the optical system.

The losses caused by elastic scattering within an optical medium are attributed to optical defects within the glass structure. The nature of the scattering is dependent on the magnitude of the defects within the structure. Particles which are larger than, or on the same scale as, the wavelength of light will scatter light incoherently. This scattering is described by Mie theory and leads to a significant loss at the defect location [75]. Particles which are smaller than the wavelength of light cause losses due to Rayleigh-type scattering [76]. This scattering, in doped silica materials such as FHD and optical fibre, is due to the density changes present in the glass on the sub-wavelength scale. The scattering has a λ^{-4} dependency, contributing to the increased losses observed in waveguides and fibres at shorter wavelengths.

In addition to these elastic scattering phenomena, inelastic scattering events may also contribute to the wavelength dependent loss. Raman scattering occurs as defects in the glass absorb radiation on the molecular level, which is emitted at a different wavelength than the input radiation due to the presence of an excited vibrational energy level, or optical phonon, within the molecule. Brillouin scattering occurs when incoming radiation is scattered from an acoustic phonon within the material. An acoustic phonon manifests itself as a time dependent variation in the optical density of a material, caused, for example, in optical fibres by a variation in the electric field of the incoming high intensity radiation itself (stimulated Brillouin scattering). In both Raman and Brillouin scattering, radiation of a different wavelength to the incident radiation is scattered,

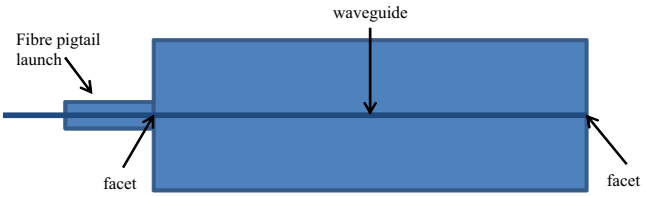

Figure 5.1: Schematic showing a typical waveguide with fibre pigtail launch and highlighted facets.

creating the inelastic scattering effects. In the silica-on-silicon devices described here however, the effects of Raman and Brillouin scattering on the total propagation loss are negligible due to the planar core dimensions and the interrogation intensities typically used.

In addition to these material-induced losses, further losses can occur due to the geometry of an optical device. Fresnel reflection losses occur at any surface at which light is reflected [77]. In the case of an optical waveguide, these reflections occur at the input and output facets of the waveguide. The light can reflect from the waveguide facets when propagating in either direction, causing multiple reflections within the waveguide itself. This phenomenon leads to the multiple reflections method described below (Section 5.2). A schematic of a typical waveguide, highlighting the input and output facets, can be seen in Figure 5.1. In a glass waveguide, the reflected intensity due to Fresnel reflections is around 4% of the input power at normal incidence to the glass/air interface, calculated by the Fresnel equation for reflectance, Equation 5.1 [78]. In our FHD silica-on-silicon platform, the Fresnel reflection loss is 3.35% at 1550 nm. The Fresnel reflection intensity is substantially higher in high index waveguides, with tantalum pentoxide demonstrating 12.6% reflection, and silicon 30.6% at 1550 nm.

$$R = \left(\frac{n_1 - n_2}{n_1 + n_2} \right)^2 \tag{5.1}$$

The sources of loss described above contribute to the total loss of the optical waveguide, but to what extent each phenomenon occurs is largely unknown. An effective loss measurement technique must be able to distinguish between the material-based loss and the geometrical loss contributions. In the following section, an account of prior art will discuss how established loss measurement techniques deal with this distinction.

5.2 Alternative loss measurement techniques

A number of loss measurement techniques have previously been implemented in order to measure the propagation loss of planar waveguides. This section provides a brief review of these techniques, from the crudest cutback method to the more involved end-fire

coupling and Fabry-Perot methods. A discussion of these methods is provided to place the new propagation loss measurement technique developed in this thesis into context. Within the confines of this chapter, 'low loss' optical waveguides are considered to have less than 1 dB/cm propagation loss, a convention used throughout the literature [79,80].

The crudest method of propagation loss measurement is to compare the loss of different lengths of waveguide. The cutback techniques were developed for fibre optics and, as the simplest propagation loss measurement technique available, can be easily transferred to the planar platform. In fibre, the approach is simple to implement; the fibre is cleaved every few metres or kilometres as appropriate, and the transmission measured. Sufficient material is cleaved from the fibre in order to measure enough loss so that it is clearly distinguishable above the variability in transmission caused by the fibre cleave [81]. In planar waveguides, the technique is similar, but it is more difficult to achieve good results. The waveguide must be cleaved and polished after each cutback step in order to achieve consistent output facets. There are two major drawbacks to the technique, the first being the dependence of the technique on coupling efficiency. Each cut and polish step will not achieve an output facet consistent with those previous, leading to changes in scattering loss and modal transmission at each step. In addition, the inconsistent Fresnel reflection loss contribution will hinder an accurate result. The second source of error is the small total loss intrinsically associated with the short planar waveguide under test. For a short, low loss waveguide, the cutback technique will not allow observation of enough total loss to distinguish between propagation loss and other sources of loss, such as Fresnel reflection losses and coupling losses.

The scattered light method of measuring propagation loss is among the simplest of the techniques employed. The method involves observing the light scattered out of the surface of the optical waveguide and analysing the response using a video camera [80]. This simple method allows automated propagation loss measurement along a waveguide, by scanning transversely and longitudinally along the waveguide to build a two dimensional image of the scatter. The method is suitable for waveguides with large loss (greater than 1 dB/cm) as enough loss is present along the waveguide to distinguish a change in the scatter. For low loss waveguides (less than 1 dB/cm), there is not enough light lost in the direction of measurement for accurate propagation loss data to be obtained.

The multiple reflections method uses a precision reflectometer to measure the reflected power from the waveguide after a number of reflections within the waveguide itself [82]. The set up is such that a reference mirror within an interferometer is scanned in order to change the path length of one of the interferometer arms. The different components of the reflected light from the waveguide travel different path lengths depending on how many successive reflections the light has made within the waveguide (Figure 5.2). By scanning the mirror to make the path lengths equal, light from the n^{th} known reflection can be measured. Taking the ratio of these reflected powers yields the loss induced during a certain number of reflections within the waveguide. By systematically scanning the

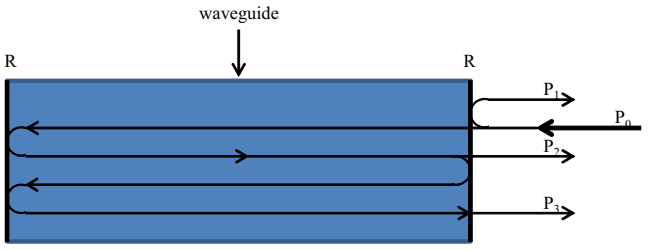

Figure 5.2: Demonstration of multiple passes observed in a waveguide in the multiple reflections technique. Power P_0 is incident on the waveguide, with reflected powers P_1, P_2 and P_3 measured on successive passes through the waveguide.

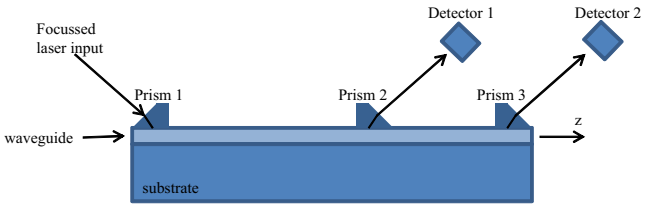

Figure 5.3: Schematic of the prism coupling loss measurement technique. Power coupled into the waveguide at prism 1 is coupled out of the waveguide at prism 2 or prism 3. The difference between the detected power at these positions enables the propagation loss of the waveguide to be inferred.

mirror, consecutive reflections can be measured, and thus the propagation loss of the waveguide calculated without prior knowledge of the waveguide length. The technique is coupling independent, as the ratio between the reflected powers is obtained and all measurements made without changing the fibre to waveguide coupling. The technique requires end facets which do not induce much additional loss on reflection in the low loss waveguide case. The technique is not independent of other sources of loss; the value obtained for the loss of the waveguide is the combination of the propagation loss and the Fresnel losses associated with each reflection at a surface.

The prism coupling method is an effective measurement technique, broadly based around the cutback method. The light coupled out of the waveguide is measured at a number of points along the length (Figure 5.3), and the values compared to obtain propagation loss data [83]. The method is suitable for lossy waveguides, but for low loss waveguides (less than 1 dB/cm), there is not enough total loss present to distinguish between propagation loss and other sources of loss. The method is also not independent of coupling efficiency, as the coupling conditions can change with each measurement at a different position on the waveguide.

The Fabry-Perot method involves building a cavity around the waveguide, and measuring the finesse of the cavity under different conditions in order to obtain loss information [79]. The data obtained is a combination of the propagation loss and the insertion loss of the waveguide. The method is dependent on the coupling into and out of the waveguide, and assumes identical coupling efficiencies. The repeatability of the measurement technique is quoted to within ± 0.1 dB over subsequent experiments, giving an idea of the relatively

high errors associated with the measurement technique. The method works best for higher refractive index materials, such as $LiNbO_3$.

The optimum end-fire coupling method involves reimaging the output light from a waveguide back into the waveguide itself as a secondary input beam to excite the guided mode. The reimaged beam is chopped to distinguish between the original guided beam and the secondary input beam. The propagation loss is measured by comparing the input power of the secondary beam to the output power of the secondary beam from the waveguide [84]. The use of a secondary input from the same low-coherence source overcomes the coupling efficiency issues, but the method cannot resolve the propagation loss of low loss waveguides due to the small intensity changes involved.

Many methods combine multiple loss measurement techniques to achieve propagation loss measurements with fewer variables. Lee et al. [85] combine the cutback method and the optimum end-fire coupling method to determine the propagation loss of the waveguide amongst other losses in one measurement process. Boudrioua et al. [86] combine the prism coupling method for light insertion with the end-fire coupling method to measure the transmitted light intensity. The measurement is independent of the coupling efficiency as the end-fire coupling measures the combination of coupling and propagation losses as the prism moves along the waveguide. However, the experimental uncertainty is high (± 0.4 dB/cm) which makes the method unsuitable for low loss waveguides.

One waveguide loss measurement technique available during this work was the loss measurement feature of the Metricon prism coupling system, described previously (Section 3.1.2.5). The technique combines the prism coupling technique with the scattered light method. The prism is used to couple to the waveguide at a single position, and the light scattered from the waveguide is measured at various points along the length via a fibre probe connected to a photodetector. The technique therefore provides the elimination of the coupling loss required, as a single coupling point is used. The Metricon system will, however, have difficulty measuring the losses of low loss waveguides due to the small amount of light scattered out of the waveguide. The repeatability of subsequent measurements is quoted as ± 5 %, and the lowest propagation loss measurable is 0.1 dB/cm, implying measurement of the propagation losses of our silica-on-silicon waveguides is close to the experimental limit of the measurement system. In addition, coupling accurately to a 5 μm waveguide core via the approximately 1 mm diameter coupling spot between prism and waveguide surface would prove difficult in the case of buried UV written waveguides such as these.

This section has provided an overview of the practical techniques employed to measure the losses of a planar waveguide. There are many techniques available to measure the propagation losses of waveguides, but none which are suitable for low loss waveguides (less than 1 dB/cm) that are independent of coupling efficiency. The method introduced

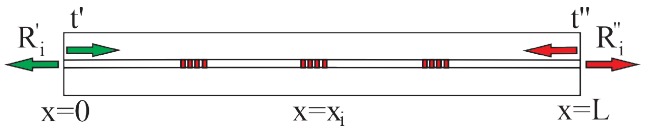

Figure 5.4: Schematic showing the measured reflectivities R_i' and R_i'' from the i^{th} grating in the waveguide. The input power incident on the grating (launched power minus coupling losses) is represented by t' and t'' from opposing directions.

here should go some way towards allowing the independent measurement of the propagation losses of waveguides, whilst remaining suitable for waveguides with a low total loss.

5.3 Theoretical basis of loss measurement technique

The development of the loss measurement technique described in this chapter involved investigation into the calculations necessary to obtain propagation loss information from the experimental data obtained. With consideration of a generic channel waveguide, as shown in Figure 5.4, with Bragg grating i at position x_i, appropriate theoretical and experimental constraints can be applied to the problem. This section will discuss this theoretical grounding for the technique and how it is applied to measured experimental data in order to obtain the propagation loss of the waveguide.

The new loss measurement technique is dependent on a number of assumptions, the first being the ability of the waveguide to support Bragg gratings and thus couple to the counter-propagating mode. Additionally, the reciprocity of the Bragg grating spectrum when interrogated from opposing directions is considered. Weak Type I Bragg gratings (Section 2.2.1) produced using the direct grating writing technique exhibit this reciprocal nature, as the refractive index contrast (Δn) and the number of grating planes are designed such that the Gaussian-apodised gratings do not become saturated 100 % reflectors [87]. This enables the fitted Gaussian peak height values (Figure 3.16) to be used to determine the reflected power from the grating at that position within the waveguide. This leads to the assumption that the central position of the Bragg gratings can be considered as the physical position of the peak reflection, as described in [87]. This assumption is key when obtaining the loss of the waveguide with respect to its length.

With this justification of the use of the fitted peak height within the theoretical considerations, a calculation of the reflected power from the grating at position x_i within the waveguide can be performed. Figure 5.4 depicts this grating at position x_i, and the additional notation used.

R_i' and R_i'' represent the reflected power from grating i when light is launched from opposing input directions. t' and t'' are the powers incident on the gratings from opposing

directions, considering the coupling losses when launched into the waveguide. L is the length of the waveguide under test, α is the loss of the waveguide (in units of cm^{-1}), and r_i and x_i represent the reflectivity and physical position of the grating within the waveguide respectively.

The power reflected by the grating at position x_i can be represented by the following relations, corresponding to launch from each direction.

$$R_i' = t'^2 r_i \exp^{-2\alpha x_i}, \qquad R_i'' = t''^2 r_i \exp^{-2\alpha(L-x_i)} \tag{5.2}$$

By taking the ratio of the reflected power from opposing launch directions, we obtain

$$\frac{R_i'}{R_i''} = \eta \exp^{-4\alpha x_i}, \qquad \text{where} \qquad \eta = \frac{t'^2}{t''^2} \exp^{2\alpha L}. \tag{5.3}$$

When the logarithm is taken:

$$\ln \frac{R_i'}{R_i''} = \ln \eta - 4\alpha x_i. \tag{5.4}$$

For a number of individual gratings within the waveguide, this ratio of reflected power can be plotted against the physical position of each grating within the waveguide. This leads to a comparison with the equation of a straight line,

$$y = mx + c. \tag{5.5}$$

y and x denote the axes of the plot, m is the gradient and c is the constant associated with the crossing point of the line and the y axis.

In order to simplify the graphical solving approach, the factor $\gamma = 4.34\alpha$ is introduced, to take into account the measurement of power in the common logarithmic scale (dB) rather than the natural logarithm. Note that the collected data, obtained in dB, can be subtracted in order to obtain the ratio, as $log_{10} \frac{R_i'}{R_i''} = R_i' - R_i''$. It can then be shown that obtaining the gradient of the plot of the reflected power ratio against the physical grating position leads to the relation

$$m = -4\alpha, \tag{5.6}$$

leading to the observation that the loss can be calculated from knowledge of the gradient. A diagram of the type of plot obtained, and how to extract the propagation loss from the data, is shown in Figure 5.5. Note that, in fitting, the technique of linear regression

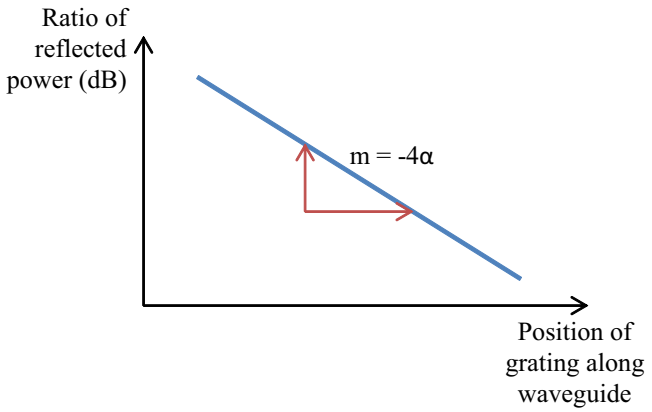

Figure 5.5: Example of the type of plot obtained when using this measurement technique. The difference in the reflected power from each grating is plotted on the y-axis against the physical position of the grating within the waveguide on the x-axis. The value of the propagation loss is obtained by inserting the gradient of the plot into Equation 5.6.

generates not only the gradient, but also an estimate of the error in the gradient. This feature makes our new approach particularly attractive for low loss waveguides.

Loss calculations are dependent on a number of further assumptions about the measurement technique itself. For reference, a schematic of the characterisation set up is shown (Figure 5.6). The function η can only be considered constant if the measurement of all of the gratings is performed in a single step, without changing the coupling efficiency at the measurement facet. The coupling efficiency is also assumed to be wavelength independent, as is the case with facet-launched waveguides of this type. The two measurements must be carried out under the same source conditions, including polarisation state, but the relative power of the broadband source can be different for each measurement so long as the background spectrum is obtained in each separate case. This allows normalisation to a constant background power level enabling the reflected power from the gratings to be measured, taking into account the coupling ratio of the 3 dB coupler in characterisation and the spectral characteristics of the source. In addition, it is assumed that the loss is constant along the entire length of the waveguide, an assumption that is corroborated by the small errors associated with the measured loss of the waveguides seen later in this chapter. This implies that FHD layer quality is consistent over the millimetre length scales involved. The propagation loss of the waveguide is known to differ spectrally over a wide wavelength band, due to the intrinsic losses and absorptions of the material at different wavelengths. The narrow band nature of this technique, requiring Bragg grating central wavelengths over a small spectral range, enables the use of the technique to characterise the losses of a waveguide at a narrow range of interest, so long as the loss across the range of wavelengths can be assumed to be flat.

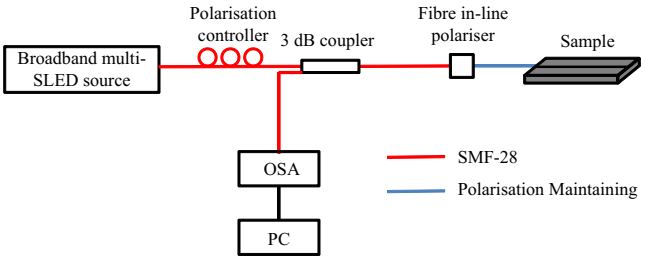

Figure 5.6: Characterisation set-up for gratings in the telecommunications band. The diagram shows the optical components of the system, and distinguishes between fibre type (single mode, polarisation maintaining) used.

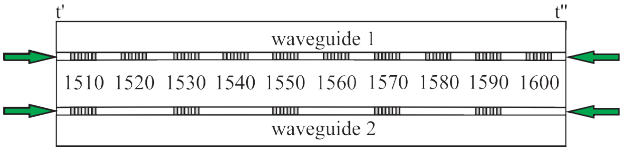

Figure 5.7: Schematic shows the grating wavelengths and positions for the waveguides fabricated for the loss technique verification procedure. The gratings are separated by channel waveguide sections. Gratings are interrogated by launching from opposing directions (arrows). Total device length is 40 mm, each grating is 2 mm long.

5.4 Fabrication and characterisation of device for method verification

The waveguides fabricated to verify the use of this grating-based technique for propagation loss measurement of a short waveguide were produced using the generic FHD and DGW techniques described previously in Chapter 3. This section describes the specifics of the methods used to fabricate the waveguides and Bragg gratings given the assumptions outlined in the previous section.

The waveguides and Bragg gratings were fabricated using the AOM Bragg grating definition method described in Chapter 3. A 40 mm by 10 mm section of wafer W8 (see Appendix C), with core thickness and refractive indices suitable for fabrication of a single mode waveguide at 1550 nm, was hydrogen loaded for 3 days to enhance photosensitivity, as described in Section 3.2.2. The DGW technique was used to inscribe two waveguides into the core layer of the photosensitive sample (Figure 5.7). The first contained ten 2 mm long Gaussian apodised Bragg gratings, with central wavelengths between 1510 and 1600 nm, spectrally spaced by 10 nm. The second contained five 2 mm long Bragg gratings with central wavelengths spaced by 20 nm. The Bragg gratings were spectrally clustered around 1550 nm in order to investigate the propagation losses of the waveguide in the low absorption region at this wavelength. Waveguide sections were inscribed between each Bragg grating, and the comparison between the five grating and the ten grating case enabled the investigation into whether Bragg gratings cause additional loss outside their spectral bandwidth.

In order to address the assumptions of Section 5.3, the following considerations were made during fabrication. The fluence was controlled so that the waveguide was strong enough to support Bragg gratings and coupling to the counter-propagating mode, but also to ensure that the Bragg gratings were not so strong that they become saturated. These controls allow use of the following assumptions, theoretically outlined above. Unsaturated Bragg gratings allow the assumption that the grating spectrum has the same spectral features given opposing launch conditions, and also that the peak reflected power from each launch can be compared to calculate propagation loss, given knowledge of the distance of waveguide traversed. The unsaturated gratings also allow the assumption that the physical central position of the Bragg grating, well known due to the accuracy and nm-level precision of the air-bearing stage system used in fabrication, corresponds to the spectral peak reflected power of the Bragg grating.

In addition, the fluence-matching technique (Section 4.3) was applied during grating fabrication to ensure that the average energy density present in the photosensitive core layer was consistent throughout the waveguide. This ensured no additional loss was caused by the Bragg grating structures outside of their spectral bandwidth.

The characterisation of the waveguides to obtain the reflected grating spectrum was carried out using the 1550 nm characterisation set up described previously (Figure 5.6). The background spectrum was also obtained, by measuring the reflected spectrum from the end facet of the fibre used to connect the channel waveguide to the characterisation system. This characterisation technique was also repeated with launch from the opposite end of the waveguide.

Characterisation parameters are adjusted for each experiment in order to obtain the best possible data for analysis of the device. Gaussian fitting to the reflected spectrum from the Bragg grating, carried out in the LabVIEW data aquisition software, is critical when determining the reflected power of the Bragg grating at the central wavelength (Figure 3.16). In order to obtain the best fit possible, whilst ensuring the fitting software runs efficiently in real time, experimental OSA parameters such as resolution and averaging are adjusted. This adjusts the number of data points available for the least squares fit to each Bragg grating spectrum, increasing the accuracy and precision of the fit. An additional adjustment can be made within the fitting software to ensure the best possible fit to the data. Each Gaussian fit is carried out within a 'window' of the total collected spectrum. Appropriate choice of the bandwidth of the window, and therefore the number of data points available to the fitting function, enables a better fit to the experimental Bragg grating reflection to be achieved.

Figure 5.8 shows the normalised reflected spectra obtained from the waveguide containing ten gratings, with opposing launch directions causing reflectivities R_i' and R_i''. The plot shows the variation in peak height of the gratings dependent on the launch direction. The state of the characterisation source was not altered between measurements in

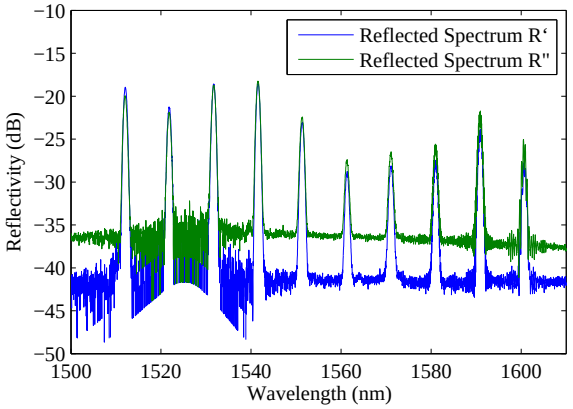

Figure 5.8: Spectra collected via characterisation of the waveguide described above (Figure 5.7), and with TE polarised source. The blue and green lines indicate the spectra obtained from different launch directions.

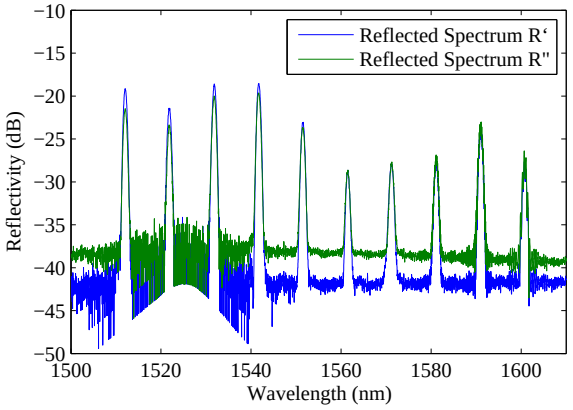

Figure 5.9: Spectra collected via characterisation of the waveguide described above (Figure 5.7), and with TM polarised source. The blue and green lines indicate the spectra obtained from different launch directions.

order to obtain comparable data points. The data shown here is for transverse electric (TE) polarisation; polarisation dependence of the propagation loss was observed when different polarisation states of the characterisation source were used. The spectral data obtained when the source was polarised in the transverse magnetic (TM) state is shown in Figure 5.9.

Control of the coupling efficiency was required to ensure it was wavelength independent and thus of equal magnitude over the entire spectral band. This was achieved by measuring the reflected spectrum from all gratings in the same measurement step, ensuring the coupling efficiency was constant. For facet launched waveguides such as these, the wavelength independence of coupling efficiency can be assumed due to the large magnitude in comparison to the waveguide propagation losses.

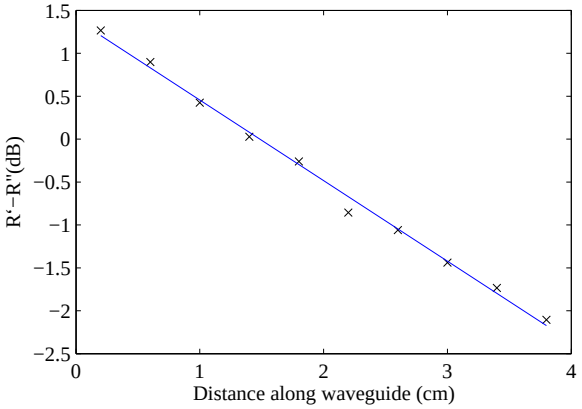

Figure 5.10: Ratio of reflected power of each grating against the position of the grating in the waveguide. Plot shows data obtained for waveguide containing ten Bragg gratings, in the TE polarisation state. Error bars within data points.

5.5 Experimental observation of loss

The data collection techniques described above enable the data necessary to calculate the propagation loss of the waveguide to be obtained. This section describes the extraction of specific information from the collected data, and manipulation of the data in order to calculate the propagation loss of the waveguide using the mathematical techniques described in Section 5.3.

The spectral data shown in Figure 5.8 was analysed using a Gaussian fitting algorithm to obtain the parameters of the gratings, as defined in Figure 3.16. In order to calculate the loss of the waveguide, the 'peak height' of the grating was obtained from the calculated data. The peak height was used to calculate the reflectivity relative to the background spectrum of each grating in dB. The waveguide was characterised from both launch facets, and the reflectivity of each individual grating obtained for each direction. By taking the ratio of the reflectivity of each grating, and plotting it against the physical position of the grating within the waveguide, the plot in Figure 5.10 was obtained.

The gradient of the plot allows calculation of the propagation loss of the waveguide. From Equation 5.6, the gradient of the straight line is four times the propagation loss of the waveguide. Thus, in this case, the propagation loss of the waveguide is 0.235 dB/cm, a value which concurs with those presented previously for equivalent silica-on-silicon UV written waveguides [88]. In all plots, the propagation loss values are obtained by dividing the observed gradient by four.

The error of the calculated propagation loss was calculated using regression analysis. The method provides an intrinsically robust value for the experimental uncertainty in the gradient and thus the propagation loss, where other authors can give only values for repeatability of the measurement. The standard error was calculated for the plot shown and yields propagation loss 0.235±0.006 dB/cm. This error consists of the statistical

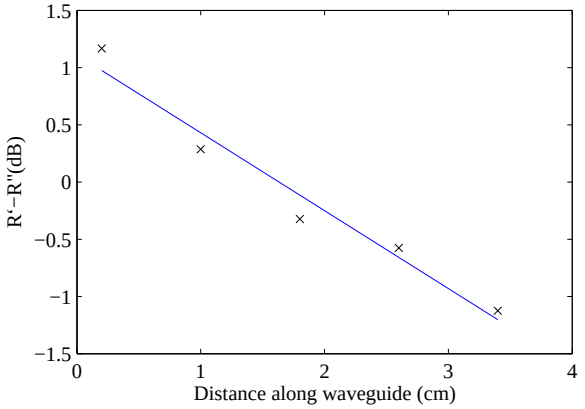

Figure 5.11: Ratio of reflected power of each grating against the position of the grating in the waveguide. Plot shows data obtained for waveguide containing five Bragg gratings in the TE polarisation state. Error bars within data points.

error in the data obtained, which includes the small fluctuations of the propagation loss over the spectral range used to interrogate the waveguide. This low error is around ten times better than reported for previous loss measurement techniques [79, 83].

A further point of investigation was whether the integrated Bragg grating structures themselves contribute any additional loss to the waveguide outside of the bandwidth of the gratings. This experiment was carried out using a waveguide on the same chip as the previous waveguide structures, with only five Bragg gratings in comparison to the initial ten. The waveguide structure is shown in Figure 5.7, waveguide 2. The waveguide was characterised and data obtained and plotted following the same procedure. The plot of this data is shown in Figure 5.11.

The calculated attenuation of this waveguide with standard error was 0.226±0.026 dB/cm. The loss value is consistent with that shown above, implying that the addition of a greater number of fluence-matched Bragg gratings does not increase the overall loss of the waveguide itself. The larger error in this case is due to the statistical errors associated with fitting a line to fewer data points.

An additional property of this loss measurement technique is the ability to measure the polarisation dependent loss of a waveguide, via adjustment of the characterisation set up. By changing the polarisation state of the incident characterisation source, depicted in Figure 5.6, both the TE and TM polarised propagation losses of the waveguide can be obtained. Figures 5.10 and 5.11 show the propagation loss in the TE polarisation state. The experimental data to calculate the propagation loss for the TM polarisation state is shown in Figure 5.12, giving a loss of 0.239±0.009 dB/cm.

This ability to measure the polarisation dependent loss enables knowledge of the characteristics of different polarisations of light traversing the waveguide, information which could be useful when designing waveguides for use as waveguide lasers or amplifiers.

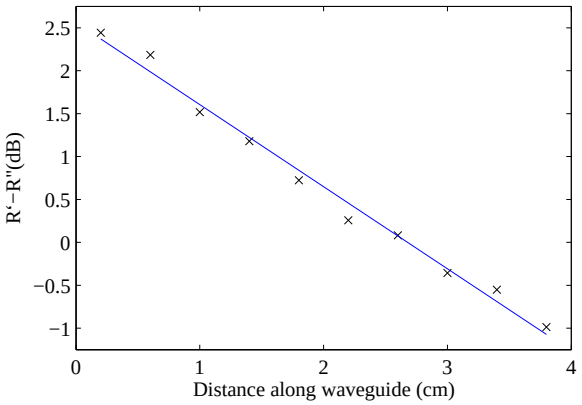

Figure 5.12: Ratio of reflected power of each grating against the position of the grating in the waveguide. Plot shows data obtained for waveguide containing ten Bragg gratings measured in the TM polarisation state. Error bars within data points.

The work presented here allows *in situ* measurement of the propagation loss of an optical waveguide, utilising integrated Bragg grating structures. The technique provides data which is independent of coupling losses and facet reflections. The technique could be employed in any material where weak Type *I* Bragg gratings are present, for example in flat fibre or chalcogenide glasses. This work has been published in Optics Letters [62].

During the period after publication of this loss measurement technique, the method was employed in a number of applications in order to measure the propagation losses of UV written waveguides in various geometries. The following sections will briefly outline these applications and the results obtained.

5.6 Loss measurement technique at 780 nm

The use of UV written waveguides at 780 nm has been under investigation by members of the author's group to look for applications in the fields of quantum optics and cold matter. Waveguides fabricated at 780 nm need to be single mode to fit these applications, so have thinner photosensitive core layers and a smaller UV writing spot diameter in order to create the correct waveguide geometry for the devices. In collaboration with the Centre for Cold Matter at Imperial College, London, the new loss measurement technique was used to corroborate their estimate of propagation losses in a single mode 780 nm UV written waveguide. Figure 5.13 shows the difference in reflected power obtained for Bragg gratings measured from opposing directions in a waveguide written for use at 780 nm. The propagation loss measured was 0.9±0.3 dB/cm at 780 nm. The large error here is due to the Gaussian fit of weak gratings at 780 nm, and the small number of data points (four) used. The data does, however, agree with the estimated value of 0.92 dB/cm quoted by Lepert et al. [72]. The 780 nm value implies that only a small fraction (less than 20 %) of the propagation loss at 1550 nm is due to Rayleigh

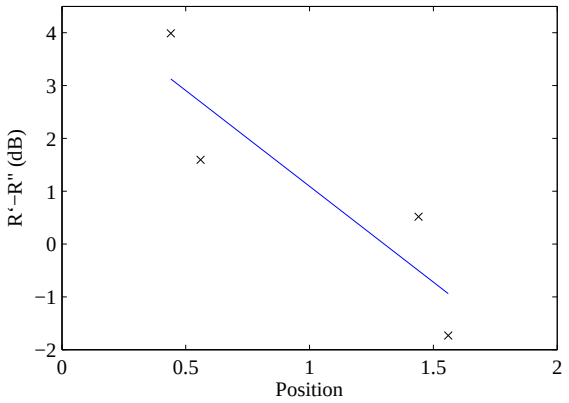

Figure 5.13: Ratio of reflected power of each grating against the position of the grating in the waveguide, for a waveguide optimised for 780 nm single mode operation. Plot shows data obtained for waveguide containing four Bragg gratings, measured in the TE polarisation state.

scattering losses, which scale as λ^{-4}. If the loss at 1550 nm was due entirely to Rayleigh scattering, the loss at 780 nm would be expected to be sixteen times larger than that at 1550 nm, in the region of 3.75 dB/cm. The relatively small loss observed here implies that the dominant propagation loss mechanism at 1550 nm is absorption, due to the proximity of the OH absorption band.

5.7 Loss measurement in slot-cut structures

The combination of UV written waveguides and micromachining techniques is the subject of intense investigation by the author's group. Collaboration between the author and fellow Ph.D. student Lewis Carpenter has led to a number of publications investigating the losses induced by micromachined slot-cut components interacting with waveguides.

One avenue of investigation was the use of diced grooves as corner mirrors. Waveguides were inscribed up to the grooves at a 45 ° incidence angle (Figure 5.14), and the optical propagation loss around the corner was measured using the loss measurement technique. A large induced defect such as the groove causes a step in the otherwise linear data used to determine the propagation loss of the waveguide. The step in the data in this case is the reflective loss of the machined component. In the case of the corner mirrors, the measured reflective loss of the corner mirror was 1.15 dB [64]. These devices are discussed in more detail in Lewis' thesis.

A second demonstration of the integration of waveguides and micromachining comes in the guise of measuring propagation loss when a waveguide crosses a diced groove. For this experiment, a waveguide was written across a 15 μm groove at 8 ° incidence (Figure 5.15), with an appropriate offset so the output guide was positioned for refraction through the air groove. An image of the groove is shown in Figure 5.16. Bragg gratings

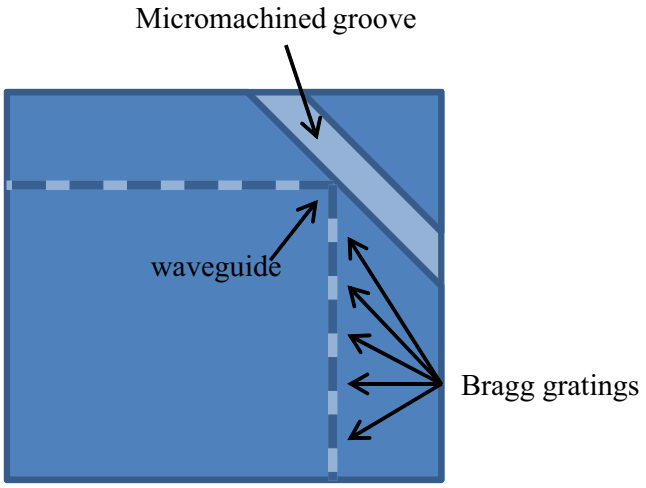

Figure 5.14: Schematic of the corner mirror device. Waveguides containing Bragg gratings were written up to the groove at an incidence angle of 45 °.

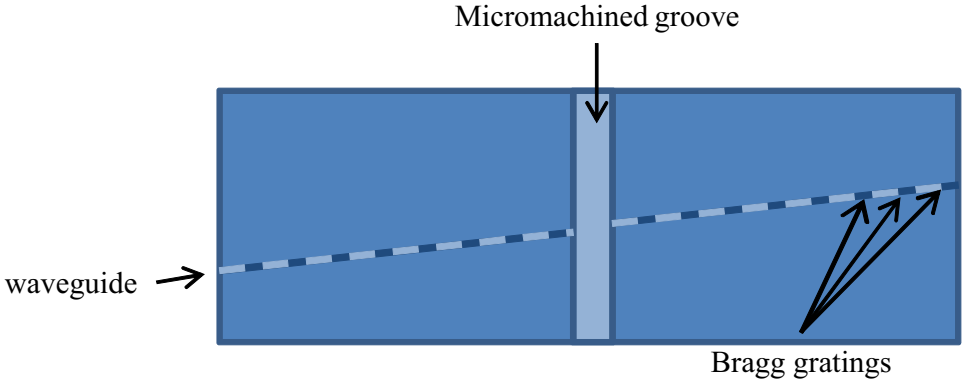

Figure 5.15: Schematic of the device used to measure the propagation loss of a waveguide intersecting a groove.

were written in the waveguide on either side of the groove to enable the loss across the groove to be calculated, considering Fresnel reflection losses. The calculated reflectivity difference can be seen in Figure 5.17.

Propagation loss across the groove was measured to be 0.63 dB (0.042 dB/μm) in the TE polarisation state. An investigation into the components of this loss was presented at the European Conference on Integrated Optics in 2010 [65], and led to the Fresnel reflection losses being considered. The device has potential applications as an absorption sensor, designed for solutions with a similar refractive index but significantly different absorption profiles at a specific wavelength, such as H_2O and D_2O.

An important point to consider when analysing this experimental data is the verticality of the side walls of the groove. A Fresnel loss component can be introduced at a non-vertical boundary, adding to the propagation losses observed across the groove. The verticality of the side walls of the groove pictured above was approx. 2.5 ° where the core layer meets the groove, and was obtained using the microscope image featured (Figure 5.16 in SPIP^{TM} (Image Metrology) surface analysis program (work carried out

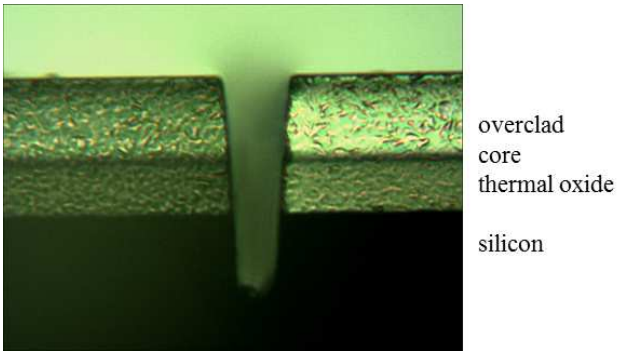

Figure 5.16: Microscope image of the channel groove fabricated for the loss measurement. The groove was physically micromachined using a high precision dicing saw and is 15 μm wide and approx. 60 μm deep, ensuring the best achievable verticality of side walls in the core region. The image shows the silicon (black, lower layer), thermal oxide, and FHD core (thin black line) and overclad (top of sample) layers.

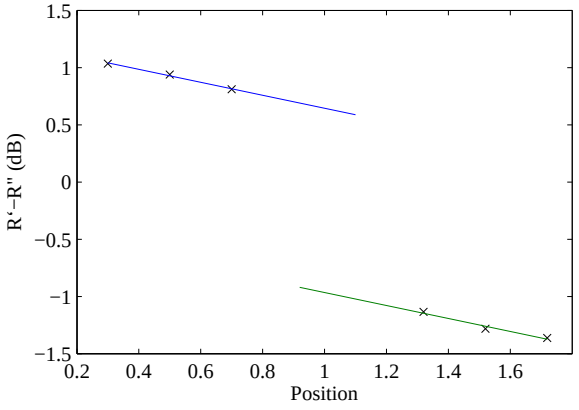

Figure 5.17: Difference in reflectivity of Bragg grating spectra measured from opposing launch conditions, in a waveguide intersecting a groove. The loss across the groove, calculated by extrapolating the propagation loss of the Bragg gratings on either side of the groove, was found to be 0.63 dB in this TE polarisation state, after consideration of Fresnel reflection losses.

by Lewis Carpenter)). The Fresnel losses at this vertical boundary can then be obtained. As can be seen in Figure 5.18, when a groove is not diced deep enough into the silicon layer, the verticality of the sidewalls is non-ideal, with an angle of 20 ° measured at the core layer, and a corresponding higher propagation loss value of 0.089 dB/μm measured across the groove.

5.8 Loss measurement in flat fibre waveguides

The loss measurement technique has also been used to measure the propagation losses of waveguides in different materials. One of these materials is flat fibre, a material developed at the Optoelectronics Research Centre. Flat fibre is fabricated in a similar

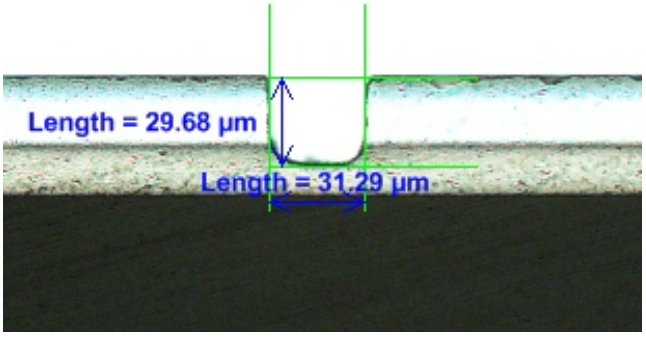

Figure 5.18: First iteration of groove loss measurement experiment. The groove here was approx. 30 μm wide and 30 μm deep, and had a propagation loss value of 21.25 dB. Note that the core layer meets the groove at the curved bottom corner of the groove

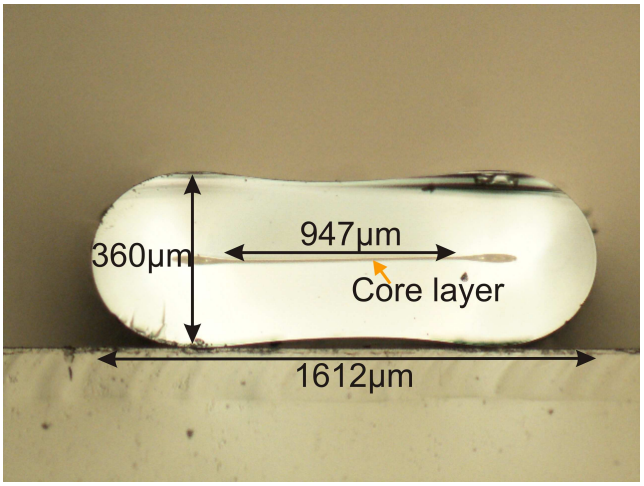

Figure 5.19: Microscope image of the end facet of flat fibre, showing bow-tie profile. Image provided by Sumiaty Ambran.

fashion to optical fibre, with manufacture of a preform which is then drawn in a fibre-drawing tower. In the case of flat fibre, a vacuum is applied across the fibre during the drawing process, creating a flattened fibre profile. The bow-tie structure of flat fibre can be observed in Figure 5.19.

The resulting structure is a planar core layer, approximately 1 mm wide and a few microns thick. The planar core layer can be doped with photosensitive materials to enable UV writing of waveguides and Bragg gratings in the core. In addition, doping with rare-earth ions enables use as waveguide lasing and amplification devices. The low loss afforded by the fibre drawing procedure, coupled with the flexibility of the planar core layer promote use of the material in low-loss integrated optics applications.

Work by fellow Ph.D. student Sumiaty Ambran on flat fibre development made use of the loss measurement technique, allowing measurement of 0.12±0.02 dB/cm propagation loss in a UV written waveguide in flat fibre. Figures 5.20 and 5.21 show the collected data and the propagation loss calculation respectively. The low losses of flat fibre ensure the

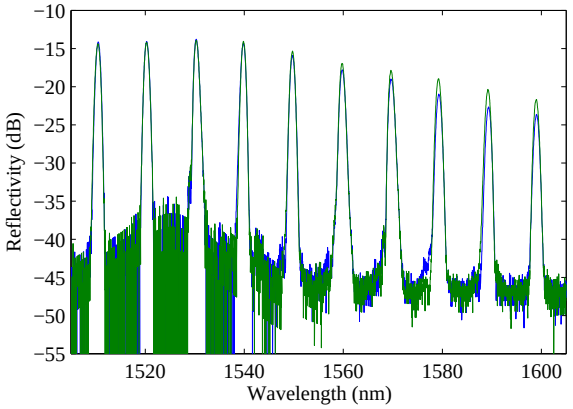

Figure 5.20: Reflected spectra collected from Bragg gratings within a flat fibre platform. The data was collected with the source polarised in the TE polarisation state. Data collected from opposing launch directions is shown. The data shown here was collected by Sumiaty Ambran.

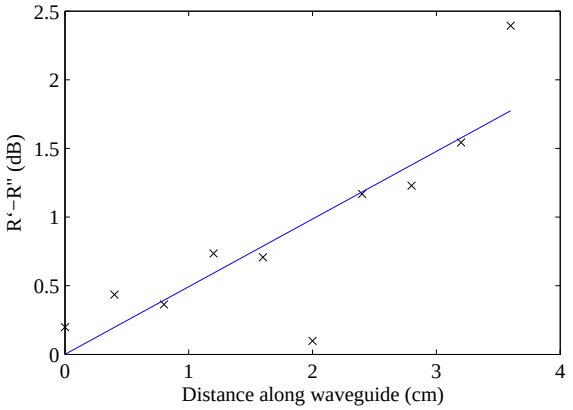

Figure 5.21: Ratio of reflected power of each grating against the position of the grating in the waveguide, for a waveguide in a flat fibre substrate. The collected data is normalised, and calculation of the gradient occurs in the same fashion as before. The data shown here was analysed by Sumiaty Ambran.

platform is suitable in telecommunications applications amongst others, and resolving the propagation loss of the waveguides accurately is critical. Further information on the losses and applications of flat fibre can be found in Sumiaty's thesis.

5.9 Loss measurement in doped FHD waveguides

The new loss measurement technique has also been implemented in the development stages of doped waveguides suitable for lasing and amplification applications. These applications require low loss waveguides in order that the gain experienced in the material is not inhibited by a highly lossy waveguide at the wavelength of interest. In collaboration with the University of Malaya, samples with solution doped regions were investigated, with fabrication of FHD in Malaysia, and waveguide and Bragg grating

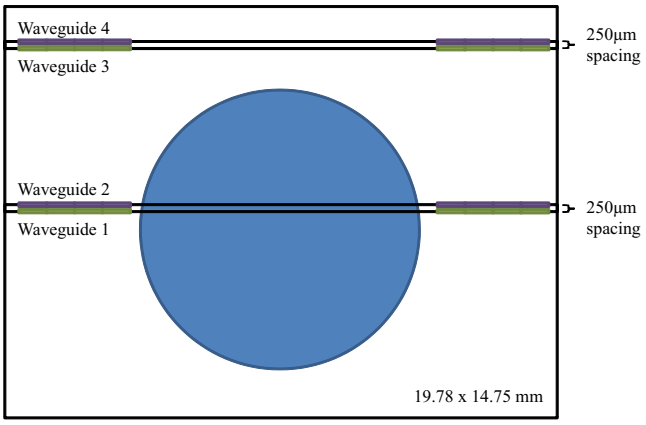

Figure 5.22: Schematic of the solution-doped chip used for the propagation loss measurement. The large circle representes the solution doped area. Green rectangles represent Bragg gratings in the 1530 nm region, purple rectangles represent Bragg gratings in the 1580 nm region. Waveguide numbers for ease of identification.

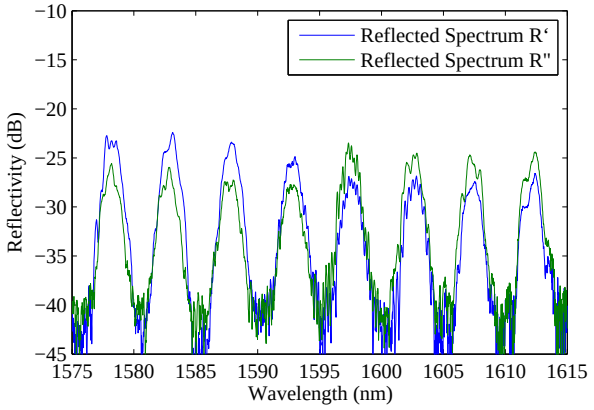

Figure 5.23: Collected reflected spectra from Bragg gratings with central wavelengths in the region 1580 nm, in waveguide 4. The reflected spectrum from opposing launch directions was obtained, to enable propagation loss calculation.

fabrication, measurement and analysis undertaken by the author. Solutions of different concentrations of erbium per unit volume were dropped onto a partially consolidated FHD wafer in a process known as solution doping [9], creating circular doped regions approximately 1 cm in diameter. Waveguides were written through these regions, and into the surrounding undoped FHD material, to compare the propagation losses in the doped and undoped regions. A schematic of the chip is shown in Figure 5.22.

Bragg gratings were fabricated in these waveguides with central wavelengths within one of two bands. In the region of 1580 nm, Bragg gratings were used to determine the loss of the waveguide UV-written in the doped and undoped regions, to compare the propagation losses of the waveguide sections alone without additional absorption losses due to the inclusion of erbium dopant in the core layer. Bragg gratings with central wavelengths around 1530 nm, within the absorption band of erbium, were used to determine the loss present within the doped region of the sample, including the

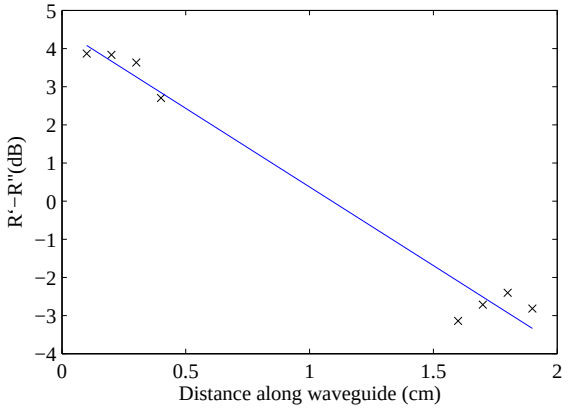

Figure 5.24: Ratio of reflected power of each grating against the position of the grating in the waveguide, for waveguide 4. The propagation loss of this waveguide is 1.03±0.06 dB/cm.

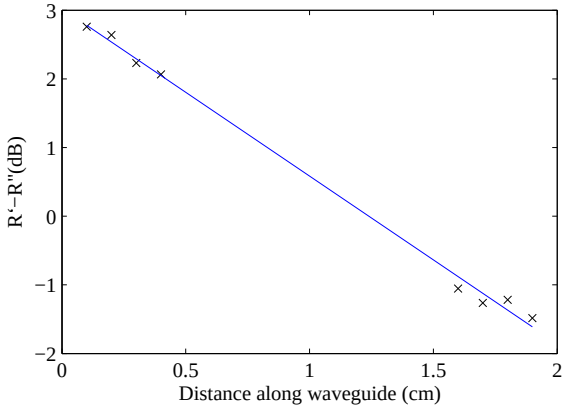

Figure 5.25: Ratio of reflected power of each grating against the position of the grating in the waveguide, for waveguide 3. The propagation loss of this waveguide is 0.61±0.02 dB/cm.

absorption losses, and in the undoped region, as an indication of potential gain within the device.

In the best case, the propagation loss at 1580 nm in the undoped FHD was 1.03±0.06 dB/cm. The observed spectra and reflectivity plots can be observed in Figures 5.23 and 5.24 respectively. In comparison, the propagation loss at 1530 nm in the undoped FHD was 0.61±0.02 dB/cm (Figure 5.25). The loss observed at 1580 nm across the widest cross section of the doped region was 3.5±0.6 dB (Figure 5.26). A waveguide written with Bragg gratings at 1530 nm, physically separated by 250 μm from the 1580 nm channel, exhibited loss in this region of 3.4±0.4 dB (Figure 5.27). These losses are calculated by extrapolating the losses obtained in the undoped waveguide, and comparing the values at a central position on the waveguide, as shown in the plots. Errors are obtained by taking the standard deviation of the difference between the measured data and the fitted line. Comparing the propagation loss values at 1530 nm and 1580 nm enables observation of the amount of loss due to absorption by the erbium dopant in this region.

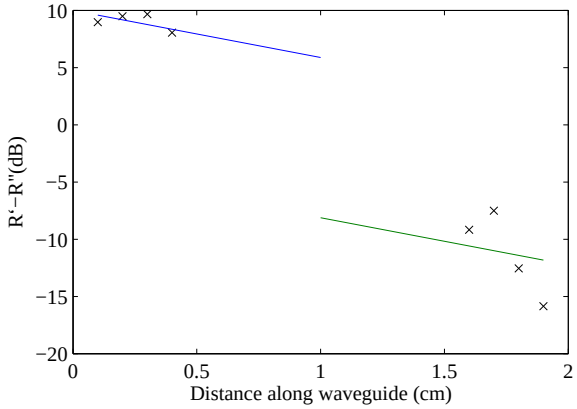

Figure 5.26: Ratio of reflected power of each grating against the position of the grating in the waveguide, for waveguide 2. The loss of this waveguide in the doped section is 3.5±0.6 dB/cm, calculated by extrapolating the loss data in the undoped region.

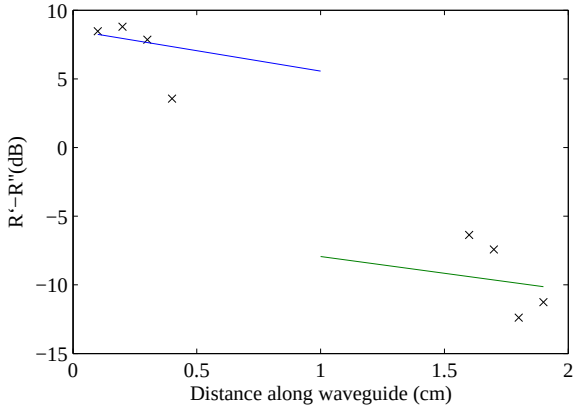

Figure 5.27: Ratio of reflected power of each grating against the position of the grating in the waveguide, for waveguide 1. The loss of this waveguide in the doped section is 3.4±0.4 dB/cm, calculated by extrapolating the loss data in the undoped region.

In the case of this sample, the propagation losses measured do not enable this observation to be made. The loss in the undoped FHD at 1580 nm is higher than that at 1530 nm, most probably caused by the condition of the FHD, fabricated outside a clean room environment. Figure 5.23 shows the poor quality gratings achieved in the glass layer, which lead to the propagation loss values and errors at least twice that of those in the case of our FHD system (Figure 5.10). As such, comparing the losses within the doped region at the two wavelengths does not give the expected higher loss in the solution doped region at the 1530 nm absorption wavelength. The propagation loss in the erbium doped region was too high to investigate the use of the waveguide as an effective amplification or lasing device, but this work provides a further demonstration of the uses of the propagation loss measurement technique.

The technique described in this chapter has aided a number of investigations into potential applications of low loss UV written waveguides. Those described here, at 780 nm, with micromachining, in doped FHD and in flat fibre, are those the author has directly

investigated and contributed to. Interrogation of these devices, and extensive literature review, has cemented the use of the new propagation loss measurement technique in applications where the aforementioned assumption criteria can be met.

5.10 Conclusions and further work

This chapter describes the design and implementation of a propagation loss measurement technique for short planar waveguides. Given a detailed account of the types of loss present in a waveguide, the developed technique is able to isolate the propagation loss of the waveguide from the coupling losses and facet reflections which hinder other propagation loss measurement techniques. The propagation loss data obtained using this technique agrees well with that quoted for similar silica-on-silicon UV written waveguides [88].

The new technique relies on a number of assumptions which concern the fabrication and characterisation of the integrated Bragg gratings. So long as these assumptions can be made, via careful design of the Type *I* Bragg gratings and measurement set up, the technique could be applied to a variety of materials, including optical fibres and photosensitive chalcogenide glasses. The technique also provides polarisation dependent propagation loss measurement, by altering the polarisation of the characterisation source, which has been presented in this chapter.

The developed technique has proven value in the wider field, enabling the propagation losses of low loss waveguides to be measured effectively with robust error analysis verifying the precision of the measurement. The technique provides consistent results for similar waveguides. The technique also proves that negligible losses are incurred by the fluence-matched UV-written Bragg gratings at wavelengths outside the bandwidth of the grating, a factor important to consider when designing effective waveguide circuitry for any application.

Future work would see the technique applied to a number of low-loss waveguide situations. Continuation of the work investigating the absorption sensing device (Section 5.7) could result in a practical measurement technique for solutions with similar refractive index but different absorption characteristics at the wavelength of interest. An implementation of the technique using a short Bragg grating fabricated within the core of a fibre pigtail would enable the coupling loss of the pigtail to the device to be measured, and monitored in order to achieve the lowest possible coupling loss between the device and the interrogation system. These developments would enable the loss measurement technique to form the foundations of an effective environmental sensing device, with the lowest possible system losses, as well as providing a means to measure and reduce the coupling losses associated with integrated optical telecommunications devices.

Chapter 6

Grating based dispersion measurement technique

Consideration of the dispersion characteristics of an optical material is key when designing application specific devices. In many cases, the dispersion of the material is considered advantageous, such as in prism spectrometers, where the dispersion of the prism allows propagating frequencies to be separated and analysed independently. However, in many other situations, the dispersion of a material is considered a hindrance, requiring extensive material engineering in order to enable the desired efficient device to be obtained, as in the case of dispersion shifted fibres. In either situation, knowledge of the dispersion characteristics is key to ensure appropriate considerations are made when designing devices.

This chapter describes the development of a dispersion measurement technique utilising integrated Bragg grating structures within an optical waveguide. The 'dispersion' in this case is the wavelength dependence of the effective refractive index of the waveguide, and is obtained by spectral interrogation of a number of Bragg gratings within the waveguide. The opportunity to interrogate the second order Bragg reflection of each grating provides a wide range of data suitable for fitting to the three term Sellmeier dispersion equation. From an empirical calculation of the waveguide dispersion component of the total dispersion, the material dispersion component can be inferred. Application of the technique to different polarisation states and higher order modes of the waveguide are presented. To conclude, a practical demonstration of this new technique is presented, to predict the wavelength of signal and idler photons produced during four wave mixing in a birefringent waveguide.

6.1 Theory of wavelength dependent dispersion

Dispersion within an optical medium is the change in the group velocity of an optical mode as it propagates through the material. For different wavelengths, the magnitude of this change will alter, introducing a wavelength dependence to the dispersion of the material. The dispersion can also be considered as the optical length of the material at a specific wavelength, and can be described by the following relation.

$$D = \frac{1}{L}\frac{d\tau}{d\lambda} \tag{6.1}$$

L is the length of the material, τ is the delay, or change in group velocity, and λ is the wavelength. In waveguides, this wavelength dependence manifests itself in two ways. Firstly, the characteristic wavelength-dependent refractive index of the medium is known as material dispersion, and is dependent solely on the refractive index variation due to irradiation at different wavelengths. In addition, the geometrical constraints of the waveguide introduce a second wavelength dependent dispersion component, known as waveguide dispersion. The origin of the waveguide dispersion can be seen as being due to the effective mode size at different wavelengths. This causes the mode to 'see' a different effective refractive index depending on the area of higher index core and lower index cladding the mode encounters.

This section will introduce the concepts of material and waveguide dispersion, providing a theoretical basis for the experimental work undertaken. The foundation of material dispersion will be discussed from the basis of the Kramers-Kronig relations, and the use of the Sellmeier curve for fitting material dispersion will be discussed. A description of waveguide dispersion will follow, defining the physical reasoning behind it, and explaining the empirical methods of calculating the effect of waveguide dispersion for the waveguide under test. Following this, a discussion of the relationship between material and waveguide dispersion will conclude the theoretical considerations behind this work.

6.1.1 Material dispersion

As previously stated, the basis of material dispersion is the wavelength dependence of the refractive index of the material when irradiated. In order to best understand the physical principles behind this phenomenon, the first part of this section deals with the complex nature of refractive index, leading to the Kramers-Kronig formalism for material dispersion, relating the real refractive index of the material to several appropriate absorption oscillators. The second part of the section will define the modelling techniques available to predict material dispersion, given prior knowledge of the wavelength-dependent refractive index. The Sellmeier relation will be presented alongside a physical interpretation of its foundation, and a discussion of the assumptions necessary to apply the fit.

This formula allows us to interpret the experimental data obtained from Bragg grating spectra (Section 6.4) in order to obtain the material dispersion component of the measured total dispersion.

6.1.1.1 The Kramers-Kronig relation

The refractive index of a medium consists of a real and an imaginary component, relating to the real dispersive index and the absorption (or gain) components of the total refractive index respectively. The total refractive index $\hat{n}(\lambda)$ is given by the sum of these components, as indicated in Equation 6.2.

$$\hat{n}(\omega) = n(\omega) + i\kappa(\omega) \tag{6.2}$$

n is the real dispersive index and κ is the extinction coefficient, related to the amount of absorption or gain experienced by electromagnetic radiation as it propagates through the material. The extinction coefficient can be defined in terms of the absorption coefficient α, which defines the frequency-dependent absorption of the material and is defined as:

$$\alpha(\omega) = 2\kappa(\omega) \tag{6.3}$$

The physical interpretation of this spectral absorption can be considered analogous to a mass on a spring argument. An electron is bound to a nucleus as a small mass is bound to a larger mass by a spring. When electromagnetic radiation is present, the system is driven by a wave $E_0 e^{-i\omega t}$, leading to oscillations which can be approximated to those of a forced damped oscillator. An electron which has mass m and charge q can undergo a resonance at frequency ω_0 which has damping (or viscous drag) γ [89]. In the presence of electromagnetic radiation this resonance can be formulated as follows:

$$\frac{d^2\boldsymbol{x}}{dt^2} + \gamma\frac{d\boldsymbol{x}}{dt} + \omega_0^2\boldsymbol{x} = \frac{q}{m}E_0 e^{-i\omega t}. \tag{6.4}$$

From this, the absorption coefficient can be obtained in the form of a complex Lorentzian. Applying electromagnetic identities for a number of molecules N, with each molecule containing f_j electrons with charge q and damping γ_j, leads to a description of the absorption coefficient α [89].

$$\alpha = 2\kappa \cong \frac{Nq^2\omega^2}{m\epsilon_0 c}\sum_j \frac{f_j\gamma_j}{(\omega_j^2 - \omega^2)^2 + \gamma_j^2\omega_2} \tag{6.5}$$

ϵ_0 is the permittivity of free space, and c the speed of light. The Kramers-Kronig relation defines the relationship between this imaginary absorptive part and the real dispersive part of the refractive index.

The relationship between n and κ can be thought of as an absorption mechanism. Incident radiation at a frequency which excites an atom causes vibration of the atom at that frequency, and re-emission of the energy with the same frequency but with a phase shift. The phase shift in the radiated light can be thought of as an increase in refractive index, the magnitude of which is dependent on the frequency of incident radiation. Similarly, the absorption component can be thought of as the phase delay of the re-emitted energy with respect to the incoming radiation. The phase shift causes interference between the emitted and incoming radiation, with absorption coinciding with the frequency where destructive interference occurs.

The derivation of the Kramers-Kronig relation can be formulated via Cauchy's theorem of complex integration, causality and Fourier analysis [90]. The relationship is expressed by

$$n\left(\omega\right) = 1 - \frac{2c\mathcal{P}}{\pi} \int \frac{\alpha(\omega)}{(\omega_j^2 - \omega^2)} d\omega, \tag{6.6}$$

where $\mathcal{P}$ is the Cauchy principal value, ω_j is the spectral position of the absorption oscillator and ω is the frequency [91].

The Kramers-Kronig relationship allows an understanding of the physical mechanisms behind the wavelength dependence of the refractive index of a material. A series of absorption oscillators are present, defining the dispersive characteristics of the regions at and between their positions. The material dispersion of a medium is therefore dependent on the position and strength of these oscillators. Given this information, or information about the variation of refractive index with wavelength between these oscillators, empirical modelling can be carried out to predict the material dispersion characteristics of a medium.

6.1.1.2 The Sellmeier equation

Various Sellmeier dispersion formulae have been demonstrated to provide a suitable empirical fit to wavelength-dependent refractive index data for both glass and non-glass materials. A development of the Cauchy dispersion equations, the Sellmeier relations allow accurate prediction of refractive index at wavelengths not only in the visible region, but also in the infrared. Comparison of the relations to other fitting formalisms has concluded that, for the accuracy required for the majority of applications, the Sellmeier relations are the most accurate available to fit this data [92].

$$n^2(\lambda) - 1 = \frac{b_1\lambda^2}{\lambda^2 - a_1} + \frac{b_2\lambda^2}{\lambda^2 - a_2} + \frac{b_3\lambda^2}{\lambda^2 - a_3} \tag{6.7}$$

The Sellmeier relations have been represented in a number of guises, the most common for glass being the three-term Sellmeier shown here (Equation 6.7). n is the refractive index, λ the wavelength and a_i and b_i the position and strength of the absorption oscillators respectively, known as the Sellmeier coefficients. Any number of oscillators can be analysed, but for most transparent materials, three oscillators are sufficient to fit the curve accurately in the visible and near IR spectral region.

The expression is solved using the non-linear least squares fit method. There are several difficulties encountered when solving for the coefficients, due to the non-linearity of the b_i terms. Assumptions are made about the starting values, the number of iterations necessary to obtain a solution, and the degeneracy of the expression itself.

The starting conditions are defined in such a way as to provide the best estimate of the oscillator conditions of the material. In the case of materials which are transparent in the visible and near-IR spectral regions, the oscillators are chosen so that two are positioned in the UV and one in the mid IR. For materials such as doped silica, coefficients are widely reported in the literature [93], and can be used as a starting point to determine the approximate position and strengths of the oscillators for specific materials.

One weakness of this three-term form (Equation 6.7) is that the degeneracy of the expression significantly affects the outcome of the fitting process. The form of the Sellmeier equation limits the effectiveness of the fit, as the three terms are mathematically identical. As such, in order to achieve an effective fit, each of the three terms must be equally weighted to find the true solution. An imbalance in the weighting of the terms can be caused by insufficient data points, an inaccuracy in the measured refractive index and wavelength data, weak absorption oscillators predicted by the fit, or the spectral position and range of the data points. Addressing some or all of these issues allows a more accurate fit to be obtained, and therefore enhanced knowledge of the position and strength of the oscillators.

The non-linear least squares fit method provides statistical errors concerning the fit to the data set. The standard deviation of the points from the fitted curve provides an estimate of the error in the fit, which can be assumed to be equal across the entire spectral band. In this way, best and worst case fits can be calculated by changing the strength of the oscillators (b_i), obtaining information about the accuracy and precision of the fit.

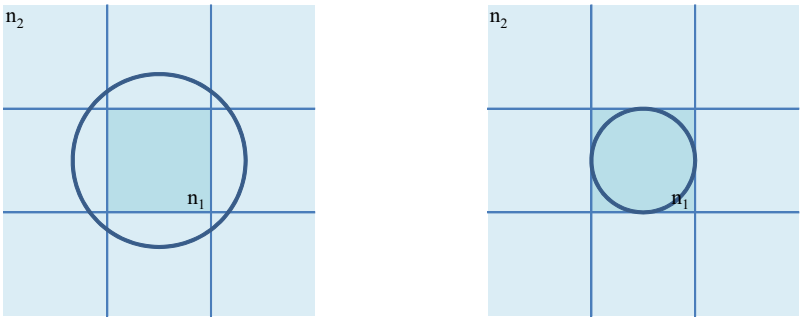

Figure 6.1: Effect of the size of the propagating mode on the effective refractive index. Larger wavelength propagating modes (left) have a larger effective mode area, and therefore have a larger n_2 contribution to the total effective refractive index. Smaller wavelength modes (right) are more confined to the core n_1 region, with a greater tendency for higher order modes to exist.

6.1.2 Waveguide dispersion

In the case of waveguides, an additional dependence on wavelength is present due to the structure of the waveguide itself. The waveguiding structure causes different parts of the mode to encounter different refractive index regions simultaneously, affecting the overall group velocity of the mode. The refractive index profile encountered by the mode is dependent on the individual refractive indices and geometry of the core and cladding regions. An overall wavelength-dependent 'effective refractive index' can be calculated for the mode given this structural information, and indicates the overall change in group velocity of the entire mode travelling through the structure. The effective refractive index is dependent on the mode size and, thus, the wavelength of the incident radiation.

Figure 6.1 illustrates the effect of changing wavelength on the effective index encountered by the propagating mode. Assuming a step index waveguide, and no material dispersion (ie. n_1 and n_2 are independent of wavelength), it can be shown that the propagating mode experiences a different effective refractive index depending on its magnitude relative to the size of the waveguide cross-section.

The size of the propagating mode is directly linked to the wavelength, given the dependence of the solution of the wave equation on frequency, as previously described in Equation 2.13. This additional wavelength dependence contributes to the measured dispersion of the refractive index of the waveguide. Given information about the refractive index and dimensions of the core and cladding regions of the waveguide, empirical calculations can be carried out in order to estimate the waveguide dispersion.

Ghatak and Thyagarajan [94] describe a method of empirical calculation of the waveguide dispersion. This calculation applies to a step index circular fibre, but can be applied to weak guides with reasonable accuracy [28]. The waveguide dispersion, D_w, can be calculated via the following relation.

$$D_w \simeq \frac{-n_2\Delta}{3\lambda_0} \times 10^7 \left(V \frac{d^2(bV)}{dV^2} \right) ps/km.nm \tag{6.8}$$

where

$$\Delta \equiv \frac{n_1^2 - n_2^2}{2n_1^2} \tag{6.9}$$

for a step index fibre.

The rightmost part of Equation 6.8, $V\frac{d^2(bV)}{dV^2}$, is given via the following empirical formula, dependent on the dimensionless waveguide parameter V of the waveguide (Equation 2.28).

$$V \frac{d^2(bV)}{dV^2} \simeq 0.080 + 0.549 \left(2.834 - V^2\right) \tag{6.10}$$

This relation gives an approximate value of the waveguide dispersion accurate to within 95% of the true value for a single mode step index fibre with V number between 1.3 and 2.3 [94]. When considering a fibre-like step index waveguide, as in this weakly guiding case, this allows reasonable estimation of the waveguide dispersion within the telecommunications band.

This empirical calculation allows an estimate of the wavelength-dependent waveguide dispersion for a given known waveguide. The contribution of this component to the total dispersion of the waveguide can be significant, depending on the geometry and materials in question. The combination of material and waveguide dispersion yields the total dispersion of the waveguide, however, these components are not strictly additive in all cases, as described in the following section.

6.1.3 Total wavelength-dependent dispersion

The dispersion measured using the technique described later in this chapter is the total dispersion of the waveguide, the combination of all wavelength-dependent phenomena contributing to the mode propagation. It is assumed throughout the course of this work that the material and waveguide dispersion components add to yield this total measured dispersion, as is presented in the literature [95]. In this section, the validity of this assumption will be discussed.

For the purposes of this technique development exercise, the waveguides considered are single-mode and allow propagation of only the fundamental guided mode over the range of wavelengths of interest. Moreover, the waveguide is considered to be 'weakly guiding', due to the small core and small refractive index difference necessary to meet the single

mode requirement outlined above. These considerations enable the additive assumption to be justified.

Marcuse [96] presents analysis of this topic, including calculation of the total dispersion of a waveguide via two separate methods. In order to prove the validity of the assumption that material and waveguide dispersion are considered additive, the waveguide dispersion is calculated independently (D_w), but also from the combination of additive and material dispersion ($D_{m+w} - D_m$). In order to consider the material and waveguide dispersion components additive, these calculations should yield the same result.

Marcuse finds, via numerical solutions of Gloge's LP mode eigenvalue equation [28], that D_{m+w} can be represented by the following relation.

$$D_{m+w} = \frac{k}{c\lambda\beta^3}\left\{\lambda^2\beta^2\left(\frac{\kappa}{k^2}\frac{d^2\kappa}{d\lambda^2} - n_1\frac{d^2n_1}{d\lambda^2}\right) + \kappa^2\left(n_1 - \lambda\frac{dn_1}{d\lambda}\right)^2 + \lambda\frac{d\kappa}{d\lambda}\left[2n_1\kappa\left(n_1 - \lambda\frac{dn_1}{d\lambda}\right) + 2\frac{\kappa\beta^2}{k^2} + n_1^2\lambda\frac{d\kappa}{d\lambda}\right]\right\} \quad (6.11)$$

D_{m+w} is the additive assumed total dispersion, β is the propagation constant of the guided mode, and κ is a parameter associated with the propagation of radiation in the core of the waveguide (see Section 2.1.2). λ is the wavelength, k is the wavenumber related to the wavelength via $k = \frac{2\pi}{\lambda}$, n is the refractive index of the core and c is the speed of light in vacuum.

D_m is then calculated by neglecting the waveguide dispersion components, by setting κ and its derivatives equal to zero, and letting $\beta = n_1 k$. Similarly, waveguide dispersion D_w is obtained by neglecting material dispersion, by fixing the core and cladding indices n_1 and n_2 to remove the wavelength dependence of the refractive index of the material. The comparison is then made between $D_{m+w} - D_m$ and D_w, to investigate the validity of the additive assumption.

Marcuse finds that the comparison of these components yields a non-zero result, indicating that the waveguide dispersion and the material dispersion are not strictly additive over the entire wavelength range. For smaller core radii, or smaller V number, the difference becomes larger, causing differences of tens of nanometres between the calculated components. However, given the typical wavelengths involved in the telecommunications band, this is a small percentage difference, and thus a small effect in the region of V number between 1.3 and 2.3, the typical regime of operation of the fabricated waveguides. Therefore, the assumption that waveguide and material dispersion are additive is used throughout this work to calculate the D_m and D_w components from the total measured dispersion. This is also assumed in the techniques described in the next section which are used to measure the dispersion of optical waveguides.

6.2 Techniques for measurement of dispersion of optical waveguides

The dispersive properties of optical materials can be measured using a variety of different techniques. Here, the most commonly used techniques are described, with analysis of their practicality in terms of application to short waveguides.

Traditional optical dispersion measurement techniques typically involve measurement of bulk glass or optical fibres. Bulk glass measurement techniques, typically using a prism formed of the material, allow the material dispersion of the medium to be measured by observing the angle of refraction of different frequencies through that material [97]. For optical fibres, the lengths of material involved allow the use of time of flight and modulation phase shift methods [98], given information about the fibre lengths and spectral width of the measurement source. These techniques yield the group delay of the source, $\frac{dn}{d\lambda}$, introducing an additional error-compounding calculation step in order to obtain the dispersive refractive index of the material.

The typically short lengths of planar waveguides inhibit the accuracy and precision of these traditional dispersion measurement techniques. Time of flight and modulation phase shift methods require metres of material and measurement over a few nanometres of spectral bandwidth in order to obtain accurate results. The bulk measurement techniques do not take into consideration the waveguide dispersion component of the total dispersion, if a prism of material can indeed be fabricated for measurement. In the case of UV written waveguides, the refractive index modification induced by direct UV writing in the formation of the waveguide could not be replicated in a bulk glass form.

A number of techniques have been demonstrated that are tailored toward the measurement of short planar waveguides. These are mainly variations on the interferometric method first described by Tateda et al. [99]. In the simplest form, the technique involves measuring the group delay of two arms of an equal path length interferometer, with the waveguide under test constituting part of one arm. The first-order wavelength-dependent dispersion is obtained by repeating the technique at a variety of frequencies. Variations on the technique allow the polarisation-dependent dispersion to be obtained [100], or white light interferometry to be implemented [101]. This modification allows the choice between the temporal (group delay) method, or the spectral technique, involving measurement of the phase or period of spectrally resolved interference fringes. These interferometric techniques allow accurate and precise measurement of the total wavelength-dependent dispersion of the waveguide via the first-order dispersion of the device. In order to obtain the wavelength-dependent refractive index, or zero-order dispersion, an additional calculation step is required, increasing the uncertainty of the measurement technique.

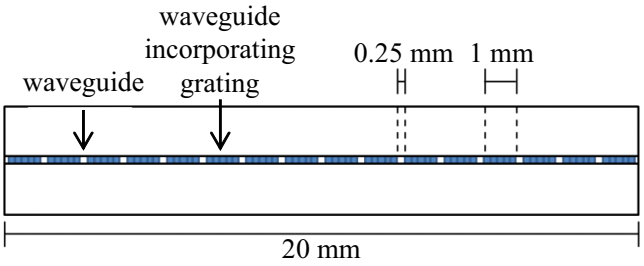

Figure 6.2: Schematic of the waveguide produced for demonstration of the dispersion measurement technique. The waveguide contains sixteen 1 mm long Bragg gratings along its length, separated by 0.25 mm sections of waveguide. The Bragg gratings have central wavelengths between 1250 nm and 1625 nm, spectrally spaced by approximately 25 nm.

The method described in this chapter allows the zero-order dispersion to be obtained directly, via measurement of the effective refractive index of Bragg grating structures within the waveguide. The large spectral range over which the effective index is measured allows an accurate representation of the zero-order dispersion to be obtained over a wide bandwidth. This allows the technique to be applied in situations where precise knowledge of the effective index of the waveguide is necessary at widely differing spectral positions, such as in non-linear interactions.

6.3 Experimental realisation of technique

The experimental technique presented here allows the total wavelength-dependent refractive index dispersion of a waveguide to be measured. The method relies on integrated Bragg grating structures within the waveguide, each with a well-defined central wavelength, in order to obtain the effective refractive index of the waveguide via the Bragg equation (Equation 2.36). This section describes the fabrication steps implemented to create a waveguide suitable for proof of principle of the technique, and the characterisation steps employed in order to obtain the appropriate data for analysis.

6.3.1 Waveguide fabrication

The basic fabrication of the DGW channel waveguides with integrated Bragg gratings follows the steps described in Chapter 3. In the following case, a 20 mm by 10 mm section of silica-on-silicon wafer (W5, see Appendix C) was hydrogen loaded to enhance photosensitivity. The waveguide was inscribed into the core of the chip via the AOM direct grating writing method (Section 3.3.2), to include sixteen 1 mm long Bragg gratings, spectrally separated by around 25 nm, along the length of the 20 mm waveguide. A schematic of the device is shown (Figure 6.2).

The gratings were physically separated by 250 μm of waveguide, and fabricated ensuring the waveguide was single-mode at 1550 nm. This was achieved via FHD core thickness design (Section 3.1.2.2), and by controlling the fluence of writing as described in Section 4.3. The gratings were Gaussian apodised (Section 4.4) to reduce the uncertainty associated with the fit of the central wavelength of the grating.

The new dispersion measurement method relies on attributes of the fabrication method previously described in this thesis. The wide detuning range of the DGW system (Section 4.1) allows gratings to be fabricated over the entire 1250-1625 nm range observed in one fabrication step, with the gratings at the periphery of the range maintaining enough reflectivity to obtain central wavelength values with small errors. Additionally, the Bragg gratings produce reflectivity spectra which are narrow. This is desirable as wide bandwidth gratings would increase the error associated with the measured central wavelength. Thirdly, the fluence matching technique is employed to ensure consistency of guidance behaviour of waveguide and Bragg grating regions at wavelengths outside the Bragg spectral regions (Section 4.3). This technique ensures the same average energy density of focussed UV radiation is present at the core of the sample at all points during waveguide and grating fabrication.

Significant design effort and consideration of these important points during fabrication leads to a waveguide suitable for demonstration of the new dispersion measurement technique. So long as these restrictions are adhered to, a waveguide such as this could be fabricated on a vast range of substrates to measure the dispersion of the specific device. The following section describes the characterisation of such a device in order to achieve the data required to demonstrate this dispersion measurement.

6.3.2 Waveguide characterisation

The device illustrated in Figure 6.2 was characterised following the basic procedure outlined in Chapter 3. The 1550 nm characterisation set up was implemented (Figure 6.3), using a broadband multi-SLED source in order to obtain the reflected spectrum of all Bragg gratings in one measurement step. The background spectrum of the multi-SLED source is plotted in red in Figure 6.4, alongside the raw data obtained in the TE polarisation state. The noise apparent in the source spectrum around 1400 nm corresponds to OH absorption in this spectral region. This accounts for the dip in reflected power of the Bragg gratings observed in this spectral region in the normalised data plot (Figure 6.5).

The broadband source was polarised, allowing scope to obtain the polarisation-dependent dispersion of the waveguide. Over the broad bandwidth of the Amonics combined multi-SLED source, maintaining polarisation is not trivial. The combination of fibrised polarisation controller prior to the 3 dB coupler, and fibre in-line polariser after (see Figure

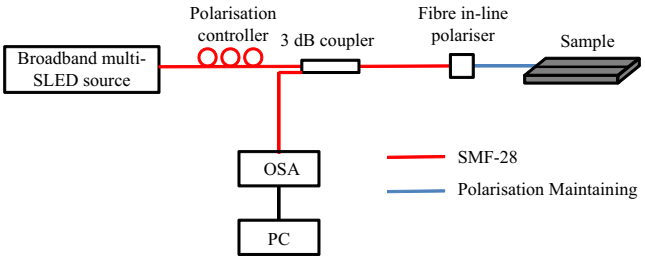

Figure 6.3: Characterisation set-up for gratings in the telecommunications band. The diagram shows the optical system components, and defines the fibre type (single mode, polarisation maintaining) used.

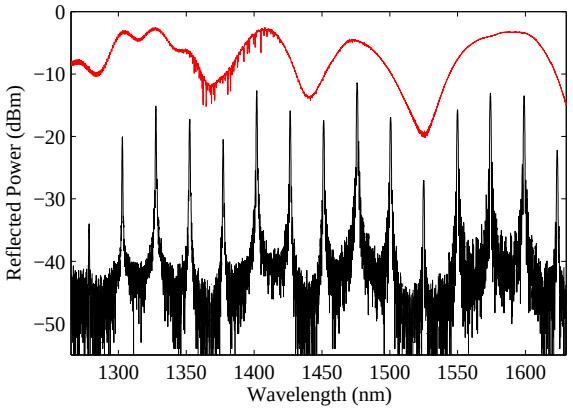

Figure 6.4: Data collected during characterisation of the waveguide. Red line is the background spectrum of the source. Black line shows the reflected spectrum of the Bragg gratings.

6.3), enable the reflected spectrum in a given polarisation state to be maximised across the entire wavelength band. Use of a polarisation maintaining (PM) pigtail to couple radiation into the waveguide enables a known polarisation state to be incident on the Bragg gratings.

A 3 dB coupler was chosen to enable collection of the back reflected data where a circulator would traditionally be used. This decision was made considering the operational bandwidth and the polarisation dependence of the circulator. For wavelengths far from the central operation wavelength of the circulator, the polarisation state is not maintained throughout the component, which can lead to spectral effects which mask the true behaviour of the device. A similar effect is observed in the case of the 3 dB coupler, but to a lesser extent over the experimental bandwidth considered here.

In order to maintain polarisation of the reflected signal, all fibres between the waveguide and the OSA are secured to the optical bench to ensure no fibre movement can occur. Movement of the fibre could cause a change in the polarisation state of the radiation within the fibre, resulting in spectral effects in the collected data. Ensuring the fibres are secured to the bench is the best attempt at maintaining the polarisation of the reflected signal available during these experiments. Purchase of polarisation maintaining

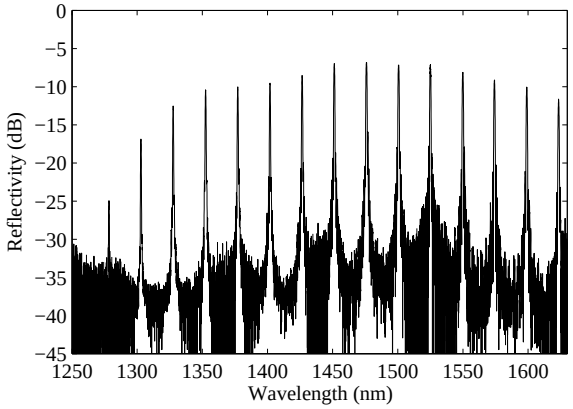

Figure 6.5: Reflected TE spectrum normalised to input power, of waveguide illustrated in Figure 6.2. The figure shows the wide detuning range of the direct grating writing system with spectral range of over 300 nm.

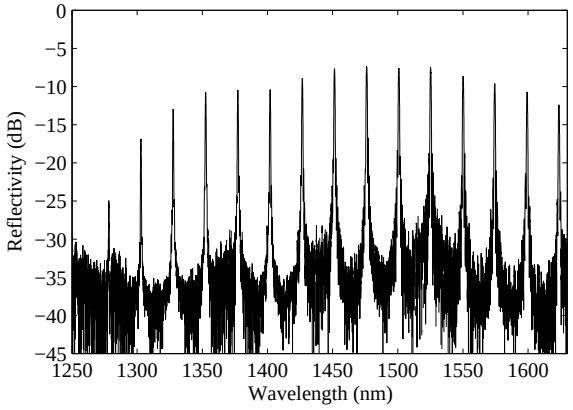

Figure 6.6: Reflected TM spectrum normalised to input power, of waveguide illustrated in Figure 6.2.

optical components such as circulators and 3 dB couplers would eliminate polarisation considerations from this set up.

Collected data (black line in Figure 6.4) was normalised against the background spectrum of the source (red) in order to observe the relative reflected power of the gratings. The normalised reflected spectrum obtained in the TE polarisation state can be observed in Figure 6.5. The TM data was also obtained in order to investigate the birefringence of the guide, and the normalised spectrum is shown in Figure 6.6.

The reflected spectrum was analysed using a Gaussian fitting algorithm in LabVIEW in order to obtain the central wavelength of each grating. Using this data alongside the Bragg equation (Equation 2.36), and given prior knowledge of the period of the fabricated grating, the effective refractive index of the waveguide at each central wavelength was obtained. This data is shown in Figure 6.7. The plot also shows the Sellmeier equation fitted to these data points, with the coefficients presented in Table 6.1. In this exercise, the Sellmeier curve was used as a fitting tool in order to calculate the shape of the

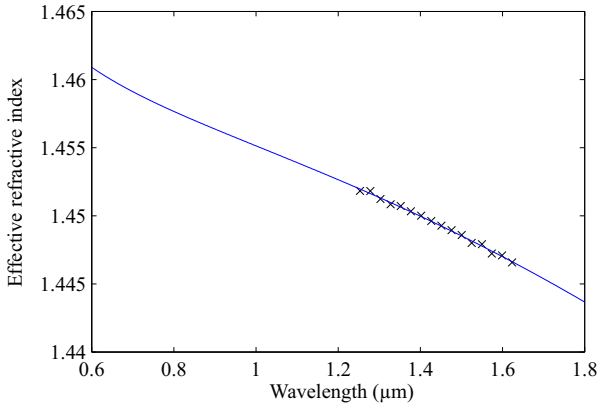

Figure 6.7: Collected effective index data (crosses), and fitted Sellmeier curve (line) for the data points collected using the 1550 nm characterisation set up in the TE polarisation state.

measured data, as this curve is the total measured dispersion of the waveguide, not the independent material dispersion the Sellmeier relation was designed for. The three oscillator style of the fit does however allow the shape of the total dispersion curve to be obtained.

The fit was calculated using the non-linear least squares fit method, with absorption oscillators located in the UV and mid infrared. The starting values of the Sellmeier coefficients, corresponding to the wavelength and strength of the oscillators, were obtained from the literature [93], where values for a heavily germanium and boron doped silica fibre are given. The fit was performed over a number of iterations, until the minimum deviation of the data points from the fitted curve was obtained. In the region with data points, the fit is good, with the standard deviation of points from fit $\pm 6 \times 10^{-5}$. However, with no data points available to ensure the quality of the fit beyond the point of inflection at the expected zero dispersion wavelength, the fit cannot be relied upon at this lower wavelength end of the spectrum.

The zero dispersion wavelength (ZDW) of a waveguide is the wavelength at which the second order dispersion of the waveguide becomes zero. Physically, this implies there is negligible dispersion at that wavelength, as the material and waveguide dispersion cancel each other out. The ZDW is important in telecommunications systems, with fibres designed so the ZDW coincides with the region of lowest loss of the material, creating a more efficient fibre for data transmission. In terms of zero-order dispersion, the ZDW appears at the point of inflection of the fitted Sellmeier curve, typically around 1300 nm for traditional silica-based waveguides.

The ZDW calculated from this fit was 1010.0 ± 0.3 nm. This is much lower than expected for a typical doped silica waveguide [93], and thus causes the fit quality at lower wavelengths to be questioned. In order to more precisely determine the behaviour of the refractive index dispersion at lower wavelengths, data points are required at the

Sellmeier coeff.	Value
a_1	0.002021561
a_2	0.006167374
a_3	97.92832809
b_1	0.541610002
b_2	0.584009155
b_3	1.256368263

Table 6.1: Sellmeier coefficients for the fitted curve in Figure 6.7, in the TE polarisation state.

lower end of the spectrum of interest. In order to achieve this whilst using the same waveguide, measurement of the waveguide was made using the 780 nm characterisation source described in Section 3.4.2. This allows the second order reflection from the Bragg gratings to be obtained.

The 780 nm characterisation set up used a frequency doubled 1550 nm femtosecond fibre laser as the source, with periodically poled $LiNbO_3$ (PPLN) as the doubling medium. Choice of PPLN parameters such as period, temperature and physical dimensions lead to controllable spectral source characteristics, including central wavelength and bandwidth. In addition, careful control of the fibre laser is required to achieve modelocking, ensuring the stability of the source over the duration of the measurement. The PPLN samples available to use during this project led to limitations in source bandwidth in the shorter wavelength region; only the 1550 nm and 1575 nm gratings were measured in this regime. The measurements were taken using an OSA, and the LabVIEW Gaussian fitting algorithm applied to obtain Bragg grating spectral parameters. The additional effective refractive index data points obtained were added to those obtained previously, and the Sellmeier fit recalculated. The Sellmeier fitting procedure had the same starting conditions obtained from the literature [93], and proceeded in the same manner to obtain the least deviation of data points from the fitted curve. The recalculated curve can be seen in Figure 6.8. The ZDW obtained from the fit is 1240.0 ± 0.3 nm, much closer to the expected value for silica-based waveguides.

The additional data points allow the Sellmeier fit to be more precise at the lower wavelength end of the spectrum. The error of the fit is calculated by taking the standard deviation of the data points away from the fitted Sellmeier curve. This can be seen in the inset of Figure 6.8. This error takes into account the experimental and analytical errors associated with the fabrication and characterisation, including the accuracy of grating period fabrication and spectra fitting errors. The standard deviation method calculates the worst case error in the Sellmeier fit, and applies it over the entire spectral range by changing the strength of the absorption oscillators in the fitted Sellmeier. The maximum deviation from the fit is shown in Figure 6.8.

The fabrication and characterisation steps of the dispersion measurement technique verification process are similar to those employed in the development of any waveguide

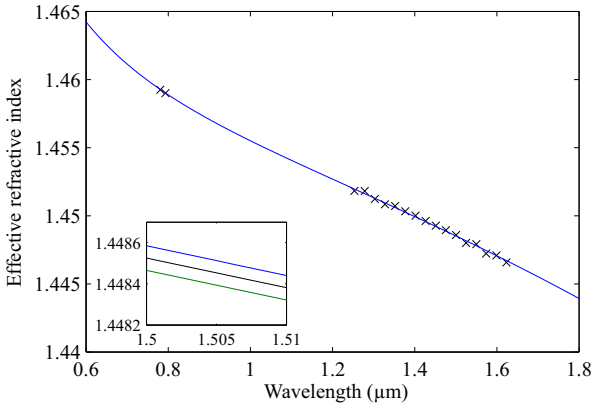

Figure 6.8: Collected effective refractive index data (crosses), and fitted Sellmeier curve (line) for the data points including second order grating reflections at 780 nm in the TE polarisation state. Inset shows calculated SD errors (blue, green) associated with the fit. Sellmeier coefficients are given in Table 6.2.

Sellmeier coeff.	Value
a_1	0.007498
a_2	0.011035
a_3	97.930
b_1	0.71813
b_2	0.401985
b_3	1.11155

Table 6.2: Sellmeier coefficients for the fitted curve in Figure 6.8, including 780 nm data points in the TE polarisation state.

and Bragg grating device using the DGW technique. It is, therefore, relatively simple to include a waveguide for measuring the dispersion of the device alongside a waveguide used for another purpose, to ensure the best possible prediction of the dispersion characteristics of the device. The total dispersion information obtained can also be used to calculate the waveguide and material dispersion components, in order to better understand the contributions of each to the overall dispersion of the guide.

6.4 Material and waveguide dispersion contributions

Knowledge of the total dispersion of the waveguide, measured as described above, can be used to design waveguides and gratings for specific purposes in a given material. However, for material design, knowing the individual contributions of material and waveguide dispersion can be useful in order to predict the dispersive response of the fabricated waveguide. This section describes the empirical calculation of the waveguide and material dispersion from the measured total dispersion of the guide.

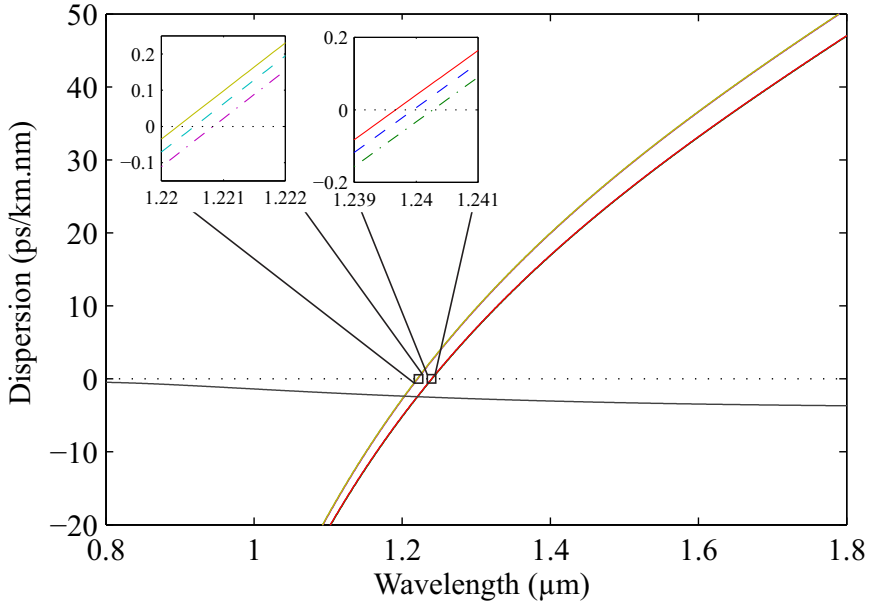

Figure 6.9: Measured total dispersion and calculated waveguide and material dispersions with fit errors in the TE case. The measured total dispersion is shown in blue (dashed line) in the main diagram and the right-most inset, with calculated fit errors in red (solid line) and green (dot-dashed line). The calculated waveguide dispersion is shown in black. The calculated material dispersion, taking into account the calculated waveguide dispersion, is shown in cyan (dashed line) in the left-most inset, with errors in yellow (solid line) and magenta (dot-dashed).

In order to calculate the total dispersion of the waveguide, the following relation was used [94].

$$D = \frac{-1}{\lambda_0 c}\left(\lambda_0^2 \frac{d^2 n}{d\lambda_0^2}\right) \times 10^9 ps/km.nm \tag{6.12}$$

This relation assumes a step index fibre allowing only single mode propagation, with negligible wavelength-dependent contribution from waveguide dispersion. By differentiating the Sellmeier equation twice, the $\frac{d^2n}{d\lambda^2}$ term can be calculated. This plot of the total measured dispersion can be seen in Figure 6.9. The errors on this plot are carried through the calculation from the errors previously described (Figure 6.8).

In order to calculate the waveguide dispersion component, the method described above is implemented (Section 6.1.2). The $\frac{Vd^2(bV)}{dV^2}$ component is calculated via the V number of the waveguide over the entire wavelength range (Equations 6.10, 6.13) for constant n_1 and n_2 measured at 1550 nm. This is used alongside Equation 6.8 to calculate the waveguide dispersion component of this guide. This is plotted in black in Figure 6.9.

Given the additive assumption described previously (Section 6.1.3), the material dispersion can then be calculated. This is shown in cyan in Figure 6.9, with yellow/magenta

displaying the calculated errors. The plot shows the small contribution of waveguide dispersion to the total measured dispersion of the waveguide, as expected for this weakly guiding device [96].

The ZDW of the waveguide can be observed on the plot where the dispersion curve crosses the wavelength axis. The ZDW for the TE polarisation state is 1240.0 ± 0.3 nm. If the material dispersion alone is considered, the ZDW is shifted by 19.5 nm to 1220.5 nm. This shows the effect that waveguide dispersion can have on the ZDW of the waveguide, as is applied in various dispersion-shifted fibre cases [102]. The data for the TM case was also measured and has ZDW 1234.0 ± 0.3 nm. In comparison to material dispersion data for bulk doped fused silica, these values are somewhat low. For germanium doped bulk silica, the material ZDW is 1309 nm, and for a boron doped glass, 1264 nm [94]. The germanium and boron co-doping of this waveguide, along with the weak index contrast of the UV written waveguide most likely cause the relatively low ZDWs observed here.

The technique described above demonstrates the ability to use integrated Bragg grating structures to measure the total dispersion of a waveguide. The theory allows calculation of the waveguide dispersion component of the total dispersion, leading, via the additive assumption, to calculation of the material dispersion of the waveguide. In addition, the ZDW and the effect of waveguide dispersion in this case have been observed. The small uncertainty in the measurement technique has been validated with data obtained via dispersion modelling and experimentally observing spontaneous four-wave mixing in a birefringent waveguide. A description of this work and the results are given in Section 6.7.

This new technique can be used to measure the polarisation dependence of the total dispersion of the waveguide, by altering the polarisation state of the characterisation source. This enables use in situations where polarisation is critical, for example in the production of parametric pairs in birefringent waveguides discussed later in this chapter. In addition, this technique could be used in other photosensitive materials, such as flat fibre or chalcogenide glasses. A further extension of this work is the application to multimode waveguides, as described in the following sections.

6.5 Fluence dependence of dispersion

The fluence at which a waveguide is UV written is critical when considering the dispersion characteristics of the waveguide. A change in the fluence manifests itself in two ways on the total measured dispersion of the waveguide. Firstly, the change in incident power on the photosensitive core layer changes the material dispersion of the core waveguide, as the magnitude of the photosensitivity-induced refractive index change in the core is intensity dependent. Secondly, the change in fluence will change the intensity

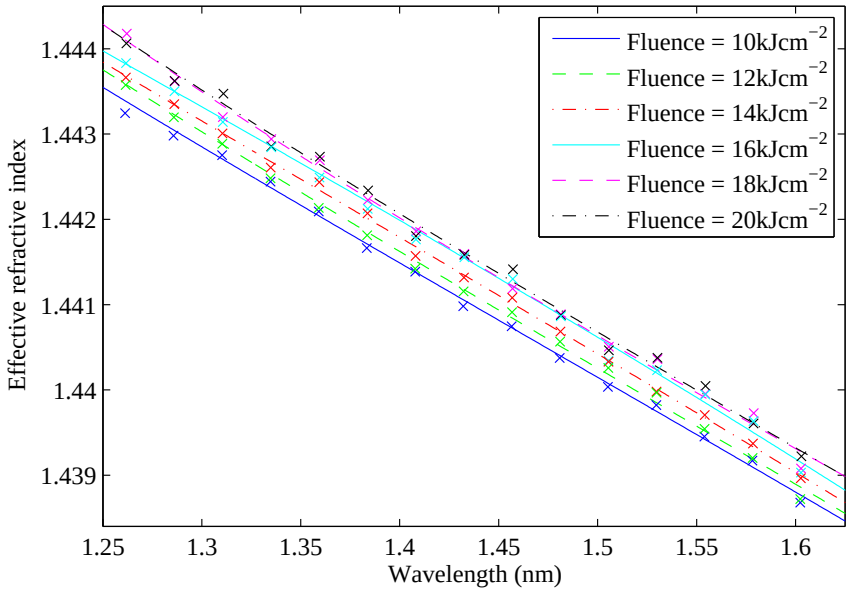

Figure 6.10: Effective refractive index data and fitted Sellmeier curves for waveguides with varying fluence. The higher fluence waveguides (above 16 kJcm^{-2}), exhibit multimode behaviour and the fitting errors increase, resulting in overlapping of calculated Sellmeier curves.

distribution in the incoming beam, affecting the physical profile of the core layer and thus the waveguide dispersion.

A set of UV written waveguides and integrated Bragg gratings with different fluence characteristics were fabricated in one silica-on-silicon chip, to demonstrate a direct comparison of the fluence contribution to the measured total dispersion of the waveguide. Waveguides with fluence values between 10 kJcm^{-2} and 20 kJcm^{-2} were fabricated, and characterised following the method outlined above. Sellmeier coefficients were obtained by following the fitting regime, with the same oscillator starting conditions each time, and the resultant effective index data points and Sellmeier curves for the six waveguides are shown in Figure 6.10.

As the waveguide fluence increases, the effective index of the waveguide also increases over the entire band, as expected. In the case of these waveguides, the increase in fluence above 16 kJcm^{-2} causes the Bragg grating reflection to transition from the weak to the strong regime (Section 2.2.1). The resultant shift in the calculated Sellmeier curve from a step increase over the entire band at lower fluence, toward a common dispersion curve at higher fluence is evidence of the strong Bragg grating response and the associated central wavelength fitting issues encountered. This data demonstrates the ability to tailor the dispersion characteristics of a waveguide by adjusting the fluence used during the UV writing process.

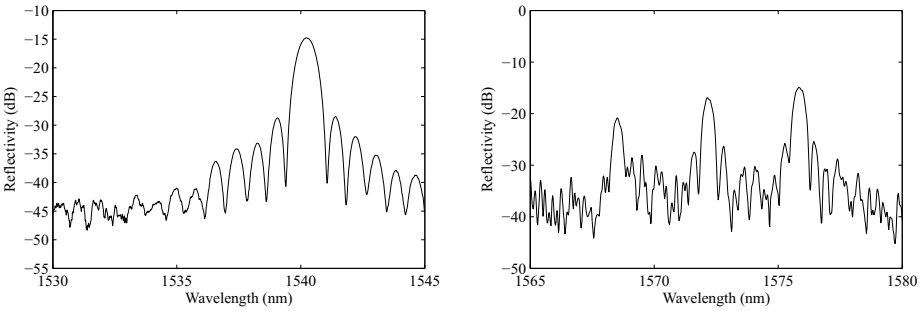

Figure 6.11: Spectral response of a Bragg grating in a single mode waveguide (left) and a multimode waveguide (right).

6.6 Multimode dispersion measurement technique

Multimode waveguides are of interest in applications such as dispersion compensation and telecommunications applications due to the large effective mode diameters and potential efficient launch into multiple modes of the guide at once. Measurement of the dispersion characteristics of higher order modes is difficult, due to the need to launch into each mode individually to use conventional techniques such as time of flight and modulation phase shift methods. Various interferometric techniques have been proposed in the case of fibres, including the use of an OSA to measure inter-modal interference over metre lengths [103]. However, these methods are not suited to short waveguides, due to the small amount of dispersion observed over centimetre lengths.

The nature of the dispersion measurement technique described above intrinsically allows the measurement of higher order modes supported by the waveguide, as optimising the launch conditions enables coupling between different modes of the guide to be observed in the Bragg grating spectra. A comparison between the reflected spectra of a Bragg grating in a single and a multi-mode waveguide can be seen in Figure 6.11. Measurement of the Bragg grating spectra in one simple step, as described above, enables information about the coupling between the forward and backward counter-propagating modes to be gleaned and interpreted via modelling of the expected effective indices of the different modes. This section describes the steps taken to obtain this information and the techniques employed to obtain the dispersive refractive index data of the higher order modes of a guide.

Higher order modes in a waveguide are introduced when the waveguide has the dimensions and index contrast required for the modes to be guided. The presence of higher order modes can be determined by calculating the V number of the waveguide. The dimensionless waveguide parameter, V, is described by

$$V = k_0 d \left(n_1^2 - n_2^2\right)^{\frac{1}{2}} \tag{6.13}$$

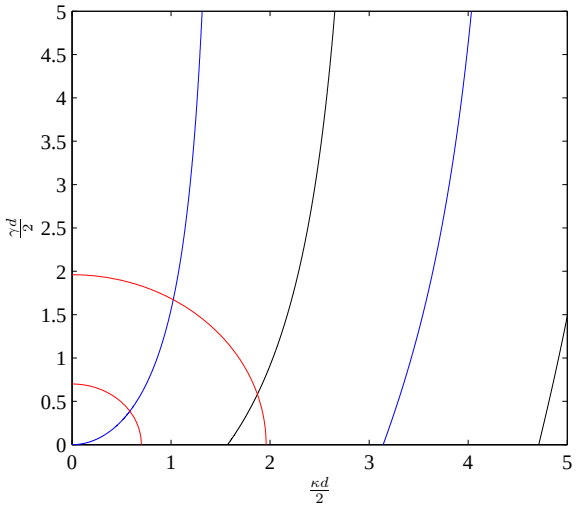

Figure 6.12: Graphical solution for the guided modes of a slab waveguide. The V number radii are calculated from the experimental determination of V number given effective index and thickness data of the fabricated FHD slab. The inner circle represents a single mode waveguide ($V = 1.40$), the outer a multimode guide ($V = 3.92$). The symmetric and asymmetric modes supported (blue and black respectively) intersect the circle representing the multimode guide.

k_0 depends on the wavelength λ_0, via $k_0 = \frac{2\pi}{\lambda}$. d is the dimension of the waveguide in the horizontal or vertical direction depending on which modes are of interest. n_1 and n_2 are the refractive index of the core and cladding respectively, at wavelength λ of interest. The larger the V number, the more modes the waveguide supports.

In a practical sense, higher order modes can be introduced by two fabrication processes. The fabrication of the FHD layer can be modified to increase the V number, by increasing the thickness of the photosensitive core layer, and also by increasing the refractive index of this layer. In this case, wafer W4 was used (Appendix C), which has a similar core thickness to the W5 sample used in the previous section, but a much larger core to cladding refractive index difference, 0.7 $\%\delta$ compared with 0.09 $\%\delta$ for the W5 sample at 1550 nm. This difference increases the $\left(n_1^2 - n_2^2\right)^{\frac{1}{2}}$ component of Equation 6.13, thus increasing V. The second method of introducing higher order modes is to increase the fluence during the UV writing process. By increasing the energy density of writing in this way, the photosensitive response of the material moves toward saturation, thus further increasing the refractive index difference between the core and cladding.

The Metricon prism coupling technique described in Section 3.1.2.5 was used to obtain data to calculate the $\left(n_1^2 - n_2^2\right)^{\frac{1}{2}}$ part of the V number equation at 1550 nm. The quarter circles with radius $\frac{V}{2}$ indicate the modes present for each of these waveguides at this wavelength. Although not a true representation of the UV written waveguide, the small additional refractive index change induced by UV writing will contribute a negligible amount to the $\left(n_1^2 - n_2^2\right)^{\frac{1}{2}}$ part of the calculation, and so was neglected in this case. As can be seen in Figure 6.12, the waveguide fabricated with the intention of

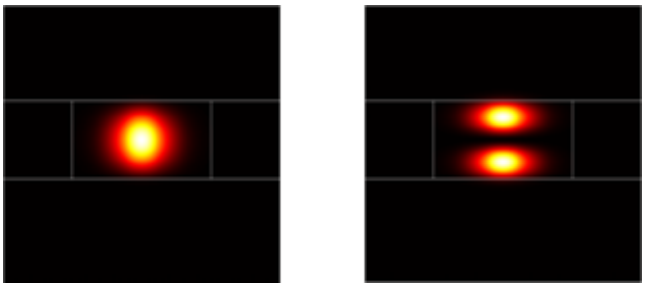

Figure 6.13: Images produced using FIMMWAVE modelling, to investigate the modes present in the multimode waveguide. The zero (left) and first (right) order TM modes are shown.

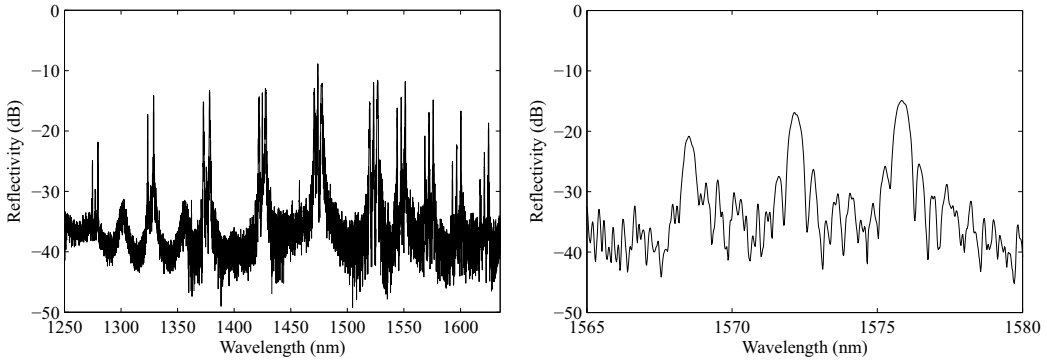

Figure 6.14: Normalised reflected spectrum from multimode waveguide in the TM case (left). Each set of three reflected peaks are the different reflected modes of the same grating (right).

being multimode shows evidence of the first asymmetric mode in addition to the first symmetric mode. From here on, the first symmetric mode will be referred to as the 'zero-order' mode and the first asymmetric mode as the 'first-order' mode [29].

Additional modelling using Fimmwave for the case of the step-index waveguide corroborates this data. Figure 6.13 shows the mode profiles for the first symmetric and antisymmetric modes, for the parameters described above, with effective refractive indices of 1.4562 and 1.4494 respectively at 1550 nm.

The experimental process to measure higher order modes is similar to that described above. The example waveguide fabricated for this experiment contained ten 1.5 mm long Bragg gratings, with central wavelengths between 1275 and 1625 nm. The core refractive index was higher than used for the devices in Section 6.3.1, and the fluence of UV writing was increased in comparison to that of the single mode waveguide in order to increase the multi-mode nature of the guide. The collected spectra from the 1550 nm characterisation set up in the TM polarisation state can be observed in Figure 6.14.

The leftmost plot shows the ten reflected grating spectra, each with three individual peaks as a consequence of coupling between the different order modes. The image on the right shows the three reflected peaks from one grating. The rightmost peak is caused by

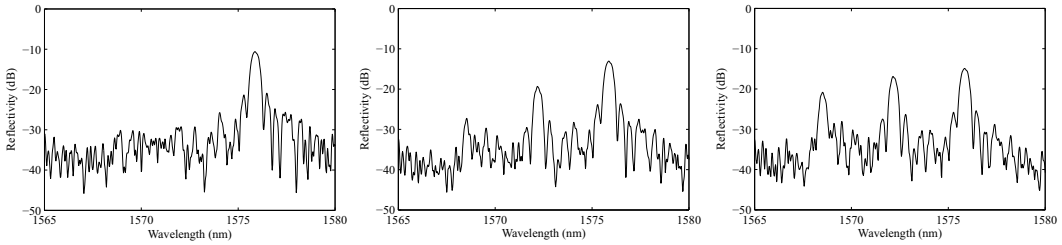

Figure 6.15: Normalised reflected spectra from multimode waveguide in the TM case, with changing vertical coupling conditions. The left-most plot shows a coupling condition where the zero-order launch mode couples predominantly into the zero-order counter-propagating mode. The right-most plot shows a coupling condition where the first-order launch mode couples predominantly into the first-order counter-propagating mode. The centre plot is the spectral response at a vertical launch position between the two.

the zero-order launched mode coupling to its counter-propagating equivalent. Similarly, the leftmost peak is cause by the first-order launched mode coupling to its counter-propagating equivalent. The central mode is located exactly halfway spectrally between the zero- and first-order modes, so is interpreted as the combination of coupling the first and zero-order launched modes into the zero- and first-order counter-propagating modes respectively. Data was also obtained at 780 nm (see Section 3.4.2).

The coupling conditions are critical when considering the multimode waveguide. As is the case for all waveguides, monitoring the reflected grating strength whilst adjusting the coupling conditions between the fibre input and the waveguide allows optimal coupling between the forward and the counter propagating zero-order modes to be achieved. In the case of the multimode waveguide, changing the launch position in the vertical direction enables preferential coupling between the first-order launched mode and the first-order counter-propagating mode. Figure 6.15 shows the spectral changes observed when launch conditions are changed from a position where the zero-order launch mode couples predominantly into the zero-order counter-propagating mode (left), to a position where the first-order launch mode couples predominantly into the first-order counter-propagating mode (right).

The fitted Sellmeier curves and data points, alongside the Sellmeier coefficients, are shown in Figure 6.16 and Table 6.3. The total dispersion curve for the zero-order mode is shown uppermost, with the curve for the first-order mode lowermost. The plot shows the distinct shift in the dispersion curve for the higher order modes of the waveguide, caused by the change in the waveguide dispersion component of the total dispersion.

In summary, the ability to determine the dispersion of individual higher order modes in a waveguide has been demonstrated using the grating based dispersion measurement technique. Using the same gratings, and one measurement step, the reflected spectra from the different order modes of the gratings are obtained. The Sellmeier curves are fitted given the identification of each of these modes of the grating. The technique has

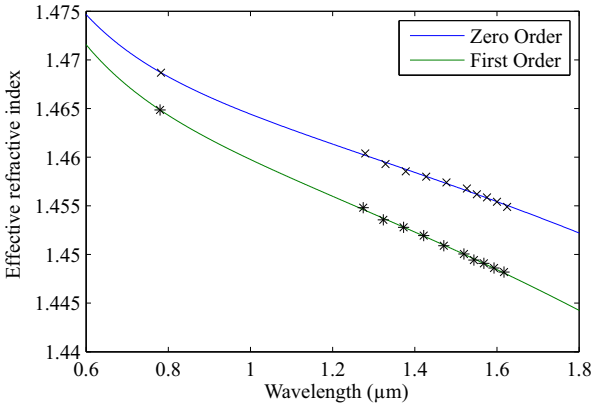

Figure 6.16: Fitted Sellmeier curves for zero- and first-order modes in the multimode guide. The upper curve is the zero-order mode, with measured data points (crosses) and the lower represents the first-order mode, with data (stars). Sellmeier coefficients are detailed in Table 6.3.

Zero order TM		First order TM	
Sellmeier coeff.	Value	Sellmeier coeff.	Value
a_1	0.006533177	a_1	0.013566323
a_2	0.01655877	a_2	0.008617706
a_3	97.92977974	a_3	97.92544581
b_1	0.683248388	b_1	0.70859326
b_2	0.460740445	b_2	0.424292567
b_3	1.134328713	b_3	1.493686971

Table 6.3: Sellmeier coefficients for fitted zero- and first-order mode dispersion curves in Figure 6.16.

practical use in any multimode waveguide which can support Bragg gratings, where knowledge of the dispersion of the individual propagating modes of the guide is important, for example in telecommunications networks.

6.7 Parametric pair production in waveguides

In order to further demonstrate the practical applications of the multi-grating dispersion measurement technique, progress has been made towards using it as a tool in the design of a waveguide suitable for non-linear interactions. In particular, the case of parametric pair production in birefringent waveguides has been investigated in collaboration with the Quantum Technologies Laboratory at the University of Oxford. The work is based on a previous publication by the Oxford group [104], in which photon pair generation via spontaneous four-wave mixing in birefringent optical fibres was demonstrated.

Spontaneous four-wave mixing (SFWM) occurs due to a third order non-linearity within an optical material. The $\chi^{(3)}$ non-linearity causes two photons from pump pulses to be

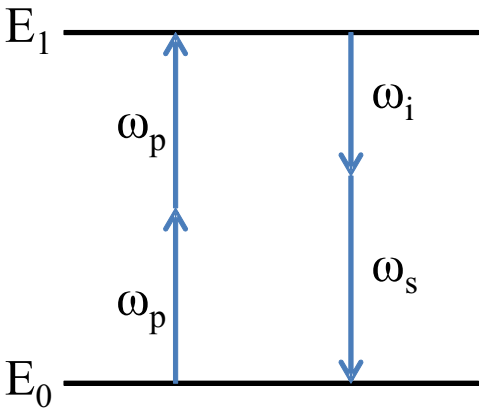

Figure 6.17: Energy conservation in four-wave mixing. Two pump photons, ω_p, are converted into a signal, ω_s, and an idler, ω_i, photon.

converted into a pair of daughter photons, the signal and the idler, due to a refractive index modulation at their frequencies. The effect occurs only when energy is conserved and phase-matching can be achieved, which dictates the allowed frequencies of the daughter photons. Figure 6.17 shows energy conservation in a four-wave mixing scenario, where two pump photons, ω_p, are converted into a signal, ω_s, and an idler, ω_i, photon. Phase-matching is achieved in a fibre or waveguide when the chromatic dispersion profile has a suitable shape.

The production of the signal and idler photons via SFWM in this case is due to the phase-matching caused by the birefringence in an asymmetric waveguide [105]. The polarisation of the generated signal and idler photons is perpendicular to the polarisation of the pump, and the spectral separation is controlled by varying the birefringence of the waveguide. Knowledge of both the dispersive behaviour of the waveguide and the birefringence is necessary in order to predict where the signal and idler photons will occur spectrally. This information can be readily gleaned via the dispersion measurement technique described above.

The dispersion measurement technique was carried out on a waveguide UV-written on the same chip as the waveguide used to host SFWM. As described in Section 6.3.1, sixteen Bragg gratings were inscribed in the waveguide, a 40 mm long device fabricated in the W10 wafer (Appendix C) and characterised to obtain the effective index information at specific wavelengths, including those at 780 nm. The Sellmeier curve in both the TE and TM polarisation states was obtained, and can be observed in Figure 6.18, alongside Sellmeier coefficients in Table 6.4.

The plot shows the TM polarisation state is oriented along the slow axis (uppermost curve) and the TE along the fast axis (lowermost). In order to observe phase-matching in the normal dispersion regime around 700 nm, the pump must be polarised along the slow axis, or in the TM state [105].

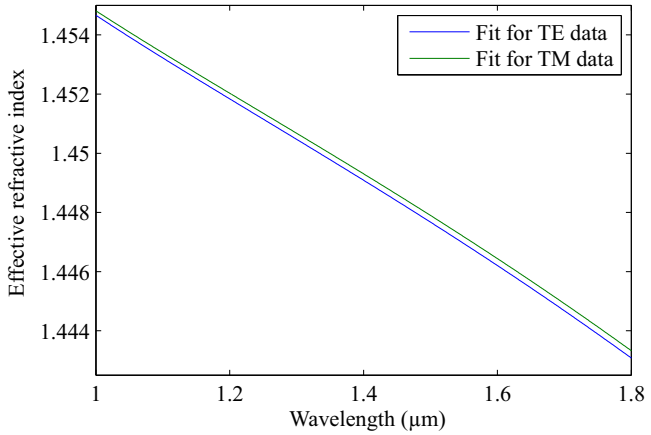

Figure 6.18: Fitted Sellmeier curves for TM and TE polarisation states in the single mode waveguide used in the parametric pair production experiment. The upper curve is the TM data, which is the slow axis of the guide, and the lower represents the TE polarisation state. Sellmeier coefficients are detailed in Table 6.4.

TM (slow axis)		TE (fast axis)	
Sellmeier coeff.	Value	Sellmeier coeff.	Value
a_1	0.006698	a_1	0.007111
a_2	0.011835	a_2	0.012034
a_3	97.93006	a_3	97.93005
b_1	0.7117077	b_1	0.711489
b_2	0.406588	b_2	0.406006
b_3	1.112472	b_3	1.113247

Table 6.4: Sellmeier coefficients for fitted TM and TE polarisation dispersion curves in Figure 6.18.

6.7.1 Birefringence of waveguides

The birefringence of the waveguide can also be calculated from the collected effective refractive index data. The effective index values for the TE and TM states of each grating are subtracted from one another in order to obtain the birefringence of the guide at the central wavelength of the Bragg grating.

By fabricating and characterising an array of similar Bragg gratings and waveguides on a single chip, an idea of the variation in birefringence across a silica-on-silicon chip can be obtained. Ten waveguides containing fourteen Bragg gratings with central wavelengths between 1250 nm and 1575 nm were fabricated, with waveguides spaced 1 mm apart on a chip (Bragg grating arrangement is similar to that in Figure 6.2). Characterisation and data manipulation yielded a birefringence value for each Bragg grating, which can then be plotted against the position of the Bragg grating within the chip, as shown in Figure 6.19. A histogram of the same data is shown in Figure 6.20. The calculated birefringence for the chip shown was $2.04 \pm 0.11 \times 10^{-4}$.

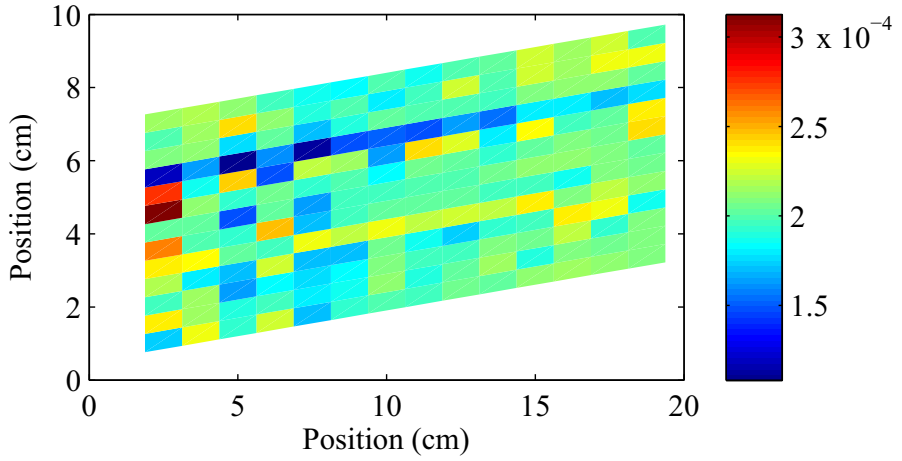

Figure 6.19: Birefringence map of a 20 × 10 mm silica-on-silicon chip. Each Bragg grating central position is at the centre of a colour block. The mean birefringence of this chip was 2.04±0.11 × 10^{-4}.

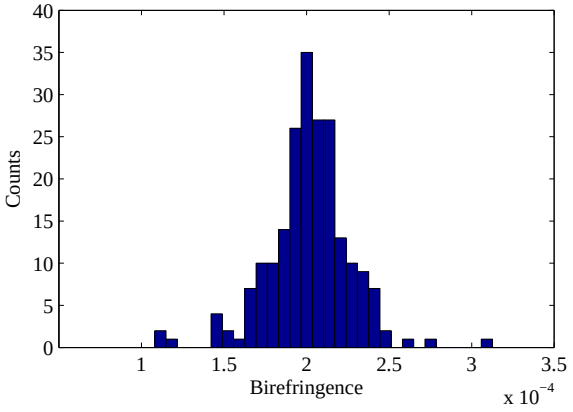

Figure 6.20: Distribution of measured birefringence values.

In the parametric pair production chip, the pump source used for parametric pair production is tunable around 700 nm, so the birefringence is obtained from the visible end of the spectrum. For the waveguide used during the experiment described in the following section, the birefringence was 2.2 × 10^{-4}.

6.7.2 Experimental procedure

The Sellmeier dispersion profile and measured birefringence are used to predict the spectral position of the signal and idler photons as the pump wavelength is changed. The wave-vector mismatch for the cross-polarised birefringent waveguide SFWM case is shown in Equation 6.14 [105].

$$\Delta k = 2\frac{\omega_p}{c}n\left(\omega_p\right) - \frac{\omega_s}{c}n\left(\omega_s\right) - \frac{\omega_i}{c}n\left(\omega_i\right) + 2\Delta n\frac{\omega_p}{c} + \frac{2}{3}\gamma P \tag{6.14}$$

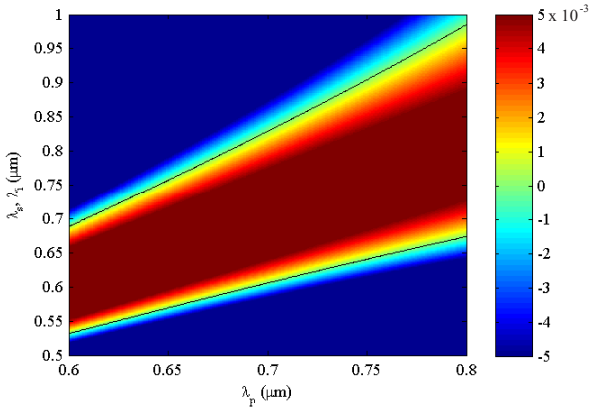

Figure 6.21: Contour plot of the solutions of the wave-vector equation for the phase-matched, energy conserved case. The uppermost black line, along the $\Delta k = 0$ contour, represents the idler photon for a given pump wavelength. The lowermost black line represents the signal photon.

Δk is the wave-vector mismatch, and is equal to zero for the phase-matched case. ω_p, ω_s and ω_i are the pump, signal and idler photon frequencies respectively. $n(\omega_p)$, $n(\omega_s)$ and $n(\omega_i)$ are the refractive indices at the pump, signal and idler frequencies respectively, determined by the fitted Sellmeier for the respective polarisation axes. c is the speed of light in a vacuum, and Δn is the birefringence of the waveguide. The final factor, $\frac{2}{3}\gamma P$, is the calculated self- and cross-phase modulation terms, also an effect of the $\chi^{(3)}$ non-linearity of the material. γ is the non-linear parameter of the fibre, and P is the pump peak power. Far from the zero dispersion wavelength, where material dispersion dominates the total dispersion of the waveguide and cross-polarised phase-matching, it can be assumed that the self- and cross-phase modulation terms are negligible.

To predict the spectral position of the signal and idler photons, the relation above (6.14) can be solved for the phase-matched case with energy conservation.

$$2\omega_p = \omega_s + \omega_i \tag{6.15}$$

The solution of the wave-vector relation given these constraints is shown in Figure 6.21 for a range of pump wavelengths. The script used to calculate these contours is shown in Appendix D.

The upper black line of the plot shows the birefringent phase-matching contour for the idler photon λ_i, and the lower line shows the contour for signal photon λ_s. This prediction of the signal and idler spectral positions allows the design of the appropriate experiment to measure possible photon pairs at these frequencies.

For corroboration of these predicted signal and idler photons, the collaborators at Oxford performed experiments to observe the spectral behaviour of the pumped waveguide. The experimental set up is shown in Figure 6.22.

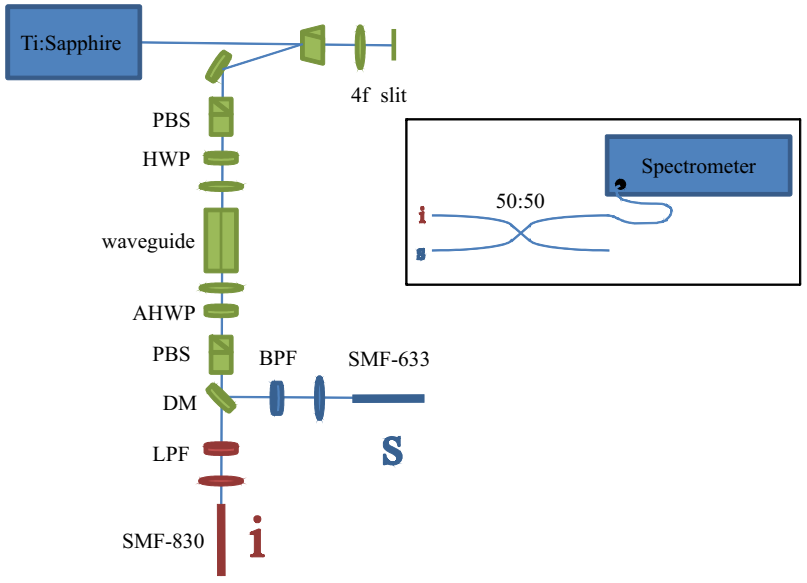

Figure 6.22: Experimental set up for generated photons observation. The output of a Ti:sapphire is spectrally filtered using a folded $4f$ prism pulse shaper, and passes through a polarising beam splitter (PBS) and half-wave plate (HWP) to control the polarisation launched into the waveguide under test. The generated signal passes through an achromatic HWP and PBS to separate the pump from the SFWM, and signal and idler are split at the dichroic mirror (DM) and filtered via band pass filter (BPF) and long pass filter (LPF), respectively. The signal and idler are coupled into fibres, and incident on a 50:50 coupler and spectrometer to obtain spectral data (inset).

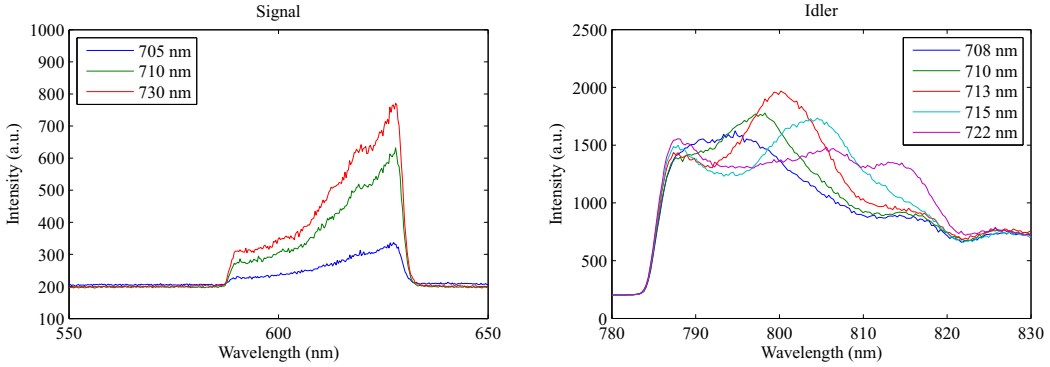

Figure 6.23: Data for the signal and idler spectral regions for the described sample, with input light polarised along the slow (TM) axis. As the pump wavelength is increased, the idler spectra changes, with the peak wavelength increasing.

The spectrally filtered output of a Ti:sapphire laser was polarised via a half wave plate and polarising beam splitter before launch into the birefringent waveguide. An achromatic half wave plate and polarising beam splitter separated the pump from the SFWM components, which were then individually coupled and launched into single mode fibre. The signal and idler components were incident on a spectrometer via a 50:50 fibre coupler in order to observe the spectral position of the photons.

The observed data for light polarised along the slow axis is seen in Figure 6.23. The data was obtained using an Andor spectrometer and camera. The step features at 630

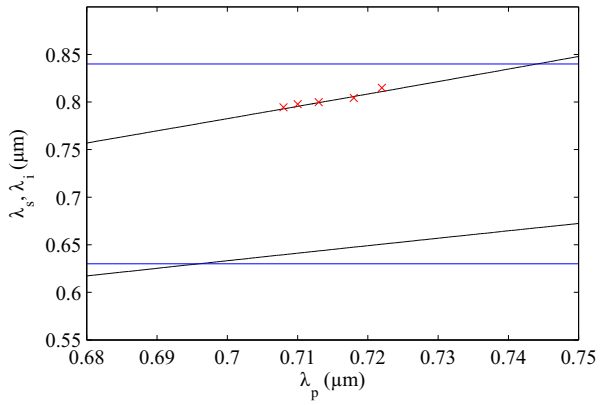

Figure 6.24: Comparison of measured idler spectral data to predicted idler wavelength modelling described above (Figure 6.18). The measured data (red crosses) agrees with the prediction (black lines, idler uppermost). The band edges of the LPF and BPF are shown (blue lines, lowermost line is the upper edge of the BPF). The expected signal data is suppressed by the BPF used to suppress the pump photons.

nm and 785 nm correspond to the edges of the long pass and band pass filters used to filter the pump out of the collected radiation. Observing the idler spectrum (right), as the pump wavelength is increased, the spectral features present around the predicted idler wavelength move toward the higher end of the spectrum. This is indicative of the SFWM process, as the non-linear interaction is dependent on the pump wavelength.

The observed wavelengths of the produced idler photons can be obtained from this collected data. The plot of the idler wavelength against pump wavelength can be observed in Figure 6.24, alongside the modelled idler data shown previously. The plot shows experimental corroboration of the predicted idler photon wavelengths for this waveguide, with standard deviation from the line $2.05 \times 10^{-3} \mu$m. For completeness, the collected data in the idler spectral region for polarisation along the fast axis is shown in Figure 6.25. The idler photon does not appear, as expected for cross polarised birefringent waveguide SFWM in the normal dispersion regime.

In the case of the signal data, the spectral change with pump wavelength is not observed. This is due to the limitations of the experimental set up. The birefringence of the waveguide is relatively small; ideally it would be around 4×10^{-4} to 6×10^{-4} in order to observe the signal and idler photons using the set of long and band pass filters available. Changing the spectral filtering bands will allow the signal photon pump response to be observed, allowing continuation of the experiment to observe single photons via counting modules, and coincidences for confirmation of photon pair generation.

An additional non-linear interaction occuring in the waveguide is the generation of Raman scatter in the wavelength region near that of the generated idler photon. The Raman contamination is due to the vibrational excitation of the material, or the presence of optical phonons. The phonons interact in a pseudo-three wave mixing process to generate Stokes and anti-Stokes photons. The Stokes frequency photons contaminate

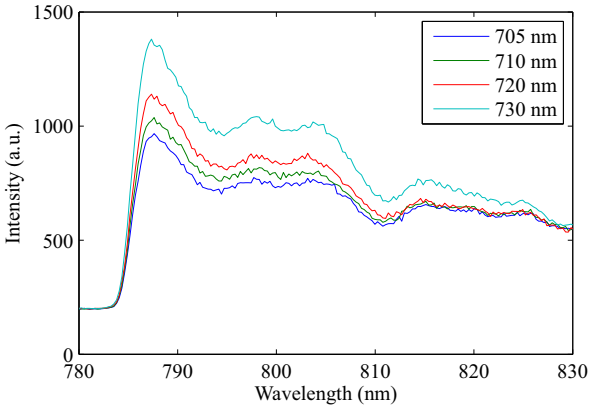

Figure 6.25: For completeness, the spectral features around the idler wavelength with the pump polarised along the fast axis. As expected, there is no spectral change with changing pump wavelength.

the idler photon spectrum, with significant Stokes production approximately 100 nm from the pump wavelength, as can be seen in the idler photon plot (Figure 6.23). A possible future experiment would involve the inclusion of a Stokes filtering Bragg grating set at the end of the waveguide, in order to suppress Raman scatter.

The application of the dispersion measurement technique to the design of birefringent waveguides suitable for SFWM has been demonstrated. The technique allows fitting of the Sellmeier curve for both the fast and slow axes of the waveguide, as well as a measurement of birefringence, allowing one simple measurement technique to collect all relevant data. The waveguide for measurement can be placed close to a waveguide without gratings for pair production, allowing a realistic estimate of the dispersive and birefringent behaviour of the SFWM waveguide to be obtained without contaminating the observed spectrum.

In terms of the SFWM experiments, further steps will be made in the future to further these promising results. Long waveguides exhibiting more birefringence will be fabricated in Southampton. This should increase the interaction length and move the signal and idler photons spectrally further from the pump, in an endeavour to avoid Raman contamination and move outwith the bounds of the filtering equipment. Work on 40 mm-long waveguides will continue at Oxford, to change the filters and observe the signal photon spectrum. Then observation of coincidences and single photon counting will be carried out to investigate the possibilities of use of the waveguide as a single photon source for quantum cryptography.

6.8 Conclusions and future work

The work described in this chapter has enabled the development of a simple grating based measurement technique to observe the total dispersion of a waveguide. The technique

development work involving design of the measurement and analysis methods has led to a single step process to obtain the wavelength dependent refractive index of the waveguide over a wide spectral band. Inclusion of the second-order reflection data from the Bragg gratings has allowed improvement of the accuracy of the technique in determining the fitted Sellmeier dispersion curve to the data.

Empirical techniques were used to interpret the data obtained in order to determine the contribution of waveguide and material dispersion to the total measured dispersion. Through calculation of the dimensionless waveguide parameter V, the expected waveguide dispersion of the guide, given waveguide refractive index and core dimensions, was calculated, and the material dispersion component subsequently inferred. This work was published in the IEEE Photonics Journal [63].

To further promote the varied applications of the technique, the method was used to identify the change in total dispersion of the waveguide for higher order propagating modes. The intentionally multimode waveguide fabricated, alongside mode identification via FIMMWAVE modelling, allowed the total dispersion of the individual modes of the waveguide to be fabricated. This work was presented at CLEO Europe 2011 [106].

A further application of the technique was investigated in collaboration with the Oxford Quantum Technologies Laboratory. Waveguides suitable for supporting spontaneous four-wave mixing via birefringence were fabricated, characterised and modelled to obtain total dispersion, birefringence and expected signal and idler photon wavelengths given pump source parameters. The group in Oxford performed the SFWM experiments, confirming the expected idler spectral dependence calculated via the dispersion measurement technique.

Future development of the work in this thesis will involve further application of the multi-grating dispersion measurement technique to other waveguides where the dispersive behaviour of refractive index is of interest. This could be in areas such as multimode telecommunications network components, where detailed knowledge of the dispersive behaviour of each mode is required in order to design materials for specific purposes. Applications to other materials such as flat fibre could also be investigated, enabling the technique to be used in the design stages of larger 2D integrated photonic circuits with dispersion dependent components. In addition, the collaborative work with the Oxford group will continue, to investigate the viability of using the technique to model the dispersive behaviour of specific waveguides for use in non-linear interactions.

Chapter 7

Conclusions

A number of distinct experimental advances were achieved during the course of this project. Firstly, improvements to the fabrication and characterisation capabilities of direct UV written waveguides and Bragg gratings were instigated, enabling substantial development of the scope of devices produced. Chapter 3 describes the fabrication techniques employed to produce the Bragg gratings described later in the thesis. Fabrication of FHD wafers with doped photosensitive core layers suitable for direct UV writing was undertaken by the author, on new equipment at the University of Southampton. Section 3.1.2.5 describes the optical interrogation of the layers fabricated using a Metricon prism coupling system, rebuilt by the author with the original 633 nm and additional 1553 nm and 980 nm film thickness and refractive index measurement capability. In addition, a characterisation set up suitable for interrogating Bragg gratings with central wavelength around 780 nm was developed, enabling research into quantum technologies and atom chips to be undertaken.

Chapter 4 describes the design parameters employed when fabricating Bragg grating structures. The ability to 'detune' the central wavelength of the Bragg grating was demonstrated, with a -3 dB detuning range of 110 nm from the optimised central wavelength achieved (Section 4.1). A number of developments were made in the apodisation of Bragg grating structures, with demonstration of the first linearly chirped Bragg grating structures via DGW (Section 4.5.1), in addition to uniform, Gaussian apodised and phase-shifted Bragg gratings. Further optical interferometer set ups were implemented with optimal central Bragg grating wavelengths in FHD at 780 nm, 1060 nm and 2 μm. This enabled the fabrication of Bragg gratings with central wavelengths between 650 nm and 2.2 μm, extending the scope of applications of gratings fabricated by DGW.

A key development in the fabrication of Bragg grating structures was the implementation of a phase control grating writing system (Section 4.6). In the first instance, a succession of piezo mirror mounts were employed to enable a phase shift in the interference pattern within the focal spot of the interferometric DGW set up. With control of the piezo

element via a sawtooth wave signal, produced via an integrator circuit fabricated by the author, the first Bragg gratings fabricated using the phase control system were achieved in FHD. Further developments included implementation of an electro-optic modulator in one arm of the interferometric set up to replace the unstable piezo mirror mount. This enabled Bragg gratings with similar performance characteristics to those created with the AOM modulation system to be fabricated, with the advantage of twice the grating effective refractive index contrast and therefore shorter Bragg grating structures. The speed of fabrication was also increased to a few minutes, given that fluence matching no longer required a reduction in sample translation speed during the grating sections to maintain the same energy density within the core.

A fundamental point to highlight here is the concept of fluence matching. Ensuring the same energy density is present in the photosensitive core layer throughout fabrication of the waveguide and Bragg grating sections enables a waveguide and grating system with constant effective refractive index to be fabricated. This ensures that the radiation propagating within the waveguide at wavelengths outside of the bandwidth of the gratings experiences no additional loss due to the presence of the grating structures. Thus, the development of the grating-based loss measurement technique was enabled.

An effective propagation loss measurement technique for short, low loss waveguides was developed (Chapter 5), enabling distinction between propagation loss and different sources of loss including Fresnel reflection losses and coupling efficiency. The theoretical implications of the technique were considered (Section 5.3), enabling an experimental technique involving a simple linear fit to collected data to yield a propagation loss value for the waveguide under test. Regressional analysis provides values for statistical errors, a robust method for reporting the small uncertainties afforded by the measurement technique (Section 5.5). Various implementations of the technique were made (Sections 5.6-5.9), such as integration of the technique with micromachined components, within different spectral regions for rare-earth doped waveguides, and flat fibre characterisation. This new analysis technique with inherent independence from coupling losses, has proven value in the wider scientific field, enabling the propagation loss characteristics of individual waveguides to be investigated using Bragg grating structures which may already be part of the operational circuitry of a device.

The final development reported here is a new dispersion measurement technique for short planar waveguides (Chapter 6). Experimental measurement of the wavelength dependent dispersion of refractive index enables the total dispersion of a waveguide to be obtained, via fitting of the Sellmeier curve and calculated coefficients. Using the known waveguide parameters, the waveguide dispersion component was empirically calculated, enabling both waveguide and material dispersion components to be obtained (Section 6.4). The nature of the measurement technique enables its use as a tool to interrogate higher order modes of the waveguide (Section 6.6), via the presence of spectrally distanced lobes on the grating spectrum in the multi-mode case. In a further development, the

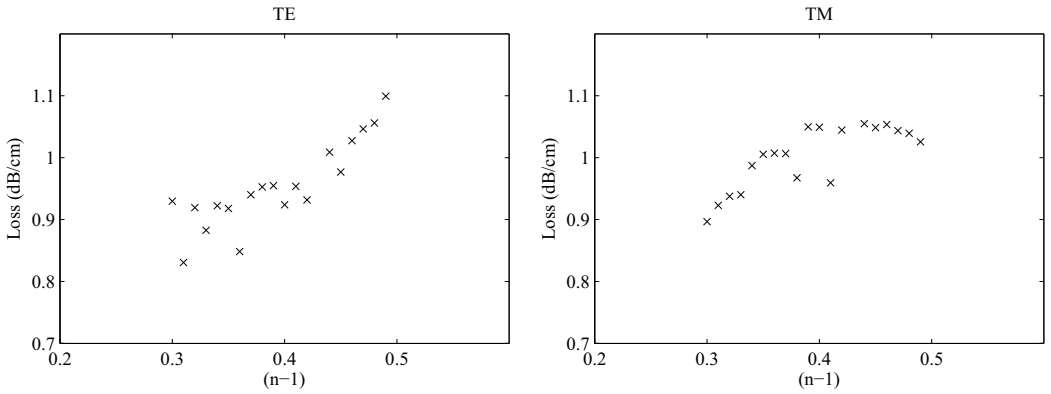

Figure 7.1: Observation of the change in loss across a groove filled with various refractive index Cargille oils. Note differing behaviour in TE and TM polarisation states.

use of this technique to interrogate waveguides which exhibit single mode guiding at 780 nm enabled the modelling of expected signal and idler frequencies in parametric pair production in a birefringent optical waveguide (Section 6.7). Experimental corroboration of this model was achieved, with potential use of the device as a single photon source under investigation in collaboration with the Oxford Quantum Technologies Laboratory.

Future development of the waveguide interrogation techniques introduced in this thesis would investigate the use of each new protocol as part of application-driven devices. In the case of the loss measurement technique, coupling losses of optical systems could be investigated via use of a series of Bragg gratings written in both device and fibre pigtail, similar to the experiments involving measurement across a groove. In this manner, coupling losses of junctions could be monitored and minimised *in situ*, enabling the lowest losses possible within an optical system.

Following the development of the propagation loss measurement technique, the ability to use the technique within a sensing capacity was the subject of preliminary investigation. The use of a groove, with Bragg gratings on either side to interrogate the loss across the groove, would allow analytes of different refractive index to be interrogated, and the absorption due to the analyte calculated. The first step toward achieving this goal is to characterise the sample with analytes of known refractive index, in this case Cargille refractive index oils. The resulting refractive index dependent loss data can be seen in Figure 7.1.

In this device, the incident waveguide had an angle of incidence of 8 degrees at the groove interface, and the waveguide offset on the opposite side of the groove was optimised so the lowest misalignment loss should occur with air (n=1) in the groove. As such, any deviation in refractive index from 1 should increase the loss observed. In the TE polarisation state, this behaviour can be observed. An approximately linear relationship between the refractive index and the loss across the groove can be observed. In the case of the TM polarisation state, however, a quadratic relationship between the refractive index and loss can be observed, with a turning point at 0.44 (n = 1.44), close to the

refractive index of the waveguide core. This is due to the approach toward refractive index matching of the glass and the refractive index oil, and the corresponding behaviour of different polarisation states under this condition.

An important point to note here is the observation of Bragg grating spectra whilst affected by refractive index oils with index greater than that of the glass core. This is the first observation within the author's research group of Bragg gratings under these conditions. In other sensing devices [50], use of material with refractive index above that of the glass core pulls the mode into the higher refractive index material, due to the evanescent field interaction, and thus the reflected mode from the Bragg grating cannot be measured. In this case, as the analyte intersects the waveguide, the incident mode is refracted through the higher index material, allowing the spectral characteristics of a Bragg grating on the opposite side of the groove to continue to be observed in reflection.

This development expands the range of analytes that could be sensed to those with higher refractive indices, expanding the scope of sensing devices based on Bragg gratings in silica-on-silicon waveguides. In addition, analytes with similar refractive index but different absorption coefficients, such as H_2O and D_2O, could be distinguished, a task which is not achievable with conventional Bragg grating evanescent field sensors. Future work would investigate the scope of analytes which could be interrogated, alongside further optimisation of the device for efficient operation.

Future developments employing the dispersion measurement technique would fall into three broad areas. Firstly, an expansion of the spectral range of available characterisation sources would enable more Bragg gratings to be observed and thus lower errors to be achieved in the dispersion measurement technique. Secondly, characterisation of more complex devices, such as multimode telecommunications network components, would enable design of materials and components to maximise data traffic in a single device over a number of modes. Finally, in order to improve the efficiency of the parametric pair production experiment, alterations to the waveguides could be made. Controllable birefringence, by altering the relative and absolute dopant levels within the silica-on-silicon FHD, would enable tailoring of the signal and idler photon wavelengths to specific applications. Tunable dispersion, as demonstrated in the fluence investigation in Chapter 6, could enable optimal dispersion characteristics to be chosen for a specific purpose. In addition, Bragg gratings within the waveguide could enable on-chip filtering for improved signal-to-noise ratio. A Bragg grating at the output end of the waveguide, with central wavelength at the pump wavelength, could enable on-chip pump filtering. A chirped Bragg grating, covering the stimulated Brillouin scattering spectral range, could enable noise reduction around the wavelength of the idler photon. Further investigation into parametric pair production in birefringent waveguides could lead to the implementation of more efficient materials for the non-linear processes involved, and heralding experiments and single photon sources for future quantum applications.

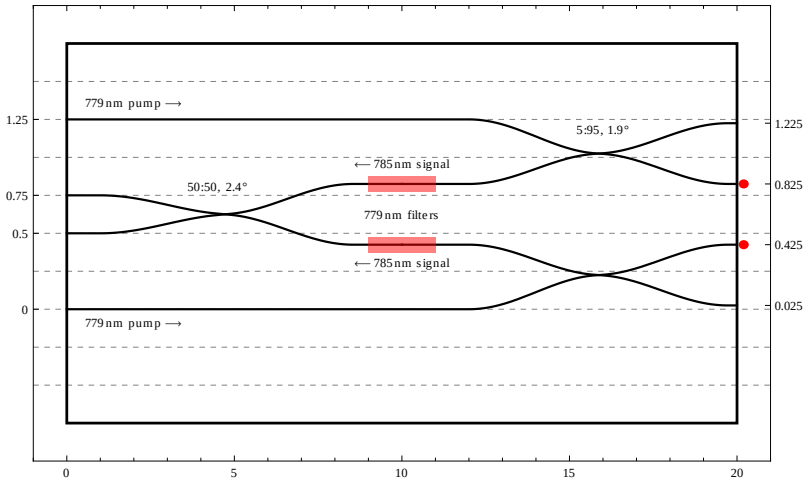

Figure 7.2: Schematic of most recent atom chip device fabricated in collaboration with Imperial College London. Image from Guillaume Lepert. Red dots indicate DBT molecules.

Collaboration with colleagues at Imperial College, London throughout the course of this project has led to advances in the direct UV writing technology, and highlighted potential applications of devices in the quantum information field. The 780 nm UV writing system was used to create waveguides with integrated Bragg grating structures, and characterisation of Bragg gratings was performed to observe the loss of the device (Section 5.6). Various iterations of device were fabricated by the author, initially with individual waveguides and integrated Bragg gratings, progressing to x-coupler devices and an investigation into the coupling behaviour of x-couplers with differing intersection angles. In addition, polishing parameters were investigated by the author and applied to these devices, prior to deposition of dielectric mirrors on the sample facets.

These steps were undertaken in order to realise a coupled-cavity atom chip design, detailed in Figure 7.2. The figure shows a waveguide realisation of a Hanbury Brown and Twiss (HBT) quantum interferometer, consisting of UV written waveguides and x-couplers. Incident 779 nm pump radiation at positions 0 and 1.25 interacts with a dibenzoterrylene (DBT) molecule (red dots) at the waveguide output, deposited by evaporation on the end facet of the waveguide. Emitted radiation from the molecule at 785 nm is then coupled into the waveguide channel, and travels through the 5:95 coupler, where 95 % of the emitted radiation is incident on the 50:50 coupler. The Bragg grating with central wavelength at 779 nm is used to reject the remaining pump power. The output waveguides at positions 0.5 and 0.75 can then be coupled to avalanche photodiodes (APDs), enabling emitted photons to be counted. The quantum interferometer can be used to observe photon bunching.

In order to successfully fabricate this chip, additional investigation into the ability to fabricate x-couplers with different output waveguide separations was required. After UV writing, the sample was polished and dielectric mirrors deposited on the end facet

adjacent to the molecule, in order to increase the device efficiency. Currently, investigation into the device performance is being undertaken at Imperial College, with results expected in the near future.

In the meantime, additional investigation into the inhibiting parameters of the fabrication techniques will be undertaken, in order to improve device performance in all our short wavelength applications. In particular, the loss of the devices (0.9 dB at 780 nm) needs to be improved to secure the longevity of the silica-on-silicon platform in quantum applications. The loss measurement described in Chapter 5 enables the losses of the devices to be determined efficiently, as waveguides and Bragg gratings are required to determine the suitability of the material for the DGW technique. The material parameters of the core layer of the device may also require alteration in order to reduce the current losses. Reduction of the core dimensions during deposition of the soot layer would ensure the single mode behaviour of the device and reduce any coupling to higher order modes which may be increasing the losses of the core mode. In addition, adjusting the absolute and relative dopant levels within the soot production phase may enable lower losses to be achieved in the glass layer, a goal which is integral to the use of the FHD silica-on-silicon platform in future.

To summarise, several fabrication technique enhancements and two completely new grating based waveguide characterisation techniques have been developed. The propagation loss measurement method enables the propagation loss of a short low loss waveguide to be measured and effectively distinguished from other sources of loss present in the guide. The second, a dispersion measurement technique, enables, through measurement of the effective refractive index of the waveguide over a broad wavelength range, calculation of the Sellmeier coefficients of the waveguide and subsequent use in the modelling of the behaviour of guides. Examples of functional devices taking advantage of both techniques have been fabricated and presented. Both techniques can be implemented within an integrated optical platform, enabling detailed device characteristics to be obtained without any device alteration or additional measurement, given an appropriate Bragg grating arrangement at fabrication. This leads to the capability to know the precise loss and dispersion characteristics of each individual device, invaluable information for the development of future sensing and telecommunications integrated photonic circuits.

Appendix A

Contributions tables

Throughout the course of this project, work was undertaken in collaboration with other researchers, both within the author's research group and at other universities. The tables shown here highlight the contributions of the author to the work undertaken. For the case of Chapters 3 and 4, the tables are provided to enable the distinction between prior work and the author's contributions to current fabrication systems; for Chapters 5 and 6, the tables are provided to clarify the contributions of the author in collaborative ventures.

Chapter 3	
Situation prior to this project	Author's contribution
Wafers fabricated at CIP to our specification and bought in.	Fabrication and characterisation of FHD wafers in Southampton (Section 3.1)
Wafer measurement carried out on Metricon at 1550 nm only, at CIP.	Metricon system at ORC rebuilt and additional 630 nm, 980 nm and 1553 nm measurement capability added (Section 3.1.2.5).
Only 1550 nm characterisation capability.	Use of 780 nm characterisation set up (Section 3.4.2) and fabrication of waveguides and Bragg gratings at this wavelength specifically for atom chip research [72].

Chapter 4	
Brief outline of work	Author's contribution
Demonstration of wide detuning range available via direct grating writing.	Fabrication, characterisation and analysis of gratings and waveguides (Section 4.1).
Demonstration of uniform and apodised Bragg gratings.	Fabrication, characterisation and analysis of Bragg gratings (Section 4.4).
Chirped Bragg grating structures.	Fabrication and spectral characterisation of waveguides and Bragg gratings (Section 4.5.1). Delay characterisation carried out by Benjamin Snow.
Phase shifted Bragg gratings	Initial demonstration of fabrication (Section 4.5.2). Further devices, characterisation and analysis carried out by Chaotan Sima.
Phase control grating writing system.	Initial demonstration of gratings using modified mirror mount with speaker piezo, and Thorlabs piezo mirror mount (Section 4.6). Improvements to system via implementation of EOM carried out by Chaotan Sima and Paolo Mennea.
Short wavelength gratings.	Fabrication, characterisation and analysis of 780 nm gratings, as part of atom chip project in collaboration with Guillaume Lepert, Imperial College, London. Implementation of 780 nm characterisation system (Section 4.7).

Chapter 5	
Brief outline of work	Author's contribution
Theoretical consideration of technique (Section 5.3).	Consideration of terms and how to obtain loss information from collected data.
Fabrication and characterisation of devices (Section 5.4).	Wafer fabrication at CIP observed during summer project. Direct UV writing and grating characterisation.
Initial data manipulation to obtain loss, based on theoretical considerations (Section 5.5).	Reflectivity of grating obtained from opposing launch conditions, plotted to obtain gradient and thus loss.
Loss at 780 nm (Section 5.6).	Fabrication, characterisation and analysis of waveguides. Loss values corroborated via collaboration with Guillaume Lepert, Imperial College, London, as part of the atom chip experiments.
Loss of a corner mirror within a grating (Section 5.7).	Assisted with analysis of collected data. Fabrication and characterisation carried out by Lewis Carpenter.
Loss across a groove (Section 5.7).	Fabrication, characterisation and analysis of waveguides. Calculation of expected losses to corroborate data.
Loss of a UV written waveguide in flat fibre (Section 5.8).	Assisted with analysis of collected data. Fabrication and characterisation carried out by Sumiaty Ambran.
Loss of rare-earth doped waveguides (Section 5.9).	Fabrication of solution doped FHD (bismuth, neodymium and erbium dopants) carried out by collaborators at the University of Malaya. Fabrication of Bragg gratings and waveguides, characterisation and analysis carried out by the author. A continuation of this work in erbium doped flat fibre has been carried out by Sumiaty Ambran, once again in collaboration with University of Malaya.

Chapter 6	
Brief outline of work	Author's contribution
Fabrication and characterisation of waveguides for method verification (Sections 6.3.1, 6.3.2).	Wafer fabrication, direct UV writing and grating characterisation. Includes setting up 780 nm characterisation rig 3.4.2.
Data analysis and extraction of dispersion data.	Appropriate fitting of Sellmeier coefficients, definition of common starting conditions. Empirical calculation of waveguide dispersion, inference of material dispersion given total measured dispersion.
Multimode dispersion experiment.	Fabrication, characterisation and analysis of multimode waveguide. Calculation of expected modes via analytical slab waveguide approach and numerical modelling using 'FIMMWAVE'.
Parametric pair production experiments.	Fabrication, characterisation and analysis of waveguides. Modelling of expected signal and idler photon wavelengths (see Appendix D). Set up and implementation of FWM experiment to observe generated photons carried out at the Oxford Quantum Technologies Laboratory, initially by Christoph Soeller. Later work carried out by Justin Spring.

Appendix B

Complete slab waveguide theory

This appendix contains a more rigorous approach to the analytical interpretation of the slab waveguide described in Section 2.1.2. The case of the transverse electric modes is analysed in more detail, and the case of the transverse magnetic modes is presented. This analytical approach is presented in a number of texts, including Griffiths [31], Ghatak and Thyagarajan [107] and Okamoto [30].

B.1 Obtaining the wave equation

Analysis of this system starts from Maxwell's equations. The general form of Maxwell's equations in matter is given in Equation B.1 [31].

$$\nabla \cdot \boldsymbol{\mathcal{D}} = \rho_f \tag{B.1a}$$

$$\nabla \cdot \boldsymbol{\mathcal{B}} = 0 \tag{B.1b}$$

$$\nabla \times \boldsymbol{\mathcal{E}} = -\frac{\partial \boldsymbol{\mathcal{B}}}{\partial t} \tag{B.1c}$$

$$\nabla \times \boldsymbol{\mathcal{H}} = \boldsymbol{\mathcal{J}}_f + \frac{\partial \boldsymbol{\mathcal{D}}}{\partial t} \tag{B.1d}$$

$\boldsymbol{\mathcal{E}}$ is the electric field, $\boldsymbol{\mathcal{B}}$ is the magnetic field, $\boldsymbol{\mathcal{H}}$ is the magnetising field and $\boldsymbol{\mathcal{D}}$ is the electric displacement field. $\boldsymbol{\mathcal{J}}_f$ is the total current density and ρ_f is the total charge density.

Equation B.1a is Gauss's law, which indicates that the flux through any closed surface is proportional to the electric charge enclosed within the surface. Gauss's law for magnetism, Equation B.1b, dictates that magnetic monopoles do no exist, and that magnetism is defined by magnetic dipoles. Faraday's law, Equation B.1c, indicates that

a changing magnetic field induces an electric field. The final equation, B.1d, is Ampère's law with Maxwell's correction. The law states that magnetic fields can be generated in two ways, by electric currents (Ampère's law, first term on the right of the equation), and by changing electric fields (Maxwell's correction, second term on the right of the equation). Maxwell's equations therefore describe the production of electric and magnetic fields by charges, currents, and changing electric and magnetic fields.

For the case of the symmetric slab waveguide depicted above, Maxwell's equations for an isotropic, linear, non-conducting and non-magnetising field are required. These are achieved by modification of the equations above considering these restrictions, allowing ρ_f and $\boldsymbol{\mathcal{J}}_f$ to go to zero for the non-conducting case, and expressing $\boldsymbol{\mathcal{B}}$ in terms of the magnetizing field $\boldsymbol{\mathcal{H}}$, defined by

$$\boldsymbol{\mathcal{B}} = \mu_0 \boldsymbol{\mathcal{H}}, \tag{B.2}$$

$$\boldsymbol{\mathcal{D}} = \epsilon \boldsymbol{\mathcal{E}} = \epsilon_0 n^2 \boldsymbol{\mathcal{E}}. \tag{B.3}$$

n is the refractive index and ϵ is the permittivity of the material in which radiation propagates. μ_0 and ϵ_0 are the permeability and permittivity of free space respectively.

Applying these conditions yields the adapted Maxwell's equations.

$$\epsilon_0 \nabla \cdot \left(n^2 \boldsymbol{\mathcal{E}}\right) = 0 \tag{B.4a}$$

$$\nabla \cdot \boldsymbol{\mathcal{H}} = 0 \tag{B.4b}$$

$$\nabla \times \boldsymbol{\mathcal{E}} = -\mu_0 \frac{\partial \boldsymbol{\mathcal{H}}}{\partial t} \tag{B.4c}$$

$$\nabla \times \boldsymbol{\mathcal{H}} = \epsilon_0 n^2 \frac{\partial \boldsymbol{\mathcal{E}}}{\partial t} \tag{B.4d}$$

At this point, a reminder of relevant vector identities is provided.

$$\nabla \times (\nabla \times \boldsymbol{A}) = \nabla (\nabla \cdot \boldsymbol{A}) - \nabla^2 \boldsymbol{A} \tag{B.5a}$$

$$\nabla \cdot (f \boldsymbol{A}) = f (\nabla \cdot \boldsymbol{A}) + \boldsymbol{A} \cdot (\nabla f) \tag{B.5b}$$

Analysis of the electric and magnetic fields via Maxwell's equations yields vectorial wave equations for the propagation of radiation in an optical medium. Considering the electric field, taking the curl of Equation B.4c yields

$$\nabla \times (\nabla \times \boldsymbol{\mathcal{E}}) = -\mu_0 \frac{\partial}{\partial t} (\nabla \times \boldsymbol{\mathcal{H}}) . \tag{B.6}$$

Rearranging via Equation B.5a, and substituting Equation B.4d gives

$$\nabla \times (\nabla \times \boldsymbol{\mathcal{E}}) = \nabla (\nabla \cdot \boldsymbol{\mathcal{E}}) - \boldsymbol{\mathcal{E}} (\nabla \cdot \nabla) \tag{B.7}$$

$$\nabla (\nabla \cdot \boldsymbol{\mathcal{E}}) - \nabla^2 \boldsymbol{\mathcal{E}} = -\mu_0 \epsilon_0 n^2 \frac{\partial^2 \boldsymbol{\mathcal{E}}}{\partial t^2}. \tag{B.8}$$

Equation B.4a can be rearranged via Equation B.5b, and written as

$$\epsilon_0 \nabla \cdot \left(n^2 \boldsymbol{\mathcal{E}}\right) = \epsilon_0 \left[n^2 \nabla \cdot \boldsymbol{\mathcal{E}} + \boldsymbol{\mathcal{E}} \cdot \nabla n^2\right] = 0, \tag{B.9}$$

then

$$\nabla \cdot \boldsymbol{\mathcal{E}} = \frac{-1}{n^2} \nabla n^2 \cdot \boldsymbol{\mathcal{E}}. \tag{B.10}$$

Substituting this into Equation B.8, the wave equation for the propagation of the electric field through a material with refractive index n can be obtained.

$$\nabla^2 \boldsymbol{\mathcal{E}} + \nabla \left(\frac{1}{n^2} \nabla n^2 \cdot \boldsymbol{\mathcal{E}} \right) - \mu_0 \epsilon_0 n^2 \frac{\partial^2 \boldsymbol{\mathcal{E}}}{\partial t^2} = 0 \tag{B.11}$$

The second term in this equation considered the inhomogeneity of the optical medium. In this case, as uniform materials are considered, this term can be neglected, leaving

$$\nabla^2 \boldsymbol{\mathcal{E}} - \mu_0 \epsilon_0 n^2 \frac{\partial^2 \boldsymbol{\mathcal{E}}}{\partial t^2} = 0. \tag{B.12}$$

A similar procedure can be applied in the case of the magnetic field. Following the steps outlined above, we obtain

$$\nabla (\nabla \cdot \boldsymbol{\mathcal{H}}) - \nabla^2 \boldsymbol{\mathcal{H}} = \epsilon_0 \left(-\mu_0 n^2 \frac{\partial^2 \boldsymbol{\mathcal{H}}}{\partial t^2} - \frac{\partial \boldsymbol{\mathcal{E}}}{\partial t} \times \left(\nabla n^2\right) \right) \tag{B.13}$$

$$\nabla^2 \boldsymbol{\mathcal{H}} + \frac{1}{n^2} \nabla n^2 \times (\nabla \times \boldsymbol{\mathcal{H}}) - \mu_0 \epsilon_0 n^2 \frac{\partial^2 \boldsymbol{\mathcal{H}}}{\partial t^2} = 0, \tag{B.14}$$

and for the homogeneous materials considered,

$$\nabla^2 \boldsymbol{\mathcal{H}} - \mu_0 \epsilon_0 n^2 \frac{\partial^2 \boldsymbol{\mathcal{H}}}{\partial t^2} = 0. \tag{B.15}$$

The propagation direction is defined as parallel to the z-direction of the coordinate system. The refractive index does not vary in this direction, so $n^2 = n^2(x, y)$. The solutions of these equations are then

$$\boldsymbol{\mathcal{E}} = \boldsymbol{E}(x, y)\, e^{i(\omega t - \beta z)}, \tag{B.16}$$

$$\boldsymbol{\mathcal{H}} = \boldsymbol{H}(x, y)\, e^{i(\omega t - \beta z)}. \tag{B.17}$$

β is the propagation constant, and ω is the angular frequency of oscillation. These equations define the modes of the system. Modes are field distributions that can propagate so that the transverse field distributions in x and y are constant as the field propagates through the waveguide in the z-direction.

Once again referring to the schematic of the symmetric slab waveguide, conditions are now set to yield solutions of this wave equation. The assumption is made that the refractive index changes only in the x direction ($n^2 = n^2(x)$). This assumption allows the following solutions to the wave equation, where $j = x, y, z$.

$$\mathcal{E}_j = E_j(x)\, e^{i(\omega t - \beta z)} \tag{B.18}$$

$$\mathcal{H}_j = H_j(x)\, e^{i(\omega t - \beta z)} \tag{B.19}$$

These solutions to the wave equation allow propagation of electric and magnetic fields within the structure defined previously (Figure 2.2), and are defined as the modes of the waveguide.

In order to determine the physical representation of these solutions, they are inserted back into the initial Maxwell's equations.

$$\nabla \times \left(E_j(x)\, e^{i(\omega t - \beta z)} \right) = -\mu_0 \frac{\partial}{\partial t} \left(H_j(x)\, e^{i(\omega t - \beta z)} \right) \tag{B.20}$$

$$\nabla \times \left(H_j(x)\, e^{i(\omega t - \beta z)} \right) = \epsilon_0 n^2 \frac{\partial}{\partial t} \left(E_j(x)\, e^{i(\omega t - \beta z)} \right) \tag{B.21}$$

Now, the x, y and z components of these equations are obtained via the definition of the curl B.22.

$$\nabla \times \boldsymbol{E} = \left(\frac{\partial E_z}{\partial y} - \frac{\partial E_y}{\partial z}\right)\hat{\boldsymbol{x}} + \left(\frac{\partial E_x}{\partial z} - \frac{\partial E_z}{\partial x}\right)\hat{\boldsymbol{y}} + \left(\frac{\partial E_y}{\partial x} - \frac{\partial E_x}{\partial y}\right)\hat{\boldsymbol{z}} \tag{B.22}$$

$$\frac{\partial E_z}{\partial y} + i\beta E_y = -\mu_0 i\omega H_x \tag{B.23}$$

$$-i\beta E_x - \frac{\partial E_z}{\partial x} = -\mu_0 i\omega H_y \tag{B.24}$$

$$\frac{\partial E_y}{\partial x} - \frac{\partial E_x}{\partial y} = -\mu_0 i\omega H_z \tag{B.25}$$

$$\frac{\partial H_z}{\partial y} + i\beta H_y = i\omega\epsilon_0 n^2 E_x \tag{B.26}$$

$$-i\beta H_x - \frac{\partial H_z}{\partial x} = i\omega\epsilon_0 n^2 E_y \tag{B.27}$$

$$\frac{\partial H_y}{\partial x} - \frac{\partial H_x}{\partial y} = i\omega\epsilon_0 n^2 E_z \tag{B.28}$$

n now describes the refractive index structure varying in the x-direction only. In the case of the symmetric slab waveguide described above, the electromagnetic fields E and H do not have y-dependency, so $\frac{\partial E}{\partial y} = 0$ and $\frac{\partial H}{\partial y} = 0$, and the equations can be re-written as follows.

$$i\beta E_y = -\mu_0 i\omega H_x \tag{B.29}$$

$$\frac{\partial E_y}{\partial x} = -\mu_0 i\omega H_z \tag{B.30}$$

$$-i\beta H_x - \frac{\partial H_z}{\partial x} = i\omega\epsilon_0 n^2 E_y \tag{B.31}$$

$$i\beta H_y = i\omega\epsilon_0 n^2 E_x \tag{B.32}$$

$$\frac{\partial H_y}{\partial x} = i\omega\epsilon_0 n^2 E_z \tag{B.33}$$

$$-i\beta E_x - \frac{\partial E_z}{\partial x} = -\mu_0 i\omega H_y \tag{B.34}$$

The first three equations (Equations B.29, B.30 and B.31) involve only E_y, H_x and H_z, and the second three (Equations B.32, B.33 and B.34) rely only on H_y, E_x and E_z. Thus two independent sets of equations have been formed. The solutions can then be interpreted as two modes, one with its electric field oscillating in the y-plane (Equations B.29, B.30 and B.31), and one with its magnetic field oscillating in the y-plane (Equations B.32, B.33 and B.34). These modes are commonly referred to as the transverse electric (TE) and transverse magnetic (TM) modes respectively, and can each be described by a second order differential equation obtained from the solution to the wave equation.

B.2 The TE modes

Taking the case of the TE modes, a description of the electric field can be obtained by manipulation of the previous equations. From Equation B.31, substituting B.29 and B.30,

$$\frac{-i\beta^2}{\omega\mu_0}E_y + \frac{1}{i\omega\mu_0}\frac{\partial^2 E_y}{\partial x^2} = i\omega\epsilon_0 n^2 E_y \tag{B.35}$$

$$\frac{1}{i\omega\mu_0}\frac{\partial^2 E_y}{\partial x^2} = \left[i\omega\epsilon_0 n^2 + \frac{i\beta^2}{\omega\mu_0}\right] E_y \tag{B.36}$$

$$\frac{\partial^2 E_y}{\partial x^2} = \left[i^2\omega^2\epsilon_0\mu 0^2 - i^2\beta^2\right] E_y \tag{B.37}$$

$$\frac{d^2 E_y}{dx^2} + \left[k_0^2 n^2 - \beta^2\right] E_y = 0. \tag{B.38}$$

k_0, the free space wavenumber, is given by $\omega\left(\epsilon_0\mu_0\right)^{\frac{1}{2}}$. Now, boundary conditions can be applied to consider the specific parameters of the symmetric slab waveguide described above. With a core layer of refractive index n_1, centred around x=0 and with thickness d, and cladding layer with refractive index n_2, the electric field within the core and cladding layers can be described as follows.

$$\frac{d^2 E_y}{dx^2} + \left[k_0^2 n_1^2 - \beta^2\right] E_y = 0, \qquad |x| < \frac{d}{2} \tag{B.39}$$

$$\frac{d^2 E_y}{dx^2} + \left[k_0^2 n_2^2 - \beta^2\right] E_y = 0, \qquad |x| > \frac{d}{2} \tag{B.40}$$

At this point, substitution of $\kappa^2 = k_0^2 n_1^2 - \beta^2$ and $\gamma^2 = \beta^2 - k_0^2 n_2^2$ are made, to form the following simplified relations.

$$\frac{d^2 E_y}{dx^2} + \kappa^2 E_y = 0, \qquad |x| < \frac{d}{2} \tag{B.41}$$

$$\frac{d^2 E_y}{dx^2} - \gamma^2 E_y = 0, \qquad |x| > \frac{d}{2} \tag{B.42}$$

The solutions of these equations can be written as follows. Equation B.41, representing the electric field within the core, has solution of the form

$$E_y(x) = A\cos(\kappa x) + B\sin(\kappa x), \qquad |x| < \frac{d}{2} \tag{B.43}$$

where A and B are constants.

Equation B.42, representing the electric field within the cladding, has solutions of the form

$$E_y(x) = \begin{cases} Ce^{\gamma x}, & x < \frac{-d}{2} \\ De^{-\gamma x}, & x > \frac{d}{2}. \end{cases} \tag{B.44}$$

At this point, further boundary conditions are applied to obtain solutions to these equations. The solution must be continuous at the core/cladding interface, ie. E_y and $\frac{dE_y}{dx}$ are continuous. The solution must also be symmetric or antisymmetric around $x = 0$ as the refractive index distribution is symmetric about this point. This leads to the solutions

$$E_y(x) = \begin{cases} A\cos(\kappa x), & |x| < \frac{d}{2} \\ Ce^{-\gamma x}, & |x| > \frac{d}{2}, \end{cases} \tag{B.45}$$

in the symmetric case, and in the antisymmetric case

$$E_y(x) = \begin{cases} B\sin(\kappa x), & |x| < \frac{d}{2} \\ \frac{x}{|x|}De^{-\gamma x}, & |x| > \frac{d}{2}. \end{cases} \tag{B.46}$$

Application of the boundary conditions in the symmetric case leads to continuities at the boundary of E_y and $\frac{dE_y}{dx}$ respectively.

$$A\cos\left(\frac{\kappa d}{2}\right) = Ce^{-\frac{\gamma d}{2}} \tag{B.47}$$

$$-\kappa A\sin\left(\frac{\kappa d}{2}\right) = -\gamma Ce^{-\frac{\gamma d}{2}} \tag{B.48}$$

Dividing Equation B.48 by Equation B.47, and multiplying each side by $\frac{d}{2}$, you obtain

$$\frac{\kappa d}{2}\tan\left(\frac{\kappa d}{2}\right) = \frac{\gamma d}{2}. \tag{B.49}$$

Applying the same boundary conditions to the antisymmetric case leads to

$$B\sin\left(\frac{\kappa d}{2}\right) = \frac{x}{|x|}De^{-\frac{\gamma d}{2}} \tag{B.50}$$

$$\kappa B\cos\left(\frac{\kappa d}{2}\right) = -\gamma\frac{x}{|x|}De^{-\frac{\gamma d}{2}} \tag{B.51}$$

$$-\frac{\kappa d}{2}\cot\left(\frac{\kappa d}{2}\right) = \frac{\gamma d}{2}. \tag{B.52}$$

These relations for the symmetric and antisymmetric modes of the guide describe the supported TE modes of the structure.

It can be more convenient, in certain situations, to display the equations describing the waveguide modes in terms of dimensionless parameters. Thus, at this point, the dimensionless waveguide parameter, or V number is introduced. The V number is dependent on the core dimension d and refractive indices of the guide at wavelength λ, and can be determined via the following relation.

$$V = k_0 d\left(n_1^2 - n_2^2\right)^{\frac{1}{2}} \tag{B.53}$$

In addition, V can be related to κ and γ by the following relation.

$$\frac{\gamma d}{2} = \left(\frac{V^2}{4} - \frac{\kappa^2 d^2}{4}\right)^{\frac{1}{2}}. \tag{B.54}$$

By rewriting Equations B.49 and B.52 in terms of V, it can be shown that

$$\frac{\kappa d}{2}\tan\left(\frac{\kappa d}{2}\right) = \left(\frac{V^2}{4} - \frac{\kappa^2 d^2}{4}\right)^{\frac{1}{2}} \tag{B.55}$$

and

$$-\frac{\kappa d}{2}\cot\left(\frac{\kappa d}{2}\right) = \left(\frac{V^2}{4} - \frac{\kappa^2 d^2}{4}\right)^{\frac{1}{2}} \tag{B.56}$$

for symmetric and antisymmetric modes respectively.

These equations represent circles of radius $\frac{V}{2}$,which can be seen in Figure B.1 plotted alongside the symmetric and antisymmetric TE modes described by Equations B.49 and B.52. The circles of radius $\frac{V}{2}$ intersect the allowed modes of the guide defined by the V number. In the plot shown, the refractive indices and core dimensions are chosen such that a single mode (inner red circle) and multimode (outer red circle) V number curve can be displayed. The single mode guide circle (inner) intersects one symmetric mode

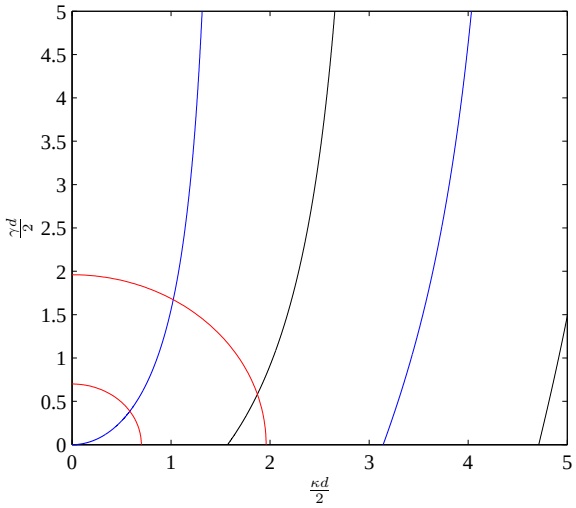

Figure B.1: Graphical solution for the guided modes of a slab waveguide. The V number radii are calculated from the experimental determination of V number given effective index and thickness data of the fabricated FHD slab. The inner circle represents a single mode waveguide ($V = 1.40$), the outer a multimode guide ($V = 3.92$). The symmetric and asymmetric modes supported (blue and black respectively) intersect the circle representing the multimode guide.

(blue lines), whilst the multimode circle intersects one symmetric and one antisymmetric mode (black). For a larger V number, with larger core dimension and/or refractive index difference $n_1 - n_2$, it can be seen from the plot and Equation B.53 that more modes will be supported by the guide.

This analytical process shows the steps required to determine the TE guided modes of the slab waveguide.

B.3 The TM modes

Taking the case of the TM modes, a description of the electric field can be obtained by manipulation of the previous equations. From Equation B.34, substituting B.32 and B.33,

$$\frac{-i\beta^2}{\omega\epsilon_0 n^2} H_y - \frac{1}{i\omega\epsilon_0}\frac{\partial}{\partial x}\left[\frac{1}{n^2}\frac{\partial H_y}{\partial x}\right] = -i\omega\mu_0 H_y \tag{B.57}$$

$$n^2\frac{\partial}{\partial x}\left[\frac{1}{n^2}\frac{\partial H_y}{\partial x}\right] + \left[k_0^2 n^2 - \beta^2\right] H_y = 0 \tag{B.58}$$

$$\frac{\partial^2 H_y}{\partial x^2} - \left[\frac{1}{n^2}\frac{\partial n^2}{\partial x}\right]\frac{\partial H_y}{\partial x} + \left[k_0^2 n^2 - \beta^2\right] H_y = 0 \tag{B.59}$$

Note the change in form from the TE case. In the case of the TM modes, the refractive index is constant in each region, so we have

$$\frac{d^2H_y}{dx^2} + \left[k_0^2 n_1^2 - \beta^2\right] H_y = 0, \qquad |x| < \frac{d}{2} \tag{B.60}$$

$$\frac{d^2H_y}{dx^2} - \left[\beta^2 - k_0^2 n_2^2\right] H_y = 0, \qquad |x| > \frac{d}{2}. \tag{B.61}$$

At this point, substitution of $\kappa^2 = k_0^2 n_1^2 - \beta^2$ and $\gamma^2 = \beta^2 - k_0^2 n_2^2$ are made, to form the following simplified relations.

$$\frac{d^2H_y}{dx^2} + \kappa^2 H_y = 0, \qquad |x| < \frac{d}{2} \tag{B.62}$$

$$\frac{d^2H_y}{dx^2} - \gamma^2 H_y = 0, \qquad |x| > \frac{d}{2} \tag{B.63}$$

At this point, the boundary conditions are applied. Since H_y and E_z are tangential components on the x-plane, H_y and $\frac{1}{n^2}\frac{\partial H_y}{\partial x}$ must be continuous at $x = \pm\frac{d}{2}$. The solution must also be symmetric or antisymmetric around $x = 0$ as the refractive index distribution is symmetric about this point. The solutions of these equations are then

$$H_y(x) = \begin{cases} A\cos(\kappa x), & |x| < \frac{d}{2} \\ Be^{-\gamma x}, & |x| > \frac{d}{2}, \end{cases} \tag{B.64}$$

in the symmetric case, and in the antisymmetric case

$$H_y(x) = \begin{cases} C\sin(\kappa x), & |x| < \frac{d}{2} \\ \frac{x}{|x|}De^{-\gamma x}, & |x| > \frac{d}{2}. \end{cases} \tag{B.65}$$

Application of the boundary conditions in the symmetric case leads to continuities at the boundary of H_y and $\frac{1}{n^2}\frac{dH_y}{dx}$ respectively.

$$A\cos\left(\frac{\kappa d}{2}\right) = Be^{-\frac{\gamma d}{2}} \tag{B.66}$$

$$\frac{1}{n_1^2}\left(-\kappa A\sin\left(\frac{\kappa d}{2}\right)\right) = \frac{1}{n_2^2}\left(-\gamma Be^{-\frac{\gamma d}{2}}\right) \tag{B.67}$$

Dividing Equation B.67 by Equation B.66, and multiplying each side by $\frac{d}{2}$, you obtain

$$\frac{\kappa d}{2}\tan\left(\frac{\kappa d}{2}\right) = \left(\frac{n_1}{n_2}\right)^2 \frac{\gamma d}{2}. \tag{B.68}$$

Applying the same boundary conditions to the antisymmetric case leads to

$$C\sin\left(\frac{\kappa d}{2}\right) = \frac{x}{|x|} D e^{-\frac{\gamma d}{2}} \tag{B.69}$$

$$\frac{1}{n_1^2}\left(\kappa C\cos\left(\frac{\kappa d}{2}\right)\right) = \frac{1}{n_2^2}\left(-\gamma\frac{x}{|x|} D e^{-\frac{\gamma d}{2}}\right) \tag{B.70}$$

$$-\frac{\kappa d}{2}\cot\left(\frac{\kappa d}{2}\right) = \left(\frac{n_1}{n_2}\right)^2 \frac{\gamma d}{2}. \tag{B.71}$$

These relations for the symmetric and antisymmetric modes of the guide describe the supported TM modes of the structure.

By rewriting Equations B.68 and B.71 in therms of V, it can be shown that

$$\frac{\kappa d}{2}\tan\left(\frac{\kappa d}{2}\right) = \left(\frac{n_1}{n_2}\right)^2 \left(\frac{V^2}{4} - \frac{\kappa^2 d^2}{4}\right)^{\frac{1}{2}} \tag{B.72}$$

and

$$-\frac{\kappa d}{2}\cot\left(\frac{\kappa d}{2}\right) = \left(\frac{n_1}{n_2}\right)^2 \left(\frac{V^2}{4} - \frac{\kappa^2 d^2}{4}\right)^{\frac{1}{2}} \tag{B.73}$$

for symmetric and antisymmetric modes respectively.

This analytical process shows the steps required to determine the TM guided modes of the slab waveguide.

There are a number of interesting points to be gleaned from the form of these equations, in comparison to the form of the TE case (Equations B.55 and B.56). The form of this equation is that of an ellipse, so the crossing point of the ellipse with the symmetric and antisymmetric modes on the plot above B.1 occurs at a slightly greater value than that of the TE mode for the same V number. Thus, the value of the propagation constant are smaller for the TM mode than for the equivalent TE modes. For weakly guiding waveguides, $n_1 \approx n_2$, so the TE and TM modes exhibit only marginally differing propagation characteristics.

A single mode waveguide exists when $0 < V < \pi$. This implies a single mode in the TE polarisation state, and a single mode in the TM polarisation state. The modes co-exist in the waveguide given non-linear input radiation. In the linear case, with electric field

polarised along either the x or y dimension of the slab, the TM or TE mode alone will exist respectively.

Appendix C

Wafer parameters

The various wafers used to fabricate the waveguides and Bragg gratings described in this thesis have different chemical and physical properties, having been produced via different recipes. This appendix details the properties of fabrication of each slab waveguide layer, prior to UV writing, in an effort to compare the typical composition with the optical behaviour observed.

Wafers W4, W5 and W8 were fabricated at CIP, whilst wafer W10 was fabricated at the ORC. Thus the recipes used to achieve similar refractive index layers are marginally different, given the differing gas flows and extract conditions at each site.

The gas flows given here are pressure compensated, given the air pressure and humidity of the lab environment on different days. The gas flows, shown here in litres per minute, cannot be directly compared for the different precursors, as the pressure at operating temperature for each is different (see Chapter 3). However, as a means of comparison between different wafers, the presence of more or less gas flow can be interpreted as a greater or lesser amount of precursor reaching the torch.

The following pages give detailed fabrication parameters for each wafer.

Wafer W4 Fabricated at CIP			
Underclad	No info		
Core	Date		
	Deposition Program		
	Run number	DN655	
	Wafer position	5	
	Consolidation Program		
	Average Refractive Index	**1.4551**	
	Average Thickness	**5.6 μm**	
	Torch gas flows	H_2	
		O_2	
		Ar	
	Process gas flows	$SiCl_4$	143
		$GeCl_4$	175
		PCl_3	-
		BCl_3	30
	Furnace gas flows	He	
		O_2	
Overclad	Date	23/07/08	
	Deposition Program	CIP Clad 1	
	Run number	ORC-2-Clad1	
	Wafer position	3	
	Consolidation Program	Clad ORC	
	Average Refractive Index	**1.4447**	
	Average Thickness	**15.2 μm**	
	Torch gas flows	H_2	6.5
		O_2	1.9
		Ar	8
	Process gas flows	$SiCl_4$	139
		$GeCl_4$	-
		PCl_3	31
		BCl_3	70
	Furnace gas flows	He	1.9
		O_2	0.9

Wafer W5 Fabricated at CIP			
Underclad	TY468-2, 16-17 μm thermal oxide		
Core	Date	22/07/08	
	Deposition Program	0deltacore	
	Run number	ORC 2-1	
	Wafer position	2	
	Consolidation Program	CoreORC2	
	Average Refractive Index	**1.4461**	
	Average Thickness	**5.64 μm**	
	Torch gas flows	H_2	5
		O_2	5
		Ar	8
	Process gas flows	$SiCl_4$	142
		$GeCl_4$	51
		PCl_3	-
		BCl_3	76
	Furnace gas flows	He	1.9
		O_2	0.9
Overclad	Date	23/07/08	
	Deposition Program	CIP Clad 1	
	Run number	ORC-2-Clad2	
	Wafer position	2	
	Consolidation Program	Clad ORC	
	Average Refractive Index	**1.4448**	
	Average Thickness	**16.4 μm**	
	Torch gas flows	H_2	6.5
		O_2	2
		Ar	8
	Process gas flows	$SiCl_4$	139
		$GeCl_4$	-
		PCl_3	31
		BCl_3	70
	Furnace gas flows	He	1.9
		O_2	0.9

Wafer W8 Fabricated at CIP			
Underclad	TY468-2, 16-17 μm thermal oxide		
Core	Date	22/07/2008	
	Deposition Program	0deltacore	
	Run number	ORC 2-1	
	Wafer position	4	
	Consolidation Program	Core ORC2	
	Average Refractive Index	**1.4461**	
	Average Thickness	**5.64 μm**	
	Torch gas flows	H_2	5
		O_2	5
		Ar	8
	Process gas flows	$SiCl_4$	142
		$GeCl_4$	51
		PCl_3	-
		BCl_3	76
	Furnace gas flows	He	1.9
		O_2	0.9
Overclad	Date	23/07/08	
	Deposition Program	CIP Clad 1	
	Run number	ORC-2-Clad2	
	Wafer position	4	
	Consolidation Program	Clad ORC	
	Average Refractive Index	**1.4448**	
	Average Thickness	**16.4 μm**	
	Torch gas flows	H_2	6.5
		O_2	2
		Ar	8
	Process gas flows	$SiCl_4$	139
		$GeCl_4$	-
		PCl_3	31
		BCl_3	70
	Furnace gas flows	He	1.9
		O_2	0.9

Wafer W10 Fabricated at ORC			
Underclad	TY471-2, 16.5 μm thermal oxide		
Core	Date	07/02/12	
	Deposition Program	Toshiba 1	
	Run number	NB38	
	Wafer position	2	
	Consolidation Program	Core 1a	
	Average Refractive Index	**1.4451**	
	Average Thickness	**5.3 μm**	
	Torch gas flows	H_2	5
		O_2	5
		Ar	8
	Process gas flows	$SiCl_4$	114
		$GeCl_4$	43
		PCl_3	-
		BCl_3	62
	Furnace gas flows	He	1.9
		O_2	0.9
Overclad	Date	08/02/12	
	Deposition Program	Toshiba clad	
	Run number	NB40	
	Wafer position	2	
	Consolidation Program	clad2	
	Average Refractive Index	**1.4439**	
	Average Thickness	**17.43 μm**	
	Torch gas flows	H_2	6.5
		O_2	1.5
		Ar	8
	Process gas flows	$SiCl_4$	137
		$GeCl_4$	-
		PCl_3	31
		BCl_3	69
	Furnace gas flows	He	1.9
		O_2	0.9

Appendix D

Four wave mixing prediction code

The calculation of the expected wavelengths of signal and idler photons in a four wave mixing scenario is a crucial step in the parametric pair production experiment outlined in Chapter 6. This appendix contains the MATLAB code used to calculate the wavelength of the signal and idler photons, given the dispersion characteristics of the waveguide and the pump wavelength.

The calculation is based on that detailed in the paper by the collaborators at Oxford, Smith et al. [104]. From a phase-matching argument, and assuming energy conservation, Equation D.1 is solved as described in Chapter 6.

$$\Delta k = 2\frac{\omega_p}{c}n\left(\omega_p\right) - \frac{\omega_s}{c}n\left(\omega_s\right) - \frac{\omega_i}{c}n\left(\omega_i\right) + 2\Delta n\frac{\omega_p}{c} + \frac{2}{3}\gamma P \tag{D.1}$$

In the case of four wave mixing,

$$2\omega_p = \omega_s + \omega_i. \tag{D.2}$$

Thus the code outlined below can be used to calculate the wavelength of the signal and idler photons given the input pump wavelength and dispersion characteristics and birefringence of the waveguide.

```
%Set the variables

H = [];
G = [];

%Sellmeier coefficients for 20 mm clad device
a=0.704380307;
b=0.006151455^0.5;
c=0.428760264;
```

```
d=0.011306558^0.5;
e=1.19195039;
f=97.92910478^0.5;

cspeed = 3*10^2;                          %Speed of light
deltan = 4.4*10^-4;                       %Birefringence
wavelength1i =(0.2:0.001:8.0);            %Calculation range

for jj = 1:length(wavelength1i)

lambdai = wavelength1i(jj);

lambdap = (0.4:0.001:1.2);

nslow= (((1+((a.*(lambdap.^2))./((lambdap.^2)-b^2))+((c.*(lambdap.^2))./
        ((lambdap.^2)-d^2))+((e.*(lambdap.^2))./((lambdap.^2)-f^2)))).^0.5)
         +deltan;
nfast= ((1+((a.*(lambdap.^2))./((lambdap.^2)-b^2))+((c.*(lambdap.^2))./
        ((lambdap.^2)-d^2))+((e.*(lambdap.^2))./((lambdap.^2)-f^2)))).^0.5;

%Calculate n with respect to defined wp and wi

np = nfast;
ni = ((1+((a.*(lambdai.^2))./((lambdai.^2)-b^2))+((c.*(lambdai.^2))./
      ((lambdai.^2)-d^2))+((e.*(lambdai.^2))./((lambdai.^2)-f^2)))).^0.5;

%Calculate wp, ws and wi from lambda, and ns from resulting ws value.

wp = ((2*pi*cspeed)./(lambdap));
wi = ((2*pi*cspeed)./(lambdai));
ws = ((2*wp)-wi);

lambdas = ((2*pi*cspeed)./ws);
ns= ((1+((a.*(lambdas.^2))./((lambdas.^2)-b^2))+((c.*(lambdas.^2))./
     ((lambdas.^2)-d^2))+((e.*(lambdas.^2))./((lambdas.^2)-f^2)))).^0.5;

%Calculate and plot the phase change vs. the pump wavelength. The zero
%crossing points of this function should give the value for ws with respect
%to the chosen wi value. Collect this data for a range of wi and plot with
%respect to wp to obtain spectrum.
deltak = (((2.*wp.*np)./cspeed)-(((ws).*ns)./cspeed)-((wi.*ni)./cspeed)+
          ((2*deltan*wp)./cspeed));
dndeltak = diff(deltak)./diff(lambdap);
absdeltak=(deltak);

H = vertcat(H,deltak);
temp = real(deltak);

for ii = 1:length(deltak) -1
    if(temp(ii) < 0 && temp(ii+1) > 0)
        if(lambdap(ii)<lambdai)
```

```
        wavelengthp=lambdap(ii);
        wavelengthi=lambdai;
        wp = ((2*pi*cspeed)./(wavelengthp));
        wi = ((2*pi*cspeed)./(wavelengthi));
        ws = ((2*wp)-wi);
        wavelengths = ((2*pi*cspeed)./(ws));
        M = [wavelengths,wavelengthp,wavelengthi];
        G = vertcat(G,M);
        end
    end
end
end

figure
contour(lambdap,wavelength1i,real(H),[0,0],'-k')
hold on
pcolor(lambdap,wavelength1i,real(H)), shading flat
colorbar
axis([0.6 0.8 0.5 1.0])
caxis([-0.005 0.005])
xlabel('\lambda_p (\mum)')
ylabel('\lambda_s, \lambda_i (\mum)')
hold off
```

Appendix E

Publications

E.1 Journal Articles

H. L. Rogers, C. Holmes, J. C. Gates, and P. G. R. Smith, "Analysis of Dispersion Characteristics of Planar Waveguides via Multi-Order Interrogation of Integrated Bragg Gratings," *IEEE Photonics Journal*, vol. 4, no. 2, pp. 310–316, Apr. 2012.

H. L. Rogers, S. Ambran, C. Holmes, P. G. R. Smith, and J. C. Gates, "*In situ* loss measurement of direct UV-written waveguides using integrated Bragg gratings.," *Optics Letters*, vol. 35, no. 17, pp. 2849–2851, Sept. 2010.

C. Sima, J. C. Gates, H. L. Rogers, P. L. Mennea, C. Holmes, M. N. Zervas and P. G. R. Smith, "Phase controlled integrated interferometric single-sideband filter based on planar Bragg gratings implementing photonic Hilbert transform," *Optics Letters*, in press, 2013.

G. Lepert, M. Trupke, E. Hinds, H. L. Rogers, J. C. Gates, and P. G. R. Smith, "Demonstration of UV-written waveguides, Bragg gratings and cavities at 780 nm, and an original experimental measurement of group delay," *Optics Express*, vol. 19, no. 25, pp. 24933–24943, 2011.

C. Holmes, L. G. Carpenter, H. L. Rogers, I. J. G. Sparrow, J. C. Gates, and P. G. R. Smith, "Planar waveguide tilted Bragg grating refractometer fabricated through physical micromachining and direct UV writing," *Optics Express*, vol. 19, no. 13, pp. 12462–12468, 2011.

C. Holmes, L. G. Carpenter, H. L. Rogers, J. C. Gates, and P. G. R. Smith, "Physical sensitivity of silica micro-cantilevers fabricated using direct UV writing and micromachining," *Journal of Laser Micro/Nano Engineering*, vol. 6, no. 1, pp. 26–30, 2011.

C. Holmes, L. G. Carpenter, H. L. Rogers, J. C. Gates, and P. G. R. Smith, "Quantifying the optical sensitivity of planar Bragg gratings in glass microcantilevers to physical deflection.," *Journal of Micromechanics and Microengineering*, vol. 21, 035014, 2011.

R. M. Parker, J. C. Gates, H. L. Rogers, P. G. R. Smith, and M. C. Grossel, "Using the photoinduced reversible refractive index of an azobenzene copolymer to reconfigure an optical Bragg grating," *Journal of Materials Chemistry*, vol. 20, no. 41, pp. 9118–9125, 2010.

L. G. Carpenter, C. Holmes, H. L. Rogers, P. G. R. Smith, and J. C. Gates, "Integrated optic glass microcantilevers with Bragg grating interrogation," *Optics Express*, vol. 18, no. 22, pp. 23296–23301, 2010.

E.2 Conference Papers

H. L. Rogers, C. Holmes, K. R. Daly, L. G. Carpenter, J. C. Gates, G. D'Alessandro and P. G. R. Smith, "Tilted Bragg grating based optical components within an integrated planar platform," in *SPIE Photonics West*, (San Francisco, USA), 2013. (Oral presentation)

H. L. Rogers, C. Holmes, P. L. Mennea, J. C. Gates, P. G. R. Smith, K. R. Daly, and G. D'Alessandro, "Experimental observation of coupling between physically separated planar waveguides utilising tilted Bragg grating structures," in *European Conference on Integrated Optics*, (Sitges, Barcelona), 2012. (Poster presentation)

H. L. Rogers, L. G. Carpenter, S. Ambran, C. Sima, D. J. Wales, B. D. Snow, R. M. Parker, C. Holmes, J. C. Gates, and P. G. R. Smith, "Direct Grating Writing - single step Bragg grating and waveguide fabrication for telecommunications and sensing applications," in *IONS NA-3*, (Stanford), 2011. (Poster presentation)

H. L. Rogers, C. Holmes, J. C. Gates, and P. G. R. Smith, "Direct refractive index measurement technique to observe waveguide dispersion," in *Conference on Lasers and Electro-Optics/International Quantum Electronics Conference*, (Munich), 2011. (Oral presentation)

H. L. Rogers, L. G. Carpenter, S. Ambran, C. Sima, B. D. Snow, R. M. Parker, C. Holmes, J. C. Gates, and P. G. R. Smith, "Direct Grating Writing - single step Bragg grating and waveguide fabrication for telecommunications and sensing applications," in *IONS 9*, (Salamanca), 2011. (Oral presentation)

H. L. Rogers, J. C. Gates, and P. G. R. Smith, "Novel technique for measuring dispersion and detuning of a UV written silica-on-silicon waveguide," in *Photon 10*, (Southampton), 2010. (Oral presentation)

H. L. Rogers, J. C. Gates, S. Ambran, and P. G. R. Smith, "New Technique for Loss Measurement of a Direct UV Written Silica-on-Silicon Waveguide using Integrated Bragg Grating Structures," in *European Conference on Integrated Optics*, (Cambridge), 2010. (Poster presentation)

L. G. Carpenter, H. L. Rogers, C. Holmes, J. C. Gates, and P. G. R. Smith, "Polish-like facet preparation via dicing for silica integrated optics," in *SPIE Photonics West*, (San Francisco, USA), 2013.

C. Sima, J. C. Gates, H. L. Rogers, P. L. Mennea, C. Holmes, M. N. Zervas and P. G. R. Smith, "Phase modulated direct UV grating writing technique for ultra-wide spectrum planar Bragg grating fabrication," in *SPIE Photonics West*, (San Francisco, USA), 2013.

L. G. Carpenter, P. L. Mennea, H. L. Rogers, C. Holmes, J. C. Gates, and P. G. R. Smith, "Integrated corner mirrors as a platform for miniaturized planar strain sensing," in *European Conference on Integrated Optics*, (Sitges, Barcelona), 2012.

C. Holmes, L. G. Carpenter, P. A. Cooper, H. L. Rogers, J. C. Gates, and P. G. R. Smith, "Micro-mechanical integrated optical structures," in *European Conference on Integrated Optics*, (Sitges, Barcelona), 2012.

C. Sima, J. C. Gates, H. L. Rogers, P. L. Mennea, C. Holmes, M. N. Zervas, and P. G. R. Smith, "Interferometric integrated planar Bragg grating filter for all-optical single-sideband suppression," in *European Conference on Integrated Optics*, (Sitges, Barcelona), 2012.

C. Sima, J. C. Gates, B. D. Snow, H. L. Rogers, C. Holmes, M. N. Zervas, and P. G. R. Smith, "All-optical signal processing using planar Bragg gratings," in *Photonics and Optoelectronics Meeting*, (Wuhan), 2011.

C. Sima, J. C. Gates, H. L. Rogers, C. Holmes, M. N. Zervas, and P. G. R. Smith, "Integrated all-optical SSB modulator using photonic Hilbert transformer with planar Bragg gratings," in *Conference on Lasers and Electro-Optics/European Quantum Electronics Conference*, (Munich), 2011.

L. G. Carpenter, H. L. Rogers, C. Holmes, J. C. Gates, and P. G. R. Smith, "Physically micromachined silica-on-silicon integrated corner mirrors," in *Conference on Lasers and Electro-Optics/European Quantum Electronics Conference*, (Munich), 2011.

L. G. Carpenter, H. L. Rogers, C. Holmes, J. C. Gates, and P. G. R. Smith, "Integrated corner mirrors physically micromachined in silica-on-silicon," in *IONS 9*, (Salamanca), 2011.

C. Sima, J. C. Gates, B. D. Snow, H. L. Rogers, C. Holmes, M. N. Zervas, and P. G. R. Smith, "Simple planar Bragg grating devices for photonic Hilbert transform," in *Photonics and Optoelectronics Meeting*, (Wuhan), 2010.

C. Sima, J. C. Gates, B. D. Snow, H. L. Rogers, C. Holmes, M. N. Zervas, and P. G. R. Smith, "Realisation of a photonic Hilbert transformer with a simple planar Bragg grating," in *Photon 10*, (Southampton), 2010.

S. Ambran, H. L. Rogers, A. S. Webb, J. C. Gates, C. Holmes, P. G. R. Smith, and J. Sahu, "A loss comparison of flat-fiber and silica-on-silicon direct UV written waveguides using a novel Bragg grating measurement technique," in *Photon 10*, (Southampton), 2010.

L. G. Carpenter, C. Holmes, H. L. Rogers, J. C. Gates, and P. G. R. Smith, "Integrated optical glass microcantilevers for displacement and pressure sensing," in *IONS 8*, (Moscow), 2010.

C. Holmes, L. G. Carpenter, H. L. Rogers, J. C. Gates, and P. G. R. Smith, "Physical sensitivity of silica microcantilevers fabricated using direct UV writing and micromachining," in *Proceedings of the 11th International Symposium on Laser Precision Microfabrication*, (Stuttgart), 2010.

C. Holmes, L. G. Carpenter, H. L. Rogers, J. C. Gates, and P. G. R. Smith, "Silica based microcantilevers fabricated using direct UV writing and micromachining for chemical and physical sensing applications," in *Laser Precision Microfabrication*, (Stuttgart), 2010.

C. Holmes, L. G. Carpenter, H. L. Rogers, J. C. Gates, and P. G. R. Smith, "Detection of first order phase transitions using direct UV written intergrated optical planar Bragg gratings intrinsically defined within a silica micro-cantilever," in *Conference on Lasers and Electro-Optics/The Quantum Electronics and Laser Science Conference*, (San Jose), 2010.

R. M. Parker, J. C. Gates, H. L. Rogers, M. C. Grossel, and P. G. R. Smith, "An Integrated Reconfigurable Bragg Grating utilising a Photoresponsive Co-polymer," in *European Conference on Integrated Optics*, (Cambridge), 2010.

C. Sima, J. C. Gates, B. D. Snow, H. L. Rogers, M. N. Zervas, and P. G. R. Smith, "Realization of a planar Bragg grating for all-optical Hilbert transformer," in *European Conference on Integrated Optics*, (Cambridge), 2010.

L. G. Carpenter, C. Holmes, H. L. Rogers, J. C. Gates, and P. G. R. Smith, "Investigating Planar Integrated Glass Cantilevers Utilizing Bragg Gratings and Mechanical Resonance in a Vacuum," in *European Conference on Integrated Optics*, (Cambridge), 2010.

B. D. Snow, H. L. Rogers, C. Holmes, J. C. Gates, C. Sima, M. Kaczmarek, and P. G. R. Smith, "UV-written planar chirped Bragg gratings for use in dispersion management," in *European Conference on Integrated Optics*, (Cambridge), 2010.

Bibliography

[1] T. H. Maiman, "Stimulated Optical Radiation in Ruby," *Nature*, vol. 187, pp. 493–494, 1960.

[2] R. Mears, L. Reekie, I. Jauncey, and D. N. Payne, "Low-noise erbium-doped fibre amplifiers operating at 1.54 μm," *Electronics Letters*, vol. 23, pp. 1026–1028, 1987.

[3] S. E. Miller, "Integrated optics: An introduction," *Bell Systems Technical Journal*, vol. 48, pp. 2059–2069, 1969.

[4] G. D. Emmerson, S. P. Watts, C. B. E. Gawith, V. Albanis, M. Ibsen, R. Williams, and P. G. R. Smith, "Fabrication of directly UV-written channel waveguides with simultaneously defined integral Bragg gratings," *Electronics Letters*, vol. 38, no. 24, pp. 1531–1532, 2002.

[5] M. Svalgaard, *Ultraviolet light induced refractive index structures in germanosilica.* Doctoral thesis, Technical University of Denmark, 1997.

[6] S. P. Watts, *Flame hydrolysis deposition of photosensitive silicate layers for the definition of waveguiding structures through direct ultraviolet writing.* Doctoral thesis, University of Southampton, 2002.

[7] I. J. G. Sparrow, *Development and Applications of UV Written Waveguides.* Doctoral thesis, University of Southampton, 2005.

[8] G. D. Emmerson, *Novel direct UV written devices.* Doctoral thesis, University of Southampton, 2003.

[9] D. A. Guilhot, *UV-written devices in rare-earth doped silica-on-silicon grown by FHD.* Doctoral thesis, University of Southampton, 2004.

[10] C. Holmes, *Direct UV Written Planar Devices for Sensing and Telecommunication Applications.* Doctoral thesis, University of Southampton, 2009.

[11] R. M. Parker, *Optofluidic Bragg grating sensors for chemical detection.* Doctoral thesis, University of Southampton, 2010.

[12] B. D. Snow, *Liquid crystal adaptive planar optical devices.* Doctoral thesis, University of Southampton, 2010.

[13] D. O. Kundys, J. C. Gates, S. Dasgupta, C. B. E. Gawith, and P. G. R. Smith, "Use of Cross-Couplers to Decrease Size of UV Written Photonic Circuits," *IEEE Photonics Technology Letters*, vol. 21, no. 13, pp. 947–949, 2009.

[14] J. Bautista and R. Atkins, "The formation and deposition of SiO_2 aerosols in optical fiber manufacturing torches," *Journal of Aerosol Science*, vol. 22, no. 5, pp. 667–675, 1991.

[15] D. S. Gill, A. Anderson, R. W. Eason, T. J. Warburton, and D. P. Shepherd, "Laser operation of an Nd:$Gd_3Ga_5O_{12}$ thin-film optical waveguide fabricated by pulsed laser deposition," *Applied Physics Letters*, vol. 69, no. 1, p. 10, 1996.

[16] E. M. Yeatman, K. Pita, M. M. Ahmad, A. Vannucci, and A. Fiorello, "Strip-Loaded High-Confinement Waveguides for Photonic Applications," *Journal of Sol-gel Science and Technology*, vol. 13, pp. 517–521, 1998.

[17] L. Eldada and L. Shacklette, "Advances in polymer integrated optics," *IEEE Journal of Selected Topics in Quantum Electronics*, vol. 6, pp. 54–68, Jan-Feb 2000.

[18] S. Somekh, E. Garmire, A. Yariv, H. L. Garvin, and R. G. Hunsperger, "Channel Optical Waveguides and Directional Couplers in GaAs - lmbedded and Ridged," *Applied Optics*, vol. 13, no. 2, pp. 327–330, 1974.

[19] G. Li, K. A. Winick, H. C. Griffin, and J. S. Hayden, "Systematic modeling study of channel waveguide fabrication by thermal silver ion exchange," *Applied Optics*, vol. 45, no. 8, pp. 1743–1755, 2006.

[20] S. Sze, *VLSI Technology.* New York: McGraw-Hill, second ed., 1988.

[21] K. M. Davis, K. Miura, N. Sugimoto, and K. Hirao, "Writing waveguides in glass with a femtosecond laser," *Optics Letters*, vol. 21, pp. 1729–1731, Nov. 1996.

[22] T. Allsop, K. Kalli, K. Zhou, G. N. Smith, M. Komodromos, J. Petrovic, D. J. Webb, and I. Bennion, "Spectral characteristics and thermal evolution of long-period gratings in photonic crystal fibers fabricated with a near-IR radiation femtosecond laser using point-by-point inscription," *Journal of the Optical Society of America B*, vol. 28, p. 2105, Aug. 2011.

[23] G. D. Marshall, R. J. Williams, N. Jovanovic, M. J. Steel, and M. J. Withford, "Point-by-point written fiber-Bragg gratings and their application in complex grating designs.," *Optics Express*, vol. 18, pp. 19844–59, Sept. 2010.

[24] W. H. Loh, M. J. Cole, M. Zervas, S. Barcelos, and R. I. Laming, "Complex grating structures with uniform phase masks based on the moving fiber-scanning beam technique," *Optics Letters*, vol. 20, no. 20, pp. 2051–2053, 1995.

[25] R. F. Bunshah, "Critical Issues in Plasma-Assisted Vapor Deposition Processes," *IEEE Transactions on Plasma Science*, vol. 18, no. 6, pp. 846–854, 1990.

[26] S. Sakaguchi, "Consolidation of silica glass soot body prepared by flame hydrolysis reaction," *Journal of Non-crystalline Solids*, vol. 171, pp. 249–258, 1994.

[27] G. Grand, J. P. Jadot, H. Denis, S. Valette, A. Fournier, and A. M. Grouillet, "Low loss PECVD silica channel waveguides for optical communications," *Electronics Letters*, vol. 26, no. 25, pp. 2135–2137, 1990.

[28] D. Gloge, "Weakly guiding fibers," *Applied Optics*, vol. 10, pp. 2252–8, Oct. 1971.

[29] A. K. Ghatak and K. Thyagarajan, "Modes in planar waveguides," in *Introduction to Fiber Optics*, ch. 7, pp. 97–131, Cambridge University Press, 1998.

[30] K. Okamoto, "Slab Waveguides," in *Fundamentals of Optical Waveguides*, ch. 2, pp. 13–26, San Diego, CA: Academic Press, first ed., 2000.

[31] D. J. Griffiths, "Electrodynamics," in *Introduction to Electrodynamics*, ch. 7, pp. 285–342, Upper Saddle River, NJ: Prentice Hall International, third ed., 1999.

[32] A. K. Ghatak and K. Thyagarajan, "TM modes of a symmetric step index planar waveguide," in *Introduction to Fiber Optics*, ch. 7, pp. 109–113, Cambridge: Cambridge University Press, first ed., 1998.

[33] K. Okamoto, "Effective index method," in *Fundamentals of Optical Waveguides*, ch. 2, pp. 35–39, San Diego, CA: Academic Press, first ed., 2000.

[34] K. S. Chiang, "Analysis of Rectangular Dielectric Waveguides: Effective-Index Method with Built-in Perturbation Correction," *Electronics Letters*, vol. 28, no. 4, pp. 388–390, 1992.

[35] J. Reitz, F. Milford, and R. Christy, "Numerical solution of electrostatic problems," in *Foundations of electromagnetic theory*, ch. 3, pp. 77–84, San Francisco, CA: Pearson Addison-Wesley, fourth ed., 2009.

[36] K. Okamoto, "Beam Propagation Method," in *Fundamentals of Optical Waveguides*, ch. 7, pp. 273–321, San Diego, CA: Academic Press, first ed., 2000.

[37] G. D. Marshall, M. Ams, and M. J. Withford, "Direct laser written waveguide-Bragg gratings in bulk fused silica.," *Optics Letters*, vol. 31, pp. 2690–1, Sept. 2006.

[38] G. Meltz, W. W. Morey, and W. H. Glenn, "Formation of Bragg gratings in optical fibers by a transverse holographic method," *Optics Letters*, vol. 14, pp. 823–825, Aug. 1989.

[39] K. O. Hill, B. Malo, F. Bilodeau, D. C. Johnson, and J. Albert, "Bragg gratings fabricated in monomode photosensitive optical fiber by UV exposure through a phase mask," *Applied Physics Letters*, vol. 62, no. 10, p. 1035, 1993.

[40] J. Canning, "Fibre gratings and devices for sensors and lasers," *Laser and Photonics Review*, vol. 2, pp. 275–289, Aug. 2008.

[41] R. Kashyap, "Theory of fiber Bragg gratings," in *Fiber Bragg Gratings*, ch. 4, pp. 119–194, San Diego, CA: Academic Press, first ed., 1999.

[42] H. Kogelnik, "Filter response of nonuniform almost-periodic structures," *The Bell System Technical Journal*, vol. 55, no. 1, pp. 109–126, 1976.

[43] T. Erdogan, "Fiber Grating Spectra," *Journal of Lightwave Technology*, vol. 15, no. 8, pp. 1277–1294, 1997.

[44] W. Callister, *Materials Science and Engineering, An Introduction.* Wiley, 7 ed., 2007.

[45] S. Sudo, M. Kawachi, T. Edahiro, T. Izawa, T. Shioda, and H. Gotoh, "Low-OH-content optical fibre fabricated by vapour-phase axial-deposition method," *Electronics Letters*, vol. 14, no. 17, pp. 534–535, 1978.

[46] M. Blankenship and C. Deneka, "The Outside Vapor Deposition Method of Fabricating Optical Waveguide Fibers," *IEEE Journal of Quantum Electronics*, vol. QE-18, no. 10, pp. 1418–1423, 1982.

[47] D. L. Williams, B. J. Ainslie, J. Armitage, R. Kashyap, and R. Campbell, "Enhanced UV photosensitivity in boron codoped germanosilicate fibres," *Electronics Letters*, vol. 29, no. 1, pp. 45–47, 1993.

[48] A. Varshneya, *Fundamentals of inorganic glasses.* San Diego: Academic Press, 1 ed., 1994.

[49] L. G. Carpenter, C. Holmes, H. L. Rogers, J. C. Gates, and P. G. R. Smith, "Investigating Planar Integrated Glass Cantilevers Utilizing Bragg Gratings and Mechanical Resonance in a Vacuum," in *European Conference on Integrated Optics*, (Cambridge), 2010.

[50] R. M. Parker, J. C. Gates, H. L. Rogers, P. G. R. Smith, and M. C. Grossel, "Using the photoinduced reversible refractive index change of an azobenzene copolymer to reconfigure an optical Bragg grating," *Journal of Materials Chemistry*, vol. 20, no. 41, pp. 9118–9125, 2010.

[51] D. A. Guilhot, G. D. Emmerson, C. B. E. Gawith, S. P. Watts, D. P. Shepherd, R. B. Williams, and P. G. R. Smith, "Single mode direct-UV-written channel waveguide laser in neodymium-doped silica on silicon," *Optics Letters*, vol. 29, no. 9, pp. 947–949, 2004.

[52] P. Tien, "Light waves in thin films and integrated optics," *Applied Optics*, vol. 10, no. 11, pp. 2395–2413, 1971.

[53] K. Hill, Y. Fujii, D. Johnson, and B. Kawasaki, "Photosensitivity in optical fiber waveguides: Application to reflection filter fabrication," *Applied Physics Letters*, vol. 32, no. 10, pp. 647–649, 1978.

[54] D. P. Hand and P. S. J. Russell, "Photoinduced refractive-index changes in germanosilicate fibers.," *Optics Letters*, vol. 15, pp. 102–104, Jan. 1990.

[55] M. Douay, W. X. Xie, T. Taunay, P. Bernage, P. Niay, P. Cordier, B. Poumellec, L. Dong, J. F. Bayon, H. Poignant, and E. Delevaque, "Densification Involved in the UV-Based Photosensitivity of Silica Glasses and Optical Fibers," *J. Lightwave Technol.*, vol. 15, no. 8, pp. 1329–1342, 1997.

[56] H. Hosono, Y. Abe, D. L. Kinser, R. A. Weeks, K. Muta, and H. Kawazoe, "Nature and origin of the 5-eV band in SiO_2:GeO_2 glasses," *Physical Review B*, vol. 46, no. 18, pp. 11445–11451, 1992.

[57] M. Fujimaki, T. Watanabe, T. Katoh, T. Kasahara, N. Miyazaki, Y. Ohki, and H. Nishikawa, "Structures and generation mechanisms of paramagnetic centers and absorption bands responsible for Ge-doped SiO_2 optical-fiber gratings," *Physical Review B*, vol. 57, no. 7, pp. 3920–3926, 1998.

[58] J. Stone, "Interactions of hydrogen and deuterium with silica optical fibers: A review," *Journal of Lightwave Technology*, vol. 5, no. 5, pp. 712–733, 1987.

[59] P. Lemaire, R. Atkins, V. Mizrahi, and W. A. Reed, "High pressure H_2 loading as a technique for achieveing ultrahigh UV photosensitivity and thermal sensitivity in GeO_2 doped optical fibres," *Electronics Letters*, vol. 29, no. 13, pp. 1191–1193, 1993.

[60] P. J. Lemaire, "Reliability of optical fibers exposed to hydrogen: prediction of long-term loss increases," *Optical Engineering*, vol. 30, no. 6, p. 780, 1991.

[61] R. M. Parker, J. C. Gates, H. L. Rogers, M. C. Grossel, and P. G. R. Smith, "An Integrated Reconfigurable Bragg Grating utilising a Photoresponsive Co-polymer," in *European Conference on Integrated Optics*, (Cambridge), 2010.

[62] H. L. Rogers, S. Ambran, C. Holmes, P. G. R. Smith, and J. C. Gates, "In situ loss measurement of direct UV-written waveguides using integrated Bragg gratings.," *Optics Letters*, vol. 35, pp. 2849–51, Sept. 2010.

[63] H. L. Rogers, C. Holmes, J. C. Gates, and P. G. R. Smith, "Analysis of Dispersion Characteristics of Planar Waveguides via Multi-Order Interrogation of Integrated Bragg Gratings," *IEEE Photonics Journal*, vol. 4, pp. 310–316, Apr. 2012.

[64] L. G. Carpenter, P. L. Mennea, H. L. Rogers, C. Holmes, J. C. Gates, and P. G. R. Smith, "Integrated corner mirrors as a platform for miniaturized planar strain sensing," in *European Conference on Integrated Optics*, (Sitges, Barcelona), 2012.

[65] H. L. Rogers, J. C. Gates, S. Ambran, and P. G. R. Smith, "New Technique for Loss Measurement of a Direct UV Written Silica-on-Silicon Waveguide using Integrated Bragg Grating Structures," in *European Conference on Integrated Optics*, (Cambridge), 2010.

[66] L. G. Carpenter, C. Holmes, H. L. Rogers, J. C. Gates, and P. G. R. Smith, "Integrated optical glass microcantilevers for displacements and pressure sensing," in *IONS 8*, (Moscow), 2010.

[67] C. B. E. Gawith, G. D. Emmerson, S. G. McMeekin, J. R. Bonar, R. I. Laming, R. B. Williams, and P. G. R. Smith, "Small-spot interference pattern for single-step 2D integration and wide wavelength detuning of planar Bragg gratings.," *Electronics Letters*, vol. 39, no. 14, pp. 1050–1051, 2003.

[68] T. Duthel, S. Jansen, M. Otto, P. Krummrich, and C. Schaffer, "Tunable all-fibre delay line filter for residual dispersion compensation in 40 Gbit/s systems," *Electronics Letters*, vol. 40, pp. 1291–1293, 2004.

[69] B. D. Snow, H. L. Rogers, C. Holmes, J. C. Gates, C. Sima, M. Kaczmarek, and P. G. R. Smith, "UV-written planar chirped Bragg gratings for use in dispersion management," in *European Conference on Integrated Optics*, (Cambridge), 2010.

[70] M. H. Asghari and J. Azaña, "All-optical Hilbert transformer based on a single phase-shifted fiber Bragg grating: design and analysis.," *Optics Letters*, vol. 34, no. 3, pp. 334–336, 2009.

[71] C. Sima, J. C. Gates, H. L. Rogers, P. L. Mennea, C. Holmes, M. N. Zervas, and P. G. R. Smith, "Interferometric integrated planar Bragg grating filter for all-optical single-sideband suppression," in *European Conference on Integrated Optics*, (Sitges, Barcelona), 2012.

[72] G. Lepert, M. Trupke, E. A. Hinds, H. L. Rogers, J. C. Gates, and P. G. R. Smith, "Demonstration of UV-written waveguides, Bragg gratings and cavities at 780 nm, and an original experimental measurement of group delay," *Optics Express*, vol. 19, no. 25, pp. 24933–24943, 2011.

[73] C. Holmes, K. R. Daly, I. J. G. Sparrow, J. C. Gates, G. D'Alessandro, and P. G. R. Smith, "Excitation of Surface Plasmons using tilted planar-waveguide Bragg gratings," *IEEE Photonics Journal*, vol. 3, no. 5, pp. 777–788, 2011.

[74] R. G. Hunsperger, "Losses in Optical Waveguides," in *Integrated Optics: Theory and Technology*, ch. 6, pp. 107–128, New York: Springer, sixth ed., 2009.

[75] J. Wilson and J. Hawkes, "Free Space Communications," in *Optoelectronics: an introduction*, ch. 9, pp. 436–438, Harlow, England: Prentice Hall Europe, third ed., 1998.

[76] K. Iizuka, "Transmission Loss of Fibers," in *Elements of Photonics, Volume II, for Fiber and Integrated Optics*, ch. 11, pp. 694–695, New York: Wiley, first ed., 2002.

[77] J. Wilson and J. Hawkes, "Single fiber jointing," in *Optoelectronics: an introduction*, ch. 8, pp. 397–402, Harlow, England: Prentice Hall Europe, third ed., 1998.

[78] A. K. Ghatak and K. Thyagarajan, "Reflection at a plane interface," in *Introduction to Fiber Optics*, pp. 16–17, 1998.

[79] T. Feuchter and C. Thirstrup, "High-Precision Planar Waveguide Propagation Loss Measurement Technique Using a Fabry-Perot Cavity," *IEEE Photonics Technology Letters*, vol. 6, no. 10, pp. 1244–1247, 1994.

[80] Y. Okamura, S. Yoshinaka, and S. Yamamoto, "Measuring mode propagation losses of integrated optical waveguides: a simple method," *Applied Optics*, vol. 22, pp. 3892–3894, Dec. 1983.

[81] A. K. Ghatak and K. Thyagarajan, "Measurement of attenuation," in *Introduction to Fiber Optics*, pp. 413–416, Cambridge University Press, 1998.

[82] S. Chen, Q. Yan, Q. Xu, Z. Fan, and J. Liu, "Optical waveguide propagation loss measurement using multiple reflections method," *Optics Communications*, vol. 256, pp. 68–72, Dec. 2005.

[83] Y. H. Won, P. C. Jaussaud, and G. H. Chartier, "Three-prism loss measurements of optical waveguides," *Applied Physics Letters*, vol. 37, no. 3, pp. 269–271, 1980.

[84] M. Haruna, Y. Segawa, and H. Nishihara, "Nondestructive and simple method of optical-waveguide loss measurement with optimisation of end-fire coupling," *Electronics Letters*, vol. 28, no. 17, pp. 1612–1613, 1992.

[85] H. M. Lee, M. C. Oh, H. Park, W. Y. Hwang, and J. J. Kim, "End-face scattering loss in integrated-optical waveguides," *Applied Optics*, vol. 36, pp. 9021–9024, Dec. 1997.

[86] A. Boudrioua and J. C. Loulergue, "New approach for loss measurements in optical planar waveguides," *Optics Communications*, vol. 137, pp. 37–40, Apr. 1997.

[87] A. Othonos and K. Kalli, "Properties of Fiber Bragg Gratings," in *Fiber Bragg Gratings*, ch. 3, pp. 95–147, Norwood, MA: Artech House, Inc., 1 ed., 1999.

[88] M. Svalgaard and M. Kristensen, "Directly UV written silica-on-silicon planar waveguides with low loss," *Electronics Letters*, vol. 33, no. 10, pp. 861–863, 1997.

[89] D. Griffiths, "Absorption and dispersion," in *Introduction to Electrodynamics*, ch. 9, pp. 392–405, Upper Saddle River, NJ: Prentice Hall International, third ed., 1999.

[90] J. Jackson, *Classical electrodynamics*. Hamilton Printing Co, 3 ed., 1998.

[91] F. Wooten, *Optical Properties of Solids*. New York: Academic Press, 1972.

[92] B. Tatian, "Fitting refractive-index data with the Sellmeier dispersion formula," *Applied Optics*, vol. 23, pp. 4477–4485, Dec. 1984.

[93] A. K. Ghatak and K. Thyagarajan, "Material Dispersion," in *Introduction to Fiber Optics*, ch. 6, pp. 78–97, Cambridge University Press, 1998.

[94] A. K. Ghatak and K. Thyagarajan, "Waveguide dispersion and design considerations," in *Introduction to Fiber Optics*, ch. 10, pp. 184–199, Cambridge University Press, 1998.

[95] D. Gloge, "Dispersion in weakly guiding fibers," *Applied Optics*, vol. 10, pp. 2442–5, Nov. 1971.

[96] D. Marcuse, "Interdependence of waveguide and material dispersion.," *Applied Optics*, vol. 18, pp. 2930–2, Oct. 1979.

[97] W. Hermann and D. U. Wiechert, "Refractive Index of Doped and Undoped PCVD Bulk Silica," *Materials Research Bulletin*, vol. 24, no. 9, pp. 1083–1097, 1989.

[98] L. G. Cohen, "Comparison of single-mode fiber dispersion measurement techniques," *Journal of Lightwave Technology*, vol. LT-3, no. 5, pp. 958–966, 1985.

[99] M. Tateda, N. Shibata, and S. Seikai, "Interferometric method for chromatic dispersion measurement in a single-mode optical fiber," *IEEE Journal of Quantum Electronics*, vol. QE-17, pp. 404–407, Mar. 1981.

[100] K. Okamoto, T. Hosaka, and H. Itoh, "Measurement of chromatic dispersions in Ti-diffused LiNbO3 optical waveguides," *Optics Letters*, vol. 13, pp. 65–67, Jan. 1988.

[101] P. Hlubina, D. Ciprian, and M. Kadulová, "Measurement of chromatic dispersion of polarization modes in optical fibres using white-light spectral interferometry," *Measurement Science and Technology*, vol. 21, p. 045302, Apr. 2010.

[102] K. Thyagarajan, R. K. Varshney, P. Palai, A. K. Ghatak, and I. C. Goyal, "A novel design of a dispersion compensating fiber," *IEEE Photonics Technology Letters*, vol. 8, pp. 1510–1512, Nov. 1996.

[103] D. Menashe, M. Tur, and Y. Danziger, "Interferometric technique for measuring dispersion of high order modes in optical fibres," *Electonics Letters*, vol. 37, no. 24, pp. 1439–1440, 2001.

[104] B. J. Smith, P. Mahou, O. Cohen, J. S. Lundeen, and I. A. Walmsley, "Photon pair generation in birefringent optical fibers.," *Optics Express*, vol. 17, pp. 23589–23602, Dec. 2009.

[105] R. H. Stolen, M. A. Bösch, and C. Lin, "Phase matching in birefringent fibers.," *Optics Letters*, vol. 6, pp. 213–215, May 1981.

[106] H. L. Rogers, C. Holmes, J. C. Gates, and P. G. R. Smith, "Direct refractive index measurement technique to observe waveguide dispersion," in *Conference on Lasers and Electro-Optics/International Quantum Electronics Conference*, (Munich), 2011.

[107] A. K. Ghatak and K. Thyagarajan, "Modes in planar waveguides," in *Introduction to Fiber Optics*, ch. 7, pp. 97–124, Cambridge: Cambridge University Press, first ed., 1998.